

UNIVERSITÄT HAMBURG

DOKTORARBEIT

---

**Long-range interacting classical particle  
systems on curved manifolds: the helix,  
torus, and Möbius strip**

---

*Dissertation*

*zur Erlangung des Doktorgrades*

*an der Fakultät für Mathematik, Informatik und Naturwissenschaften,*

*Fachbereich Physik,*

*der Universität Hamburg*

*vorgelegt von*

**Ansgar Frederik SIEMENS**

Hamburg

December 5, 2024

Gutachter/innen der Dissertation:	Prof. Dr. Peter Schmelcher PD Dr. Elena Vedmedenko
Zusammensetzung der Prüfungskommission:	Prof. Dr. Daniela Pfannkuche Prof. Dr. Peter Schmelcher Dr. Thore Posske Prof. Dr. Nils Huse PD Dr. Elena Vedmedenko
Vorsitzende der Prüfungskommission:	Prof. Dr. Daniela Pfannkuche
Datum der Disputation:	25.11.2024
Vorsitzender Fach-Promotionsausschusses PHYSIK:	Prof. Dr. Markus Drescher
Leiter des Fachbereichs PHYSIK:	Prof. Dr. Wolfgang J. Parak
Dekan der Fakultät MIN:	Prof. Dr. Norbert Ritter





*This is for you.*



# Abstract

This thesis investigates the behavior of classical ions and dipoles that are confined to curved geometries. The combination of confining forces and the interactions between particles gives rise to geometry-dependent effective interactions. The latter exhibit different characteristics compared to interactions in flat geometries. For instance, Coulomb-interacting ions confined to a helical path exhibit oscillating effective interactions, allowing two or more ions to form a bound state. One example of such a bound state are two ions trapping each other on opposite sides of a helix winding. The diverse phenomenology induced by such geometry-dependent effective interactions is studied in detail throughout this thesis by considering a wide range of geometries, and both isotropic and anisotropic interparticle interactions.

We first investigate the impact of external electric fields on the properties of ions confined to a helix. We consider many-body equilibrium configurations on a toroidal helix, focusing on the evolution of these configurations in the presence of a static external electric field. We are able to characterize the statistical properties of these equilibria. Additionally, we find that by varying the field strength a crossover between staggered and ordered equilibrium configurations occurs. This crossover persists for a wide range of system parameters.

Next, we explore time-dependent fields. We analyze the dynamics of a single particle confined to a toroidal helix, driven by an either oscillating or rotating external field. Using phase space analysis, we identify a mechanism responsible for effectively inducing directed transport of the particle, with the transport direction being determined by the initial conditions. Remarkably, this directed transport occurs even without any bias or asymmetries in the driving potential. In the case of the oscillating external field, adding a static potential along the helical path will change the systems behavior to that of a generalized Kapitza pendulum.

We also investigate what happens when considering *anisotropic* dipole-dipole interactions instead of *isotropic* Coulomb interactions. We begin with a system of freely rotating dipoles at fixed equidistant positions along a helical path. Our analysis of the ground-state equilibrium configurations reveals a complex behavior and shows a dependence on geometrical parameters, such as the helix radius and the (parametric) distance between two dipoles along the helix. In particular, the equilibrium configurations can be uniquely described by integer tuples that can be mapped to fractions of the number-theoretical Farey sequence, while in the parameter space, a self-similar bifurcation tree akin to the Stern-Brocot tree is identified.

Beyond helical geometries, we explore dipole arrays on curved two-dimensional surfaces. For this setup, the geometric curvature can lead to a ground state exhibiting domain walls that separate regions of different dipole alignments. These curvature-induced domain walls behave differently from typical (degeneracy-induced) domain walls. We highlight these differences by examining the domain-walls response to an external field, as well as the impact of the domain-wall on the dispersion of excitations. Notably, for the latter example, low-energy dynamics are confined within the domains, without being able to cross the boundary of the domain wall. Finally, we show that the emergence and annihilation of these curvature-induced domains are accompanied by structural crossovers that are indicated by a dip in the 2D compression modulus.



# Zusammenfassung

Diese Dissertation untersucht das Verhalten von klassischen Ionen und Dipolen, die in gekrümmten Geometrien eingeschlossen sind. Die Kombination aus Zwangskräften und den Wechselwirkungen zwischen den Teilchen führt zu geometrieabhängigen effektiven Wechselwirkungen. Letztere zeigt einen anderen Character als Wechselwirkungen in flachen Geometrien. Beispielsweise zeigen Coulomb-wechselwirkende Ionen, die auf einem Helix-Pfad eingeschlossen sind, oszillierende effektive Wechselwirkungen, die es zwei oder mehr Ionen ermöglichen, einen gebundenen Zustand zu bilden. Ein Beispiel für einen solchen gebundenen Zustand ist, wenn sich zwei Ionen auf entgegengesetzten Seiten einer Helix-Windung einfangen. Diese Dissertation untersucht die vielfältige Phänomenologie, die durch solche geometrieabhängigen effektiven Wechselwirkungen hervorgerufen wird, wobei eine breite Auswahl von Geometrien sowie sowohl isotrope als auch anisotrope Interpartikelwechselwirkungen betrachtet werden.

Wir untersuchen zunächst die Auswirkungen von externen elektrischen Feldern auf die Eigenschaften von Ionen, die auf einer Helix eingeschlossen sind. Die Untersuchung beginnt mit Vielteilchen-Gleichgewichtskonfigurationen auf einem toroiden Helix und konzentriert sich auf die Entwicklung dieser Konfigurationen in Gegenwart eines statischen externen elektrischen Feldes. Wir charakterisieren die statistischen Eigenschaften dieser Gleichgewichtszustände. Darüber hinaus stellen wir fest, dass durch Variation der Feldstärke ein Übergang zwischen ungeordneten und geordneten Gleichgewichtskonfigurationen auftritt. Dieser Übergang besteht über einen weiten Bereich von Systemparametern hinweg.

Als Nächstes untersuchen wir zeitabhängige Felder. Wir analysieren die Dynamik eines einzelnen Teilchens, das auf einem toroiden Helix eingeschlossen ist und von einem oszillierenden oder rotierenden externen Feld angetrieben wird. Anhand einer Phasenraumanalyse identifizieren wir einen Mechanismus, der für die effektive Induzierung eines gerichteten Transports des Teilchens verantwortlich ist, wobei die Transportrichtung durch die Anfangsbedingungen bestimmt wird. Bemerkenswerterweise tritt dieser gerichtete Transport auch ohne jeglichen Bias oder Asymmetrien im antreibenden Potential auf. Im Falle des oszillierenden externen Feldes führt das Hinzufügen eines statischen Potentials entlang der Helix dazu, dass sich das Verhalten des Systems zu dem eines generalisierten Kapitza-Pendels ändert.

Außerdem untersuchen wir, was passiert, wenn *anisotrope* Dipol-Dipol-Wechselwirkungen anstelle von *isotropen* Coulomb-Wechselwirkungen berücksichtigt werden. Wir beginnen mit einem System aus frei rotierenden Dipolen an festen equidistanten Positionen entlang einer Helix. Unsere Analyse der Gleichgewichtskonfigurationen im Grundzustand zeigt ein komplexes Verhalten und eine Abhängigkeit von geometrischen Parametern wie dem Helixradius und der (parametrischen) Entfernung zwischen zwei Dipolen entlang der Helix. Insbesondere können die Gleichgewichtskonfigurationen eindeutig durch ganzzahlige Tupel beschrieben werden, die auf Bruchteile der zahlentheoretischen Farey-Folge abgebildet werden können, während wir im Parameterraum einen selbstähnlichen Bifurkationsbaum identifizieren der dem Stern-Brocot-Baum ähnelt.

Über die helikalen Geometrien hinaus erforschen wir Dipolarrays auf gekrümmten 2D-Oberflächen. Bei diesem Setup kann die geometrische Krümmung dazu führen, dass der Grundzustand Domänenwände aufweist, die Regionen unterschiedlicher Dipolausrichtungen voneinander trennen. Diese durch Krümmung induzierten Domänenwände verhalten sich anders als typische (durch Entartung induzierte) Domänenwände: Wir verdeutlichen diese Unterschiede anhand der Reaktion der

Domänenwände auf ein externes Feld sowie mit dem Einfluss der Domänenwände auf die Dispersion von Anregungen. Insbesondere bei letzterem Beispiel ist die Dynamik von kleinen Anregungen auf die Domänen beschränkt, ohne dass die begrenzende Domänenwand überschritten werden kann. Schließlich zeigen wir, dass die Erzeugung und Vernichtung dieser durch Krümmung induzierten Domänen von Strukturübergängen begleitet wird, die durch einen Einbruch im 2D-Kompressionsmodul gekennzeichnet sind.

# Contents

<b>Abstract</b>	<b>vii</b>
<b>Zusammenfassung</b>	<b>ix</b>
<b>Contents</b>	<b>xii</b>
<b>Preface</b>	<b>xvii</b>
<b>1 Introduction</b>	<b>1</b>
1.1 Structure and overview . . . . .	2
<b>2 Interacting particles and helical confinement</b>	<b>5</b>
2.1 Classical Coulomb systems and Wigner crystals . . . . .	5
2.2 The helical ion model . . . . .	7
2.2.1 The significance of the helical geometry . . . . .	7
2.2.2 The model . . . . .	8
2.2.3 Progress on the helical ion model . . . . .	10
2.3 Outline of Scientific contributions [A1–A3] . . . . .	12
2.3.1 Outline: Tunable order of helically confined charges [A1] . . . . .	14
2.3.2 Outline: External field-induced dynamics of a charged particle on a toroidal helix [A2] . . . . .	15
2.3.3 Outline: Driven toroidal helix as a generalization of the Kapitza pendulum [A3] . . . . .	16
<b>3 Helical dipole chains</b>	<b>17</b>
3.1 Properties and arrangements of classical dipole chains . . . . .	17
3.2 Cylindrical lattices and phyllotaxis . . . . .	19
3.3 Outline of scientific contribution [A4] . . . . .	21
3.3.1 Outline: Formation and crossover of multiple helical dipole chains [A4] . . . . .	21
<b>4 Dipole arrays on curved surfaces</b>	<b>23</b>
4.1 Equilibrium properties of dipole lattices . . . . .	23
4.2 Electric dipoles in ferroelectrics and dipolar rotors . . . . .	24
4.3 Magnetic dipoles and their interactions . . . . .	25
4.3.1 General considerations regarding magnetic dipole arrays . . . . .	25
4.3.2 Magnetic dipoles on curved surfaces . . . . .	26
4.4 Outline of Scientific contributions [A5, A6] . . . . .	27
4.4.1 Outline: Geometry induced domain-walls of dipole lattices on curved structures [A5] . . . . .	28
4.4.2 Outline: Compression-induced crossovers for the ground-state of classical dipole lattices on a Moöbius strip [A6] . . . . .	29

<b>5</b>	<b>Scientific Contributions</b>	<b>31</b>
5.1	Tunable order of helically confined charges . . . . .	33
5.2	External-field-induced dynamics of a charged particle on a closed helix	43
5.3	Driven toroidal helix as a generalization of the Kapitza pendulum . . .	53
5.4	Formation and crossover of multiple helical dipole chains . . . . .	61
5.5	Geometry induced domain-walls of dipole lattices on curved structures	73
5.6	Compression-induced crossovers for the ground-state of classical dipole lattices on a Moöbius strip . . . . .	91
<b>6</b>	<b>Summary and outlook</b>	<b>99</b>
6.1	Summary of the scientific contributions [A1–A6] . . . . .	99
6.2	Outlook . . . . .	100
6.2.1	Outlook regarding the helical ion model . . . . .	100
6.2.2	Outlook regarding curved dipole lattices . . . . .	102
	<b>Bibliography</b>	<b>105</b>
	<b>Acknowledgements</b>	<b>123</b>
	<b>Eidesstattliche Versicherung / Declaration of oath</b>	<b>125</b>

# List of Figures

2.1	Effective Coulomb interaction in a helical geometry . . . . .	10
3.1	The van Iterson diagram . . . . .	20



# List of Abbreviations

<b>1D</b>	<b>1 Dimensional</b>
<b>2D</b>	<b>2 Dimensional</b>
<b>3D</b>	<b>3 Dimensional</b>
<b>DW</b>	<b>Domain-Wall</b>
<b>GS</b>	<b>Ground-State</b>
<b>NN</b>	<b>Nearest Neighbor</b>
<b>NNN</b>	<b>Next Nearest Neighbor</b>
<b>OCP</b>	<b>One-Component Plasma</b>
<b>FK model</b>	<b>Frenkel-Kontorova model</b>
<b>BTA</b>	<b>trialkylbenzene-1,3,5-tricarboxamide</b>
<b>MOF</b>	<b>Metal-Organic Framework</b>



# Preface

## Outline of this thesis

This cumulative thesis is based on the publications [A1–A6]. These works investigate model systems and explore the effects of confining long-ranged interacting particles to curved geometries. An overview of these contributions, as well as their embedding within the wider literature, are provided in Chapters 2–4.

Chapter 2 addresses classical Coulomb-interacting ions confined to a helical geometry. It provides a general overview of classical Coulomb systems, as well as the existing literature on helically confined ions - together with an overview of the related scientific contributions [A1–A3].

Chapter 3 covers helical dipole chains. It includes an overview of classical dipole chains, as well as cylindrical phyllotaxis. The chapter concludes with an outline of the scientific contribution [A4].

Chapter 4 is concerned with the properties of dipole lattices spanned across curved manifolds. It gives an overview of classical dipole lattice systems and discusses the characteristics of magnetic and electric dipole arrays. It continues with an outline of the scientific contributions [A5, A6].

All scientific contributions are presented in Chapter 5. Finally, a summary of this thesis and concluding remarks are given in Chapter 6.

## Publications covered by this thesis

- [A1] A. Siemens and P. Schmelcher, “Tunable order of helically confined charges”, *Phys. Rev. E* **102**, 012147 (2020).
- [A2] A. Siemens and P. Schmelcher, “External-field-induced dynamics of a charged particle on a closed helix”, *Phys. Rev. E* **103**, 052217 (2021).
- [A3] J. F. Gloy, A. Siemens, and P. Schmelcher, “Driven toroidal helix as a generalization of the Kapitza pendulum”, *Phys. Rev. E* **105**, 054204 (2022).
- [A4] A. Siemens and P. Schmelcher, “Formation and crossover of multiple helical dipole chains”, *J. Phys. A: Math. Theor.* **55**, 375205 (2022).
- [A5] A. Siemens and P. Schmelcher, “Geometry induced domain-walls of dipole lattices on curved structures”, *J. Phys. A: Math. Theor.* **56**, 495702 (2023).
- [A6] A. Siemens, F. A. O. Silveira, and P. Schmelcher, “Compression-induced crossovers for the ground state of classical dipole lattices on a Möbius strip”, *Phys. Rev. E* **109**, 064125 (2024).

## Further publications

- [A7] A. Siemens, Y. Zhang, J. Hagemester, E. Y. Vedmedenko, and R. Wiesendanger, “Minimal radius of magnetic skyrmions: statics and dynamics”, *New J. Phys.* **18**, 045021 (2016).
- [A8] J. Hagemester, A. Siemens, L. Rózsa, E. Y. Vedmedenko, and R. Wiesendanger, “Controlled creation and stability of  $k\pi$  skyrmions on a discrete lattice”, *Phys. Rev. B* **97**, 174436 (2018).
- [A9] A. Siemens and P. Schmelcher, *Classical scattering and fragmentation of clusters of ions in helical confinement*, Sept. 2024, [arXiv:2409.04852](https://arxiv.org/abs/2409.04852).

## Background and declaration of personal contributions to the publications [A1–A6]

The first work [A1] was an attempt to understand for the first time the many-body equilibrium configurations of ions confined to a toroidal helix, and their dependence on a static external electric field. In [A2], we then became interested in the dynamics arising when time-dependent electric fields are employed to drive particles in helical confinement. This led to a third work [A3], which demonstrated that, when a static potential is added to the setup, the driven toroidal helix behaves like a generalized Kapitza pendulum.

The next step was to go beyond isotropic Coulomb interactions and consider anisotropic dipole-dipole interactions. In [A4], we explored the physics of freely rotating dipoles placed equidistant along a helical path. Motivated by the complexity already arising for the ground-state in the (comparatively simple) setup studied in [A4], we set out in [A5] to explore two-dimensional Bravais dipole lattices spanned on the surface of curved or deformed structures. Finally, in [A6], we wanted to explore the effects of topologically non-trivial geometries on dipole lattices.

All of the aforementioned works were supervised by Prof. Dr. Peter Schmelcher. For Refs. [A1, A2, A4, A5], all calculations, as well as the writing of the manuscript and the preparation of the figures were done by me. In the work [A3], I assisted in the analysis of the results and was responsible for writing the manuscript. All calculations from [A3] were carried out by Flemming Gloy. For Ref. [A6], I contributed to the calculations, assisted in the analysis of the results, and wrote the manuscript. The remaining calculations of Ref. [A6] were performed by Felipe A. O. Silveira.

The publications [A7] and [A8] arose out of work completed during my Bachelor’s and Master’s degrees and are not part of the scientific contributions of this thesis.

The publication [A9] is currently in the peer review process and also not part of the scientific contributions of this thesis.

## Chapter 1

# Introduction

At the core of all mathematical descriptions of the world are assumptions about the geometry of space. Most often this geometry is assumed to be Euclidean (or more generally a Hilbert space), i.e. a flat geometry. Nowadays, methods to confine dynamics to a lower dimensional (i.e. one or two-dimensional) subspace are feasible in experiments. Low-dimensional systems have recently attracted considerable interest since they can possess features that are absent in higher dimensions [1, 2]. Furthermore, when these low-dimensional systems are not flat but exhibit a curved geometry they can possess additional properties, e.g. related to the topology of the confining manifold. In addition to the dependence on geometry, these effects generally also depend on the intrinsic components of the confined system, such as interactions. In other words, one can expect these properties to be strongly system-dependent. But can general claims be made regarding the impact of geometric curvature on the properties of physical systems? This question is not easy to answer. However, some general considerations require only a basic mathematical intuition: Most prominently, curvature impacts the geodesics, i.e. the shortest distance between two points, and thereby also the trajectories of any dynamics taking place. One well-known example is the gravitational lensing of photons in the presence of massive objects [3, 4]. Similar scattering effects can also be expected for dynamics in other systems exhibiting geometric curvature, such as phonons traveling in a curved two-dimensional (2D) material. Beyond that, the presence of geometric curvature can lead to the emergence of geometric phases - a connection that is studied also in differential geometry as holonomy. This is demonstrated for example by the Foucault pendulum, where this geometric phase relates to the change of the rotation angle during each period of the pendulum oscillation [5, 6].

The above examples highlight only two general (and rather intuitive) effects of geometric curvature: its impact on geodesics and the emergence of geometric phases. Besides such general effects, one can envision novel curvature-induced properties arising, e.g., due to interactions between particles. It is particularly interesting to consider systems of interacting particles confined to a curved 1D or 2D manifold - especially when the interactions themselves are not confined to this manifold and instead depend on the Euclidean separation of the particles. This creates systems with mixed dimensionality - 3D interactions vs 1D or 2D confinement - and non-trivial curvature-dependent properties. Prior investigations of such mixed-dimensional setups have already been performed [7–12]: In the case of ions confined to a helical geometry, it was demonstrated that the curvature enables the ions to condense into stable few or many-body bound states even if the interactions are purely repulsive [7] (more details are given in Secs. 2.2.2 and 2.2.3). Works like Ref. [7] are the key motivation for the scientific contributions provided in this thesis. Specifically, this thesis further explores the impact of curved confinement on long-range interacting many-body systems.

## 1.1 Structure and overview

The scientific contributions [A1–A6] of this thesis are clustered into three groups:

- The impact of external fields on ions in helical confinement [Refs. [A1–A3], Chapter 2]
- The ground state properties of helical dipole chains [Ref. [A4], Chapter 3]
- The properties of dipole arrays on curved surfaces [Refs. [A5, A6], Chapter 4]

Chapters 2-4 address for each group the relevant literature and summarize the scientific contributions [A1–A6]. The scientific contributions are then presented in Chapter 5. Finally, Chapter 6 gives a summary and outlook. Below is an overview of each chapter of this thesis.

### Overview of Chapter 2

This chapter introduces the literature and mathematical concepts related to the scientific contributions [A1–A3]. The scientific contributions are concerned with the impact of external electric fields on model systems of classical ions in helical confinement. The chapter starts in Sec. 2.1 with an overview of classical Coulomb systems and Wigner crystals. Then, the helical ion model (which is used for all scientific contributions discussed in this section) is introduced in Sec. 2.2. Besides introducing the systems Lagrangian, the section also contains a general overview of helical structures in physics (Sec. 2.2.1), as well as a review of the literature related to the helical ion model 2.2.3. Finally, an outline of the scientific contributions [A1–A3] is given in Sec. 2.3.

### Overview of Chapter 3

This chapter introduces the literature and mathematical concepts related to the scientific contribution [A4]. The scientific contribution investigates the ground state properties of helical dipole chains. The chapter starts with an overview of the properties of (linear) dipole chains in Sec. 3.1. Mathematical patterns related to those used for the ground state classifications in [A4] have previously been relevant in the field of phyllotaxis - the study of the arrangement of lateral organs in plants. A brief overview of the relevant discoveries in the field of phyllotaxis is provided in Sec. 3.2. Finally, Ref. [A4] is outlined in Sec. 3.3.

### Overview of Chapter 4

This chapter introduces the literature and mathematical concepts related to the scientific contributions [A5, A6]. The scientific contributions study the properties of classical dipole arrays on curved surfaces. The chapter starts in Sec. 4.1 with an overview of the equilibrium properties of classical dipole lattices. Then Secs. 4.2 and 4.3 respectively discuss relevant setups of electric and magnetic dipole arrays. This includes a discussion of magnetic dipole arrays on curved surfaces. Finally, Sec. 4.4 outlines the scientific contributions [A5] and [A6].

### Overview of Chapter 5

This chapter contains the scientific contributions [A1–A6]. An outline of each contribution is provided in Secs. 2.3, 3.3, and 4.4.

**Overview of Chapter 6**

This chapter summarizes the scientific contributions of Chapter 5 and provides an outlook that discusses possible future investigations.



## Chapter 2

# Interacting particles and helical confinement

This chapter reviews the relevant literature related to classical ions confined to helical geometries and subsequently presents an overview of the scientific contributions [A1–A3].

Section 2.1 provides an overview of classical Coulomb systems in flat geometries. An in-depth overview of the helical ion model, which is the model used in the scientific contributions [A1–A3], is given in Sec. 2.2. It includes a general motivation of the helical geometry in Sec. 2.2.1, a mathematical description of the helical ion model in Sec. 2.2.2, and a discussion of related literature in Sec. 2.2.3. The chapter concludes with an outline of the scientific contributions [A1–A3].

## 2.1 Classical Coulomb systems and Wigner crystals

“There is an amusing analogy between the configuration of classical charges in two dimensions and the arrangement of quantum dots. Quantum dots are trapped, spin-aligned electrons in a magnetic field pinned down in a substrate—the problem is treated in a fully quantum mechanical way. Hartree–Fock calculations of the configurations include angular momentum, and have large exchange terms in the interaction. Yet the patterns obtained [...] are remarkably similar to the classical calculations of charges confined to two dimensions.”

- J. P. Schiffer

"Order in confined ions" J. Phys. B: At. Mol. Opt. Phys. 36, 511-523 (2003)

In 1934, Eugene Wigner predicted that systems of Coulomb-interacting electrons can possess a crystalline phase - the Wigner crystal [13]. He predicted that this crystalline ordering would occur whenever the Coulomb energy in the system dominates over the electron kinetic energies. In many Coulomb systems, such as metals, Wigner crystal phases will therefore only emerge for very low temperatures. The requirement of low kinetic energies has made the direct observation of Wigner crystals rather difficult. While measurement techniques, such as scanning tunneling microscopy, do possess the spatial resolution to detect Wigner crystals, they also add perturbations that can alter the electron configuration [14]. Nevertheless, signatures of electronic Wigner crystals have been detected in a large number of systems [15–19]. And in 2021, 87 years after their prediction, the first real-space imaging of an electronic Wigner crystal was obtained [14]. In that regard, one should note that

ionic Wigner crystals provide a more accessible platform [20–22] and have been proposed for a number of applications including quantum computing [23], or research on exotic stellar objects [24].

Wigner crystals can be treated classically, provided that the inter-particle distance of the ions is large enough. This level of ‘quantumness’ of a Wigner crystal can be classified by the ratio of the deBroglie length  $\Lambda = h/\sqrt{2\pi mk_B T}$  of the electrons (or ions) to the average inter-particle distance  $a$ . When the ratio is  $\Lambda/a \geq 1$  - which is the case for most materials - the system has to be treated with quantum mechanics. However, if  $\Lambda/a < 1$ , a classical description is applicable.

A simple model that captures the physics of Wigner crystals is the one-component plasma (OCP) [25]. The model describes the (statistical) mechanics of classical Coulomb-interacting ions (point particles) in the presence of a uniformly ‘smeared out’ background charge. The behavior of this model depends mainly on the relative strength of thermal fluctuations to the strength of the Coulomb coupling. For very weak Coulomb coupling, the system is in a gas phase that is characterized by an almost collisionless motion of the ions. For weak to moderate Coulomb coupling, rapid collisions can be observed and the system is said to be in a liquid phase. The crossover between the gas and liquid phase can be detected from microscopic properties, e.g., through a minimum in the reduced shear viscosity [26, 27]. When crossing a critical coupling strength, a first-order liquid-to-solid phase transition can be observed [28–32]. Above this critical Coulomb coupling strength, Wigner crystals will form. And while the model is (in most cases) a drastic oversimplification, it is widely used as a reference system, e.g., in studies of electron dynamics in metals or studies of strongly coupled plasmas. For example, the model can be used to estimate system properties that are directly impacted by strong Coulomb coupling and otherwise difficult to estimate, such as diffusion coefficients [33, 34], thermal conductivity [35–37], or shear viscosity [27, 33].

In finite-size systems, the properties of the OCP depend also on the trapping geometry. For example for a 2D Coulomb system, the density profile is only uniform when the trapping potential is harmonic - with non-uniform density distributions arising for different trapping geometries. In the limit case of hard-wall boundary conditions, the density profile will resemble that of a hollow shell [31]. In this regard, there has been a strong interest in understanding the properties of Coulomb systems with boundary conditions that effectively confine the ions to a (quasi) 1D subspace. Common setups for studying effective 1D Coulomb systems employ parabolic traps [38–43]. The equilibrium configurations of these systems depend almost exclusively on the particle density and can emerge as complex configurations, including linear chains, zig-zag configurations, helical ‘chains’, or multiple interwoven helical ‘chains’ [44, 45]. The configuration space of this system can be represented by a complex bifurcation tree that depends on the particle density within the trap [41]. Similar equilibrium configurations have been reported for different (quasi-1D) trap geometries, including linear, spherical, or toroidal traps [46–48]. Experimental realizations [39, 46] of these quasi-1D setups have been realized with dusty plasmas - a type of low-temperature plasma containing macroscopic-sized charged particles [49–51].

The OCP is only one (rather simple, yet prominent) type of model where classical Coulomb interactions between ions can be relevant for experimental setups. In addition to the OCP, there are other microscopic or mesoscopic setups where the behavior of confined ions can be treated classically. One example worth mentioning are counter-ions being adsorbed and moving along the surfaces of a macroion [52]. These macroions can take various shapes including cylinders [53, 54], spheres

[53–55], and helices [56]. The counter-ions can be mobile [57], and the Coulomb repulsion between counter-ions can lead to the formation of Wigner crystals [58, 59]. In theoretical models, these macro-ions can sometimes be treated as hard surfaces with uniform charge distributions, whereas the counter-ions are then treated based on statistical dynamics.

## 2.2 The helical ion model

Coulomb systems similar to the OCP (see Sec. 2.1) have been studied for a variety of boundary conditions, including helical confinement [7, 60]. This section demonstrates the rich properties emerging in long-range interacting Coulomb systems when they are confined to a helical path.

Section 2.2.1 gives a brief overview of helical structures in physics and highlights some of the general motivations driving contemporary investigations of helical systems. Section 2.2.2 explains the mathematical model employed in [A1–A3] and discusses the most significant effects of helical confinement. Finally, Sec. 2.2.3 provides an overview of the relevant literature regarding ions in helical confinement.

### 2.2.1 The significance of the helical geometry

“[...] we only poorly understand why there exist so many spiraling galaxies and nebulae in our universe but we do have a reasonable good idea of why DNA and many protein molecules spiral. We understand the basic mechanism by which the chambered nautilus generates its logarithmic spiral home but we do not understand how it is possible for the framed narwhal, the unicorn of the sea, to possess two spiraling teeth located on each side of a bilaterally symmetric body that *both* spiral in a left-handed direction. [...] For a narwhal to have tusks originating on opposite sides of the body which are both asymmetric and identical, not the mirror image of one another, is highly paradoxical. ”

- R. I. Gamow

"Spirals in nature" Phys. Teach. 17, 14-22 (1979)

“From the deep universe to hurricanes, a tendrilled vine in a garden to an apple peel, human genes to flower shapes, spirals or helices are everywhere in nature. Why would the seeds of sunflowers strictly arrange in a “Fibonacci spiral”? Why would ammonites coil themselves into an “Archimedean screw”? These ordered arrangements look surprising yet mysterious in the chaotic surroundings. ”

- Z. Ren and P. Gao

"A review of helical nanostructures" Nanoscale 6, 9366 (2014)

Helical structures are ubiquitous and appear at almost all length scales. The most prominent naturally-occurring helical structure is perhaps the DNA double helix. Due to its important role in biology, DNA has been researched extensively in biology, chemistry, and physics. Besides DNA, prominent naturally occurring nano-scale helices include the  $\alpha$ -helices in proteins, the triple helix of poly proline-glycine helices in collagen, and the helix of protein sub-units in the tobacco mosaic virus, to

just name a few. The formation of molecular helices is often accompanied by certain properties or functionalities arising from the helical geometry. General examples of these properties include the optical activity of chiral molecules [61] or an increased stability regarding deformations [62, 63]. Examples for specialized functionality arising from helical geometries are ubiquitous in nature. For many biological molecular helices, the helical shape has an impact on biological functions, such as biological information storage or cell proliferation [64]. Another well-known example is the impact of chirality - whether a molecule is left- or right-handed - on its function. This impact of chirality on molecule-function is evident in, e.g., the taste of amino-acids, which - depending on chirality - is either sweet or tasteless [65].

There is a great interest in understanding the properties, the controlled assembly, and the possible applications of nano-scale helical structures [66, 67]. These nano-scale helices are envisioned for applications including optoelectronics [68], sensors [69], responsive materials [70], helical logic devices [71, 72], single-molecule electronics [73], nano-scale 'machines' [74], and more. There is already great experimental control over the manufacturing of helical structures. Common methods for the assembly of helical structures include guided fabrication methods [75, 76], as well as self-organized processes [77, 78]. Especially for large-scale self-organized structures, the origin of helical growth patterns is often a result of a chirality transfer from the molecular level to macromolecular or supramolecular structures [70]. One noteworthy example for artificially created helical nano-structures are 'coiled' carbon nano-tubes [67, 79]. Helical carbon nano-tubes with helix radii as small as  $\sim 20$  nm have been created in laboratory environments [80]. Further information on the fabrication of helical nano-structures, as well as their properties, are discussed in a multitude of review articles (e.g. Refs. [66, 67, 69, 70, 79, 81–83]).

Beyond material science, helical structures also appear in a wide range of other systems. One example that was already mentioned in Sec. 2.1 are Coulomb-interacting ions in parabolic traps, which have been shown to self-organize into intertwinning helical arrays [39, 41, 44–48]. In that regard, it is interesting to note that actual helix-shaped traps for neutral atoms have been realized with evanescent light fields around a thin optical fiber [84] (related setups are also described in Refs. [85, 86]). Another example that is featured later in this thesis are phyllotactic (helix) patterns appearing during the growth of certain biological systems (with some applications in physics - see Sec. 3.2 for details). These helices in phyllotaxis are interesting because they naturally emerge from a 'simple' model of closest packing densities on a cylinder; and despite their simplicity, they can explain the presence of the golden ratio and the Fibonacci sequence in many biological systems. An overview of phyllotaxis in cylindrical systems, as well as examples of phyllotactic patterns appearing in physics, is given in Sec. 3.2.

Note that the purpose of the above text is only to motivate the properties of helical structures, and to provide a basic picture of contemporary research interests regarding nano-scale helical structures. It is not concerned with experimental realizations of the helical Coulomb systems investigated in Refs. [A1–A3].

### 2.2.2 The model

The scientific contributions [A1–A3] use the helical ion model. It describes classical Coulomb-interacting ions confined to a helical path. This path can be described with

the following parametric function

$$\mathbf{r}(u) = \begin{pmatrix} x(u) \\ y(u) \\ z(u) \end{pmatrix} = \begin{pmatrix} \rho \cos(u) \\ \rho \sin(u) \\ hu/2\pi \end{pmatrix}, \quad (2.1)$$

where  $\rho$  and  $h$  are the helix radius and pitch, respectively. The parametric coordinate  $u$  in Eq. 2.1 is assigned a unique value for each point on the helix and can be interpreted as an angular coordinate; whenever  $u$  increases by  $2\pi$ , the position on the helix changes by one winding. The helix shape is determined by the ratio of the parameters  $\rho$  and  $h$ : In the limit of  $\rho/h \rightarrow 0$  the confining path  $\mathbf{r}(u)$  becomes effectively a straight line, whereas in the opposite limit, i.e.  $\rho/h \rightarrow \infty$ , the helix effectively degenerates into a circle.

A system of  $N$  identical ions with mass  $m$  and charge  $q$ , confined to the helical path defined by Eq. 2.1, is described by the following Lagrangian

$$\mathcal{L}(u_1, u_2, \dots, u_N) = \sum_{i=1}^N \frac{m}{2} \dot{\mathbf{r}}^2(u_i) - \sum_{\substack{i,k=1 \\ i < k}}^N \frac{1}{4\pi\epsilon_0} \frac{q^2}{|\mathbf{r}(u_i) - \mathbf{r}(u_k)|}, \quad (2.2)$$

where  $u_i$  is the position of the  $i$ -th particle in parametric coordinates, and the mass and charge are respectively denoted as  $m$  and  $q$ . The confining forces that prevent the ion from leaving the helical path are automatically considered by only allowing the particle positions  $\mathbf{r}(u)$ . Inserting  $\mathbf{r}(u)$  from Eq. 2.1 yields

$$\mathcal{L}(u_1, u_2, \dots, u_N) = \sum_{i=1}^N \xi \dot{u}_i^2 - \sum_{\substack{i,k=1 \\ i < k}}^N \frac{1}{4\pi\epsilon_0} \frac{q^2}{\sqrt{2\rho^2 (1 - \cos(\Delta u_{ik})) + \left(\frac{h}{2\pi}\right)^2 (\Delta u_{ik})^2}}, \quad (2.3)$$

where  $\Delta u_{ik} = (u_i - u_k)$  is the parametric distance of the  $i$ -th and  $k$ -th particle, and  $\xi = m |\partial \mathbf{r}(u) / \partial u|^2 / 2 = m (\rho^2 + (h/2\pi)^2) / 2$  is the particles effective mass. Equation 2.3 shows that the confinement to a helical path drastically changes the behavior of the ions: The denominator of the potential energy term has two summands - a linear term and an oscillating term. By changing the helix geometry (specifically the ratio  $\rho/h$ ), one can tune between a dominantly repulsive ( $h \gg \rho$ ) or a dominantly oscillating ( $h \ll \rho$ ) interaction potential. In the straight line limit ( $\rho/h \rightarrow 0$ ) the potential becomes purely repulsive, whereas in the limit of a circular geometry ( $\rho/h \rightarrow \infty$ ) interaction becomes purely oscillatory.

The behavior is easy to predict for the two limit cases discussed above. Outside of these limits, i.e.  $\rho/h \in ]0, \infty[$ , both the oscillating and the repulsive term contribute significantly to the interaction potential. Above a critical value of  $\rho/h$ , the oscillating term becomes strong enough to allow for the formation of bound states. Figure 2.1 explains the behavior for a system of two ions and a helix with  $\rho/h = 1.25$ . A possible two-ion equilibrium configuration is indicated by the two dark blue dots in Fig. 2.1(a). The ions form a bound state by trapping each other on opposite sides of a helix-winding: Neither ion can change its position along the helix without decreasing the Euclidean distance between them, thereby increasing the Coulomb repulsion. This is indicated in the figure: when one ion moves (as shown by the red arrows) towards the positions marked by the orange dots, the Euclidean distance between the ions decreases. The potential energy as a function of the parametric distance  $\Delta u$  of the ions along the helix is shown by the orange line in Fig. 2.1(b). For

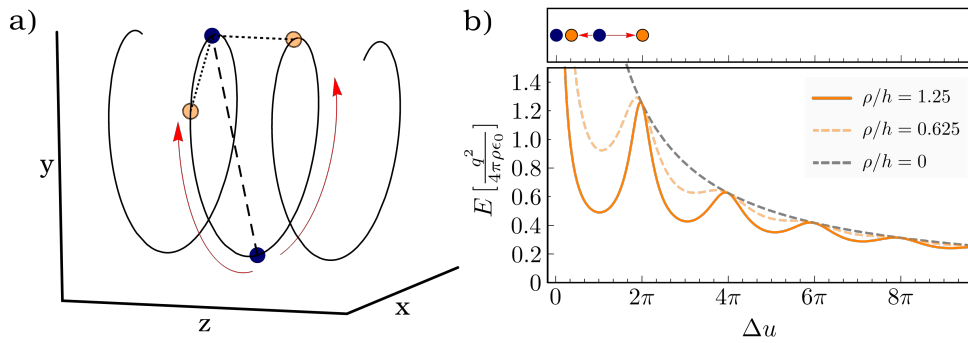


FIGURE 2.1: (a) Equilibrium configuration of two ions (dark blue) on a helix with  $\rho/h = 1.25$ . Neither ion can move along the helix without decreasing their Euclidean distance. This is exemplified by the two orange dots: Moving one ion (as indicated by the red arrows) to these positions visibly decreases the Euclidean distances. (b) The potential energy for two ions with distance  $\Delta u$  for a helix with  $\rho/h = 1.25$  (orange line),  $\rho/h = 0.625$  (yellow dashed line), and  $\rho/h = 0$  (gray dashed line). For reference, the upper panel shows the positions indicated in (a).

reference, the top panel indicates the configuration of the blue and orange dots from Fig. 2.1(a). The potential landscape shows that for  $\rho/h = 1.25$  there are several other stable equilibrium configurations for the two-ion system - besides the one shown in Fig. 2.1 (a): Each of these potential minima occurs close to where the relative distance becomes an odd multiple of  $\pi$ , corresponding to a ‘distance’ of  $0.5, 1.5, 2.5, \dots$  helix windings<sup>1</sup>. The depth and number of potential wells can be tuned by varying the ratio  $\rho/h$ . An example for  $\rho/h = 0.625$  is shown by the dotted orange curve in Fig. 2.1(b): this second curve has fewer and more shallow minima than the curve for  $\rho/h = 1.25$ . By decreasing  $\rho/h$ , the oscillating part of the potential becomes weaker compared to the repulsive part.

Bound states consisting of more than two particles are also possible. However, predicting these many-body equilibrium configurations can be non-trivial, even for just three particles. Further insight into the equilibrium configurations featuring three ions can be found in Ref. [7]. The scientific contribution [A1] also investigates the statistical properties of many-body equilibrium configurations on a toroidal helix.

### 2.2.3 Progress on the helical ion model

This section provides a literature overview concerning the helical ion model. There have been investigations of setups similar to the helical ion model, such as studies on helically confined excitons (i.e., oppositely charged electron-hole pairs) [87, 88], or polarized dipoles in helical confinement [89–92]. Of course, beyond that, there exists a plethora of works providing insights into the impact of curved geometry on confined interacting particles, including studies of cylindrical geometries [93], and spheres [94]. In that regard, one notable and relevant mathematical problem is the

<sup>1</sup>For an equilibrium configuration of two ions, we actually get  $\Delta u \geq (2n + 1)\pi, n \in \mathbb{N}_0$ ; with the distance being exactly  $\Delta u = (2n + 1)\pi$  only for the case of  $h = 0$ . For  $h > 0$ , the equilibrium distances will always be (albeit only slightly) greater.

Thomson problem [95], which is concerned with finding the ground state configuration of Coulomb-interacting ions on a sphere. The following overview will, however, focus strictly on works that consider equally charged ions in helical confinement as defined in Sec. 2.2.2.

Perhaps the most significant feature of the helical ion model is the emergence of an oscillating effective interaction as described in Sec. 2.2.2. Many of the aforementioned works on excitons and dipoles in helical confinement ‘rediscover’ this effective interaction for their specific setups and rarely explore the consequences of such an oscillating interaction further. However, in the case of Coulomb-interacting ions, the properties arising from the helical confinement have been studied in more detail, e.g., by exploring the three-body equilibrium configurations [7].

The helix possesses a translation invariance, which allows bound states to travel collectively (i.e., with a constant center-of-mass velocity) along the helix. More mathematically, in a helical geometry, the center of mass motion decouples from the relative motion of the ions. However, defects or inhomogeneities along the helix break this translation invariance, causing a coupling of the center-of-mass and the relative motion, which can lead to effects such as the scattering or trapping of bound states at these inhomogeneities [8].

On a *toroidal* helix, the translational invariance is broken globally. As a result, charges in a toroidal helix geometry can be ‘pinned’ to equilibrium positions, such that inducing a current along the helical path requires the applied voltage to be larger than a (geometry-dependent) critical value [11]. In addition to the collective motion of bound states, some work has been dedicated to understanding the dynamics of phonons in (crystalline) many-body bound states [9, 10]. There, it has been shown that the toroidal helix geometry has a strong impact on the phonon-dynamics. Specifically for a (crystalline) bound state of ions confined to a toroidal helix, the phonon band structure can be inverted by varying the helix radius [9]. For a critical helix radius, the band structure even becomes almost degenerate (i.e., almost flat), thereby effectively preventing linear excitations from spreading through the system [9], and giving rise to complex nonlinear dynamics [10].

Finally, the impact of bound states of ions on the mechanical properties of the helix has also been investigated. There, it has been shown that the bound ions lead to unusual contributions to the systems bending response [12].

Especially relevant for the scientific contributions in this thesis is Ref. [96] - the first exploration of the impact of an external electric field on the helical ion model. Similar to the Coulomb forces, the forces arising from the external field are also partially compensated by the confining forces (see Secs. 2.2.2 or 2.3 for details) and lead to a geometry-dependent electric potential. Reference [96] demonstrated that external fields can be used to induce controlled transitions between different equilibrium configurations of two ions. The scientific contributions [A1–A3] are all continuing this line of research and explore the effects arising in the presence of (both static and time-dependent) external fields.

### A comment on the quantum helical ion model

One question that comes to mind is, of course: What happens if we go from a classical to a quantum system? While this thesis is purely concerned with classical systems, there have been some related works on quantum particles in helical confinement that are worth a brief comment. When quantum systems are confined to a curved geometry, the constraints on the particle motion will lead to an additional

potential term (of geometric origin) in the Hamiltonian [97–99]. Specifically for electrons confined to a helical path the quantization procedure has already been calculated [91]. Just like in the classical case, the effective interaction potential shows oscillatory behavior allowing for the formation of a bound state of two ions [60]. However, in the case of a quantum system, this state will be unstable, since the ions can dissociate by tunneling through the potential barrier. Nevertheless, for a helix radius that is much larger than the helix pitch, the lifetime of the lowest energy bound state has been estimated [60]. Specifically for two electrons confined to a helix with a radius of  $R \sim 10^{-8} m$ , the lifetime of the bound state was predicted to be larger than  $\tau > 10^{15} s \sim 10^7 yr$ . [60]. Similar calculations of the spectra and wavefunctions of bound states of (polarized) dipoles in helical geometries have been performed [90]. There, it was shown that for moderate interaction strengths, the formation of well-defined ‘chains’ (i.e., bound states that are similar to the classical predictions) can be observed in many-body quantum systems [91]. Of course, in the regime of weak interactions, the particles tend to delocalize and show (depending on circumstances) either gas or Luttinger-liquid behavior [92].

Finally, there are also works on discretized (i.e., tight-binding-like) models of interacting particles in helical geometries - sometimes referred to as the helical Hubbard model. In the helical Hubbard model, discrete lattice sites are arranged along a helical path, and the hopping amplitude between distant lattice sites scales according to their (Euclidean) distance. A limiting case of this model are zig-zag Hubbard chains [100, 101], which are also referred to as the  $t_1$ - $t_2$  Hubbard model [102–104]. Apart from this special case, studies on the helical Hubbard model include investigations of wave packet dynamics [105], the interaction of wave packets with defects [106], a modulational instability that leads to the breakdown of breather modes [107–109], the possibility of Thouless pumping [110], and more [111–113]. It is interesting to note, that the model has also been used to model DNA electronics [114].

## 2.3 Outline of Scientific contributions [A1–A3]

The scientific contributions [A1–A3] explore properties of the helical ion model, albeit with slight modifications from the Lagrangian derived in Sec. 2.2.2: All three works consider a *toroidal* helix geometry and external electric fields. For completeness, the Lagrangian used in the scientific contributions [A1–A3] is derived below.

### Toroidal helix Lagrangian

A toroidal helix with torus radius  $R$  and a total of  $M$  helix windings can be parameterized as follows:

$$\mathbf{r}_t(u) = \begin{pmatrix} x(u) \\ y(u) \\ z(u) \end{pmatrix} = \begin{pmatrix} (R + \rho \cos(u)) \cos(u/M) \\ (R + \rho \cos(u)) \sin(u/M) \\ \rho \sin(u) \end{pmatrix}, \quad (2.4)$$

where the integer  $M$  corresponds to the number of helix windings,  $\rho$  is the helix radius, and  $u$  is the position of the ion on the helix in parametric coordinates. From the condition that the helix is closed, i.e.,  $\mathbf{r}_t(u) = \mathbf{r}_t(u + 2\pi M)$ , it is possible to derive the relation  $Mh = 2\pi R$ , where  $h$  is the helix pitch. Similar to the case of the straight helix, we can obtain the Lagrangian - already accounting for the constraints on the particle positions - by replacing the parametric positions  $\mathbf{r}(u)$  in Eq. 2.2 with the

parametric positions  $\mathbf{r}_t(u)$  on the toroidal helix. By doing that, we obtain

$$\mathcal{L}(u_1, u_2, \dots, u_N) = \sum_{i=1}^N \frac{m}{2} \zeta(u_i) \dot{u}_i^2 - \sum_{\substack{i,k=1 \\ i < k}}^N \frac{1}{4\pi\epsilon_0} \frac{q^2}{|\mathbf{r}_t(u_i) - \mathbf{r}_t(u_k)|} \quad (2.5)$$

where  $u_i$  and  $u_k$  denote positions of the  $i$ -th and  $k$ -th ion on the toroidal helix and

$$\zeta(u_i) = r^2 + [R + \rho \cos(u_i)]^2 / M^2 \quad (2.6)$$

is the effective mass of the  $i$ -th ion. The position dependence of the effective mass term  $\zeta(u_i)$  arises from the choice of parametric coordinates and, if desired, can be removed when converting to arclength coordinates  $s$  which are defined as

$$s : u \mapsto s(u) = \int_0^u \left| \frac{\partial \mathbf{r}_t(u')}{\partial u'} \right| du' \quad (2.7)$$

The pairwise Coulomb potential term in Eq. 2.5 behaves slightly differently than the Coulomb term for the straight helix. Most importantly, on the toroidal helix, the Coulomb potential cannot be expressed by the relative distance of the ions alone. The relative position of the ions within a winding (i.e. whether it is closer or farther from the torus center) is also relevant for the potential energy. This can be seen by evaluating the Coulomb term in Eq. 2.5:

$$|\mathbf{r}_t(u_i) - \mathbf{r}_t(u_k)|^{-1} = \left[ 4 \sin^2 \left( \frac{u_i - u_k}{2M} \right) (R + \rho \cos(u_i)) (R + \rho \cos(u_k)) + 4\rho^2 \sin^2 \left( \frac{u_i - u_k}{2} \right) \right]^{-\frac{1}{2}} \quad (2.8)$$

The pairwise Coulomb interaction for the toroidal helix is periodic in  $u$  and exhibits - in the short range - decaying oscillations with increasing distance of the ions, similar to those shown in Fig. 2.1(b). A more detailed discussion of the potential landscape of ions on the toroidal helix can be found in Ref. [A1].

### Impact of an external electric field

The external electric field that is considered in the scientific contributions [A1–A3] is modeled with an additional potential term in the Lagrangian. The potential energy of an ion with charge  $q$  in an external field  $\mathbf{E}(\mathbf{r}, t)$  is given by  $V_{Field} = q\mathbf{E}(\mathbf{r}, t) \cdot \mathbf{r}$ . In the following, we only consider homogeneous fields  $\mathbf{E}(\mathbf{r}, t) = \mathbf{E}(t) = (E_x(t), E_y(t), E_z(t))^T$ . For  $N$  ions at positions  $\mathbf{r}_t(u_i)$  on a toroidal helix, this homogeneous field results in an electric potential energy given by

$$\begin{aligned} V_{Field} &= \sum_{i=1}^N q\mathbf{E}(t)\mathbf{r}_t(u_i) \\ &= q \sum_{i=1}^N \left[ [R + \rho \cos(u_i)] [E_x(t) \cos(u_i/M) + E_y(t) \sin(u_i/M)] + E_z(t)\rho \sin(u_i) \right] \end{aligned} \quad (2.9)$$

This electric potential energy oscillates with the position of each ion on the helix. In general, the minima of this electric potential will not align with the positions that minimize the Coulomb interaction energy. Adding the electric potential given in Eq. 2.9 to the Lagrangian will therefore add competing interactions to the system.

### Contributions [A1–A3]

The scientific contribution [A1], outlined in Sec. 2.3.1, explores the many-body equilibrium states of ions confined to a toroidal helix in the presence of a static external electric field. It is demonstrated that the electric field strength can be used to tune a structural crossover of equilibrium configurations. The scientific contributions [A2] and [A3], outlined in Secs. 2.3.2 and 2.3.3, consider the dynamics induced by time-varying external fields.

### 2.3.1 Outline: Tunable order of helically confined charges [A1]

The scientific contribution [A1] explores the many-body equilibrium configurations of ions on a toroidal helix - both with and without a static external field. This work is also the first proper investigation of the many-body equilibrium configurations of ions in helical confinement. Previous investigations focused either on few-body phenomena (see e.g. Ref. [7]), or on symmetric (crystalline) equilibrium configurations (see Refs. [9–11]). The electric field considered in [A1] is static and aligned along the  $z$ -axis (according to the notation of Eq. 2.4). This electric field favors particles at discrete positions  $u = 2\pi n, n \in \mathbb{N}_0$ , whereas the Coulomb interaction favors particle distances of  $\Delta u = (2n + 1)\pi, n \in \mathbb{N}_0$ . The question posed in this work is: how do these competing interactions impact the equilibrium configurations of our system of ions in helical confinement?

These two potential terms favoring particle order on different length scales are reminiscent of the Frenkel–Kontorova model (FK model); one of the fundamental and universal tools of low-dimensional nonlinear physics [115]. The FK model uses spring-mass chains in a periodic (typically sinusoidal) potential to model solid-state systems. Initially, the model has been used to describe the structure and dynamics of a solid in the vicinity of a dislocation core [116, 117]. Since then, significant interest has been directed at understanding complex dynamics exhibited by the FK model and its variations, such as the study of solitons in a continuum analog of the FK model [118–121]. The complex behavior in FK models typically emerges when the equilibrium length of the springs is not commensurable with the wavelength of the periodic potential - a potential landscape similar to that of the helically confined ions in an external field. While a direct mapping of our setup to the FK model is not possible, the inherent similarities between the two setups suggest that similar complex behavior could be present in the helical ion model whenever a static external field is present.

In [A1], the many-body equilibrium configurations are investigated as follows: We first consider an example system and identify all possible equilibrium configurations for the case of a vanishing external field. These equilibrium configurations are then classified with an order parameter to demonstrate a tendency of amorphous ordering of the ions on the helix. We demonstrate a structural crossover that occurs as the strength of the external electric field is increased. This crossover changes the particle order from amorphous configurations in the field-free case to equidistantly spaced ions in the case of a dominating external field. This crossover is analyzed and characterized statistically. We then discuss the impact of parameter variations on the crossover, specifically focusing on variations of the system size, the number of particles per helix winding, and the helix radius. This discussion shows the persistence of the crossover for a wide range of parameters.

### 2.3.2 Outline: External field-induced dynamics of a charged particle on a toroidal helix [A2]

The scientific contribution [A2] investigates the impact of time-dependent fields on the dynamics of helically confined ions. The setup consists of a single ion confined to a toroidal helix while being driven by an external electric field. Two types of periodic driving fields are considered: an oscillating field and a rotating field, both aligned in the torus plane (xy-plane as per the notation of Eq. 2.4). As described in Sec. 2.2.2, the confining forces of the helical path can be combined with the forces exerted by the field into an effective interaction of the ion with the external field. For the oscillating and the rotating field, the corresponding effective potentials (respectively denoted as  $V_x$  and  $V_{xy}$ ) are given by

$$V_x(u, t) = qE [R + \rho \cos(u)] \cos(u/M) \cos(\omega t) \quad (2.10)$$

$$V_{xy}(u, t) = -qE \cos(\omega t - u/M) [R + \rho \cos(u)], \quad (2.11)$$

where  $E$  is the amplitude of the driving field,  $\omega$  is the frequency of the driving field,  $t$  is the time, and  $R, \rho, M$ , and  $u$  respectively correspond to the torus radius, the helix radius, the number of windings, and the ion position in parametric coordinates.

Periodic driving has been thoroughly investigated in the context of chaos research. Significant interest in driven systems has been directed towards understanding how periodic driving potentials can be used to control chaotic dynamics. One of the most significant results in that regard is the relation between directed transport of particles and the symmetries of the driving potential: For directed transport to be present, the equations of motion should not possess any of the two following spatiotemporal symmetries [122]

$$u \rightarrow -u + \delta_u \quad t \rightarrow t + \delta_t \quad (2.12)$$

$$u \rightarrow u + \delta_u \quad t \rightarrow -t + \delta_t, \quad (2.13)$$

where  $u$  is the particles spacial coordinate,  $t$  is the time, and  $\delta_u$  and  $\delta_t$  are (arbitrary) constants. Driving potentials that break these symmetries have been used to achieve a wide range of control over chaotic dynamics [123], such as inducing directed transport of particles without requiring any bias (such as a net voltage) [124–129], the implementation of velocity filters [130, 131] or spectrometers [132, 133], and even to gather energy from thermal fluctuations [134, 135]. One can easily see, that from the two considered driving potentials (Eqs. 2.10 and 2.11) only  $V_{xy}$  is breaking the symmetries described in Eqs. 2.12 and 2.13. Nevertheless, this work demonstrates a mechanism by which a non-zero average velocity for chaotic trajectories can be observed for both  $V_{xy}$  and  $V_x$ . The identification of these trajectories, as well as the explanation of the underlying mechanism, is one of the key results of this work.

The trajectories that allow for this directed transport can only be observed for low driving amplitudes. The emergence of these trajectories during a transition from a large to a low driving amplitude is investigated, and the transition is characterized. The behavior is explained by the split-up of a chaotic phase space region into two separate regions.

A similar separation of the chaotic phase space region has also been found in the case of the rotating external field and very large driving amplitudes. Chaotic trajectories become ‘trapped’ around the global minimum of  $V_{xy}$  for certain driving amplitudes.

For both types of phase-space separations, the mechanism can be linked to terms in the driving potential that arise from the finite helix radius  $\rho$ . The results of [A2] also include a phase-space analysis that characterizes the most prominent types of trajectories arising due to  $V_x$  and  $V_{xy}$ .

### 2.3.3 Outline: Driven toroidal helix as a generalization of the Kapitza pendulum [A3]

The scientific contribution [A3] builds directly on the results of [A2] (discussed in Sec. 2.3.2 above). Similar to the setup investigated in [A2], we consider a single particle on a toroidal helix and a periodically sinusoidal oscillating driving field. The key difference to [A2] is, that this time, we consider an additional static potential  $V_s(u) = V_0 \cos(u/M)$  along the helix. The total potential of an ion at a position  $u$  along the path is then given by

$$V(u, t) = qE [R + \rho \cos(u)] \cos(u/M) \cos(\omega t) + V_0 \cos(u/M), \quad (2.14)$$

where the integer  $M$  corresponds to the number of helix windings,  $R$  and  $\rho$  are the torus and helix radius,  $E$  is the amplitude of the driving field,  $\omega$  is the driving frequency, and  $V_0$  is the amplitude of the static potential. Interestingly, in the limit case of vanishing helix radius  $\rho \rightarrow 0$  the equations of motion for an ion moving in this potential coincide with the equations of motion of the well-known Kapitza pendulum [136].

The Kapitza pendulum is a pendulum driven by an oscillating pivot. A main feature of this pendulum is, that it possesses two stable fixed points: Firstly, the trivial fixed point corresponding to a pendulum position in the minimum of the static potential  $V(u)$  at  $u = M\pi$ . The second stable fixed point corresponds to the pendulum in the maximum of the static potential  $V(u)$  at  $u = 0$ . This second fixed point is stabilized by the driving forces and becomes an unstable fixed point in the limit of vanishing driving forces. The Kapitza pendulum, or more specifically the underlying equation of motion, has been relevant for real-world problems, such as explaining the stability of the design of bipedal walking [137].

The setup studied in [A3] can be considered a generalization of the Kapitza pendulum: Features beyond those of the Kapitza pendulum emerge for finite helix radii  $\rho > 0$ . We analyze the impact of finite helix radii on the stability of the two main fixed points with a linear stability analysis. This allows us to analytically derive the system parameters for which the fixed points are stable. These analytical results are subsequently compared to (and show good agreement with) numerical simulations. We find a strong dependence of the dynamics around the fixed point at  $u = M\pi$  on the helix radius. In contrast, the effect of  $\rho$  on the fixed point at  $u = 0$  is almost negligible. We additionally investigate the impact of a finite helix radius on the phase space and discover prominent dynamical ‘phases’ that are absent in the Kapitza limit, such as directed chaotic trajectories that move (on average) by one helix winding every driving period.

## Chapter 3

# Helical dipole chains

The discussion of Chapter 2 has provided many examples of intriguing effects that arise when long-range Coulomb-interacting particles are confined to a helical geometry. This naturally raises the question if similar - or perhaps even more complex - behavior can be observed when the (isotropic) Coulomb interactions are replaced by dipole-dipole interactions. One can expect that the anisotropic nature of the dipole-dipole interactions will lead to behavior that differs from that of the ions in Chapter 2. As an initial step in this direction, the scientific contribution [A4] investigates the equilibrium properties of interacting dipoles that are equidistantly spaced along a helical path.

This chapter provides an embedding of [A4] into the existing literature. An overview of classical dipole chains is given in Sec. 3.1. Next, Sec. 3.2 discusses the field of Phyllotaxis [138], where geometric arrangements similar to those investigated in [A4] have previously been relevant. Finally, Sec. 3.3 provides an overview of the scientific contribution [A4].

### 3.1 Properties and arrangements of classical dipole chains

One-dimensional chains of interacting dipoles are the main building blocks of many physical models and have been rigorously studied in the past. The preparation of a strictly linear chain can be achieved [139–141] using lithography methods [142], or through self-organized processes [143]. Experimental studies of dipole chains typically focus on polar molecules with permanent dipole moments. Although these are molecular systems, quantum effects can be neglected and dipole chains may be treated classically when the dipole moments and moments of inertia are sufficiently large, as has been shown for certain systems of polar molecular rotors [144, 145]. In addition to chains of freely rotating dipoles, setups exist where the dipole rotation is restricted to a single rotational degree of freedom [145–147]. Any such restriction of the dipole rotation can impact the overall ground state dipole orientation: Freely rotating dipoles in a straight chain arrange head-to-tail, while dipoles that are constrained to rotate perpendicular to the chain (see e.g. certain molecular dipolar rotors discussed in Ref. [148]) align in an anti-parallel configuration. Due to the underlying symmetries, such as the invariance of the total energy with respect to the inversion of all dipoles, these dipole chains support a large number of (often non-trivial) excited states. These excited states can take the form of stable kinks [149], or even entire domains separated by domain walls. This large number of stable equilibrium configurations makes dipole chains interesting candidates for applications, since they allow for example the controlled encoding of information within a dipole chain [150].

A chain of interacting dipoles with rotational degrees of freedom is a complex system of nonlinear coupled oscillators and exhibits interesting dynamical behavior. Studies of the energy transfer along one-dimensional dipole chains have been carried out for both freely rotating, as well as various constrained dipole chains [145–147]. In particular, complex dynamical behavior can be seen even in the shortest dipole ‘chains’ [151]. Conversely, for large chains, analytical solutions exist that describe the dynamics of soliton waves traveling along the chain [152]. For more general dynamical excitations of the dipoles, both chaotic motion and soliton-like transport have been observed [153, 154]. The soliton-like transport of excitations allows for efficient energy transfer along a linear chain [145–147, 155–157]. Furthermore, simulations have demonstrated that dipole chains could be used as waveguides that can transport signals below the diffraction limit [158–160], thereby overcoming size limits for guiding and modulating light.

Besides the ‘simple’ dipole chain, there have also been investigations of slightly modified setups. A relevant example are chains with closely-spaced dipoles where the dipole approximation does not hold anymore [157]. In these models, an ultrasensitivity to small periodic modulations has been demonstrated [157]. In that regard, other interesting works that are related - but less relevant to [A4] - include studies of temperature effects on classical dipole chains [161], or the dynamics of spin-waves in chains of magnetic dipoles [162–164].

So far, the above discussion of the properties of dipole chains focused mainly on strictly linear chains. However, the geometric arrangement of dipoles can also impact the system properties. For example, a circular arrangement of dipolar rotors shows a rich structure of stable as well as unstable equilibrium configurations that depend on the overall symmetries of the arrangement [165]. Moreover, setups involving two merging 1D dipole chains have been used to build controllable switches and logic gates [166].

Specifically helical arrangements of classical dipolar rotors - such as those setups investigated in [A4] - have not been studied in great detail: One example of an experimentally accessible system containing a helical arrangement of dipoles are stacks of BTA (trialkylbenzene-1,3,5-tricarboxamide) molecules [167, 168]. Each BTA molecule consists of three dipolar rotors attached to a central circular molecule. These BTA molecules can self-arrange into stacks, and within a stack, the total energy is minimized when the dipolar rotors align along head-to-tail chains. A naturally occurring rotation of the molecules at each layer of the stack leads to a ground state consisting of a helical dipole chain. Another rather prominent (and admittedly remote) example of such a helical arrangement of dipoles in nature are the dipoles in the secondary structure of proteins that are aligned due to hydrogen bonds between different windings of  $\alpha$ -helices [169–172].

Beyond such examples, the studies with perhaps the closest relation to [A4] are investigations of magnetic nanowires (e.g. Refs. [173] and [174]). However, in these works, the equilibrium properties are dominated by interactions other than the dipole-dipole interaction<sup>1</sup>. Prominent, but less relevant for [A4], are systems where dipoles possess motional degrees of freedom. Examples include Hubbard models that consider dipoles in various geometries, such as zig-zag chains [175, 176] or ladders [177, 178].

---

<sup>1</sup>Magnetic systems - including magnetic wires - are discussed in more detail in Sec. 4.3

## 3.2 Cylindrical lattices and phyllotaxis

“Given the intersecting curves, the mathematical manipulation and description of continued fractions becomes a feature with which Botany has nothing to do, nor is it at all helpful in any direction. Such expressions may attract the mathematician, but they repel the botanist.”

- A. H. Church (1865-1937)

*"On the relation of phyllotaxis to mechanical laws" p. 344*

“According to the theory I am working on now there is a continuous advance from one pair of parastichy numbers to another, during the growth of a single plant... You will be inclined to ask how one can move continuously from one integer to another. The reason is this - on any specimen there are different ways in which the parastichy numbers can be reckoned; some are more natural than others. During the growth of a plant the various parastichy numbers come into prominence at different stages. One can also observe the phenomenon in space (instead of in time) on a sunflower. It is natural to count the outermost florets as say 21 + 34, but the inner ones might be counted as 8 + 13. Church is hopelessly confused about it all, and I don't know any really satisfactory account, though I hope to get one myself in about a year's time.”

- A. M. Turing (1912-1954)

*(from a letter of 28th May, 1953)*

The scientific contribution [A4] investigates a helical dipole array. From a purely geometric point of view, this helical array is a special case of a cylindrical Bravais lattice. Such cylindrical lattices have previously been relevant for a variety of biological systems, especially in the field of Phyllotaxis [138] - the study of the formation of lateral organs in plants. There, it was realized that the arrangement of these lateral organs, such as plant leaves, often follows spiral patterns that correspond to the solution of a closest packing problem of circles on a cylinder. Of course, the biological (or rather the chemical) origin of these growth patterns has been understood to be a result of self-organized directed transport of growth hormones (auxin) [179–183]. But already long before the biochemistry behind these patterns was uncovered, the studies of closest packing densities had wide-ranging success in explaining plant growth - especially in explaining the occurrence of the golden ratio, the Fibonacci sequence, or the Luca sequence in nature. The geometric properties responsible for this pattern formation are relevant for the ground state of the helical dipole array studied in [A4]. Therefore, we will now provide a brief overview of selected phyllotaxis concepts.

In 1837, the Bravais brothers were the first to explain phyllotactic patterns with the geometry of point lattices on a cylinder [184]. They were the first to realize that the eye-catching spirals - e.g. in the arrangement of scales of pinecones or pineapples - are secondary structures originating from a single generating helix. These secondary spirals are called parastichy helices and typically correspond to helical paths that connect a lattice point to its nearest or next-nearest neighbor. Each parastichy helix can be assigned an integer number that counts how many of these spirals fit on the cylinder. Alternatively, this number can be obtained by counting the number of lattice points that the generating helix passes before passing the same parastichy

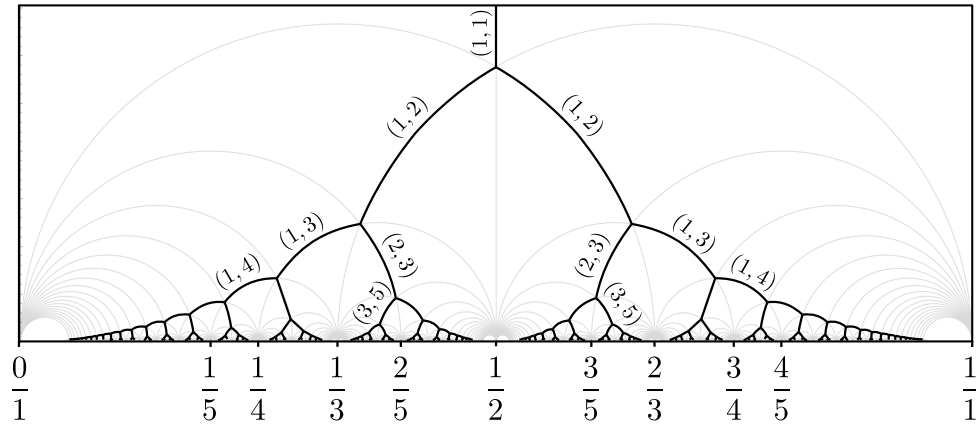


FIGURE 3.1: Sketch of the van Iterson diagram.

It maps the possible arrangement of spheres on a cylindrical surface - with the condition that spheres are placed equidistant along a generating helical path. This distance along the generating helix (relative to the length of a helix winding) is mapped on the horizontal axis. The vertical axis shows the radius of the spheres. Possible configurations (corresponding to local minima in the packing density) are given by the black lines. See Ref. [186] for details.

helix for the second time. These integers are used to classify the lattice (or leaf) configurations. Specifically, the classification uses a parastichy pair  $(m, n)$  that corresponds to the two visually most dominant parastichy helices. In addition to these visually dominant parastichy helices, other less dominant parastichies are possible. For the majority of plants, the parastichy numbers of all possible parastichy helices correspond to the values of the Fibonacci sequence - although, of course, in finite lattices, the sequence is only reproduced to a finite length. Besides the Fibonacci sequence, other sequences, such as the Luca sequence, can also sometimes appear [185]. While the Bravais model succeeded to some extent in providing a theoretical foundation for the geometrical arrangements of leaves, they ultimately failed to explain why certain sequences appear much more frequently in phyllotactic systems than others.

Since the inception of the Bravais model of cylindrical phyllotaxis, the geometric understanding and interpretation of phyllotaxis has greatly improved [187–190]. Many of these later studies treat the problem by considering the closest packing problem of spheres - instead of lattice points - on a cylinder. The full subset of possible closest packing solutions has been found by van Iterson [186] and can be visualized with the so-called van Iterson diagram - a self-similar bifurcation diagram (see Fig. 3.1). Each line in the van Iterson diagram corresponds to a specific lattice configuration that can be characterized by a visually dominant parastichy pair  $(m, n)$ . At each bifurcation in the diagram, an ‘allowed’ lattice configuration splits into two new ‘allowed’ configurations with different parastichy classifications  $(m, n)$ . Overall, as one descends this self-similar bifurcation tree, the parastichy numbers that classify the increasing number of ‘allowed’ configurations can be mapped to a mathematical sequence - the Farey sequence [191]. A lattice configuration that results in parastichy numbers that correspond to the Fibonacci series is obtained only for those configurations that are located on a specific path through the bifurcation diagram.

Reasons for the absolute prevalence of the Fibonacci sequence over other possible sequences, such as the Luca sequence, have been provided by physicists studying,

e.g., certain energetic treatments of cylindrical phyllotaxis [192]. Their considerations result in bifurcation diagrams very similar to that of van Iterson - with one striking difference: Their bifurcation diagrams show discontinuities located directly at the bifurcation points. As a result, at each bifurcation one of the two branches is always energetically preferred over the other. A nicely written and more detailed explanation is provided by Levitov [192]. During the growth of a plant, the stem (i.e. the cylinder radius) grows and the lattice configuration will smoothly descend through the ‘allowed’ configurations as they are determined by the van Iterson diagram. As long as the system follows the energetically preferred branch it will result in a lattice where all the parastichy numbers map to the Fibonacci sequence. According to Levitov’s model, other sequences emerge by mistake, whenever the system accidentally evolves along the ‘wrong’ branch in the van Iterson diagram.

The above-discussed geometrical properties of cylindrical phyllotaxis are not exclusive to botany and occur in a variety of helical or cylindrical systems - for example certain polypeptide chains [193]. Furthermore, Erickson [194] connected parastichy patterns to a variety of biological systems, including microtubules, the microfilaments of actin, the flagella of bacteria, and even the protein coats of viruses. This widespread occurrence of parastichy helices in nature has changed the contemporary discussion of phyllotaxis from its originally purely botanical viewpoint into a more general study of growth and self-organization. Specifically in physics, the geometrical considerations of cylindrical phyllotaxis have found applications in a variety of theoretical and experimental studies [195–201].

### 3.3 Outline of scientific contribution [A4]

As shown in Sec. 3.1, chains of classical dipoles possess a richness of static and dynamic properties. It was also shown that new properties and functionalities can emerge when the dipoles are not arranged along straight equidistant chains (see e.g. Refs. [165, 166]). But what happens when a dipole chain is arranged along a helical path? This question becomes rather intriguing when considering the complex phyllotactic patterns exhibited by cylindrical lattices discussed in Sec. 3.2: For example, how do the Fibonacci numbers and the golden ratio manifest in the dipole equilibrium configurations?

The scientific contribution [A4] investigates the ground state properties of classical helical dipole chains. The rich phenomenology found in [A4] provided the motivation for all remaining scientific contributions in this thesis, i.e. [A5] and [A6], which are both discussed in Chapter 4. In the following, the setup and key results of [A4] are outlined.

#### 3.3.1 Outline: Formation and crossover of multiple helical dipole chains [A4]

The scientific contribution [A4] investigates the ground state configurations of helically arranged dipole chains. In this setup, the dipoles can freely rotate and are positioned equidistant along a helical path. The position of the  $n$ -th dipole along the chain is then given by

$$\mathbf{r}_n(\Delta) := \begin{pmatrix} \rho \cos(n \Delta) \\ \rho \sin(n \Delta) \\ h n \Delta / 2\pi \end{pmatrix}, \quad (3.1)$$

where  $\Delta$  is the divergence angle, i.e., the (angular) distance between two dipoles along the helix,  $\rho$  is the helix radius, and  $h$  is the helix pitch. Due to the helical shape, the nearest neighbor in Euclidean space does not necessarily correspond to the nearest neighbor along the helical path. As a consequence, the equilibrium configurations show a complex dependence on the geometrical parameters, namely the helix radius  $\rho$  and the spacing  $\Delta$  of the dipoles along the helical path. The positions  $\mathbf{r}_n$  of the dipoles along the helix can be directly mapped to the lattice points of cylindrical lattices, just like the phyllotactic systems discussed in Sec. 3.2. It is therefore no surprise that we can employ considerations similar (but not identical!) to those used in phyllotaxis to classify and predict the equilibrium configurations of our helical dipole chains.

The ground states of helical dipole chains are classified for *arbitrary* system parameters  $\rho$  and  $\Delta$  - in contrast to the closest packing constraints in phyllotactic systems. In fact, we provide a classification of the ground state configurations for all parameters - except for the closest packing configurations. Details on the differences and similarities between the state classifications used in [A4] and phyllotaxis are provided in [A4]. In the following, we will only address non closest packing configurations.

As a key result, [A4] classifies the ground state dipole configurations of the helical dipole chain. These configurations consist of multiple interwoven head-to-tail dipole chains that are akin to the parastichy helices in phyllotactic systems. Each ground state dipole configuration can be mapped to an element of the Farey sequence<sup>2</sup>, which allows us to derive a self-similar phase diagram - related to the Stern-Brocot tree - that characterizes these ground-state configurations. This mapping is used to derive an analytical expression for predicting the ground state dipole orientations for a given Farey fraction and given geometrical parameters  $h$ ,  $\rho$ , and  $\Delta$ . The difference between nearest-neighbor and all-to-all interactions on the dipole equilibrium configurations is also discussed.

Overall, the scientific contribution [A4] demonstrates that the helical arrangement of dipoles can lead to intriguing and complex properties exceeding those of the strictly linear dipole chain. Of course, the self-similar phase diagram and the state characterization using fractions of the Farey series are specific to the arrangement of the dipoles along a helical path. But what happens if a different geometry is explored? Are there properties of dipoles arranged along curved manifolds somehow guided by some underlying principles, such that the ground state configuration can be predicted from the geometry of the manifold? These and similar questions have motivated the works [A5] and [A6], which study the properties of dipole lattices spanned on curved surfaces and are discussed in Ch. 4.

---

<sup>2</sup>Note that this mapping differs from the mapping used in phyllotaxis.

## Chapter 4

# Dipole arrays on curved surfaces

Chapter 3 demonstrated that the properties of dipole chains are significantly impacted by the geometry underlying their arrangement - especially if the geometry is not flat but curved. Inspired by the complex ground state properties emerging already in 1D helical dipole chains, the scientific contributions [A5] and [A6] investigate the properties of 2D dipole arrays on curved surfaces. This chapter reviews the relevant literature related to the scientific contributions [A5, A6].

Section 4.1 discusses the general equilibrium properties of dipole lattices in flat geometries. Section 4.2 continues with the properties and applications of ferroelectrics, which are materials exhibiting electric dipole order. Section 4.3 addresses the properties of magnetic dipole lattices and highlights the differences between electric and magnetic dipoles. Finally, Sec. 4.4 outlines the scientific contributions [A5] and [A6].

### 4.1 Equilibrium properties of dipole lattices

Classical dipole lattices have been studied for a variety of lattice geometries, including Bravais lattices [202–204], as well as special cases, such as the Kagome lattice [205, 206]. However, finding the ground state configuration for an arbitrary lattice geometry proves to be quite difficult. Of course, well-defined theories for finding these ground state configurations have been proposed. For example, one of the first such theories was the Luttinger-Tisza method [207], which provides solutions for common systems, such as the square lattice [208].

During the search for the ground state configurations of these dipole lattices, it was discovered that for certain lattice geometries, the ground state becomes continuously degenerate - even though the underlying lattice possesses only discrete symmetries [209]. The origin of this degeneracy has not yet been fully understood, however, it has been shown to occur for a wide range of geometries [208, 210–213]. In particular, for certain geometries in 3D, this degeneracy exists with respect to two parameters, whereas in the case of a 2D lattice, this is reduced to a degeneracy with respect to one parameter. For example, the ground state energy of a 2D square dipole lattice is invariant under a collective rotation of all dipoles. This degeneracy can be lifted even by small perturbations (arising from e.g. lattice disorder or non-zero temperature) in an order-by-disorder transition [210, 214].

For Bravais lattice geometries with non-degenerate ground states, the most favorable dipole orientations are typically striped patterns, where the dipoles align in stripes along head-to-tail chains. Neighboring head-to-tail chains align either parallel or anti-parallel with each other, depending on the underlying lattice geometry. However, even for a given lattice geometry the specific ground state configuration depends also on the system size and shape. For example, in large systems,

the energy may sometimes be minimized by the formation of vortex states [215, 216]. Certain boundary conditions induce shape anisotropies that impact the dipole equilibrium configurations. In the case of a triangular lattice, the ground state can - depending on the system size - exhibit both stripe and vortex patterns, and even domain walls for certain lattice shapes with large aspect ratios [215].

Beyond the ground state, dipole lattices can exhibit equilibrium configurations consisting of domains with different dipole orientations that are separated by domain walls. Especially for magnetic dipole arrays, this feature has been exploited for technological applications, such as information storage [217]. These domains and domain walls typically arise from a ground state degeneracy, and their presence can then be linked to a discrete symmetry breaking. More generally, domain walls are topological solitons [218, 219] and can be described mathematically within general frameworks, such as the Landau theory of phase transitions [220, 221]. Aside from dipole lattice systems, domain walls have been observed in a variety of systems including optics [222, 223], magnetic Bose-Einstein condensates [224], and even string theory [225].

## 4.2 Electric dipoles in ferroelectrics and dipolar rotors

The most prominent class of materials featuring electric dipoles are perhaps ferroelectrics [226–228]. Whether a material is ferroelectric depends first and foremost on its underlying crystal structure: Crystal structures can be categorized into 32 possible point group symmetries, 21 of those are non-centrosymmetric, and 20 of them are piezoelectric. Of those 20 piezoelectric crystal structures, 10 are pyroelectric and possess spontaneous electric polarization. Ferroelectrics form a sub-group of pyroelectric materials and are characterized by having a switchable electric polarization.

This switchable electric polarization makes ferroelectrics an invaluable ingredient for modern electronic devices. For example, they are used as ferroelectric field-effect transistors [229], sensors [230], or photonic devices [231]. Furthermore, there is active research on new technological applications of ferroelectrics, such as nonvolatile memories [232], negative capacity field-effect transistors [233, 234], neuromorphic memories [235–239], and logic-in-memory devices [240–242]. Common examples of ferroelectric materials include ceramic perovskites, such as  $\text{BaTiO}_3$ , or  $\text{PbTiO}_3$ . Due to the reliance on the underlying crystal structure, ferroelectric materials generally possess one or more preferred axes for the electric polarization - the polar axes. Rotating the polarization away from this polar axis is only possible at a substantial energy cost. Nevertheless, continuous rotation of the electric polarization has been experimentally observed in thin ferroelectric films [243].

Another approach for realizing arrays of freely rotating dipoles is using dipolar molecular rotors [148, 244]. This has been done for example in the context of metal-organic frameworks (MOF) [245, 246]. MOFs are complex materials where inorganic building blocks (metal ions) are linked with organic molecules. In the so-called rotor-MOFs [247], these linkers can possess rotational degrees of freedom, as well as permanent electric dipole moments [248, 249]. However, it should be noted that the dipole rotation in rotor-MOFs is typically restricted to one rotation axis. In addition to bulk materials, MOFs can be arranged in a variety of one and two-dimensional structures [250–254]. Furthermore, MOFs have been reported to exhibit switchable ferroelectric order [255, 256].

The formation of long-range polarization order in a system of electric dipoles generally depends on the dipole strength and the distance between dipoles. For

most solid-state materials, the dipole strength is typically less than 10 Debye, and rarely exceeds 50 Debye. In this context, it is interesting to note that extremely large dipole moments of the order of 1000 Debye have been realized with Rydberg molecules [257]. Dipole-dipole interactions between crystalline arrangements of Rydberg atoms are already exploited in Rydberg-tweezer array setups [258, 259], with possible applications in quantum computing [260], or nonlinear quantum optics [261].

### 4.3 Magnetic dipoles and their interactions

The properties and applications of crystalline arrays of magnetic dipoles are discussed. The discussion is split into two parts. Section 4.3.1 gives a general overview and Sec. 4.3.2 discusses magnetism on curved surfaces.

#### 4.3.1 General considerations regarding magnetic dipole arrays

The magnetic dipole moment of an object is linked to an angular momentum via the gyromagnetic ratio. This relation can be very nicely observed on the macroscopic scale with the Barnett effect [262] which shows the magnetization of an uncharged body under rotation, or with the Einstein–de Haas effect [263, 264], showing the inverse, i.e., the rotation of a body when the magnetization changes. As a result of this coupling, the magnetic properties of a material depend on the angular momenta of its constituents. It should be noted, that other effects, such as currents within a material, can also significantly contribute to the overall magnetic moment of a solid. However, in the following, we will focus on materials where the dominant contribution to the global magnetic field comes from the atoms at the lattice sites of a crystal.

The magnitude  $m$  of the magnetic moment of each atom in a solid can be related to its total angular momentum  $J$  [265, p. 368] with

$$m = g_J \mu_B \sqrt{j(j+1)}, \quad (4.1)$$

where  $g_J$  is the Landé  $g$ -factor,  $\mu_B$  is the Bohr magneton, and  $j$  is the angular momentum quantum number. This relation to the angular momentum impacts the dynamics of magnetic dipoles in the presence of an external magnetic field. Namely, when a magnetic dipole aligns with an external field to minimize its energy it experiences a torque. Due to a linear relation between magnetic moment and angular momentum, the torque consequently also acts on the angular momentum. This causes the so-called Larmor precession of the dipole around the direction of the external field [266]. The dynamics of a classical magnetic moment  $\mathbf{m}$  in an external (effective) magnetic field  $\mathbf{B}$  are described by the Landau-Lifshitz-Gilbert (LLG) equation [267, 268]

$$\frac{d\mathbf{m}}{dt} = \gamma \left( \mathbf{m} \times \mathbf{B} - \eta \mathbf{m} \times \frac{d\mathbf{m}}{dt} \right), \quad (4.2)$$

where  $\gamma$  is the gyromagnetic ratio and  $\eta$  is a material-specific damping parameter. In addition to dipole-dipole interactions, the formation of long-range order in a magnet is often influenced by a variety of magnetic interactions, such as exchange type [269] or the Dzyaloshinskii-Moriya interaction [270–272]. These magnetic interactions are often much stronger than the dipole-dipole interaction and dominate the orientations of magnetic dipole moments. The competition between magnetic interactions

for different equilibrium configurations can give rise to interesting equilibrium and dynamical properties. For example, a combination of exchange and Dzyaloshinskii-Moriya interactions can lead to non-collinear equilibrium configurations, such as spin-spiral states [273, 274] and even soliton-like structures like magnetic skyrmions [275–277]. Such non-collinear states have been envisioned for a variety of applications [278], including high-density storage devices [279, 280] and logic gates [281, 282].

In the past, the study of magnetic dipole arrays has focused on systems that are dominated by exchange-type interactions. However, there is interest in magnetic systems interacting dominantly with dipole-dipole interactions. Significant interest has been extended into systems, such as magnetic pyrochlore oxides (especially of the type  $A_2^{3+}B_2^{4+}O_7$ ) which feature both exchange-type and strong dipole-dipole interactions [283]. It has been shown that the properties of these magnetic pyrochlore oxides can be described by classical spins interacting with exchange and dipolar interactions [284]. A similar competition between dipolar and exchange interactions has been observed in thin magnetic films and other quasi-two-dimensional systems [285].

Long-range order of magnetic dipoles arising purely from dipole-dipole interactions is difficult to achieve on the microscopic level. Even when the distances between neighboring magnetic dipoles are large enough to suppress the exchange interaction, it is possible for non-magnetic atoms to mediate the exchange process, such as during the super-exchange mechanism [286] or the Dzyaloshinskii-Moriya interaction. Nevertheless, there are some creative approaches to realize microscopic systems interacting purely with dipole-dipole interactions. One example are lithographically prepared (single-domain) magnetic islands [287]: Within each island, the magnetic moments align ferromagnetically due to the exchange interaction. The entire island then acts as one magnetic dipole, such that the interactions between islands are dipole-dipole interactions.

### 4.3.2 Magnetic dipoles on curved surfaces

The properties of magnetic dipole arrays have also been studied with respect to geometric curvature. In the last decade, a rigorously formulated theory of magnetism in curved geometries - sometimes referred to as curvilinear magnetism [288] - has been developed [289, 290]. It has been demonstrated that curved geometries can induce two types of effective interactions: an effective Dzyaloshinskii-Moriya interaction, and an effective anisotropy. These effective interactions can be exploited in a variety of scenarios: For example, the induced DM interaction can be exploited to create topological states in materials that by themselves (i.e., without curvature) are unable to stabilize these configurations [291]. In magnetic wires, the curvature can suppress the Walker breakdown of domain walls (see also Refs. [292, 293]) and thereby allow for massive domain wall velocities [294]. Other examples of curvature-induced properties include the pinning of domain walls to regions with strong curvature (e.g. the bending regions of a wire) [295], curvature-induced domain wall motion [296, 297], asymmetric spin-wave dispersion in helical magnetic nanowires [174], curvature-induced magnon modes [298] and magnonic crystals [173], and the appearance of geometrical phases [299] or Berry phases [300]. A detailed overview can be gained from recent review articles on the topic [288, 301–304]. Despite this wealth of phenomena, the number of experimental studies of curvature effects is still limited [301].

It should be noted, that all above-mentioned curvilinear magnetic works treat (if at all) the dipole-dipole interaction as a small perturbation. They do not capture the physics of systems with dominating dipole-dipole interactions. The properties emerging in curvilinear systems dominated by dipole-dipole interactions are explored in the scientific contributions [A5] and [A6].

#### 4.4 Outline of Scientific contributions [A5, A6]

The scientific contributions [A5] and [A6] were motivated by the complex ground state properties exhibited by the helical dipole chains (see Ch. 3 for details). In contrast to the (effective) 1D system studied in [A4], the scientific contributions [A5] and [A6] are concerned with the properties of 2D dipole arrays that are arranged on curved surfaces. Together these works provide a first step towards understanding the impact of geometric curvature on lattice systems with long-range dipole-dipole interactions.

The contributions [A5] and [A6] share the same mathematical considerations, which are outlined below. In general, a classical electric dipole is characterized by a vector  $\mathbf{d}$  - with the magnitude  $d = |\mathbf{d}|$ . In [A4] and [A5], we arrange such dipoles on a curved surface and focus on the resulting dipole orientations in the ground state. The curved surface can in general be written as a parametric function

$$\mathcal{F} : \mathbb{R} \times \mathbb{R} \rightarrow \mathbb{R}^3 \quad ; \quad (\theta, \phi) \mapsto \mathcal{F}(\theta, \phi), \quad (4.3)$$

where  $\theta$  and  $\phi$  are the internal parametric coordinates of the surface (not necessarily angles). We consider dipole positions that are equidistant in the parametric coordinates, with fixed (parametric) distances  $\Delta\theta$  and  $\Delta\phi$  along the  $\theta$  and  $\phi$  directions. This creates a rectangular lattice in the parametric coordinates, where the parametric position of the dipole in the  $n$ -th row and  $m$ -th column is given trivially by  $(n\Delta\theta, m\Delta\phi)$ . The corresponding position in Euclidean (3D) space is then given by

$$\mathbf{r}_{nm} = \mathcal{F}(n\Delta\theta, m\Delta\phi). \quad (4.4)$$

In the case of a finite lattice with  $N$  rows and  $M$  columns, the indices can be 'simplified' by mapping all possible dipole positions to a single integer  $i$ , such that  $\mathbf{r}_i = \mathbf{r}_{nm}$  with  $n = \text{Mod}(i, N)$  and  $m = \lfloor i/N \rfloor$  and  $i \in [1, NM]$ . The total energy due to dipole-dipole interactions between all dipoles is then given by

$$V(\Delta\theta, \Delta\phi, \mathbf{d}_1, \dots, \mathbf{d}_{NM}) = \sum_{\substack{i,k=1 \\ i < k}}^{NM} \frac{1}{4\pi\epsilon_0} \left[ \frac{\mathbf{d}_i \mathbf{d}_k}{|\mathbf{r}_i - \mathbf{r}_k|^3} - \frac{3 [\mathbf{d}_i \cdot (\mathbf{r}_i - \mathbf{r}_k)] [\mathbf{d}_k \cdot (\mathbf{r}_i - \mathbf{r}_k)]}{|\mathbf{r}_i - \mathbf{r}_k|^5} \right]. \quad (4.5)$$

Note that for any given geometry  $\mathcal{F}(\theta, \phi)$ , the energy only depends on the dipole orientations  $\mathbf{d}_i$  and the (parametric) lattice spacings  $\Delta\theta$  and  $\Delta\phi$ . In the scientific contributions [A4] and [A5], we are mainly interested in finding the dipole ground state configurations and their dependence on  $\Delta\theta$  and  $\Delta\phi$  for a given geometry  $\mathcal{F}(\theta, \phi)$ .

Finding the ground state for a given geometry  $\mathcal{F}(\theta, \phi)$  is a non-trivial problem. The scientific contributions [A5] and [A6] mainly consider cases where the curvature radius is larger than the spacing between neighboring dipoles. By doing that, we exclude completely arbitrary arrangements of dipoles and force some correlation of the Euclidean dipole positions. For sufficiently large curvature radii, the dipole

arrangement can be treated locally as an (almost) flat lattice with (reasonably) well-defined primitive lattice vectors. Such a locally flat lattice only changes gradually across the surface  $\mathcal{F}(\theta, \phi)$ . This constraint can be exploited when determining the dipole equilibrium configurations.

#### 4.4.1 Outline: Geometry induced domain-walls of dipole lattices on curved structures [A5]

The scientific contribution [A5] investigates the general impact of geometric curvature on dipole lattices. The work is split into three parts: The first part discusses the general properties of dipole lattices on a curved or deformed surface. The second part discusses the universality of these effects and demonstrates their more general character with an example consisting of a dipole lattice spanned on the surface of a torus. The third part analyzes the dynamics of excitations in the toroidal dipole lattice.

The first part of [A5] shows that a curved or otherwise deformed lattice geometry can lead to the formation of domains and domain walls in the ground state. The dipoles of neighboring domains are oriented along different lattice directions. We derived a tool, the so-called gamma parameter, which can predict the positions of the domains and the domain walls directly from the lattice geometry. The gamma parameter is defined as

$$\gamma(\theta, \phi, \Delta\theta, \Delta\phi) := \frac{|\mathcal{F}(\theta, \phi) - \mathcal{F}(\theta + \Delta\theta, \phi)|}{|\mathcal{F}(\theta, \phi) - \mathcal{F}(\theta, \phi + \Delta\phi)|}. \quad (4.6)$$

The gamma parameter predicts the ground state dipole orientation for each point  $(\theta, \phi)$  on the surface  $\mathcal{F}$ . Wherever  $\gamma < 1$ , the dipoles will align along the  $\theta$ -direction, and for  $\gamma > 1$  along the  $\phi$ -direction (see Eq. 4.3 for a definition of  $\theta$  and  $\phi$ ). Domain walls generally form at positions where  $\gamma = 1$ , i.e. where the Euclidean distances to the nearest and next-nearest neighbors are equal. These curvature-induced domain walls behave different from the ordinary (degeneracy-induced) domain walls. We demonstrate this by showing the response of the domain wall to an external electric field. For low field strengths, the domain-wall position is shifted proportional to the field strength. Above a critical field strength, the domain wall splits into two domain walls surrounding a newly formed ferroelectric domain. We explain the formation of this new ferroelectric domain with the continuous ground state degeneracy appearing in dipole lattices where the nearest neighbor and next-nearest neighbor distances are equal (see also Ref. [209] for details).

In the second part of [A5], we validate and expand our understanding of the domain wall properties and formation by investigating a dipole lattice spanned on the surface of a torus. We find a good agreement between the numerically calculated domain wall positions and analytical predictions based on the gamma parameter. The electric field response of the domain wall, which was observed in the first part, could be replicated in the toroidal dipole lattice. This is notable insofar as the angle between the external field and the domain wall changes continuously along the domain wall.

Finally, in the third part, the dynamics of small amplitude excitations are analyzed in the limit of a harmonic approximation. We find a strong tendency of the eigenmodes to stay confined within the boundary of a domain. Due to this, all small amplitude excitations are unable to cross the boundary of the domain wall and are therefore prohibited from dispersing over the entire torus surface.

#### 4.4.2 Outline: Compression-induced crossovers for the ground-state of classical dipole lattices on a Möbius strip [A6]

The scientific contribution [A5] has demonstrated the basic properties of dipole lattices on curved manifolds. Motivated by this, we set out to investigate the properties of dipole lattices in a (topologically) non-trivial and non-orientable geometry. The scientific contribution [A6] considers the ground state properties of dipoles on a Möbius strip.

The scientific contribution [A6] provides an overview of the possible types of ground state configurations. Just like in [A5], the gamma parameter (see Eq. 4.6) can be used to accurately predict the formations of geometry-induced domains and domain walls in the systems ground state. Based on the gamma parameter, it is argued that all relevant dipole equilibrium configurations can be reached by varying the width of the Möbius strip while keeping the other system parameters constant. The dipole equilibrium configurations and their dependence on the Möbius strip width are subsequently analyzed. In the limit of a narrow Möbius strip width, there is only a single domain. When the width increases, a second domain will emerge and spread across the strip and eventually cover the entire surface of the Möbius strip.

The transition from a narrow to a wide strip (and vice versa) is then treated as an (adiabatic) compression or stretching of the strip. The total energy of the system during such compression is then analyzed together with the corresponding 2D (compression) modulus [305]. We highlight and explain different types of crossovers. Crossovers that are related to the creation or annihilation of a domain appear as sharp dips in the 2D modulus. A second type of crossover is linked to a saddle point on the Möbius strip. Specifically, there is a critical width for which one of the domains has expanded so far around the Möbius strip that it connects with itself exactly at this saddle point. Around this critical width, the domain sizes show great sensitivity to changes in the Möbius strip width. This second type of crossover also appears as a sharp dip in the 2D modulus. We also detect a crossover during which the system changes from favoring compression to resisting it.



## Chapter 5

# Scientific Contributions

In this chapter, we list our publications [[A1](#)–[A6](#)].



**Tunable order of helically confined charges**Ansgar Siemens<sup>1,\*</sup> and Peter Schmelcher<sup>2,1,†</sup><sup>1</sup>Zentrum für Optische Quantentechnologien, Fachbereich Physik, Universität Hamburg, 22761 Hamburg, Germany<sup>2</sup>Hamburg Center for Ultrafast Imaging, Universität Hamburg, 22761 Hamburg, Germany

(Received 20 March 2020; accepted 6 July 2020; published 27 July 2020)

We investigate a system of equally charged Coulomb-interacting particles confined to a toroidal helix in the presence of an external electric field. Due to the confinement, the particles experience an effective interaction that oscillates with the particle distance and allows for the existence of stable bound states, despite the purely repulsive character of the Coulomb interaction. We design an order parameter to classify these bound states and use it to identify a structural crossover of the particle order, occurring when the electric field strength is varied. Amorphous particle configurations for a vanishing electric field and crystalline order in the regime of a strong electric field are observed. We study the impact of parameter variations on the particle order and conclude that the crossover occurs for a wide range of parameter values and even holds for different helical systems.

DOI: [10.1103/PhysRevE.102.012147](https://doi.org/10.1103/PhysRevE.102.012147)**I. INTRODUCTION**

One of the most important unsolved packing problems is the Thomson problem [1]. It considers the question of the minimum energy configuration of  $N$  equally charged particles confined to the surface of a sphere. This rather mathematical problem, as well as its generalizations, are still relevant for research in physics, mathematics, chemistry, and biology [2–8], including, e.g., structural chemistry, virus morphology, and even engineering problems such as the optimal positioning of communication satellites. In this work we study the related problem of  $N$  long-range interacting particles confined to a one-dimensional (1D) path with nontrivial geometry.

One-dimensional interacting many-body systems are a field of steadily growing interest, in particular due to the fact that the properties of these 1D structures can be drastically different from those of bulk materials [9,10]. This renders them interesting candidates for, e.g., nanoelectronics and photonic applications [11–13]. Prominent approaches for confining particles to 1D space include carbon nanotubes (CNT) [14–16] as 1D nanowires or the trapping of particles in evanescent fields of thin nanofibers [17–20]. Artificially prepared 1D structures with nontrivial geometry include helices [15,16,19,21–25]. Helical structures offer several advantages, such as an increased robustness with regard to deformations [26,27], rendering them a desirable class of systems. Experimental preparatory techniques have succeeded in designing helical structures with diameters as small as 10 nm [15,28].

Charged particles confined to a helical structure can give rise to interesting properties, such as the optical activity of chiral molecules [29,30]. However, many approaches to the physics of helical systems are based on approximations with continuous charge densities or noninteracting particles. In

recent years, a series of theoretical works have demonstrated that a fascinating behavior can emerge when long-range interactions between helically confined particles are taken into account [31–41]. In these works, corresponding phenomena and effects are exposed by focusing on a model of ballistic Coulomb-interacting particles confined to a helical structure. It was shown that the Coulomb interaction, together with the constraining forces of the helix can form an effective 1D interaction potential that oscillates with the particle distance on the helix [31,32]. Depending on the helix geometry, this potential can possess several minima, at which the Coulomb forces are exactly canceled by the constraining forces. This allows the particles to “condense” into stable latticelike 1D particle chains on the helix, even when their interactions are purely repulsive.

As a direct consequence of the oscillating effective interactions, interacting particles on inhomogeneous helices were shown to exhibit interesting dynamics, such as the binding or dissociation of particles by scattering at such an inhomogeneity [34]. Investigations of interacting particles on a toroidal helix showed that the band structure and dispersion of the phonons can be controlled by the helix radius [35]. For the toroidal helix, a critical radius was found, at which the oscillations of individual particles decouple, and excitations are prevented from dispersing through the helical system [35,36].

The unique properties arising from the oscillating effective interactions are not limited to the structure and dynamics of charged particles. The overall mechanical behavior of the helix is equally affected. This can, for example, be observed in the unusual electrostatic resistance to a bending of the helix [38]: When interactions between the particles are considered, it was found, that for a fixed particle density, the system switches periodically between favoring and resisting the bending when the length of the helix is varied. Additionally, for large helix radii, the system’s ground state (GS) was found to drastically change for just slight variations in the bending, resulting in a discontinuous GS bending response.

\*asiemens@physnet.uni-hamburg.de

†pschmelc@physnet.uni-hamburg.de

The above examples demonstrate the unique physics occurring when long-range interactions between helically confined particles are considered. A common denominator of these investigations is the dependence of the unique properties on the helix geometry. Another degree of freedom can be added by applying an external electric field. Due to the confinement, a static electric field will create an oscillating potential landscape similar to that of the Coulomb interaction. Intriguingly, the oscillations of both interactions will in general have different characteristic length scales, leading to competing interactions, and a resulting behavior and properties that can easily be tuned by varying the electric field strength. A first step in that direction was taken in Ref. [39], where time-dependent electric fields were proposed to realize state transfers between arbitrary equilibrium configurations in a helical system with two charged particles.

In the above spirit, we study here the influence of an electric field on the static properties of charged particles on a toroidal helix. We identify two distinct phases of order that depend on the external field strength: an amorphous-like phase that persists for weak electric fields and a phase with crystalline order that is adopted in the presence of strong electric fields. We demonstrate the possibility of continuously switching between the phases by varying the electric field strength. Furthermore, we verify the existence of the observed phases for a large parameter space.

This work is structured as follows. Section II describes the confinement of charged particles to a toroidal helix and the resulting effective interactions in detail. In Sec. III, we then show the structural phase transition for an example system. We start by demonstrating amorphous ordering for individual particle configurations. Subsequently, an order parameter is designed and the disorder of the system is classified. Then we demonstrate how a continuous transition from amorphous to lattice ordering can be induced by tuning the electric field strength. In Sec. IV we demonstrate the generality of our results for a wide parameter range. Our conclusions and outlook are provided in Sec. V.

## II. CHARGED PARTICLES ON A TOROIDAL HELIX

We consider a system of  $N$  equally charged particles confined to a 1D path defined by a parametric function  $\mathbf{r}(u) : \mathbb{R} \rightarrow \mathbb{R}^3$ . The particles are subject to a gradient force  $\mathbf{F}_E = q\mathbf{E}$  in form of an external electric field and interact via Coulomb forces  $\mathbf{F}_C = \lambda \mathbf{e}_{ij} / |\mathbf{r}(u_i) - \mathbf{r}(u_j)|^2$ , where  $\lambda = q^2 / 4\pi\epsilon_0$  is the coupling constant, and  $u_i$  and  $u_j$  are the positions of the interacting particles in parametric coordinates. Since the particles are only allowed to move along the 1D path  $\mathbf{r}(u)$ , they additionally experience confining forces. The confining forces cancel all forces acting perpendicular to the path, resulting in an effective force parallel to the tangential vector  $\partial_u \mathbf{r}(u)$ . Mathematically, the consideration of confining forces corresponds to a projection of forces on the parametric curve. With

$$\text{proj}(\mathbf{a}, \mathbf{b}) := (\mathbf{a} \cdot \mathbf{b}) \cdot \frac{\mathbf{b}}{\|\mathbf{b}\|}$$

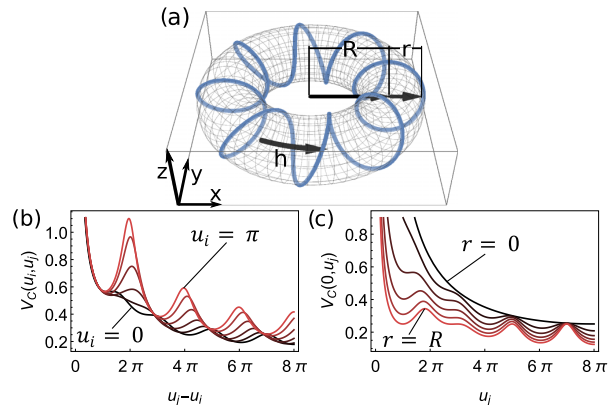


FIG. 1. (a) A toroidal helix with  $M = 8$  windings for the parameter values  $r/h = 1.6/\pi$ ,  $R = 2$ . (b) The Coulomb potential  $V_C(u_i, u_j)$  for the same parameters as (a) and different fixed values of  $0 \leq u_i \leq \pi$ . The position  $u_j = \pi M = 8\pi$  corresponds to particle positions on opposite sides of the torus. Coloring varies from red ( $u_i = \pi$ ) to black ( $u_i = 0$ ). (c) The Coulomb potential  $V_C(0, u_j)$  for the same parameters as (a) and different helix radii  $0 \leq r \leq R$ . Coloring varies from black for  $r = 0$  to red for  $r = R$ .

the effective force on a particle can be written as

$$\mathbf{F}_{\text{eff}}^{(i)} = \text{proj} \left[ q\mathbf{E} + \sum_{i \neq j}^N \frac{\lambda \mathbf{e}_{ij}}{|\mathbf{r}(u_i) - \mathbf{r}(u_j)|^2}, \frac{d\mathbf{r}(u_i)}{du_i} \right]. \quad (1)$$

The effective force on a particle vanishes if the sum of all forces is perpendicular to the confining path. Despite repulsive interactions between the particles, the geometry of the path can thereby allow for the existence of equilibrium states where the effective forces on all particles vanish. These stable equilibrium configurations correspond to minima in the potential energy, which is given by

$$V_{\text{tot}} = V_E + V_C = \sum_{i=1}^N q\mathbf{E} \cdot \mathbf{r}(u_i) + \sum_{i < j}^N \frac{\lambda}{|\mathbf{r}(u_i) - \mathbf{r}(u_j)|}. \quad (2)$$

Equation (2) already accounts for the effects of the confinement by only allowing for particle positions on the parametric curve  $\mathbf{r}(u_i)$ .

The effects of confining forces are particularly relevant for paths with nontrivial geometry in the form of nonvanishing curvature. A simple class of systems satisfying this demand—while at the same time being common enough to occur in nature—are helical systems. Here we investigate the properties of equilibrium configurations on a toroidal helix. An example of such a system is visualized in Fig. 1(a). The particle positions on a toroidal helix are given by the following parametrization in Euclidean space:

$$\mathbf{r}(u_i) := \begin{cases} [R + r \cos(u_i)] \cos(u_i/M) \\ [R + r \cos(u_i)] \sin(u_i/M) \\ r \sin(u_i) \end{cases}, \quad \begin{matrix} u_i \in [0, 2\pi M] \\ i \in [1 \dots N] \end{matrix}, \quad (3)$$

where  $R$  is the torus radius,  $r$  is the helix radius, and  $M$  the number of windings. Since we want the helix to close after circling around the torus exactly once, the parameters

must satisfy the relation  $Mh = 2\pi R$ , where  $h$  is the helix pitch. The parametric coordinate  $u_i$  of the  $i$ th particle can be interpreted as an angle. If  $u_i$  changes by an amount of  $2\pi$ , then the position on the helix changes by exactly one winding. Since the toroidal helix has  $M$  windings,  $\mathbf{r}(u_i)$  is invariant under translations by  $u_i \rightarrow u_i + 2\pi M$ . For easier comparison between systems with different parameters, we introduce the filling factor  $v = N/M$  as the ratio of particles per winding.

### A. Coulomb potential

Since the confinement can drastically change the underlying potential landscape, we will now discuss the effects of the confinement on the two sums of Eq. (2) individually. For the Coulomb potential, already the contribution of two particles shows an immense complexity compared to the Coulomb interaction of “free” particles. When written as a direct function of the parametric coordinates  $u_i$  and  $u_j$ , the two-particle Coulomb potential  $V_C^{ij} := V_C(u_i, u_j)$  of the particles  $i$  and  $j$  is given by:

$$V_C^{ij} = 2\lambda \left\{ \sin^2 \left( \frac{u_i - u_j}{2M} \right) [R + r \cos(u_i)][R + r \cos(u_j)] + r^2 \sin^2 \left( \frac{u_i - u_j}{2} \right) \right\}^{-\frac{1}{2}}. \quad (4)$$

This potential directly depends on the helix parameters and can—depending on the helix geometry—possess several minima. Minima in the Coulomb potential correspond to positions, where the particles cannot move further along the helix, without decreasing their (3D) distance to each other, for example, by trapping each other on opposite sides of a helix winding. The general behavior of Eq. (4) is indicated by Fig. 1(b) which shows multiple cross sections of the potential for various fixed values of  $u_i$ . Contrary to the Coulomb interaction of “free” particles, the effective Coulomb interaction of particles on a toroidal helix cannot be described by the relative particle distance alone. As a consequence, the cross sections of  $V_{\text{tot}}$  are different for different positions of  $u_i$ . This also implies that both particles can experience slightly different potential wells and compete for minimization of the total potential energy. Note that the above-described behavior is a direct consequence of the toroidal helix being bent since in the case of a homogeneous helix the effective interaction can be described using only the relative particle distance. The influence of the helix radius on the effective Coulomb potential is shown in Fig. 1(c). The figure shows the change of a single cross section for variations of  $r$  in the range  $0 \leq r \leq R$ . With decreasing  $r$ , the stability of the minima decreases. For small values of  $r$ , some of the equilibria become unstable. In the limit of  $r \rightarrow 0$ , the oscillations disappear, leaving only a single stable minimum. In this minimum, both particles are positioned on opposite sides of the toroidal helix with a distance of  $\Delta_{ij} = \pi M$ .

### B. Electric field

The potential energy contribution of the electric field  $V_E$  is similarly influenced by the confining forces. In this paper, we consider an electric field in the  $z$  direction. The potential

energy  $V_E$  then simplifies to:

$$V_E = \sum_{i=1}^N qEr \sin(u_i). \quad (5)$$

Similarly to the Coulomb potential,  $V_E$  also oscillates with the particle positions. Both interactions therefore support the formation of equilibrium configurations. However, the characteristic length scales of the oscillations of  $V_E$  and  $V_C$  are in general different. From this, one may already expect fundamentally different behavior for the regimes of dominating Coulomb interaction and dominating electric field.

From the above discussion, it is easy to see that the potential landscape of a system with  $N$  particles can become quite complex since it consists of  $(N - 1)!$  sums of functions like Eq. (4), in addition to the potential  $V_E$  given by Eq. (5). Already systems with only a few particles can support a plethora of minima [31] that in general can only be found within numerical calculations. With this, the tasks of finding the equilibria of systems with large particle numbers can quickly become computationally expensive.

In the following, we will describe the structural phase transition of the equilibria, occurring when the electric field strength is varied. Our results are given in dimensionless parameters, where energies are measured in units of  $\lambda/\alpha = q^2/4\pi\epsilon_0$ , and—due to the scale invariance—distances can be scaled by the constant  $\alpha = 2h/\pi$ . For an initial overview over the effective behavior, we use the following parameter values:  $M = 8$ ,  $N = 10$ ,  $r = 0.8$ , and  $R = Mh/2\pi = 2$ .

A final remark on our computational approach is in order: The minima of  $V_{\text{tot}}$  for  $E = 0$  are obtained with a quasi-Newton method [42,43]. For different electric field strength, the minima were obtained using an interior-point method [44] by stepwise varying  $E$  and calculating the new minima while using the minima of the previous step as an initial guess.

## III. STRUCTURAL CROSSOVER

In this section, we investigate the equilibrium configurations of charged particles on the toroidal helix and show how a transition from amorphous-like to crystalline particle ordering can be induced by varying the external electric field strength. While this structural crossover is a general effect that can be observed for a wide parameter regime, the specific equilibria can be influenced by the helix parameters. Consequently, the results shown in this section will contain some parameter-specific features. A generalization of the results to different parameter regimes is discussed in Sec. IV.

### A. The minima of the helical Coulomb potential

We start by demonstrating amorphous particle ordering for the case of a vanishing external electric field. In this case, the potential landscape simplifies to  $V_{\text{tot}} = V_C$ . Here we want to convey a basic intuition for the equilibrium particle configurations in this regime.

#### 1. The ground state

We start by examining the GS of the system, visualized in Figs. 2(a)–2(c). For  $E = 0$ , the particles minimize their energy

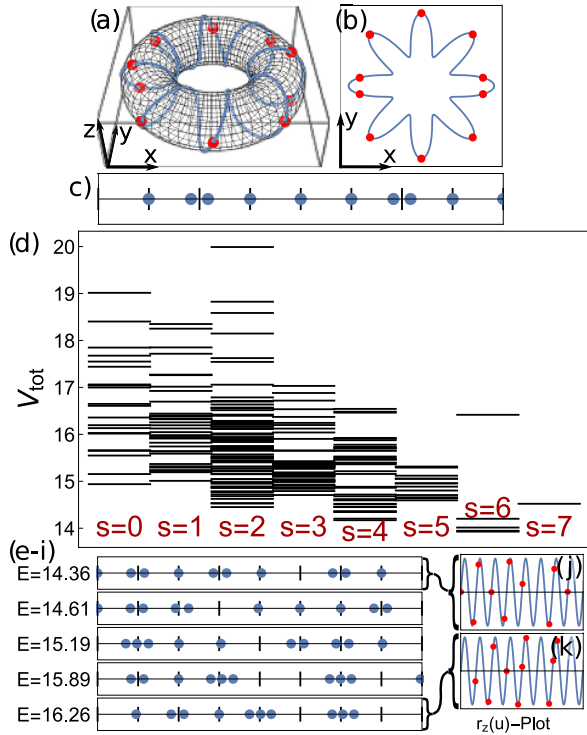


FIG. 2. [(a)–(c)] Visualizations of the ground state: (a) 3D view, (b)  $xy$  projection, and (c) parametric coordinates. Vertical lines in (c) indicate the outermost part of a winding. (d) Energies of stable states sorted by the number of singlets  $s$ . [(e)–(i)] Example minima in parametric coordinates, sorted by their energy. Vertical lines again indicate the outermost part of each winding. [(j) and (k)] Different visualizations of the equilibria of (e) and (i), showing the  $z$  component of the particle positions  $r_z(u) = r \sin(u)$  as a function of the parametric coordinate. For emphasis, the possible particle positions are marked by the blue line.

by maximizing their distances. Our system is small enough such that all particles interact significantly with each other, and positions close to the center of the torus are avoided. If we had as many particles as windings (filling factor  $\nu = 1$ ), in the GS, then each particle would occupy the outermost point of a winding. However, since we have 10 particles and only 8 windings, some of the helix windings are occupied by several particles. When two particles occupy the same winding [45], they want to align at a distance corresponding to the first minimum of the two-particle Coulomb interaction. Slight deviations from this distance are caused by interactions with neighboring particles.

## 2. Nomenclature

From the top view of our system in Fig. 2(b) it is intuitive that the energy of any configuration will increase if a particle moves closer toward the center of the torus. We will now use this effect to introduce some helpful nomenclature. We split the toroidal helical path into  $M$  windings and characterize the minima by the distribution of particles onto these windings.

These distributions will be called *x-lets*: A winding with only a single particle is called a *singlet*, one with two particles a *doublet*, and so on. By this definition, the GS depicted in Figs. 2(a)–2(c) consists of six singlets and two doublets.

## 3. Excited states

An overview of the excited states is given in Fig. 2(d). It shows the energy of all minima sorted by their number of singlets  $s$ . Each minimum is represented by a black horizontal line. The ground state can be found in the column for states with  $s = 6$  singlets. In total 710 distinct minima were found in the potential landscape for  $E = 0$ . The minima seem to be equally distributed over a large energy range. We observe a decrease of the occupied energy range for an increasing number of participating singlets. Example visualizations of excited states are shown in Figs. 2(e)–2(i) together with their corresponding energy. The particle positions in Figs. 2(e)–2(i) follow a simple pattern: The particles try to accumulate around the outermost part of a winding. If they share a winding with other particles, then they somewhat deviate from this lattice order, creating staggered particle configurations. The distance between particles that share a winding is approximately the same for doublets and triplets and corresponds to about 30% of the length of a winding—a significant deviation from a crystalline lattice ordering.

The distances between particles in doublets and triplets are visualized in Figs. 2(j) and 2(k). They respectively show the same equilibria as Figs. 2(e) and 2(i) and additionally include the  $z$  position of each particle. We can see that for example the particles in doublets prefer to align almost on opposite sides of the winding to maximize their distance.

For our chosen parameters, all minima follow the same pattern as the five example excited states in Figs. 2(e)–2(i): The total particle number  $N$  is split up into singlets, doublets, triplets, and in some cases even quadruplets, which are then distributed among the windings. Therefore, every minimum is uniquely characterized by a specific sequence of x-lets.

## B. Classifying the particle order

Now we design an order parameter to classify the particle order of every equilibrium particle configuration in a mathematically more rigorous way. Any quantifiable order that can be observed for most of the minima will likely be linked to a symmetry of the confining manifold. The toroidal helix possesses a discrete rotational symmetry. It is invariant under a rotation of  $2\pi n/M$  with  $n \in \mathbb{N}$  around its center. In our parametric coordinates  $u_i$  this corresponds to a discrete translation symmetry. We have already seen hints for this translation symmetry in the discussion above. From Eq. (5), we can see that this symmetry holds even in the presence of an electric field in  $z$  direction. Our order parameter should therefore also reflect this symmetry. From Eq. (3) and the definition of  $V_E$ , we can also see that the symmetry is broken if the field has a component perpendicular to the  $z$  direction, which is why this case is not considered in this work. With this in mind, we define our order parameter  $\Theta$ :

$$\Theta = 1 - \frac{1}{\pi} \sqrt{\frac{\sum_i (d_i - \mu)^2}{N}} \quad \text{with} \quad \mu = \frac{1}{N} \sum_i d_i, \quad (6)$$

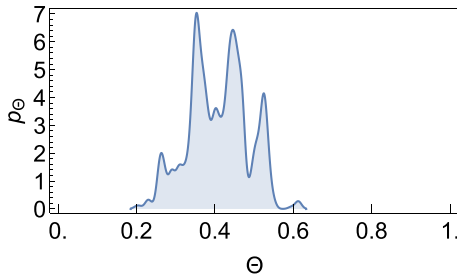


FIG. 3. Probability density  $p_\Theta$  for finding a minimum with a specific order  $\Theta$  for a system with  $M = 8$ ,  $r = 0.8$ ,  $h = \pi/2$ ,  $R = 2$ , and  $N = 10$ .

where  $d_i = \text{Mod}(u_i + \pi, 2\pi) - \text{Mod}(u_{i+1} + \pi, 2\pi)$  are the truncated next-neighbor (tNN) distances. The  $d_i$  can be interpreted as a relative deviation of the neighboring particle positions within their winding. The second summand of  $\Theta$  in Eq. (6) is simply the normalized standard deviation of the tNN distances.

As an order parameter,  $\Theta$  is in the range  $[0, 1]$ .  $\Theta$  is 1 if all  $d_i$  are the same and the particles show a lattice symmetry.  $\Theta$  decreases with increasing deviation from this translation symmetry.

We can now use this order parameter to characterize the order of the equilibria. From Fig. 2(b) we can see that the particles in the GS are mostly aligned at the outermost point of each winding. With the exception of the two doublets, the particles already possess a translation symmetry. However, the two doublets distort 6 of the 10 tNN distances from perfect lattice ordering, resulting in  $\Theta_{\text{GS}} = 0.613$ . The order of the minima shown in Figs. 2(e)–2(i) is 0.535, 0.517, 0.377, 0.453, and 0.342 respectively. In this fashion, we can calculate the order parameter for every minimum. The results are shown in Fig. 3 as a probability density  $p_\Theta$ . The order parameter  $\Theta$  of a minimum is (approximately) proportional to the number of singlets  $s$ . The large peak around  $\Theta \sim 0.53$  consists entirely of minima with  $4 \leq s \leq 6$ . The peaks around  $\Theta \sim 0.45$  and  $0.35$  consist of minima with  $2 \leq s \leq 4$  and  $0 \leq s \leq 3$ , respectively. As we will see,  $p_\Theta$  will evolve as a bulk when the electric field strength is increased. For our purposes, the statistics of  $p_\Theta$  is well described by the mean value  $\overline{p_\Theta}$  and the standard deviation  $\sigma(p_\Theta)$ . For the curve of Fig. 3 we get  $\overline{p_\Theta} = 0.420$  and  $\sigma(p_\Theta) = 0.071$ .

### C. Forcing crystalline ordering

We will now show the crossover to crystalline particle configurations in the presence of a static external electric field. For the evaluation, the minima for  $E > 0$  are obtained by tracing the minima found for  $E = 0$  while the electric field is increased adiabatically, i.e., we do not actively search for newly created minima, which are only stabilized by the electric field. In practice, we varied the electric field in steps of  $\Delta E = 0.002$  and calculated the new equilibrium positions using the equilibria of the previous step as initial guesses.

### 1. Order parameter evolution

The evolution of  $p_\Theta(E)$  for an adiabatic increase of  $E$  can be seen in Fig. 4(a). The information is split up into the mean value (blue), the minimum and maximum (dotted black), and the standard deviation (red) (denoted as  $\overline{p_\Theta}(E)$ ,  $\min[p_\Theta(E)]$ ,  $\max[p_\Theta(E)]$ , and  $\sigma[p_\Theta(E)]$ , respectively). Close to  $E = 0$ , there is a small range where  $\overline{p_\Theta}(E)$  changes very little, while the variance increases. In this field range, most of the complex changes in the potential landscape, including the annihilation of minima, take place. For our chosen parameters, about  $\sim 16.5\%$  of all minima are annihilated in this phase. When a minimum is annihilated, there will be a sudden jump in the tNN distances, corresponding to particles changing their winding. This sudden change of particle positions is the reason for the increase of  $\sigma(p_\Theta)$  in the low field regime. The specific bifurcation scenarios by which these annihilations take place depend strongly on the chosen system parameters and can quickly get quite complex [39]. For larger fields,  $\overline{p_\Theta}(E)$  increases with  $E$  while the variance decreases, indicating a transition to minima with lattice order. In this regime, variations in the electric field only adjust the particle positions while their distribution among the windings persists. From  $\min[p_\Theta(E)]$  we can see that a large-enough field can impose order in the system—independent of the initial particle configuration.

### 2. Relative particle positions

The reason why an increase of the electric field strength causes an increase in our order parameter can be understood from the behavior of individual particles during the transition. For this purpose, we consider the nearest-neighbor (NN) distances  $q_i := u_i - u_{i+1}$  of the particles. Figure 4(b) shows a statistic of the occurring NN distances for  $E = 0$  (dark blue) and  $E = 25$  (orange). For  $E = 0$ , we see a relatively sharp peak at a distance of slightly less than  $\pi$ , very close to the first minimum in the Coulomb potential. It is caused by the particles with a NN in the same winding, i.e., the doublets, triplets, and so on. It is also possible that the NN particle is in a neighboring winding. Therefore, we also see NN distances around the value of  $2\pi$ . There are also smaller probabilities for finding a NN at distances around  $4\pi$ ,  $6\pi$ , and  $8\pi$ . They correspond to the cases with one, two, and three empty windings between the NN particles.

The evolution of this statistics with variations of the electric field strength is shown in the insets of Fig. 4(b). In both insets, the information is split up into five curves, each representing the evolution of a peak in the probability density. The upper inset shows that the variance of each peak decreases with increasing  $E$ , while the lower inset describes a continuous shift of the mean position of each peak to multiples of  $2\pi$  when  $E$  is increased. For large electric fields, the result are sharp peaks in the distribution  $p(q_i)$  at distances of  $2\pi n$ ,  $n \in \mathbb{N}_0$  [see Fig. 4(b) (orange)], corresponding to a lattice ordering with a lattice constant of  $2\pi$ . The dominating electric field drives the particles along the  $z$  direction and forces a clustering around the top of the helix windings.

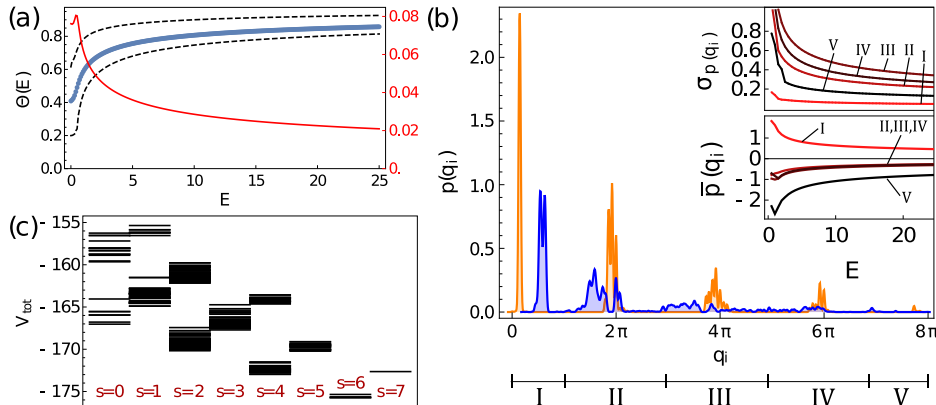


FIG. 4. (a) Evolution of the order parameter  $\Theta$  when the electric field  $E$  is increased adiabatically; with the mean value  $\overline{p_\Theta}$  (blue), the minimum and maximum  $\text{Min}(p_\Theta)/\text{Max}(p_\Theta)$  (dotted black), and the variance  $\sigma[p_\Theta(E)]$  (thin red). Note the different scale of the variance. (b) Normalized statistics of nearest-neighbor distances for  $E = 0$  (dark blue) and  $E = 25$  (orange). The two insets correspond to the variance  $\sigma_{p(q_i)}$  and mean (modulo  $2\pi$ )  $\overline{p}(q_i)$  of individual peaks in the statistics (regions I–V) as a function of  $E$ . (c) Energies of equilibrium configurations for  $E = 25$ , sorted by their number of singlets  $s$ .

### 3. Potential landscape

The fundamental change of system properties for large  $E$  is evident from the energies of individual minima [Fig. 4(c)]. Compared to the case  $E = 0$  shown in Fig. 2(d), the minima are now sorted into narrow “bands” with little relative distance in energy. The minima of each band contain the same number of singlets, doublets, and so on. These bands are formed because, for these large fields, the interaction between particles is only significant when they share a winding. Therefore, for large  $E$ , the specific number of  $x$ -lets in a minimum has a greater impact on the energy than their relative ordering.

Furthermore, since the potential landscape for a dominant electric field is qualitatively described by the potential  $V_E$ , we can also estimate the stability of minima in this regime. Transitioning to another minimum requires a particle to change its winding and therefore to move past the transition state at which the particle is located at the down most point of a winding. Using Eq. (5) and neglecting the Coulomb interaction, this transition requires energy in the order of  $\Delta E = 2Er$ . In theory, these energy barriers can be made arbitrarily large. The increased stability in large electric fields can also be used to tune a more common, temperature-induced, order-disorder transition.

## IV. GENERALIZATION TO PARAMETER VARIATIONS

We will now discuss the influence of parameter variations on the transition between amorphous and crystalline particle ordering. Since the clustering of particles at the top of the helix windings can always be enforced if  $E$  is large enough and  $r > 0$ , we will focus our discussion on arguments for the persistence of amorphous ordering for parameter variations in the absence of the external electric field.

### A. System size

In the previous section, we have observed the tendency of particles to avoid positions close to the center of the torus.

This effect is a direct consequence of the small system size and can be suppressed by reducing the ratio of  $r/R$ . Here we study the impact of the ratio  $r/R$  on the system by increasing the winding number  $M$  (and consequently increasing  $R$  due to the relation  $Mh = 2\pi R$ ) while maintaining a constant filling factor  $\nu = N/M$  and helix pitch  $h$ . Note that due to the large number of minima and the numerical challenge of finding *all* of them, data for systems with  $M > 8$  were obtained from a random subset of minima and not every possible equilibrium configuration in the potential landscape for these specific parameters. The number of minima  $\eta$  considered for each subset has been chosen such that the total number of particles used for the statistics is about  $\eta\nu M \sim 30\,000$ . To ensure that this statistics is representative for the system, we verified that repeated calculations with different random subsets give very similar results.

The influence of increasing the winding number (and thereby increasing the torus radius) is analyzed in Fig. 5. A general overview is given by Figs. 5(a)–5(c) which show the particle positions in parametric coordinates over a distance of eight windings for systems with a total of  $M = [8, 64, 128]$  windings and a constant filling of  $\nu = 1.25$ . Figure 5(a) represents a system with  $M = 8$ , where all particle positions are close to the outermost part of the windings which are indicated by the vertical lines. With increasing  $M$  [Figs. 5(b) and 5(c)], this specific position dependence disappears such that in (c) the particle positions look almost random.

Further insight into the size effects can be gained from the analysis in Fig. 5(d). It shows the probability density  $p_u$  for finding a particle at a specific position within a winding for a system with  $M = 8$  (blue) and a much larger setup with  $M = 128$  (orange). We can see that, for  $M = 8$ , particles avoid positions close to the center of the torus (positions 0 and  $2\pi$  in the figure). In addition, there is a peak at  $\pi$ , indicating an increased likelihood of finding a particle at the outermost part of a winding (with a distance of  $R + r$  from the torus center). This peak is mostly caused by the singlets which—due to their lack of close neighbors—hardly deviate in terms of their

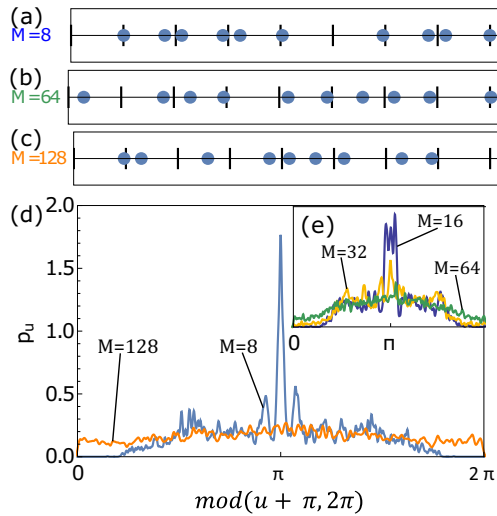


FIG. 5. [(a)–(c)] Particle positions (cutout of eight windings) of equilibrium configurations in parametric coordinates for a constant filling  $v = 1.25$  and (a)  $M = 8$ , (b)  $M = 64$ , and (c)  $M = 128$ . (d) Probability density  $p_u$  for finding a particle at a certain position in a winding for  $M = 8$  (blue) and  $M = 128$  (orange). The inset shows  $p_u$  for  $M = 16, 32, 64$  (purple, yellow, green), respectively.

position from the outermost part of the winding. In contrast, this dependence of  $p_u$  on the position within a winding is hardly visible for  $M = 128$ . For  $M = 128$ , the system is a good approximation of the straight helix with  $M, R \rightarrow \infty$  and a constant probability density of  $1/2\pi$ . Interestingly (except for the peak at  $\pi$ ), the probability density  $p_u$  for  $M = 8$  is of similar order in the range  $[\pi/2, 3\pi/2]$ , indicating that the particle positions for  $M = 8$  are far less predictable than the visualizations of Figs. 2(e)–2(i) might suggest.

Figure 5(d) shows only the cases of very small ( $M = 8$ ) and very large ( $M = 128$ ) systems. A better understanding of the evolution of the probability distribution  $p_u$  between these two regimes can be gained from the Fig. 5(e). It shows the curves  $p_u$  for different intermediate values of  $M$ . An interesting observation is that for increasing  $M$  the peak at  $\pi$  broadens and then disappears, before any significant change in the “avoided” region around 0 and  $2\pi$  can be observed. The reason for this is that when  $M$  is increased, the forces of NNs begin to dominate over the combined interactions with all other particles. In general, the positions of singlets are more strongly affected than doublets or triplets since they, due to their lack of close neighbors, require less energy to slightly shift their position. Only for (much) larger  $M$ , the torus gets big enough such that the effect of particles avoiding positions close to the center of the torus becomes negligible. The described behavior implies that for increasing  $r/R$  the particles deviate from the pattern for equilibrium particle positions described in the previous section.

An increase of the winding number is therefore responsible for an increase of the disorder—at first due to the shift in singlet positions and for larger  $M$  due to the loss of any preferred position within the windings. Specifically for the

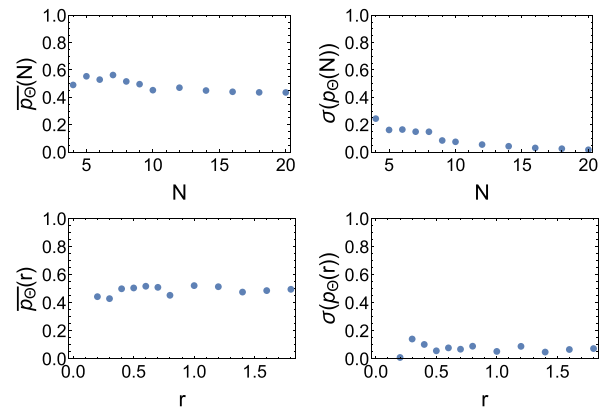


FIG. 6. The mean  $\overline{p_\Theta}$  and variance  $\sigma(p_\Theta)$  of the order parameter for variations of [(a) and (b)] the particle number  $N$  and [(c) and (d)] the helix radius  $r$ . All figures were obtained for  $M = 8$  and  $E = 0$ .

values of Fig. 5(d): When the winding number is increased from  $M = 8$  to  $M = 128$ , the distribution of  $p_\Theta$  changes from the values of Fig. 3 [ $\overline{p_\Theta} = 0.42$  and  $\sigma(p_\Theta) = 0.071$ ] to  $\overline{p_\Theta} = 0.24$  and  $\sigma(p_\Theta) = 0.03$ . Since the amorphous particle order persists in the limiting case of the straight helix, we can assume that the described behavior is valid for a large parameter range of helical systems.

## B. Impact of the helix radius and the filling factor

### 1. Filling factor

So far, we have explored the impact of the winding number on the properties of our helical setup, while keeping the filling factor  $v$  and the helix radius  $r$  constant. Now we examine the respective effects of the latter two parameters on the particle order for  $E = 0$ . We investigate the filling factor  $v = N/M$  by varying the particle number  $N$  while maintaining a constant number of windings  $M$  to prevent the occurrence of additional effects on the order parameter due to the system size. The mean and variance of the distribution  $p_\Theta$  for different particle numbers are shown in Figs. 6(a) and 6(b), where the particle number is varied in the range 4...20. The mean value is approximately  $\overline{p_\Theta} \sim 0.5$ , while the variance decreases with increasing  $N$ .

The overall behavior of  $p_\Theta$  with changes in the particle number can be explained as follows: It is in general unfavorable for a winding to have a much larger particle density than its surrounding windings. Consequently, lower-order  $x$ -lets, such as singlets or doublets, are increasingly suppressed with increasing filling factor  $v$ . Compare for example the case of  $N = 10$  to  $N = 20$ : In the former, the average equilibrium particle configuration contains about  $\sim 2.8$  singlets ( $\sim 34\%$ ), whereas, for  $N = 20$ , the average number of singlets per equilibrium configuration is about  $\sim 1.4$  ( $\sim 18\%$ ). We also know from the discussion of the previous section, that the NN distances of particles that share a winding are very similar. Since our order parameter only requires these NN distances as input, slightly different particle distributions among the

windings will (for large  $N$ ) only have a small impact on the order parameter. Consequently, the variance of the distribution  $p_\Theta$  decreases with increasing filling factor  $v$ .

A final remark is in order for the extreme cases of very low ( $N \ll M$ ) and very large ( $N \gg M$ ) filling factors. While the parameter range explored in Figs. 6(a) and 6(b) does not have any adverse effect on the structural crossover, the disorder for  $E = 0$  can be affected in the limits  $v \rightarrow 0$  and  $v \rightarrow \infty$ . In case of  $N \ll M$ , the system is too scarcely populated to define any (useful) particle ordering. On the other hand, in the limit of  $N \gg M$ , the average particle distance will approach zero. We assume that in this case, the equilibria for  $E = 0$  will consist of particles with crystalline ordering—although in small systems a slight position dependence of the lattice constant may appear due to the previously discussed size effects.

## 2. Helix radius

The helix radius can be varied in the range  $0 \leq r \leq R$ . When  $r$  is varied within this range, we (again) obtain an almost constant mean value of  $\overline{p_\Theta} \sim 0.5$  [see Fig. 6(c)]. While the corresponding variance  $\sigma(p_\Theta)$  is also approximately constant for most of the parameter range, it becomes zero below a critical helix radius [see Fig. 6(d)]. This is because the number of equilibrium states can be tuned with the helix radius (specifically the ratio of  $r/h$ ) and for low values of  $r$ , the system only possesses a single equilibrium state. Otherwise, the behavior of  $p_\Theta$  for variations of  $r$  is mainly determined by two competing effects: First, an increase in the helix radius increases the ratio of  $r/R$  and thereby increases the size effect (and the order parameter) similar to the description above for variations of  $M$ . Second, at the same time, the helix radius also tunes the number of particles that can be stabilized within a single winding. From the discussion of Fig. 3, we know that equilibria with higher-order  $x$ -lets will be less ordered than, e.g., those with a large number of singlets. Consequently, this second effect alone will lead to a decrease of the order parameter for increasing  $r$ . The values of Figs. 6(c) and 6(d) are the result of the competition between those two effects.

To summarize the parameter variations: The disorder increases with increasing  $M$ . The influence of  $v$  is only relevant in the limits of very large or very low  $v$ . Increasing  $r$  will increase the disorder as long as the ratio  $r/R$  does not change significantly; otherwise competing effects can also decrease the disorder.

## V. SUMMARY AND CONCLUSION

In this work, we considered an effective interaction arising from the confinement of Coulomb interacting particles to a

1D toroidal helix. The effective interaction allows for the existence of a plethora of stable equilibrium particle configurations. We investigated the properties of these equilibrium configurations in the presence of an external electric field and found a structural crossover that can be tuned by varying the electric field strength. For a vanishing electric field, we found a preference for amorphous particle ordering, whereas, in the regime where the electric field dominates over the Coulomb interaction, the particles cluster within the helix windings and order themselves in crystalline structures. Especially in the regime of low electric fields, the specific particle positions of the equilibria can depend on the helix geometry and the particle number. We therefore also explored the general effects occurring when these parameters are varied. While some parameter variations can influence the overall order of the equilibria, the amorphous ordering for  $E = 0$  persists for a large parameter range. Notable limits to this parameter range are low helix radii and both the upper and lower limits of the filling factor.

A natural continuation of this work consists in the investigation of the quantum mechanics of helically confined particle chains. Here the question arises whether we obtain a fundamentally different behavior compared to the classical system. In case of equilibrium states, this concerns the structure of the eigenstates and the question for the existence of a quantum mechanical counterpart for the multitude of minima in the classical description. For the dynamics, it will be interesting to see if the intriguing phenomena found in the classical description [34–37] survive and to what extent they are modified. First steps toward a quantum mechanical description of particle chains in helical confinement were already taken in Refs. [40,41].

Another promising direction for future works is the study of the optical properties of particles in a curved confinement. Helical 1D nanowires have already been proposed as terahertz antennas [46]. Modeling the system as nonlinearly coupled oscillators, the observation of complex dynamics—such as higher harmonics generation or period-doubling under external driving—is very likely. In this case, the electric field could be used to switch from a disordered state with a highly nontrivial optical response to a more ordered regime.

## ACKNOWLEDGMENT

A.S. thanks A. K. Mukhopadhyay for a careful reading of the manuscript.

- [1] J. Thomson, *Lond. Edinb. Dubl. Philos. Mag. J. Sci.* **7**, 237 (1904).
- [2] E. L. Altschuler, T. J. Williams, E. R. Ratner, R. Tipton, R. Stong, F. Dowla, and F. Wooten, *Phys. Rev. Lett.* **78**, 2681 (1997).
- [3] D. J. Wales and S. Ulker, *Phys. Rev. B* **74**, 212101 (2006).
- [4] Y. Levin and J. J. Arenzon, *Europhys. Lett.* **63**, 415 (2003).

- [5] H. W. Kroto, J. R. Heath, S. C. O'Brien, R. F. Curl, and R. E. Smalley, *Nature* **318**, 162 (1985).
- [6] D. Mehta, J. Chen, D. Z. Chen, H. Kusumaatmaja, and D. J. Wales, *Phys. Rev. Lett.* **117**, 028301 (2016).
- [7] C. J. Marzec and L. A. Day, *Biophys. J.* **65**, 2559 (1993).
- [8] B. Berger, P. W. Shor, L. Tucker-Kellogg, and J. King, *Proc. Natl. Acad. Sci. USA* **91**, 7732 (1994).
- [9] Y. Lan, Y. Wang, and Z. F. Ren, *Adv. Phys.* **60**, 553 (2011).

- [10] L. Samuelson, C. Thelander, M. Björk, M. Borgström, K. Deppert, K. Dick, A. Hansen, T. Mårtensson, N. Panev, A. Persson, W. Seifert, N. Sköld, M. Larsson, and L. Wallenberg, *Physica E* **25**, 313 (2004).
- [11] P. Avouris and J. Chen, *Mater. Today* **9**, 46 (2006).
- [12] R. A. Hatton, A. J. Miller, and S. R. P. Silva, *J. Mater. Chem. A* **18**, 1183 (2008).
- [13] P. Avouris, M. Freitag, and V. Perebeinos, *Nat. Photon.* **2**, 341 (2008).
- [14] S. Ijima and T. Ichihashi, *Nature* **363**, 603 (1993).
- [15] A. Shaikjee and N. J. Coville, *J. Adv. Res.* **3**, 195 (2012).
- [16] K. T. Lau, M. Lu, and D. Hui, *Composit. B: Eng.* **37**, 437 (2006).
- [17] R. Garcia-Fernandez, W. Alt, F. Bruse, C. Dan, K. Karapetyan, O. Rehband, A. Stiebeiner, U. Wiedemann, D. Meschede, and A. Rauschenbeutel, *Appl. Phys. B* **105**, 3 (2011).
- [18] E. Vetsch, S. T. Dawkins, R. Mitsch, D. Reitz, P. Schneeweiss, and A. Rauschenbeutel, *IEEE J. Sel. Top. Quant. Electron.* **18**, 1763 (2012).
- [19] D. Reitz and A. Rauschenbeutel, *Opt. Commun.* **285**, 4705 (2012).
- [20] E. Vetsch, D. Reitz, G. Sagué, R. Schmidt, S. T. Dawkins, and A. Rauschenbeutel, *Phys. Rev. Lett.* **104**, 203603 (2010).
- [21] P. Tran, B. Alavi, and G. Gruner, *Phys. Rev. Lett.* **85**, 1564 (2000).
- [22] Z. G. Yu and X. Song, *Phys. Rev. Lett.* **86**, 6018 (2001).
- [23] V. Prinz, V. Seleznev, A. Gutakovskiy, A. Chehovskiy, V. Preobrazhenskii, M. Putyato, and T. Gavrilova, *Physica E* **6**, 828 (2000).
- [24] O. G. Schmidt and K. Eberl, *Nature* **410**, 168 (2001).
- [25] M. Bhattacharya, *Opt. Commun.* **279**, 219 (2007).
- [26] J. F. Marko and E. D. Siggia, *Macromolecules* **27**, 981 (1994).
- [27] A. A. Kornyshev, D. J. Lee, S. Leikin, and A. Wynveen, *Rev. Mod. Phys.* **79**, 943 (2007).
- [28] V. Ivanov, J. Nagy, P. Lambin, A. Lucas, X. B. Zhang, X. F. Zhang, D. Bernaerts, G. Van Tendeloo, S. Amelinckx, and J. Van Landuyt, *Chem. Phys. Lett.* **223**, 329 (1994).
- [29] P. Drude, *Lehrbuch Der Optik*, 2nd ed. (Hirzel, Leipzig, 1906).
- [30] J. J. Maki and A. Persoons, *J. Chem. Phys.* **104**, 9340 (1996).
- [31] P. Schmelcher, *Europhys. Lett.* **95**, 50005 (2011).
- [32] O. Kibis, *Phys. Lett. A* **166**, 393 (1992).
- [33] J. K. Pedersen, D. V. Fedorov, A. S. Jensen, and N. T. Zinner, *J. Phys. B: At. Mol. Opt. Phys.* **47**, 165103 (2014).
- [34] A. V. Zampetaki, J. Stockhofe, S. Krönke, and P. Schmelcher, *Phys. Rev. E* **88**, 043202 (2013).
- [35] A. V. Zampetaki, J. Stockhofe, and P. Schmelcher, *Phys. Rev. A* **91**, 023409 (2015).
- [36] A. V. Zampetaki, J. Stockhofe, and P. Schmelcher, *Phys. Rev. E* **92**, 042905 (2015).
- [37] A. V. Zampetaki, J. Stockhofe, and P. Schmelcher, *Phys. Rev. E* **95**, 022205 (2017).
- [38] A. V. Zampetaki, J. Stockhofe, and P. Schmelcher, *Phys. Rev. E* **97**, 042503 (2018).
- [39] J. Plettenberg, J. Stockhofe, A. V. Zampetaki, and P. Schmelcher, *Phys. Rev. E* **95**, 012213 (2017).
- [40] J. K. Pedersen, D. V. Fedorov, A. S. Jensen, and N. T. Zinner, *J. Mod. Opt.* **63**, 1814 (2016).
- [41] J. K. Pedersen, D. V. Fedorov, A. S. Jensen, and N. T. Zinner, *J. Phys. B: At. Mol. Opt. Phys.* **49**, 024002 (2016).
- [42] L. E. Scales, *Introduction to Non-Linear Optimization* (Springer, New York, 1985).
- [43] J. Nocedal and S. J. Wright, *Numerical Optimization* (Springer, New York, 2006).
- [44] S. P. Boyd and L. Vandenberghe, *Convex Optimization* (Cambridge University Press, Cambridge, 2004).
- [45] Windings are separated at positions closest to the center of the torus, i.e., odd multiples of  $\pi$  in parametric coordinates.
- [46] T. P. Collier, A. M. Alexeev, C. A. Downing, O. V. Kibis, and M. E. Portnoi, *Semiconductors* **52**, 1813 (2018).



**External-field-induced dynamics of a charged particle on a closed helix**Ansgar Siemens<sup>1,\*</sup> and Peter Schmelcher<sup>1,2,†</sup><sup>1</sup>Zentrum für Optische Quantentechnologien, Fachbereich Physik, Universität Hamburg, Luruper Chaussee 149, 22761 Hamburg, Germany<sup>2</sup>Hamburg Center for Ultrafast Imaging, Universität Hamburg, Luruper Chaussee 149, 22761 Hamburg, Germany (Received 5 February 2021; accepted 7 May 2021; published 27 May 2021)

We investigate the dynamics of a charged particle confined to move on a toroidal helix while being driven by an external time-dependent electric field. The underlying phase space is analyzed for linearly and circularly polarized fields. For small driving amplitudes and a linearly polarized field, we find a split up of the chaotic part of the phase space, which prevents the particle from inverting its direction of motion. This allows for a nonzero average velocity of chaotic trajectories without breaking the well-known symmetries commonly responsible for directed transport. Within our chosen normalized units, the resulting average transport velocity is constant and does not change significantly with the driving amplitude. A very similar effect is found in case of the circularly polarized field and low driving amplitudes. Furthermore, when driving with a circularly polarized field, we unravel a second mechanism of the split up of the chaotic phase space region for very large driving amplitudes. There exists a wide range of parameter values for which trajectories may travel between the two chaotic regions by crossing a permeable cantorus. The limitations of these phenomena, as well as their implication on manipulating directed transport in helical geometries are discussed.

DOI: [10.1103/PhysRevE.103.052217](https://doi.org/10.1103/PhysRevE.103.052217)**I. INTRODUCTION**

Helical structures and patterns can be frequently found in nature, with systems ranging from molecules such as DNA or amino acids to self-assembled configurations of particles in nanotubes [1]. Especially for quasi-one-dimensional (quasi-1D) structures, the helical geometry can offer advantages such as increased stability and resistance to deformations [2,3]. In the last decades great progress was made in attempts to synthesize artificial 1D nanostructures, such as helical CNT's [4], with hopes for applications in nanoelectronic circuits [5–8]. Therefore, there is a great interest in understanding how the electronic properties of 1D structures are affected by helical geometries.

Already in minimal models, intriguing phenomena can result from the geometric confinement to a 1D helix. It was demonstrated that, due to the geometry, ballistic long-range Coulomb interacting particles on a 1D helical path can form bound states [9,10] and can even build 1D lattice structures [10–12]. Novel physics resulting from this behavior has been reported in several works discussing relevant setups [13–20]. Effects range from mechanical properties, such as an unusual electrostatic bending response [12], to intriguing nonlinear dynamics, such as the scattering of bound states at an inhomogeneity in the 1D path [13] or the tuning of the dispersion relation of a 1D chain of bound particles by varying the helix radius [14]. In the latter example, a degeneracy of the band structure for a specific helix radius was identified, which prevents excitations from dispersing through the system.

In helical systems, the novel effects typically emerge due to the fact that the acting forces are partially compensated by confining forces of the helix, and are therefore not limited to Coulomb interactions. Effects of dipole-dipole interactions [16–18], as well as external electric fields [11,20] have been explored. Previous investigations of external electric fields considered adiabatically varying forces and demonstrated the possibility of using an external electric field for controlled state transfer [20], and inducing crystalline lattice ordering of particles [11]. For crystalline particles on a closed helix exposed to a static electric field, an unconventional pinned-to-sliding transition has been observed [19]. Investigating the dynamics of confined particles being driven by time-dependent external forces is therefore a natural next step.

Periodic driving is at the core of many intriguing phenomena, such as resonances and chaos. In driven systems, already simple models can often yield quite complex dynamics and give valuable insight into real physical systems. For example, the model of a driven Morse oscillator can give insight into the (vibrational) stability of molecules [21]. In the same spirit, particles in driven double well potentials have been studied to explain the tunneling dynamics (or the suppression thereof) through a potential barrier [22–28]. Studies of driven Hamiltonian systems, i.e., particle dynamics in time-dependent periodic potentials, often possess a focus on the manipulation of transport phenomena due to the choice of the driving potential. There, the transport of diffusive trajectories is usually induced by breaking certain spatiotemporal symmetries [29–35]. However, other manipulation techniques, such as the possibility of switching between ballistic and diffusive motion by introducing localized disorder [36], have been demonstrated. Furthermore, the presence of spatially varying forces has been linked to a variety of intriguing

\*asiemens@physnet.uni-hamburg.de

†pschmelc@physnet.uni-hamburg.de

phenomena, such as the formation of density waves [37]. Based on this understanding of driven systems, a plethora of applications, including velocity filters [37,38], spectrometers [39–41], or batteries extracting energy from thermal fluctuations [32–34,41–46], have been proposed.

Motivated by the complexity arising when particles are confined to curved space, we investigate in this work the influence of time periodic forces on particles in helical confinement. As a prototype, we consider a single particle confined to a toroidal helix, being driven by either an oscillating or a rotating electric field. The combination of driving and confining forces leads to spatially and temporally varying effective forces. For a wide range of driving amplitudes, the systems phase space resembles that of a particle in either a standing wave (oscillating driving field) or a running wave (rotating driving field). However, for very low driving amplitudes, as well as for large driving amplitudes in case of the oscillating field, we identify two different scenarios by which the chaotic phase space region can be split. We explain how these splits are induced by the different scales of oscillations in the driving potential, and how they influence the corresponding transport phenomena.

Our paper is structured as follows. Section II contains the parametrization of the toroidal helix, a discussion of the Lagrangian, and the general equations of motion for our setup. We further discuss the considered driving laws. In Secs. III and IV we investigate and analyze the dynamics in the presence of driving with a linearly polarized and a circularly polarized electric field, respectively. Finally, in Sec. V we provide our conclusions.

## II. PARTICLES IN HELICAL GEOMETRIES WITH EXTERNAL DRIVING

We consider a single particle with charge  $q$  confined to move along a toroidal helix [see Fig. 1(a) for a visualization]. The parametrization of the particle's positions is then given by the following equation:

$$\mathbf{r}(u) := \begin{pmatrix} (R + r \cos(u)) \cos(u/M) \\ (R + r \cos(u)) \sin(u/M) \\ r \sin(u) \end{pmatrix}, \quad u \in [0, 2\pi M], \quad (1)$$

where  $R$  is the torus radius determining how strongly our helix is bent,  $r$  is the radius of the helix, and  $M$  is the total number of helical windings. Since the path is closed we have  $\mathbf{r}(u) = \mathbf{r}(u + 2\pi M)$ , and the parameters obey the following restriction,  $R = Mh/2\pi$ , where  $h$  is the pitch of the helix. When  $u$  changes by an amount of  $2\pi$ , the particle moves the distance of one winding on the helix. When  $u$  changes by an amount of  $2\pi M$ , the particle circles once around the torus and is exactly at the same position it started in.

The driving force is assumed to be caused by an external electric field  $\mathbf{E}$ . The potential energy  $V(u, t)$  of the particle is then given by

$$V(u, t) = q\mathbf{E}(t) \cdot \mathbf{r}(u). \quad (2)$$

Our system is then described by the following Lagrangian:

$$\mathcal{L} = \frac{m}{2} \left( \frac{d\mathbf{r}(u)}{dt} \right)^2 - q\mathbf{E} \cdot \mathbf{r}(u). \quad (3)$$

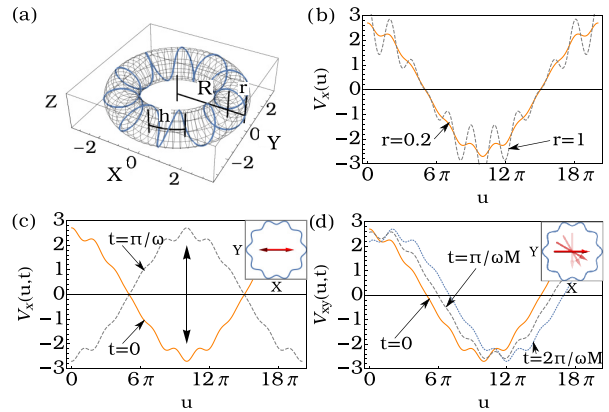


FIG. 1. (a) A 3D illustration of the parametric function  $\mathbf{r}(u)$ , for  $M = 10$ ,  $r = 0.8$ , and  $R = 2.5$ . (b) The potential  $V_x(u)$  created by a static field in the  $x$  direction shown for toroidal helices with  $M = 10$ ,  $R = 2.5$ , and helix radii of  $r = 0.2$  (orange) and  $r = 1$  (dotted gray). (c) The potential landscape  $V_x(u, t)$  for a linearly polarized oscillating field in  $x$  direction shown for  $t = 0$  (orange) and  $t = \pi/\omega$  (dashed gray). The inset in the top right corner visualizes the driving direction of the field (red) for a top view of the setup. (d) The potential landscape  $V_{xy}(u, t)$  for driving with a circularly polarized field in the  $xy$  plane shown for the times  $t = [0, \pi/\omega M, 2\pi/\omega M]$ . After the time  $t = 2\pi/\omega M$  the motion of the potential repeats, being shifted by  $\Delta u = 2\pi$ . Again, the inset in the top right corner visualizes the driving field (red) for a top view of the setup.

Equation (3) already accounts for the confining forces of the setup by only allowing positions  $\mathbf{r}(u)$  on the parametric helical curve. Since  $\mathbf{r}(u)$  is known, we can already evaluate the derivative in the kinetic energy term and rewrite Eq. (3) as

$$\mathcal{L} = \frac{m}{2} \zeta(u) \left( \frac{du}{dt} \right)^2 - q\mathbf{E} \cdot \mathbf{r}(u), \quad (4)$$

where  $\zeta(u) := [d\mathbf{r}(u)/du]^2 = r^2 + [R + r \cos(u)]^2/M^2$ . From this, we obtain the following equations of motion for an arbitrary driving field  $\mathbf{E}(t)$ :

$$\zeta(u) \frac{d^2u}{dt^2} = \frac{1}{2} \frac{d\zeta(u)}{du} \left( \frac{du}{dt} \right)^2 - \frac{q\mathbf{E}(t) \cdot d\mathbf{r}(u)}{m \, du}. \quad (5)$$

Let us now take a closer look at the driving potential  $V(u, t) = q\mathbf{E}(t) \cdot \mathbf{r}(u)$  created by the electric field. Even in the static case, i.e., without time dependence, the potential can become quite complex and possesses multiple minima. This is shown in Fig. 1(b) for a static field parallel to the  $x$  axis. In this case the electric field is given by  $\mathbf{E} = E\mathbf{e}_x$  and the potential energy becomes

$$V_x(u) = qE[R + r \cos(u)] \cos(u/M). \quad (6)$$

This potential consists of two terms: The  $R \cos(u/M)$  term creates a long-wavelength cosine-shaped potential that is maximal at the position that extends most into the  $x$  direction (for  $u = 0$  or  $u = 2\pi M$ ) and minimal for the position extending most into the negative  $x$  direction (for  $u = \pi M$ ). Since it is caused by the overall toroidal shape of the curve  $\mathbf{r}(u)$  we will call this the torus-induced potential (TIP). On top of that, there is a smaller modulation given by the  $r \cos(u) \cos(u/M)$

term. Since this modulation originates from the helix windings we will call this the winding-induced potential (WIP). The amplitude of the WIP can be modulated via the helix radius  $r$  [shown in Fig. 1(b) for  $r = 0.2$  and  $r = 1$ ]. Due to the  $\cos(u/M)$  dependence, the WIP oscillational amplitude also changes with the position on the torus. The amplitude is largest for  $u \in [0, \pi M, 2\pi M]$  and vanishes for  $u \in [\pi M/2, 3\pi M/2]$ . The number of minima in the modulation is determined by the number of helical windings  $M$ .

In this work we focus on two different time-dependent fields: Driving with a field oscillating parallel to the  $x$  axis, and driving with a field rotating in the  $xy$  plane. In the first case, the driving field becomes  $\mathbf{E}(t) = E \cos(\omega t) \mathbf{e}_x$ . The resulting potential  $V_x(u, t)$  is a standing wave with the shape shown in Fig. 1(c)

$$V_x(u, t) = qE[R + r \cos(u)] \cos(u/M) \cos(\omega t). \quad (7)$$

When we consider an electric field rotating in the  $xy$  plane the driving becomes slightly more complex. In this case, the electric field can be written as  $\mathbf{E}(t) = E \{\cos(\omega t), \sin(\omega t), 0\}$  and the potential landscape becomes

$$V_{xy}(u, t) = -qE \cos(\omega t - u/M)[R + r \cos(u)]. \quad (8)$$

Figure 1(d) visualizes the time evolution of this potential by showing the potential landscape at different times  $t$ . The three curves in the figure correspond to the cases  $t = 0$  (orange),  $t = \pi/\omega M$  (gray), and  $t = 2\pi/\omega M$  (blue). Due to the symmetries of the toroidal helix, we only need to consider the time  $\Delta t = 2\pi/\omega M$  needed to rotate by one winding to understand the driving, since the potential movement repeats after this time; it is just shifted by a distance of  $\Delta u = 2\pi$ . The time evolution of the potential landscape resembles a crawling motion: The local extrema of the potential oscillate between being a potential minimum and a potential maximum, with a constant phase shift of  $2\pi/M$  between neighboring minima (or maxima). A video showing the time evolution of  $V_{xy}(u, t)$  can be found in the Supplemental Material [47]. It should also be noted that for  $V_{xy}(u, t)$  the equations of motion are not symmetric with regard to the spatiotemporal symmetries given by  $(u \rightarrow -u + \Delta u, t \rightarrow t + \tau)$  and  $(u \rightarrow u + \Delta u, t \rightarrow -t + \tau)$ ; a necessary criterion for directed transport within the chaotic sea [29,31]. In contrast, these symmetries are conserved for  $V_x(u, t)$ .

We can eliminate redundant parameters by introducing dimensionless units. Without loss of generality, we choose to express distances in units of  $2h/\pi$  and time in units of  $\omega/2\pi$ . We also normalize the particle mass and charge to  $m = q = 1$  (which is the same as absorbing both values in the driving amplitude). The remaining independent system parameters are the winding number  $M$ , the helix radius  $r$ , and the driving amplitude  $E$ .

A final remark on our computational approach is in order: The equations of motion are numerically integrated with the Dormand-Prince method, a Runge-Kutta method with variable step size. The maximal step size of our time steps was chosen as  $\Delta t = 0.01$ . It was verified that this maximum step size produces accurate results even for driving amplitudes as large as  $E > 2000$ , which is much larger than any driving amplitude used in this work.

### III. PARTICLE DYNAMICS FOR A LINEARLY POLARIZED FIELD

In this section we will analyze the dynamics when the system is driven by an electric field oscillating parallel to the  $x$  axis. For this we will examine the phase space of the system and understand how it is decomposed for different parameter regimes. The dimensions of the phase space are made up of the three parameters: position  $u$ , momentum  $p$ , and time  $t$ . Since our Lagrangian is periodic in time, we can use a Poincaré surface of sections (PSOS)—specifically a stroboscopic map—to visualize the phase space in a two-dimensional stroboscopic  $u(p)$  dependence. Note, that our momentum  $p$  refers to the canonical momentum given by

$$p = \frac{du/dt}{m(r^2 + \{[R + r \cos(u)]/M\}^2)}. \quad (9)$$

We start our investigation by considering a toroidal helix with  $M = 10$  and  $r = 0.2$ . Figure 2 shows the PSOS of the system for electric field amplitudes  $E = 80$ ,  $E = 20$ , and  $E = 4$ . As we will see, the phase space for large and intermediate driving amplitudes will closely resemble that of a particle in a standing wave [48]. However, for low driving amplitudes, we observe novel features of the dynamics arising from the interplay of WIP and TIP. The investigation of these dynamics and their implication for manipulating directed transport will be the main result of this section.

In Fig. 2(a), for  $E = 80$ , we observe a mixed phase space that mainly allows three different kinds of trajectories: Chaotic trajectories, and two types of (quasi)periodic trajectories, which we will refer to as Type-I and Type-II trajectories. Type-I trajectories (marked I and  $\bar{I}$  in the figure) are invariant spanning curves [49,50] for which the particle momentum is too large to be significantly affected by the driving. The driving results only in a weak modulation of their dynamics. Towards smaller momenta the Type-I trajectories border on a sea of chaotic trajectories, which contains two large regular islands. These regular islands correspond to the Type-II trajectories and describe motion around the torus in phase with the driving period, i.e., after one driving period the particle on a Type-II trajectory has circled the torus exactly once. Both regular islands describe the same kind of motion, but in opposite directions.

As one might expect, the size of the chaotic portion of phase space decreases when the driving amplitude is decreased. This can be seen in Fig. 2(b) where  $E = 20$ . The Type-I trajectories, as well as the two main fixed points we identified in the previous figure are still present. However, the chaotic region now occupies a much smaller momentum range of the phase space. In addition, at the center of the chaotic region around  $p \approx 0$  additional fixed points appear in the phase space, e.g., at  $[u, p] \approx [10.5, 0.45]$ ,  $[15.7, 0.8]$ , and  $[20.7, 0.45]$ . They correspond to initial conditions in which the particle stays within a narrow range of  $u$  and is hardly affected by the driving. The reason for their appearance is as follows: When the driving amplitude decreases, so does the acceleration of the particle. Below a certain threshold the particle has hardly moved before the driving field accelerates the particle in the opposite direction. With decreasing driving amplitude an increasing amount of trajectories with initial

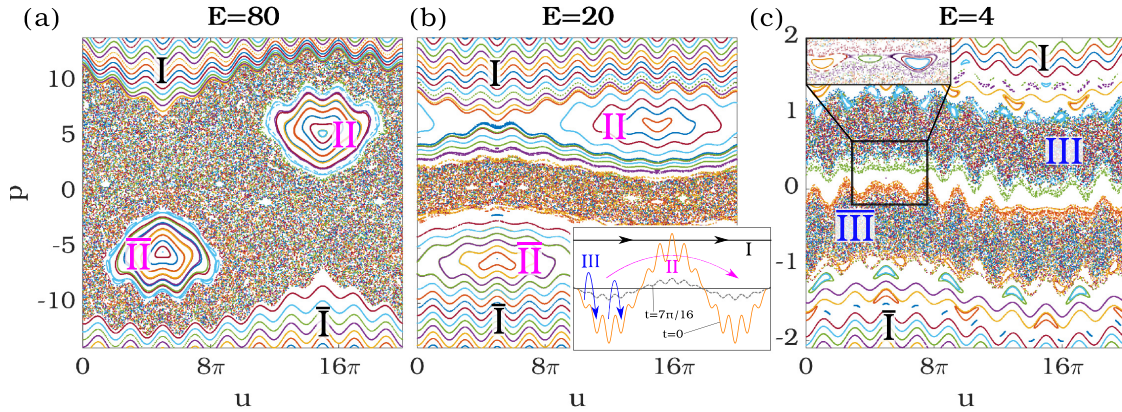


FIG. 2. Poincaré surfaces of sections (PSOS) for a particle on the toroidal helix, driven by a linearly polarized oscillating field for (a)  $E = 80$ , (b)  $E = 20$ , and (c)  $E = 4$ . Different colors are assigned to the trajectories for easier differentiation. Each PSOS features between 45 and 75 trajectories, each simulated for 2000 driving periods. (Quasi)periodic trajectories between the two chaotic regions (around  $p = 0$ ) in (c) are only shown in the inset [top left of (c)] to emphasize the splitting of the chaotic sea into two parts in the main figure. The inset in (b) visualizes the particle motion on  $V_x(u)$  for the three different types of trajectories (I–III) during a driving period in the range  $u \in [-2\pi M/3, 2\pi M/3]$ . The symbols  $\bar{\text{I}}$ – $\bar{\text{III}}$  mark the inverse of trajectories (I–III), i.e., trajectories moving in the opposite direction. (I) Quasifree trajectories that are too fast to be significantly affected by the driving. (II) Trajectories belonging to the large regular islands with the fixed points at  $|p| \approx 5.35$ , which move around the torus once during every driving period. (III) The chaotic trajectories (after the chaotic sea has split) move by one winding during each driving period.

conditions around  $p = 0$  will exhibit this behavior. The effect on the phase space can be seen in Fig. 2(c) for  $E = 4$  (note the adjusted range of  $p$  values). Here the driving amplitude is sufficiently small, such that for every  $u$  there is a (quasi)periodic trajectory [pictured only in the inset of Fig. 2(c)] close to  $p = 0$  that is hardly affected by the driving and mostly stays in place. An interesting result is, that the appearance of these trajectories is splitting the chaotic sea into two parts: One with  $p > 0$  [marked III in Fig. 2(c)] and one with  $p < 0$  (marked  $\bar{\text{III}}$ ), which we will refer to as Type-III trajectories. This has significant consequences for the dynamics. Type-III trajectories starting in the chaotic region with  $p > 0$  will remain there and maintain a strictly positive momentum. Inverting the direction of movement is impossible, since that requires slowing down and crossing the region of regular islands around  $p = 0$ . The same is of course true for trajectories starting in the chaotic region with  $p < 0$ . In other words: When the chaotic sea splits up, we transition from a single chaotic sea in which all trajectories have an average velocity of zero, to two completely separated (symmetric) chaotic seas in which chaotic trajectories have an average velocity of either  $+2\pi$  (upper chaotic sea) or  $-2\pi$  (lower chaotic sea).

In Fig. 3 we take a closer look at this split up of the chaotic sea. A close up of the split appearing in the PSOS is shown in Figs. 3(a)–3(c). For clarity, the PSOS's of Figs. 3(a)–3(c) only contain initial conditions from the chaotic region with  $p < 0$ . In Fig. 3(a), at  $E = 7$ , the emerging (quasi)periodic regions around  $p = 0$  are clearly visible. However, changing the direction of motion is still possible and happens indeed frequently. The momentum evolution  $p(t)$  of a representative example trajectory is shown in Fig. 3(d) (blue curve). From this  $p(t)$  curve we can see that already for  $E = 7$  there are effectively two momentum ranges the particle can be confined to. The particle frequently switches between having

either positive or negative momentum for extended periods of time.

When the driving amplitude is decreased further to  $E = 4$  [see Fig. 3(b)], the two chaotic phase space regions are almost separated from each other. An inversion of the direction of movement now happens much less frequently. In the phase space this can be seen from the decreasing density for  $p > 0$ . From the corresponding example trajectory in Fig. 3(d) (red curve), we see that the momentum inversion now also takes a much longer time than for  $E = 7$ . It takes our example trajectory almost  $\sim 2200$  driving periods to change its momentum from  $p < 0$  to  $p > 0$ .

Finally, for  $E = 3$  [Fig. 3(c)], the two phase space regions are completely separated from each other. None of our trajectories cross into the phase space region with  $p > 0$ . In this regime, the dynamics of all simulated trajectories resemble that of our example trajectory in Fig. 3(d) (yellow curve): The trajectories are chaotic while sustaining a strictly negative momentum.

A better understanding of the Type-III trajectories can be gained from statistical averages. We consider the average velocity  $v_{av}$ , as well as the mean switch time  $t_s$ . For a set of trajectories  $u(u_i, p_i, t)$  with initial conditions  $u(t = 0) = u_i$  and  $p(t = 0) = p_i$  the average velocity is determined by averaging the mean velocities of all trajectories

$$v_{av} = \frac{1}{NT} \sum_{i=1}^N \int_0^T \frac{du(u_i, p_i, t)}{dt} dt, \quad (10)$$

where  $T$  is the simulation time of individual trajectories. We define the mean switch time as the average time a particle spends with  $p > 0$  (or  $p < 0$ ) before inverting the direction of its motion. Note, that within our numerical simulations, there are limitations regarding the calculation and accuracy of  $t_s$ .

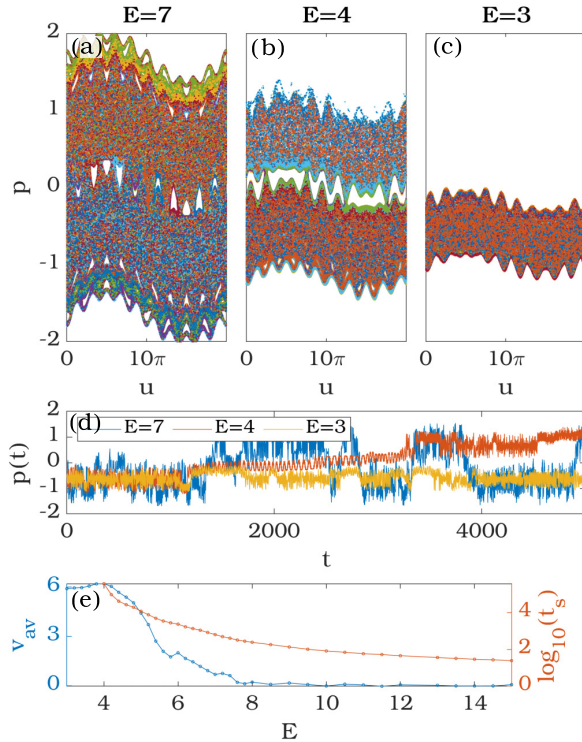


FIG. 3. (a)–(c) PSOS created from  $\sim 10^3$  trajectories with initial conditions in the chaotic sea ( $u \in [0, 1]$  and  $p \in [-0.42, -0.62]$ ). Each particle was simulated for 5000 driving periods. The appearance of stable trajectories around  $p = 0$  splits the chaotic sea into two seas, when the driving amplitude  $E$  is decreased. (d) Representative example trajectories emanating in the chaotic sea for  $p < 0$  for  $E = 3$  (yellow),  $E = 4$  (orange), and  $E = 7$  (blue). The two momentum regimes the particles are confined to are clearly visible. Transition between the two regimes is more likely for larger driving amplitudes. (e) The average transport velocity  $v_{av}$  and switch time  $t_s$  as a function of the driving amplitude. Each data point was obtained from simulation numbers and times similar to those of (a)–(c).

We can only determine  $t_s$  accurately from our simulations, if we (on average) observe at least one switch in the time  $T$ . Since each trajectory was simulated for  $T = 5000$  driving periods, our value of  $t_s$  is accurate for values below  $t_s \lesssim 2500$ . In practice, we simulate  $10^3$  trajectories for 5000 time steps, count the total number of switches  $n$  in all simulations, and then calculate  $t_s = 0.5 \cdot 10^7 / n$ .

Figure 3(e) shows both  $v_{av}$  and  $t_s$  as a function of the driving amplitude. For better insight into the dynamics of the Type-III trajectories both curves were only obtained from trajectories with  $p(t = 0) > 0$ . Until the split up of the chaotic region at about  $E = 4$  both quantities increase with decreasing driving amplitude. From  $t_s$  we see that long before the two chaotic regions are separated from each other, the particles perform very long flights without inverting the direction of their motion. Even for  $E = 7$ , where the chaotic regions are still reasonably well connected in the phase space [see Fig. 3(a)], we have a mean switch time of  $t_s > 600$  driving periods.

In the figure, our mean switch time exceeds the critical value of  $t_s = 2500$  for driving amplitudes  $E < 6$ . As stated above, we cannot accurately calculate  $t_s$  in this regime of driving amplitudes because the change of the direction of motion happens too infrequently. Consequently, in this regime the choice of initial conditions [ $p(t = 0) < 0$ ] becomes apparent in the statistics of  $v_{av}$ . While  $t_s > 2500$ , the average velocity  $v_{av}$  increases with increasing  $t_s$ . When the two chaotic phase space regions splits up at around  $E = 4$ ,  $v_{av}$  reaches a plateau [see  $v_{av}$  in Fig. 3(e)]. After the split up, the Type-III trajectories have a consistent mean velocity of slightly less than  $v_{av} \approx 2\pi$ . This velocity corresponds to a position change of about one helix winding during each driving period. More precisely, each driving period the chaotic Type-III trajectories move between neighboring minima in the WIP. Therefore, the dynamics of Type-III trajectories are similar to the Type-II trajectories, except that they are mostly determined by the minima of the WIP with the TIP being a perturbation that is mostly responsible for the chaos. In contrast, the Type-II trajectories are mostly determined by the minima of the TIP, with the WIP acting as a perturbation. For even lower driving amplitudes the perturbation due to the TIP becomes small enough for the Type-III trajectories to stabilize into a series of fixed points [similar to the ones shown in Fig. 4(a) for a rotating driving field].

Since the Type-III trajectories emerge due to the WIP, it is no surprise that the occurrence of the phase space split depends on the helix radius  $r$ . For larger values of  $r$ , the (quasi)periodic trajectories around the Type-III fixed points will already stabilize for larger values of  $E$ , since the relative strength of the perturbation due to the TIP decreases. For a large enough  $r$ , it is possible for the Type-III fixed points to stabilize before the chaotic region is splitting up. In extreme cases this may even prevent the occurrence of chaotic Type-III trajectories.

The only independent system parameter we did not discuss so far is the winding number  $M$ . Changing  $M$  does not significantly affect the overall dynamics. However, due to the relation  $R = Mh/2\pi$  and our choice of units (thereby setting  $h = \pi/2$ ), changing  $M$  will change the torus radius  $R$ , thereby changing the momentum of the Type-II trajectories. This, in turn, changes, e.g., the driving amplitude required for a mixed phase space as shown in Fig. 2(a). This also changes the ratio of  $r/R$  and may cause the periodic Type-III fixed points to stabilize at different driving amplitudes. Increasing  $M$  also increases the number of extrema in the WIP, leading to more fixed points in the (quasi)periodic Type-III trajectories once they stabilize. Besides this, however, the split up of the chaotic phase space region is mostly unaffected.

#### IV. PARTICLE DYNAMICS IN THE PRESENCE OF A CIRCULARLY POLARIZED FIELD

Another intriguing split up in the phase space can be observed when driving with a circularly polarized field in the  $xy$  plane. In this case, the driving law is characterized by the time-dependent potential landscape  $V_{xy}(u, t)$  given in Eq. (8). In this section, we will encounter trajectories that are very similar to the Type-I-III trajectories that were classified in Sec. III. We will again refer to them as Type-I, -II, and -III

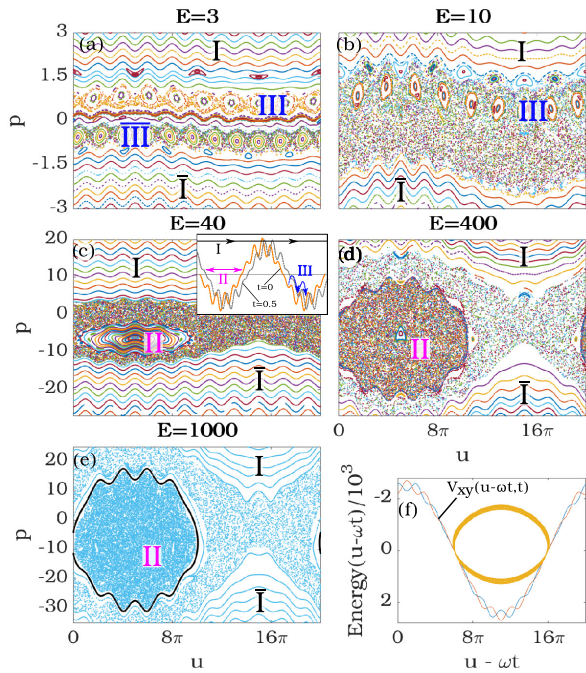


FIG. 4. Poincaré surfaces of sections (PSOS) for a particle on a toroidal helix driven by a circularly polarized field in the  $xy$ -plane. The inset in (c) visualizes the dynamics of different trajectories (I, II, and III) on  $V_{xy}(u, t)$  in the range  $u \in [-2\pi M/3, 2\pi M/3]$ . The symbols I–III mark the inverse of trajectories (I–III), i.e., trajectories moving in the opposite direction. (I) Quasifree trajectories that are too fast to be significantly affected by the driving. (II) Trajectories that are trapped in a well of the potential  $V_{xy}$  and move around the torus once during every driving period. (III) Chaotic and regular trajectories that (after the chaotic sea has split) move one helical winding during each driving period. The PSOS are shown for driving amplitudes of (a)  $E = 3$ , (b)  $E = 10$ , (c)  $E = 40$ , (d)  $E = 400$ , and (e)  $E = 1000$ . In (e) the coloring was changed to emphasize the split of the chaotic region; except for one highlighted periodic trajectory (black) all data points are colored blue. The two chaotic regions correspond to chaotic motion that is trapped in the moving potential, and chaotic motion that is (on average) slower than the moving potential. The yellow curve in (f) shows the motion of the highlighted (black) trajectory of (e) in the moving potential.

trajectories. Type-I trajectories are again invariant spanning curves that limit the momentum of chaotic trajectories and are hardly affected by the driving. Type-II trajectories move around the torus in phase with the driving. This time, however, the potential  $V_{xy}$  describes a running wave, and the Type-II trajectories correspond to particles that are trapped in one of the moving potential wells. Type-III trajectories refer to trajectories that are unable to invert their direction of movement and move between successive minima of  $V_{xy}$  during each driving period with an average velocity of  $v_{av} = 2\pi$ .

An overview of the phase space for  $M = 10$  and  $r = 0.2$  is given in Figs. 4(a)–4(e). For a large part, the phase space is very similar to the one shown in the previous section: There is a large regular island of Type-II trajectories corresponding to motion around the torus in phase with the driving period. The

size of the corresponding chaotic region increases with the driving amplitude and leads to a mixed phase space for large  $E$ . The chaotic region is surrounded by Type-I trajectories. Also, the  $r \sin(u)$  dependence of  $V_{av}$  leads to the presence of Type-III trajectories for very low driving amplitudes, which, due to perturbations in form of the  $R$ -dependent term in  $V_{av}$ , can be chaotic and lead to a splitting of the chaotic sea similar to the one discussed in Sec. III. At the same time, however, there are major differences. Since our driving law breaks parity and time inversion symmetries in the equations of motion, the resulting phase space is not symmetric anymore. Instead of two fixed points with Type-II trajectories as in Fig. 2, there is now only one that corresponds to motion around the torus with the same direction as the rotation of the driving field. Furthermore, the emergence of Type-III trajectories with decreasing driving amplitude is not symmetric anymore. For our example parameters (quasi)periodic Type-III trajectories with  $p > 0$  emerge even before the split of the chaotic sea has begun [see Fig. 4(b)].

The most interesting difference, however, emerges for very large driving amplitudes. Whereas in the case of a linearly oscillating driving field a larger driving amplitude mostly leads to an increased chaotic region, new structures can emerge in the phase space when driving with a rotating large amplitude field. For very large driving amplitudes [see Fig. 4(e)] regular (quasi)periodic trajectories appear and split up the chaotic sea into two regions. These (quasi)periodic trajectories correspond to Type-II trajectories that move around the toroidal helix in phase with the driving. This can be seen from Fig. 4(f), which shows the path of the highlighted (black) trajectory from Fig. 4(e) in the driving potential. For convenience, the data is plotted in a moving reference frame that is moving in phase with the driving potential.

The two different chaotic regions in Fig. 4(e) correspond to different kinds of chaotic motion. The chaotic region surrounded by the newly stabilized periodic Type-II trajectories consists entirely of trajectories that are trapped in a valley of our driving potential. While the motion is chaotic, each trajectory will on average move in phase with the driving, once around the toroidal helix during each driving period. These trajectories are consequently also Type-II trajectories—just chaotic and not (quasi)periodic. With increasing driving amplitude, the chaotic Type-II trajectories will stabilize into periodic Type-II trajectories.

Before the driving amplitude is large enough to stabilize any of these new (quasi)periodic Type-II trajectories, there is a long intermediary range of driving amplitudes during which the two chaotic regions are separated from each other by a permeable cantorus (i.e., an unstable KAM torus). A corresponding phase space is shown in Fig. 4(d). The presence of the cantorus allows for an appealing dynamics of the chaotic trajectories. When they cross the cantorus, they switch between two different kinds of chaotic motion. An example for such a trajectory is shown in Fig. 5(a) for a driving amplitude of  $E = 500$ . The plotted trajectory  $u(t) + 2\pi Mt$  has a negative (or positive) slope if the particle is moving faster (or slower) around the torus than the rotating driving field. The particle in the figure starts in the chaotic region outside of the cantorus barrier (i.e., it is not a Type-II trajectory). In this region it will (on average) be too slow to move in

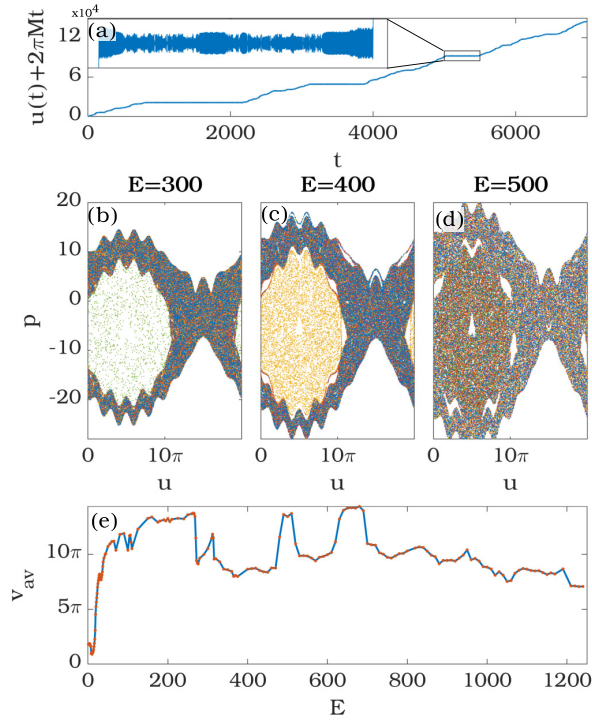


FIG. 5. (a) Example trajectory in a comoving reference frame that moves in phase with the driving field. When the particle crosses the cantorus and becomes a chaotic Type-II trajectory,  $u(t) - 2\pi Mt$  will become constant, which is demonstrated in the inset. (b)–(d) Each figure shows a PSOS for six trajectories (with the same initial conditions for each figure) for (b)  $E = 300$ , (c)  $E = 400$ , and (d)  $E = 500$ . In (b) and (c) only one of the six trajectories manages to cross the cantorus, whereas in (d) all trajectories frequently switch between the two types of chaotic motion. (e) Average velocity for particles started in the chaotic sea with initial conditions chosen close to  $[u, p] \approx [15\pi, 0]$ . Each data point was obtained from  $10^3$  trajectories, each simulated for  $10^4$  driving periods. The chaotic Type-II trajectories are faster than those from the other chaotic region, so the velocity decreases with decreasing permeability of the cantorus.

phase with the driving field. Once it crosses the cantorus, the dynamics become that of a chaotic Type-II trajectory. This is highlighted by the inset, which zooms into a small region of the trajectory during which the particle crosses the cantorus, briefly becomes a chaotic Type-II trajectory, and then crosses the cantorus again into the other chaotic region. The times particles spend as chaotic Type-II trajectories follow a power law with a critical exponent that depends on the driving amplitude and the permeability of the cantorus.

The permeability of the cantorus does not simply decrease with the driving amplitude until the two chaotic regions are separated from each other. It switches multiple times between being more or less permeable before the driving amplitude is large enough to separate the two chaotic regions. This is demonstrated in Figs. 5(b)–5(d). They each show the PSOS of six trajectories (with the same initial conditions  $[u, p]$  used for each figure) for various driving amplitudes. For  $E = 300$

and  $E = 400$ , the two regions are almost separated from each other and in both cases only one of the trajectories manages to cross the cantorus. Despite the vast difference in driving amplitudes, there is very little difference in the permeability of the cantorus. In contrast, for  $E = 500$  all of the trajectories switch frequently between the two regions. In this case, the presence of a cantorus is not even obvious from the phase space alone. Only when looking at the individual trajectories [such as the one shown in Fig. 5(a)], we can distinguish between the different chaotic dynamics of the two chaotic regions.

The average velocity is different for both chaotic regions, and we shall use this to analyze the split up of the chaotic region. This is shown in Fig. 5(e). It shows the average velocity  $v_{av}$  as a function of the driving amplitude. Each data point was obtained from  $10^3$  trajectories started in the chaotic region around  $[u, p] \approx [15\pi, 0]$ , and with simulation times of  $10^4$  driving periods for each trajectory. Note, that for very low  $E$ , when the Type-III trajectories for  $p > 0$  and  $p < 0$  are separated by invariant spanning curves (i.e., Type-I trajectories), we chose initial conditions with  $p < 0$ , leading to some bias in the data for very low  $E$ . Note also, that the curve may slightly change for different simulation times, if the switch time for the cantorus crossing exceeds the simulation time.

At first, for very low  $E$ ,  $v_{av}$  decreases with increasing driving amplitude, which is caused by a combination of Type-III trajectories disappearing with increasing  $E$ , and a bias in our initial conditions [compare  $v_{av}$  in Fig. 3(e) and discussion thereof]. Then,  $v_{av}$  will (mostly) increase with increasing driving amplitude until  $E \approx 270$ . This increase is due to the chaotic sea expanding and changing its mean momentum. Above  $E \approx 270$ , the cantorus appears and splits the chaotic region in two, resulting in a sharp drop of  $v_{av}$ . From then on, there are peaks in  $v_{av}$  whenever the trajectories can frequently switch between the two chaotic regions: (e.g., the plateau around  $E = 500$ ). Around  $E \sim 900$ , the cantorus stabilizes into periodic Type-II trajectories and the two chaotic regions become fully separated from each other.

Similar to the phase space splitting for low driving amplitudes discussed in Sec. III, this split likely originates from the two different scales of oscillations in the driving potential. The cantorus orbits are mainly stabilized due to the large scale oscillation  $\sim qER \cos(\omega t - u/M)$  of the running wave, with the smaller oscillations  $\sim qEr \cos(u) \cos(\omega t - u/M)$  acting as a perturbation that (for a wide parameter range) prevents the Type-II trajectories from stabilizing and becoming periodic. Due to the position dependence of the smaller oscillations, the perturbation is always stronger for trajectories that are tightly bound, i.e., closer to the fixed point, than for those with greater variations of  $\dot{u}(t) - v_{av}$ . This perturbation increases with increasing the helix radius  $r$  and therefore a larger helix radius requires larger driving amplitudes for the chaotic region to split up. Similar to the discussion of Sec. III, the winding number  $M$  changes the ratio of  $r/R$  and the velocity of the Type-II trajectories. This can influence the general parameter regimes in which the split up of the chaotic phase space region is encountered, however, we did not observe any changes in the underlying physics when varying the winding number  $M$ .

### V. SUMMARY AND CONCLUSION

We have investigated the dynamics of a charged particle confined to a toroidal helix, which is exposed to external driving forces originating from a time-dependent electric field. The main results consist in the phenomenological description and understanding of two different mechanisms for the split up of the chaotic phase space region, both with their own interesting consequences for the dynamics. We showed that for low driving amplitudes the two different spatial scales of oscillating potential lead to a split up of the chaotic region around  $p = 0$ . This prevents chaotic trajectories to invert the direction of their motion and leads to a consistent average velocity of  $|v_{av}| \approx 2\pi$  for all diffusive trajectories. Especially notable is that this split allows for chaotic particle trajectories with nonzero average velocity, even in a case where the spatiotemporal symmetries that are usually associated with chaotic transport are not broken by the driving field. Our understanding of this split and the resulting dynamics is certainly also of interest in the context of Brownian motors.

Specifically for driving with a circularly polarized field in the  $xy$  plane, we found another mechanism for the split up of the chaotic sea, this time splitting off a chaotic region in which particles are trapped in a valley of the driving potential. Trajectories confined to this separate region of the phase space

move around the torus in phase with the driving field and will have a consistent average velocity of  $v_{av} = 2\pi M$ . Before this region is completely separated from the remainder of the chaotic sea, there is a very large range of driving amplitudes for which the trajectories can switch between the two chaotic regions by crossing a permeable cantorus. The probability of crossing the cantorus fluctuates heavily with the driving amplitude. The origin of this separation has been identified as a small perturbation of the driving potential, that is most influential around the extrema of the running wave and vanishes in between those extrema.

The presented split ups of the chaotic phase space region are not unique to setups with confining forces and mainly depend on the different scales of oscillations in the driving potential. A realization of similar physics in a driven lattice with spatially varying forces, or with ultracold atoms in an optical lattice seem feasible. Furthermore, recent experiments have demonstrated the possibility of confining neutral atoms to a helical path [51], however, in such setups, the realization of our driving forces may be a challenge.

### ACKNOWLEDGMENT

The authors thank Aritra K. Mukhopadhyay for helpful discussions.

- 
- [1] G. Vernizzi, K. L. Kohlstedt, and M. O. de la Cruz, The electrostatic origin of chiral patterns on nanofibers, *Soft Matter* **5**, 736 (2009).
  - [2] J. F. Marko and E. D. Siggia, Bending and twisting elasticity of DNA, *Macromolecules* **27**, 981 (1994).
  - [3] A. A. Kornyshev, D. J. Lee, S. Leikin, and A. Wynveen, Structure and interactions of biological helices, *Rev. Mod. Phys.* **79**, 943 (2007).
  - [4] K. T. Lau, M. Lu, and D. Hui, Coiled carbon nanotubes: Synthesis and their potential applications in advanced composite structures, *Compos. Part B-Eng* **37**, 437 (2006).
  - [5] P. Avouris and J. Chen, Nanotube electronics and optoelectronics, *Mater. Today* **9**, 46 (2006).
  - [6] P. Avouris, M. Freitag, and V. Perebeinos, Carbon-nanotube photonics and optoelectronics, *Nature Photonics* **2**, 341 (2008).
  - [7] R. A. Hatton, A. J. Miller, and S. R. P. Silva, Carbon nanotubes: A multi-functional material for organic optoelectronics, *J. Mater. Chem.* **18**, 1183 (2008).
  - [8] A. Shaikjee and N. J. Coville, The synthesis, properties and uses of carbon materials with helical morphology, *J. Adv. Res.* **3**, 195 (2012).
  - [9] O. Kibis, Electron-electron interaction in a spiral quantum wire, *Phys. Lett. A* **166**, 393 (1992).
  - [10] P. Schmelcher, Effective long-range interactions in confined curved dimensions, *Europhys. Lett.* **95**, 50005 (2011).
  - [11] A. Siemens and P. Schmelcher, Tunable order of helically confined charges, *Phys. Rev. E* **102**, 012147 (2020).
  - [12] A. V. Zampetaki, J. Stockhofe, and P. Schmelcher, Electrostatic bending response of a charged helix, *Phys. Rev. E* **97**, 042503 (2018).
  - [13] A. V. Zampetaki, J. Stockhofe, S. Krönke, and P. Schmelcher, Classical scattering of charged particles confined on an inhomogeneous helix, *Phys. Rev. E* **88**, 043202 (2013).
  - [14] A. V. Zampetaki, J. Stockhofe, and P. Schmelcher, Dynamics of nonlinear excitations of helically confined charges, *Phys. Rev. E* **92**, 042905 (2015).
  - [15] A. V. Zampetaki, J. Stockhofe, and P. Schmelcher, Degeneracy and inversion of band structure for Wigner crystals on a closed helix, *Phys. Rev. A* **91**, 023409 (2015).
  - [16] J. K. Pedersen, D. V. Fedorov, A. S. Jensen, and N. T. Zinner, Formation of classical crystals of dipolar particles in a helical geometry, *J. Phys. B* **47**, 165103 (2014).
  - [17] J. K. Pedersen, D. V. Fedorov, A. S. Jensen, and N. T. Zinner, Quantum single-particle properties in a one-dimensional curved space, *J. Mod. Opt.* **63**, 1814 (2016).
  - [18] J. K. Pedersen, D. V. Fedorov, A. S. Jensen, and N. T. Zinner, Quantum few-body bound states of dipolar particles in a helical geometry, *J. Phys. B* **49**, 024002 (2016).
  - [19] A. V. Zampetaki, J. Stockhofe, and P. Schmelcher, Pinned-to-sliding transition and structural crossovers for helically confined charges, *Phys. Rev. E* **95**, 022205 (2017).
  - [20] J. Plettenberg, J. Stockhofe, A. V. Zampetaki, and P. Schmelcher, Local equilibria and state transfer of charged classical particles on a helix in an electric field, *Phys. Rev. E* **95**, 012213 (2017).
  - [21] M. E. Goggin and P. W. Milonni, Driven Morse oscillator: Classical chaos, quantum theory, and photodissociation, *Phys. Rev. A* **37**, 796 (1988).
  - [22] M. Büttiker and R. Landauer, Traversal Time for Tunneling, *Phys. Rev. Lett.* **49**, 1739 (1982).

- [23] A. Pimpale, S. Holloway, and R. J. Smith, Tunnelling through moving barriers, *J. Phys. A: Math. Gen.* **24**, 3533 (1991).
- [24] P. F. Bagwell and R. K. Lake, Resonances in transmission through an oscillating barrier, *Phys. Rev. B* **46**, 15329 (1992).
- [25] J.-Y. Ge and J. Z. H. Zhang, Quantum mechanical tunneling through a time-dependent barrier, *J. Chem. Phys.* **105**, 8628 (1996).
- [26] J. L. Mateos and J. V. José, Energy transfer of a chaotic particle in a classical oscillating potential barrier, *Physica A* **257**, 434 (1998).
- [27] J. L. Mateos, Traversal-time distribution for a classical time-modulated barrier, *Phys. Lett. A* **256**, 113 (1999).
- [28] E. D. Leonel and P. V. E. McClintock, Chaotic properties of a time-modulated barrier, *Phys. Rev. E* **70**, 016214 (2004).
- [29] S. Flach, O. Yevtushenko, and Y. Zolotaryuk, Directed Current Due to Broken Time-Space Symmetry, *Phys. Rev. Lett.* **84**, 2358 (2000).
- [30] H. Schanz, M.-F. Otto, R. Ketzmerick, and T. Dittrich, Classical and Quantum Hamiltonian Ratchets, *Phys. Rev. Lett.* **87**, 070601 (2001).
- [31] N. R. Quintero, J. A. Cuesta, and R. Alvarez-Nodarse, Symmetries shape the current in ratchets induced by a biharmonic driving force, *Phys. Rev. E* **81**, 030102(R) (2010).
- [32] P. Reimann, Brownian motors: Noisy transport far from equilibrium, *Phys. Rep.* **361**, 57 (2002).
- [33] P. Hänggi and F. Marchesoni, Artificial Brownian motors: Controlling transport on the nanoscale, *Rev. Mod. Phys.* **81**, 387 (2009).
- [34] S. Denisov, S. Flach, and P. Hänggi, Tunable transport with broken space-time symmetries, *Phys. Rep.* **538**, 77 (2014).
- [35] F. Renzoni, Driven Ratchets for Cold Atoms, in *Advances In Atomic, Molecular, and Optical Physics* (Elsevier, Amsterdam, 2009), Vol. 57, pp. 1–32.
- [36] T. Wulf, B. Liebchen, and P. Schmelcher, Disorder Induced Regular Dynamics in Oscillating Lattices, *Phys. Rev. Lett.* **112**, 034101 (2014).
- [37] C. Petri, F. Lenz, B. Liebchen, F. Diakonov, and P. Schmelcher, Formation of density waves via interface conversion of ballistic and diffusive motion, *Europhys. Lett.* **95**, 30005 (2011).
- [38] T. Wulf, C. Petri, B. Liebchen, and P. Schmelcher, Analysis of interface conversion processes of ballistic and diffusive motion in driven superlattices, *Phys. Rev. E* **86**, 016201 (2012).
- [39] J. F. Wambaugh, C. Reichhardt, and C. J. Olson, Ratchet-induced segregation and transport of nonspherical grains, *Phys. Rev. E* **65**, 031308 (2002).
- [40] A. K. Mukhopadhyay, B. Liebchen, and P. Schmelcher, Simultaneous Control of Multispecies Particle Transport and Segregation in Driven Lattices, *Phys. Rev. Lett.* **120**, 218002 (2018).
- [41] S. Matthias and F. Müller, Asymmetric pores in a silicon membrane acting as massively parallel brownian ratchets, *Nature (London)* **424**, 53 (2003).
- [42] R. K. Schmitt, J. M. R. Parrondo, H. Linke, and J. Johansson, Molecular motor efficiency is maximized in the presence of both power-stroke and rectification through feedback, *New J. Phys.* **17**, 065011 (2015).
- [43] V. Serreli, C.-F. Lee, E. R. Kay, and D. A. Leigh, A molecular information ratchet, *Nature (London)* **445**, 523 (2007).
- [44] D. Cubero and F. Renzoni, Hidden Symmetries, Instabilities, and Current Suppression in Brownian Ratchets, *Phys. Rev. Lett.* **116**, 010602 (2016).
- [45] R. D. Astumian and M. Bier, Fluctuation Driven Ratchets: Molecular Motors, *Phys. Rev. Lett.* **72**, 1766 (1994).
- [46] R. D. Astumian, Thermodynamics and Kinetics of a Brownian Motor, *Science* **276**, 917 (1997).
- [47] See Supplemental Material at <http://link.aps.org/supplemental/10.1103/PhysRevE.103.052217> for a video of the time evolution of Eq. (8).
- [48] C. R. Menyuk, Particle motion in the field of a modulated wave, *Phys. Rev. A* **31**, 3282 (1985).
- [49] N. Saitô, H. Hirooka, J. Ford, F. Vivaldi, and G. Walker, Numerical study of billiard motion in an annulus bounded by non-concentric circles, *Physica D* **5**, 273 (1982).
- [50] A. Loskutov, A. B. Ryabov, and L. G. Akinshin, Properties of some chaotic billiards with time-dependent boundaries, *J. Phys. A: Math. Gen.* **33**, 7973 (2000).
- [51] D. Reitz and A. Rauschenbeutel, Nanofiber-based double-helix dipole trap for cold neutral atoms, *Opt. Commun.* **285**, 4705 (2012).



**Driven toroidal helix as a generalization of the Kapitza pendulum**J. F. Gloy,<sup>1</sup> A. Siemens<sup>1,\*</sup> and P. Schmelcher<sup>1,2,†</sup><sup>1</sup>Zentrum für Optische Quantentechnologien, Fachbereich Physik, Universität Hamburg, Luruper Chaussee 149, 22761 Hamburg Germany<sup>2</sup>Hamburg Center for Ultrafast Imaging, Universität Hamburg, Luruper Chaussee 149, 22761 Hamburg Germany

(Received 25 January 2022; accepted 26 April 2022; published 5 May 2022)

We explore a model system consisting of a particle confined to move along a toroidal helix while being exposed to a static potential as well as a driving force due to a harmonically oscillating electric field. It is shown that in the limit of a vanishing helix radius, the governing equations of motion coincide with those of the well-known Kapitza pendulum—a classical pendulum with oscillating pivot—implying that the driven toroidal helix represents a corresponding generalization. It is shown that the two dominant static fixed points present in the Kapitza pendulum are also present for a finite helix radius. The dependence of the stability of these two fixed points on the helix radius, the driving amplitude, and the static potential are analyzed analytically. These analytical results are subsequently compared to results corresponding of numerical simulations. Additionally, the most prominent deviations of the driven helix from the Kapitza pendulum with respect to the resulting phase space are investigated and analyzed in some detail. These effects include an unusual transition to chaos and an effective directed transport due to the simultaneous presence of multiple chaotic phase space regions.

DOI: [10.1103/PhysRevE.105.054204](https://doi.org/10.1103/PhysRevE.105.054204)**I. INTRODUCTION**

Helical shapes are naturally occurring in nature, arising, e.g., through hydrogen bonds in alpha-helix segments of proteins or in molecules such as DNA and alpha-keratin. Furthermore, helical structures can emerge through long-range order in self-organizing systems on cylindrical surfaces [1–3] or can be artificially created by rolling up thin sheets into cylinders [4–7]. Helical structures can also appear in trapping potentials induced by light fields around optical fibers [8,9] which can be loaded with neutral cold atoms. An advantage of the helical shape is the increased stability with regard to deformations [10,11], making helical nanostructures desirable for future applications, e.g., in nanocircuits.

Besides occurring in nature, helical systems of charged particles have recently been explored in the literature thereby demonstrating a number of intriguing effects emerging due to the geometry, such as interactions that oscillate with the (parametrized) distance along the helix [12]. These effects have been studied in lattice systems with long-range hopping [13,14], as well as in more fundamental models of classical charges moving on helices [15–22]. In such model systems, it has been demonstrated that based on the oscillating effective interactions, static setups already become very complex since particles are able to localize into irregular latticelike structures [16,20] exhibiting a plethora of possible equilibrium configurations [12,21]. By varying the helix geometry, it is possible to tune a variety of effects, such as scattering of bound states at local defects [15], band structure inver-

sion and degeneracies [16,17], or unusual pinned to sliding transitions [18] in crystalline configurations on a toroidal helix.

Inspired by the demonstrated richness of effects of charged particles on a helix, we explore here a system consisting of a single particle confined to a toroidal helix in the presence of an oscillating driving field and a static potential. In a previous study [22], the corresponding phase space in the absence of the static potential and the related directed transport have been investigated. Here, we build upon these results and explore the effects of an additional spatially oscillating static potential. We show that the governing equations map to the equations for the Kapitza pendulum [23] in the limit of a vanishing helix radius. For a nonvanishing helix radius, a dynamical behavior beyond that of the Kapitza pendulum emerges. Our main results include a stability analysis of two major fixed points corresponding to the two major fixed points in the Kapitza pendulum. We derive and analyze some of the most prominent dynamical phases arising in the phase space of our driven helical particle system.

This paper is structured as follows: In Sec. II, we explain our setup and derive the underlying equations of motion. We show that in the limit of a vanishing helix radius, the equations of motion simplify to those of the Kapitza pendulum. Therefore, the main features of the Kapitza pendulum are briefly summarized in Sec. III. The main results are provided in Secs. IV and V, addressing the driven helix away from the Kapitza limit. In Sec. IV, the influence of a finite helix radius on the stability of the two fixed points of the Kapitza pendulum is analyzed analytically. These analytical results are then compared with the results of corresponding numerical simulations. In Sec. V, major dynamical effects emerging for a finite helix radius are investigated. A discussion and outlook are presented in Sec. VI.

\*asiemens@physnet.uni-hamburg.de

†pschmelc@physnet.uni-hamburg.de

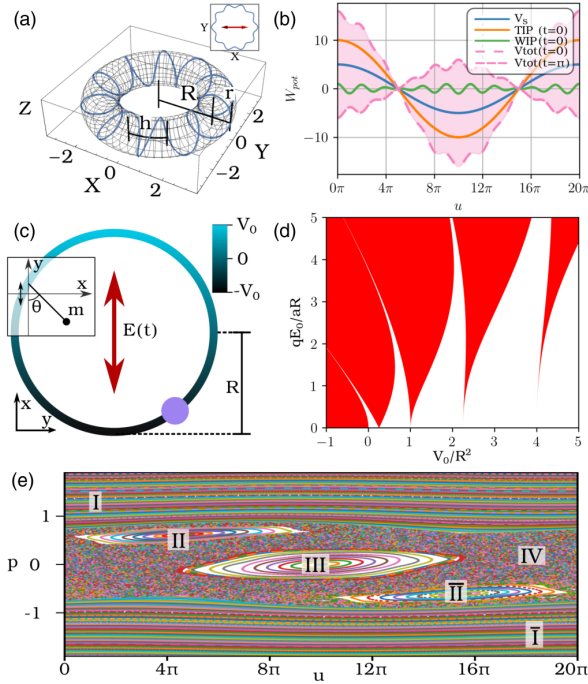


FIG. 1. (a) A 3D sketch of the torus and the toroidal helix with the parametric function  $\mathbf{r}(u)$ , for  $M = 10$ ,  $r = 0.8$ , and  $R = 2.5$ . The inset in the top right visualizes the direction of the driving electric field. (b) The potential energy created by the driving electric field  $E(t)$  (TIP, orange and WIP, green) and the static potential  $V(u)$  (blue) shown for a toroidal helix with  $M = 10$ ,  $R = 2.5$ ,  $V_0 = 5$ , and a helix radius of  $r = 0.1$ . (c) Visualization of the Kapitz limit  $r \rightarrow 0$ . The toroidal helix becomes a circle in the  $xy$  plane. The potential energy induced by the static potential is indicated by the color. For comparison, a schematic of the Kapitz pendulum is shown in the inset on the left. (d) Visualization of the Ince-Strutt diagram highlighting the regions where the two major fixed points of the Kapitz pendulum are stable (white) or unstable (red). (e) Poincare surface of section (PSOS) in the Kapitz limit  $r \rightarrow 0$  for  $V_0 = 5$  and  $E_0 = 3$ . The most prominent types of trajectories are shown: (I) rotators that are not significantly affected by the driving, (II) trajectories circling in phase around the ring with the driving, (III) bounded trajectories centered at the minimum of the static potential, and (IV) chaotic trajectories. Trajectories marked  $\bar{\text{II}}$  circle around the ring in the opposite direction as those trajectories marked II.

## II. DRIVEN TOROIDAL HELIX

We consider a charged particle with charge  $q$  confined to frictionlessly move on a geometry of the shape of a toroidal helix [see Fig. 1(a)]. Additionally, the particle is subject to a static potential and driven by a harmonically oscillating electric field. The confining geometry is parametrized as follows:

$$\mathbf{r}(u) := \begin{pmatrix} (R + r \cos(u)) \cos(u/M) \\ (R + r \cos(u)) \sin(u/M) \\ r \sin(u) \end{pmatrix}, u \in [0, 2\pi M], \quad (1)$$

where  $M$ ,  $R$ ,  $r$  are the number of helix windings, the radius of the torus, and the radius of the helix, respectively. The parametrized position  $u$  on the helix can be interpreted as an angle. If  $u$  changes by  $2\pi$ , the particle moves by exactly one helical winding. The static potential  $V(u)$  at each position  $\mathbf{r}(u)$  is defined as

$$V_S(u) = V_0 \cos\left(\frac{u}{M}\right). \quad (2)$$

The potential created by the periodic driving electric field  $\mathbf{E}(t)$  is modeled according to the corresponding Stark term:

$$V_E(u, t) = q\mathbf{E}(t) \cdot \mathbf{r}(u) = q \cos(\omega t) \mathbf{E}_0 \cdot \mathbf{r}(u). \quad (3)$$

We consider a sinusoidally oscillating electric field with a polarization in the torus plane ( $x$  direction). With this, the potential energy induced by the driving field becomes

$$V_E(u, t) = qE_0(R + r \cos(u)) \cos(u/M) \cos(\omega t). \quad (4)$$

This potential consists of two parts: one depending on the torus radius  $R$  and one depending on the helix radius  $r$ . They will from now on be referred to as torus-induced potential (TIP) and winding-induced potential (WIP), respectively. An understanding of the potential experienced by the particle while moving along the helix can be gained from Fig. 1(b). The figure shows the energy due to the static potential [blue curve, compare Eq. (2)] and the energy due to the driving electric field at  $t = 0$  [orange and green curves for the TIP and WIP respectively, see Eq. (4)] for a toroidal helix with  $M = 10$ ,  $R = 2.5$ ,  $V_0 = 5$ , and  $r = 0.8$ . The total potential  $V_{\text{tot}}(u, t) = V_E(u, t) + V_S(u)$  contains both the static potential  $V_S(u)$  and the field potential  $V_E(u, t)$ . Due to the time dependence of the driving field, the total potential energy is, of course, also time dependent. Specifically, the shown TIP and WIP will oscillate with  $\cos(\omega t)$ , resulting in the total energies  $V_{\text{tot}}(u, t = 0)$  [pink dotted line in Fig. 1(b)] for a field aligned in positive  $x$  direction, and  $V_{\text{tot}}(u, t = 0.5\pi/\omega)$  [pink densely dotted line in Fig. 1(b)] half a driving period later when the field is aligned in the negative  $x$  direction. The pink shaded area indicates the range of potential energies covered for each position  $u$  during a driving period. An increase of  $r$  will lead to an increase of the amplitude of the WIP. In the limit of  $r \rightarrow 0$ , the WIP will vanish and the fine structure of  $V_{\text{tot}}$  disappears. The number of extrema in the total potential energy can therefore be tuned by varying  $r$ .

The driven helix is then described by the following Lagrangian:

$$\begin{aligned} \mathcal{L} &= \frac{m}{2} \left( \frac{d\mathbf{r}(u)}{dt} \right)^2 - q \cos(\omega t) \mathbf{E}_0 \cdot \mathbf{r}(u) - V_0 \cos\left(\frac{u}{M}\right) \\ &= \frac{m}{2} (r^2 + a^2(R + r \cos(u))^2) \dot{u}^2 \\ &\quad - qE_0(R + r \cos(u)) \cos(\omega t) \cos(au) - V_0 \cos(au), \end{aligned} \quad (5)$$

where  $a = 1/M$  is the inverse of the winding number. It is sensible to introduce the parameter  $l(u)$  defined as

$$l^2(u) := \frac{1}{a^2} (r^2 + a^2(R + r \cos(u))^2). \quad (6)$$

Using this expression, the Lagrangian can be written as

$$\mathcal{L} = \frac{ma^2}{2} l^2(u) \dot{u}^2 - \left( V_0 + qE_0 \frac{\sqrt{l^2(u)a^2 - r^2}}{a} \cos(\omega t) \right) \cos(au). \quad (7)$$

With  $p = \partial \mathcal{L} / \partial \dot{u} = ma^2 l^2(u) \dot{u}$ , the Lagrangian in Eq. (7) corresponds to the following Hamiltonian:

$$\mathcal{H} = [2ma^2 l^2(u)]^{-1} p^2 - \left( V_0 + qE_0 \frac{\sqrt{l^2(u)a^2 - r^2}}{a} \cos(\omega t) \right) \cos(au). \quad (8)$$

The Lagrangian in Eq. (7) efficiently accounts for the confining forces by only allowing positions along the helix  $\mathbf{r}(u)$ . From this Lagrangian, we obtain the following equation of motion:

$$m[r^2 + a^2(R + r \cos(u))^2] \ddot{u} - V_0 a \sin(au) - qE_0 \cos(\omega t) [r \sin(u) \cos(au) + a(R + r \cos(u)) \sin(au)] + ma^2 r \sin(u) (R + r \cos(u)) \dot{u}^2 / 2 = 0. \quad (9)$$

Some of the parameters in the Lagrangian of Eq. (7) and of the equation of motion in Eq. (9) are redundant and can be absorbed by other parameters. The redundant parameters are the driving frequency  $\omega$ , the torus radius  $R$ , the particle mass  $m$ , and charge  $q$  of the particle. These quantities can, without loss of generality, be eliminated by rescaling the remaining relevant parameters as follows:

$$\tilde{t} = t \frac{\omega}{2\pi}, \quad \tilde{r} = \frac{r}{R}, \quad \tilde{E} = \frac{4\pi^2 qE}{mR\omega^2}, \quad \tilde{V} = \frac{4\pi^2 V}{mR^2\omega^2}. \quad (10)$$

In the limit of  $r \rightarrow 0$ , we get  $l^2(u) = R^2$ , and the Lagrangian from Eq. (7) becomes the Lagrangian of the Kapitza pendulum [23]:

$$\mathcal{L}_K = \frac{m}{2} a^2 R^2 \dot{u}^2 + (V_0 + qE_0 R \cos(\omega t)) \cos(au). \quad (11)$$

The equivalence between the Kapitza pendulum and the toroidal helix in the limit of  $r \rightarrow 0$  is further indicated in Fig. 1(c) and its inset. The driving electric field and static potential along the toroidal helix are, respectively, equivalent to the oscillating pivot and the gravitation potential in the Kapitza pendulum.

### III. THE KAPITZA PENDULUM LIMIT

To be self-contained, we briefly demonstrate the main features of our system that are already known from the Kapitza pendulum. The Kapitza pendulum is a classical pendulum with an oscillating pivot as depicted in the inset of Fig. 1(c). One of the most interesting aspects of the Kapitza pendulum is regarding the fixed points in the underlying equations of motion. In addition to the expected fixed point where the pendulum is in its potential minimum (corresponding to  $u = M\pi$ ), the Kapitza pendulum can have another stable fixed point in the upper position (corresponding to  $u = 0$ ). This second fixed point is stabilized due to the driving forces from the

oscillating pivot. In the Kapitza limit of  $r \rightarrow 0$ , the equation of motion shown in Eq. (9) simplifies to

$$ma^2 R^2 \ddot{u} = [V_0 a + qE_0 \cos(\omega t) a R] \sin(au). \quad (12)$$

From Eq. (12), the two fixed points at  $u = 0$  and  $u = M\pi$ —respectively corresponding to the Kapitza pendulum in the upper and lower position—can be easily identified. The stability of these fixed points can be determined by linearizing Eq. (12) around these two fixed points. This results in the following equation:

$$mR^2 \ddot{u} = u(\pm V_0 + qE_0 R \cos(\omega t)), \quad (13)$$

where in case of the fixed point at  $u = 0$  we obtain a positive sign of the first summand and a negative sign in the case of the fixed point at  $u = M\pi$ . Equation (13) is also known as the Mathieu equation [compare Eq. (14) below]. The parameter regions for which the Mathieu equation has periodic bounded solutions can be determined from the Ince-Strutt diagram [24] shown in Fig. 1(d). In this diagram, the white areas mark regions where periodic solutions of Eq. (13) exist, i.e., where the fixed point is stable, whereas in the red regions, no bounded solutions exist, i.e., the fixed point is unstable, which can lead to an exponential increase of  $|p|$ . Further away from the fixed point, this unbounded growth of energy and momentum is suppressed by the nonlinearities of  $V_{\text{tot}}(u, t)$ . As can be seen from Eq. (13), positive values on the  $(V_0/R^2)$ -axis of Fig. 1(d) describe the stability of the fixed point at  $u = 0$ , whereas negative values describe the stability of the fixed point at  $u = M\pi$ .

The below-given discussions in Secs. IV and V feature an analysis of the phase space for  $r > 0$  to understand the dynamics for a wide range of initial conditions. To better contextualize these results, the most prominent types of trajectories in the Kapitza limit are now discussed. Since our phase space is made up of three parameters (position  $u$ , momentum  $p$ , and time  $t$ ), we can use a Poincaré surface of section (PSOS)—specifically, a stroboscopic map—to visualize the phase space in a two-dimensional stroboscopic  $u(p)$  mapping. A general overview of the most prominent possible types of trajectories in the Kapitza limit is given in Fig. 1(e). For large enough momentum, there will always be (quasi)periodic trajectories bounding the chaotic sea, corresponding to a fast rotational motion around the torus which is not significantly affected by the driving. They are marked (I) in the figure (or  $\bar{\text{I}}$  for trajectories moving in the opposite direction). With increasing  $|p|$ , the corresponding invariant tori approach a constant behavior. Islands of regular motion around the two fixed points at  $u = 0$  and  $u = M\pi$  and are marked (III). Additionally, it is possible to stabilize (quasi)periodic trajectories circling around the torus in phase with the driving field. This type of motion occurs in the regions marked (II) and ( $\bar{\text{II}}$ ) in Fig. 1(e). Chaotic trajectories [marked (IV)] will in general be present for all  $E_0 > 0$ . Through variation of  $E_0$  and  $V_0$ , it is possible to tune the presence of the trajectories of types (II)–(IV). All these trajectories are also encountered for arbitrary  $r > 0$ —albeit for different parameter combinations than for  $r = 0$ .

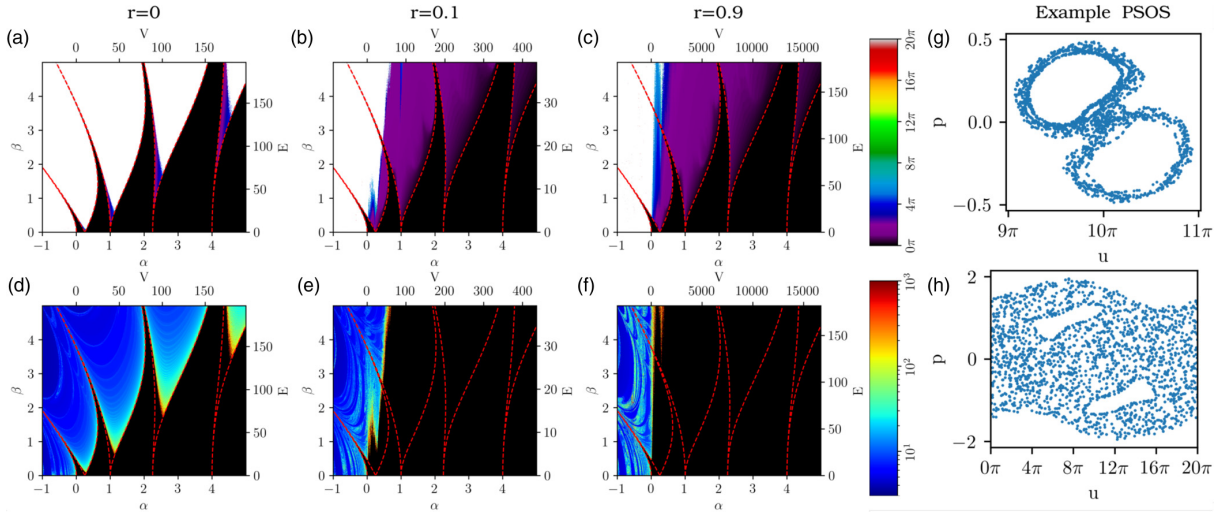


FIG. 2. Comparison of numerical calculations to the analytically predicted stability of the major fixed points in the generalized Kapitza pendulum. (a)–(c) Maximal distance in phase space between the fixed point (at  $u = M\pi$  for  $\alpha > 0$  and at  $u = 0$  for  $\alpha < 0$ ) and a trajectory starting at a distance of  $10^{-8}$  from this point after a simulation time of 1000 driving periods. White color indicates that the particle moves at least once around the torus. The parameter regions where our analytical calculations based on Eqs. (14)–(16) predict the fixed points to be stable are marked by the dotted red lines. (d)–(f) The time needed for the particle to move once around the torus. The used trajectories are the same as in (a)–(c). Again, the corresponding Ince-Strutt diagram is indicated by the dotted red lines. (g), (h) Example PSOS for trajectories from the purple and white regions.

#### IV. STABILITY ANALYSIS

We will now consider the general case of a finite helix radius  $r > 0$  and investigate how the helix radius influences the stability of the two fixed points discussed in Sec. III. The persistence of these fixed points in the generalized setup can be directly verified by inserting the initial conditions  $\dot{u} = 0$  and  $u = 0$  (or  $u = M\pi$  for the second fixed point) into the general equations of motion given by Eq. (9). In addition to an analytical stability analysis through linearization of the equations of motion in the vicinity of the fixed point, we investigate the particle dynamics close to the fixed point via numerical simulations. Note that from now on, all calculations are performed using the scaling introduced in Eq. (10). We start with the analytical considerations and linearize the general equations of motion in Eq. (9) around the two fixed points. Similar to the Kapitza limit, the resulting approximate equations of motion are described by the Mathieu equation, except that this time the coefficients of the Mathieu equation additionally depend on the helix radius. The general Mathieu equation is given by

$$\ddot{u} + (\alpha - \beta \cos(\tau))u = 0. \quad (14)$$

For the first fixed point at  $u = 0$ , the parameters  $\alpha$  and  $\beta$  are given by

$$\begin{aligned} \alpha_1 &= -\frac{V_0 a^2}{4\pi^2(r^2 + a^2(1+r)^2)}, \\ \beta_1 &= \frac{E_0(a^2(1+r) + r)}{4\pi^2(r^2 + a^2(1+r)^2)}. \end{aligned} \quad (15)$$

For the second fixed point at  $u = M\pi$  we have

$$\begin{aligned} \alpha_2 &= \frac{V_0 a^2}{4\pi^2[r^2 + a^2(1 + (-1)^M r)^2]} \\ \beta_2 &= \frac{E_0(a^2(1 + (-1)^M r) + (-1)^M r)}{4\pi^2[r^2 + a^2(1 + (-1)^M r)^2]}. \end{aligned} \quad (16)$$

The factor  $(-1)^M$  in Eq. (16) accounts for the difference in the potential energy at  $u = M\pi$  between setups with even and odd winding numbers. In the following, all shown data are for an even winding number  $M = 10$ . For even  $M$ , we get  $\alpha_1 = -\alpha_2$  and  $\beta_1 = \beta_2$  and we can therefore visualize the stability of both fixed points in the same diagram. Different choices (i.e., odd values) of  $M$  will change the parameters  $\alpha$  and  $\beta$  but to the best of our knowledge do not lead to significantly different behavior or dynamics.

Using Eqs. (14) to (16), we can establish and analyze the Ince-Strutt diagram to determine the parameter sets for which the two fixed points of our driven helix are stable. This is illustrated in Fig. 2 for several values of the helix radius  $r$ . The boundaries of the analytically obtained stability tongues (i.e., regions where the fixed points are predicted to be stable) obtained from Eqs. (14)–(16) are marked by red dotted lines. The colors in Fig. 2 visualize the results of the numerical calculations and provide insight into the dynamics in the immediate vicinity of the fixed points. These numerical results are obtained by calculating the trajectory of a particle starting within an  $\epsilon$  environment of the fixed points. If the fixed point is stable, the resulting motion is (quasi)periodic; in case it is unstable, the particle will explore a significant region of the phase space. More specifically, we use the initial

condition of  $(u, p) = (M\pi + 10^{-8}, 0)$  and simulated the dynamics for 1000 driving periods. For each trajectory, the maximal phase space distance of the trajectory to the fixed point is determined. These results are shown in Figs. 2(a)–2(c), where each pixel corresponds to a distance obtained from a single trajectory. In total, 675 000 trajectories were simulated for each of the subfigures Figs. 2(a)–2(c). The black areas indicate that the particle stays in the immediate vicinity of the fixed point, whereas the white color shows that the particle moves at least once around the torus. The agreement with the analytically determined stability diagrams can be clearly seen in Fig. 2. However, an increase of the helix radius  $r$  leads to a significant change of the dynamics of unbounded trajectories for the fixed point at  $u = M\pi$  (i.e., positive values of  $V_0$  in the figure). Increasing  $r$  increases the size of the regions where the particle moves a significant distance away from the fixed point but does not explore the complete phase space (i.e., the purple and blue regions in the figure). In the white regions of the figure, the unstable fixed point is (usually) part of the chaotic sea, allowing the particle to explore the entire toroidal helix. A PSOS for a corresponding example trajectory can be seen in Fig. 2(h). An example PSOS for a trajectory from the purple and blue regions is shown in Fig. 2(g). The dynamics in the blue and purple regions of the figures will be described in more detail in Sec. V.

In contrast to the fixed point at  $u = M\pi$ , judging from Figs. 2(a)–2(c), the behavior outside of the analytically obtained stability tongue for the fixed point at  $u = 0$  (negative values of  $V_0$  in the figure) seems to be hardly affected by changes of  $r$ . One intuitive explanation for this is that  $V_S(u)$  has a maximum at  $u = 0$  and at infinitesimal distances from this point the particle will experience a force away from the fixed point, thereby preventing the existence of trajectories similar to the one shown in Fig. 2(g).

To provide insight into the trajectories in the white regions, we determine the time needed until a distance of  $2\pi M$  is reached for the first time. The corresponding results are shown in Figs. 2(d)–2(f). We observe that for increasing  $r$  the transition from (quasi)periodic to chaotic trajectories in the vicinity of the analytically obtained stability-tongue borders changes from a (relatively) smooth transition for  $r = 0$  to a rather abrupt transition for large  $r$ .

## V. PHASE-SPACE ANALYSIS

In addition to the modifications of the stability of the two fixed points of the Kapitza pendulum, the driven helix also exhibits various dynamical phases that appear only for a non-vanishing radius  $r > 0$ . In this section, the most significant of these features are described and analyzed.

One interesting characteristic concerns the unusual mechanism by which the dynamics in the vicinity of the fixed point at  $u = M\pi$  transitions from (quasi)periodic to chaotic motion. It might be natural to expect that the breakup of invariant tori happens first for those trajectories with larger phase-space distance to the fixed point when the system is exposed to a perturbation. However, in contrast to this expectation, we observe that trajectories close to the fixed point become chaotic—resulting in a chaotic phase space region that is centered around an unstable fixed point and separated from the

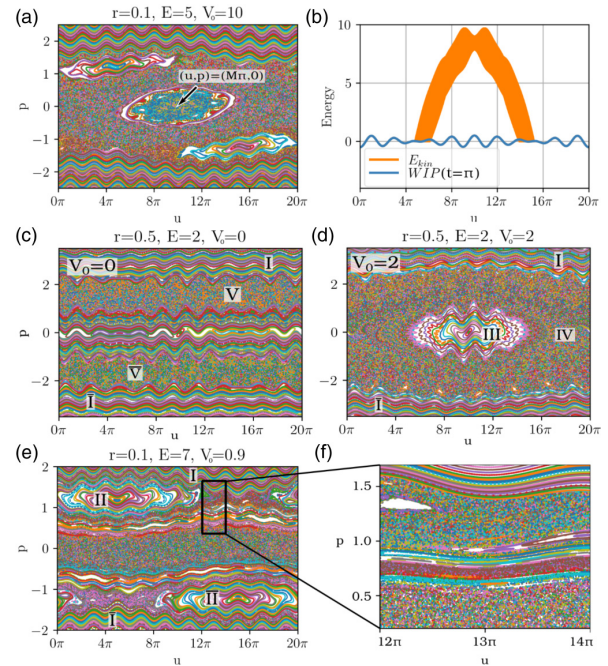


FIG. 3. (a) Poincaré surface of sections (PSOS) for  $r = 0.1$ ,  $E_0 = 5$ , and  $V_0 = 10$ . Trajectories close to the fixed point at  $(u, p) = (M\pi, 0)$  (indicated by the arrow) become chaotic while (quasi)periodic trajectories with greater phase space distances from the fixed point prevail. (b) Potential energy due to the WIP, as well as the range of kinetic energy values taken by one of the (quasi)periodic trajectories that separates the two chaotic regions shown in (a). (c), (d) PSOS for  $r = 0.5$ ,  $E_0 = 2$  and  $V_0 = 0$  (c),  $V_0 = 2$  (d). The two separated chaotic seas marked V and  $\bar{V}$  in (c) become connected when  $V_0$  is of similar order as  $E_0$ . (e), (f) PSOS for  $r = 0.1$ ,  $E_0 = 7$ , and  $V_0 = 0.9$  showing the presence of three distinct chaotic regions. The upper chaotic region is highlighted in (f).

main chaotic sea by a region with (quasi)periodic trajectories, i.e., a regular island. The size of this chaotic region can be tuned by varying the helix radius  $r$ . The results are chaotic trajectories with a tunable motional amplitude (i.e., tunable maximal distance from the fixed point) around the fixed point. This effect is demonstrated in the PSOS in Fig. 3(a). In the figure, one can clearly identify the (quasi)periodic trajectories and regular regions separating the chaotic trajectories that are trapped around the fixed point at  $(u, p) = (M\pi, 0)$  from those chaotic trajectories that can explore the entire toroidal helix. For small parameter regions, the simultaneous presence of multiple bands of (quasi)periodic trajectories centered around the (unstable) fixed point at  $(u, p) = (M\pi, 0)$ , but separated from one another by chaotic phase space regions, could be observed.

The reason for this peculiar transition to chaos can be elucidated by the changes in the potential landscape for increasing  $r$ . For  $r \ll R$ , the radius dependent oscillations (the WIP, with a period of  $2\pi$ ) of the potential can be treated as a perturbation to the  $r \rightarrow 0$  limit. This perturbation will be largest at the global extrema of the potential at  $u = 0$  and  $u = M\pi$  and will vanish at  $u = M\pi/2$  and  $u = 3M\pi/2$  [see Fig. 1(b)]. This

heavy oscillatory character of the time-dependent potential landscape can induce chaotic motion—provided the particle moves slow enough to be affected. From a comparison with Fig. 1(e), it can be seen that this is more likely for trajectories oscillating closer to the fixed point and less likely with increasing phase space distance of the trajectory from the fixed point. Consequently, trajectories closer to the fixed point (i.e., closer to the global minimum of the potential landscape) will be stronger affected by this perturbation and will become chaotic for smaller values of  $r$  than their more distant counterparts. These arguments are supported by Fig. 3(b), which shows the WIP-potential energy at  $t = \pi$ , together with the set of kinetic energy values  $\{E_{\text{kin}}(u(t)) | 0 < t < 2000\pi\}$  taken by the particle during a representative (quasi)periodic example trajectory confining the chaotic phase space region around the fixed point. It can be seen that the kinetic energy is for the most part much larger than the perturbation by the WIP. Only close to those points where the WIP vanishes does the kinetic energy also become comparatively small.

Another interesting effect that is absent in the Kapitza limit concerns the emergence of chaos in the regime of weak driving forces. In the regime of small driving amplitudes, two separate chaotic phase space regions, that are arranged symmetrically with respect to a point inversion symmetry through the point  $(u, p) = (M\pi, 0)$ , can appear—one consisting of trajectories with only positive momenta, the other consisting of trajectories with only negative momenta [see regions marked V and  $\bar{V}$  in Fig. 3(c)]. They are similar to the trajectories marked (II) and  $(\bar{\text{II}})$  in Fig. 1(e) in the sense that they also correspond to motion around the torus with strictly positive or negative momentum. However, instead of moving once around the torus during each driving period, these trajectories are chaotic and move on average by one helix winding during each driving period. The average velocity in these trajectories is therefore slower by a factor of  $1/M$  compared to the average velocity of the type-II (and  $-\bar{\text{II}}$ ) trajectories. These trajectories appear only in the case of a finite helix radius  $r$ . The (quasi)periodic trajectories separating the two chaotic regions correspond mostly to very slow (quasi)periodic motion of the particle around the torus and in some cases to (quasi)periodic oscillations of the particle within one helix winding. The origin and mechanism of this effect has previously been explored in the absence of the static potential [22]. When the static potential is added, the two chaotic regions will persist while  $V_0 \ll E_0$ . However, when  $V_0$  is increased, the chaotic regions also increase and will fuse when  $V_0$  is of similar order of magnitude as  $E_0$ , thereby resulting in a phase space similar to the one shown in Fig. 3(d). In the figure,  $V_0$  is sufficiently large, such that all slowly moving (quasi)periodic trajectories will be part of the regular island around the fixed point at  $(u, p) = (M\pi, 0)$  [marked III in Fig. 3(d)] and none of the separating trajectories persist.

Another interesting effect concerns the influence of a finite helix radius on the trajectories moving around the torus in phase with the driving [see regular islands marked II and  $\bar{\text{II}}$  in Fig. 1(e)]. As shown in Figs. 3(e) and 3(f), chaotic regions separated from the main chaotic region which is centered around  $p = 0$  can appear around these regular islands. The dynamics in the chaotic regions that surround the regular

islands marked II and  $\bar{\text{II}}$  in Fig. 3(e) correspond to motion where the particle moves around the torus (on average) in phase with the driving frequency. A necessary condition for this effect to occur is that the driving amplitude is small enough, such that the chaotic sea centered around  $p = 0$  does not surround the corresponding two regular islands. Analogous to the effect shown in Figs. 3(a) and 3(b), these chaotic regions are caused by perturbations of the trajectories due to the WIP. One difference to this previously discussed effect is that the regular islands marked II and  $\bar{\text{II}}$  are, respectively, located at the positions  $u = M\pi/2$  and  $u = 3M\pi/2$  where the WIP vanishes. The perturbation is consequently stronger for trajectories with larger phase space distances from the fixed point.

## VI. SUMMARY AND DISCUSSION

We have demonstrated that the dynamics of a charged particle confined to a toroidal helix while being exposed to a static potential and a driving electric field represent a generalization of the Kapitza pendulum in the sense that in the limit of a vanishing helix radius their equations of motion coincide. We discuss the effects of a finite helix radius while focusing on two different aspects: the stability of the two prominent fixed points of the Kapitza pendulum, and the impact of a nonzero helix radius on the structure of the phase space and the corresponding dynamics. For a finite helix radius, the dynamics in the linearized neighborhood of the main fixed points can be approximated by a Mathieu equation with modified parameter values. From this, the general stability of both fixed points for different driving amplitudes  $E_0$ , static potential amplitudes  $V_0$ , and helix radii  $r$  have been determined analytically. These analytical results agree with those of corresponding numerical simulations. The latter show that the dynamics in the extended neighborhood of the fixed point at  $u = M\pi$  can change significantly for increasing  $r$ , whereas for the fixed point at  $u = 0$  no such changes could be observed. Specifically, the change in dynamics can be directly observed in the phase space, where for an increasing helix radius the fixed point at  $(u, p) = (M\pi, 0)$  can undergo an unusual transition to chaos. Additionally, two other prominent dynamical phases that only appear for finite helix radii have been discovered. These phases are characterized by the presence of multiple separate chaotic seas in the phase space. Especially notable is that the presence of multiple chaotic seas allows for chaotic particle trajectories with nonzero average velocity (i.e., directed transport), even though the spatiotemporal symmetries that are usually associated with a vanishing directed transport [here  $(u, p, t) \rightarrow (-u \text{Mod}(2M\pi), -p, t)$  and  $(u, p, t) \rightarrow (u, -p, -t)$ ] are not broken by the driving field. Notable are also the (quasi)periodic trajectories separating the two chaotic seas for small driving amplitudes and finite  $r$ , since they correspond to regular (directed) motion with very low momentum around the torus.

The observed dynamics in our driven helix to be seen as a generalized Kapitza pendulum is a direct consequence of the additional WIP appearing in the corresponding equations of motion. Some of the described effects are even occurring in parameter regimes where the WIP can be treated as a perturbation to the Kapitza pendulum. Therefore, an educated

guess would be that other periodic position-dependent small amplitude perturbations of the Kapitza pendulum will result in a dynamic similar to the one observed here. Consequently, we

expect that many of the described effects can be found, e.g., in a mechanical Kapitza pendulum with position-dependent length.

- 
- [1] K. L. Kohlstedt, F. J. Solis, G. Vernizzi, and M. O. de la Cruz, *Phys. Rev. Lett.* **99**, 030602 (2007).
  - [2] G. Vernizzi, K. L. Kohlstedt, and M. O. de la Cruz, *Soft Matter* **5**, 736 (2009).
  - [3] S. Srebnik and J. F. Douglas, *Soft Matter* **7**, 6897 (2011).
  - [4] K. T. Lau, M. Lu, and D. Hui, *Composites Part B* **37**, 437 (2006).
  - [5] N. M. Rodriguez, A. Chambers, and R. T. K. Baker, *Langmuir* **11**, 3862 (1995).
  - [6] A. Shaikjee and N. J. Coville, *J. Adv. Res.* **3**, 195 (2012).
  - [7] O. G. Schmidt and K. Eberl, *Nature (London)* **410**, 168 (2001).
  - [8] D. Reitz and A. Rauschenbeutel, *Opt. Commun.* **285**, 4705 (2012).
  - [9] M. Bhattacharya, *Opt. Commun.* **279**, 219 (2007).
  - [10] J. F. Marko and E. D. Siggia, *Macromolecules* **27**, 981 (1994).
  - [11] A. A. Kornyshev, D. J. Lee, S. Leikin, and A. Wynveen, *Rev. Mod. Phys.* **79**, 943 (2007).
  - [12] P. Schmelcher, *Europhys. Lett.* **95**, 50005 (2011).
  - [13] J. Stockhofe and P. Schmelcher, *Phys. Rev. A* **91**, 023606 (2015).
  - [14] Z. G. Yu and X. Song, *Phys. Rev. Lett.* **86**, 6018 (2001).
  - [15] A. V. Zampetaki, J. Stockhofe, S. Krönke, and P. Schmelcher, *Phys. Rev. E* **88**, 043202 (2013).
  - [16] A. V. Zampetaki, J. Stockhofe, and P. Schmelcher, *Phys. Rev. A* **91**, 023409 (2015).
  - [17] A. V. Zampetaki, J. Stockhofe, and P. Schmelcher, *Phys. Rev. E* **92**, 042905 (2015).
  - [18] A. V. Zampetaki, J. Stockhofe, and P. Schmelcher, *Phys. Rev. E* **95**, 022205 (2017).
  - [19] J. Plettenberg, J. Stockhofe, A. V. Zampetaki, and P. Schmelcher, *Phys. Rev. E* **95**, 012213 (2017).
  - [20] A. V. Zampetaki, J. Stockhofe, and P. Schmelcher, *Phys. Rev. E* **97**, 042503 (2018).
  - [21] A. Siemens and P. Schmelcher, *Phys. Rev. E* **102**, 012147 (2020).
  - [22] A. Siemens and P. Schmelcher, *Phys. Rev. E* **103**, 052217 (2021).
  - [23] P. L. Kapitza, *Usp. Fiz. Nauk* **44**, 7 (1951).
  - [24] E. I. Butikov, *Am. J. Phys.* **86**, 257 (2018).



# Formation and crossover of multiple helical dipole chains

Ansgar Siemens<sup>1</sup>  and Peter Schmelcher<sup>1,2,\*</sup> 

<sup>1</sup> Zentrum für Optische Quantentechnologien, Fachbereich Physik, Universität Hamburg, Luruper Chaussee 149, 22761 Hamburg, Germany

<sup>2</sup> Hamburg Center for Ultrafast Imaging, Universität Hamburg, Luruper Chaussee 149, 22761 Hamburg, Germany

E-mail: [asiemens@physnet.uni-hamburg.de](mailto:asiemens@physnet.uni-hamburg.de) and [pschmelc@physnet.uni-hamburg.de](mailto:pschmelc@physnet.uni-hamburg.de)

Received 31 May 2022, revised 29 July 2022

Accepted for publication 3 August 2022

Published 19 August 2022



CrossMark

## Abstract

We investigate the classical equilibrium properties and metamorphosis of the ground state of interacting dipoles with fixed locations on a helix. The dipoles are shown to align themselves along separate intertwined dipole chains forming single, double, and higher-order helical chains. The number of dipole chains, and their properties such as chirality and length scale on which the chains wind around each other, can be tuned by the geometrical parameters. We demonstrate that all possible configurations form a self-similar bifurcation diagram which can be linked to the Stern–Brocot tree and the underlying Farey sequence. We describe the mechanism responsible for this behavior and subsequently discuss corresponding implications and possible applications.

Keywords: classical mechanics, long-range interactions, bifurcations, dipolar interaction

(Some figures may appear in colour only in the online journal)

## 1. Introduction

Efforts of miniaturization of functional devices have been progressing steadily in the last decades. Due to advances in material science, it is now possible to manufacture a plethora of one-dimensional (1D) nano-materials for experimental use [1–7]. An especially intriguing class of 1D materials are chains of particles with permanent dipole moments, since it is possible to controllably encode information [8] and transfer energy along a linear chain [9–14] by exciting the orientation of the dipoles from an equilibrium state. It has also been shown that dipole

\*Author to whom any correspondence should be addressed.

chains can be assembled into logic gates [15], allowing to steer the energy transfer. Furthermore, simulations show that they could be used as waveguides that are able to transport signals below the diffraction limit [16–18], thereby overcoming size limits for guiding and modulating light. Realizing such quasi-1D molecular arrays in experimental studies is possible [19–21], for example through self-organization [22] or by artificial creation through various lithography methods [23]. Usually, the studies of molecular arrays focus on arrangements on planar surfaces or studies of bulk materials—with more sophisticated geometric configurations being much less explored. From a material science point of view, these more sophisticated structures can possess several advantages, such as the increased stability and resistance to deformation observed in helical nanostructures [24, 25]. Elaborate three-dimensional setups of permanent dipoles with significant (angular) mobility could for example be realized in frameworks which integrate dipolar rotors [26–31] into porous materials. In such materials, the orientation of rotors under the influence of external electric fields [30–33], as well as the emergence of ordered phases at low temperatures due to dipole–dipole interactions between rotors [28] have been demonstrated. The possible applications of such frameworks as molecular machines and sensors [34] has triggered many studies on their artificial fabrication—with the ultimate goal of creating a crystalline array of dipolar rotors that has a ferroelectric (FE) ground state (GS) at room temperature [35]. One example for such a class of materials are metal-organic frameworks (MOF) [36], which are materials consisting of inorganic building units (metal ions) that are linked with organic molecules. Specifically in the so-called rotor MOFs, these linkers can possess permanent quasi-free rotating dipole moments [37, 38], that could be arranged into arbitrary structures.

As a prototype model system for arrays of dipoles, we consider here a chain of equally spaced dipoles arranged along a helix. It has previously been shown, that the combination of long-range interactions and helical structures can lead to a variety of novel properties and dynamics [39–46], such as oscillating effective interaction potentials [39], band structure degeneracies [41, 42], or unusual transport properties in the presence of a driving field [46]. Specifically dipoles in helical geometries have been studied in lattice models with long-range hopping [47], and in classical setups with fixed dipole orientations [48].

Motivated by the interesting effects found in the above works on model systems, we investigate here the configurations of a helical dipole chain with fixed positions of the dipoles and find the GS to exhibit multiple crossovers between states that consist of a tunable number of superimposed helical dipole chains that wind around each other with either positive or negative chirality. Employing geometrical considerations that have previously been relevant in the field of Phyllotaxis [49], we determine the underlying phase diagram and classify the resulting self-similar bifurcation diagram using fractions of the Farey sequence. The organizational principles of this emergent order and transitions between the occurring phases are explored.

### 1.1. Helical dipole chains

Our setup (see figure 1(a)) consists of dipoles placed on a helix with radius  $\rho$  and pitch  $h$ . The location of the  $n$ th particle is then given by the following parameterization

$$\mathbf{r}_n := \begin{pmatrix} \rho \cos(n \Delta) \\ \rho \sin(n \Delta) \\ h n \Delta / 2\pi \end{pmatrix}, \quad (1)$$

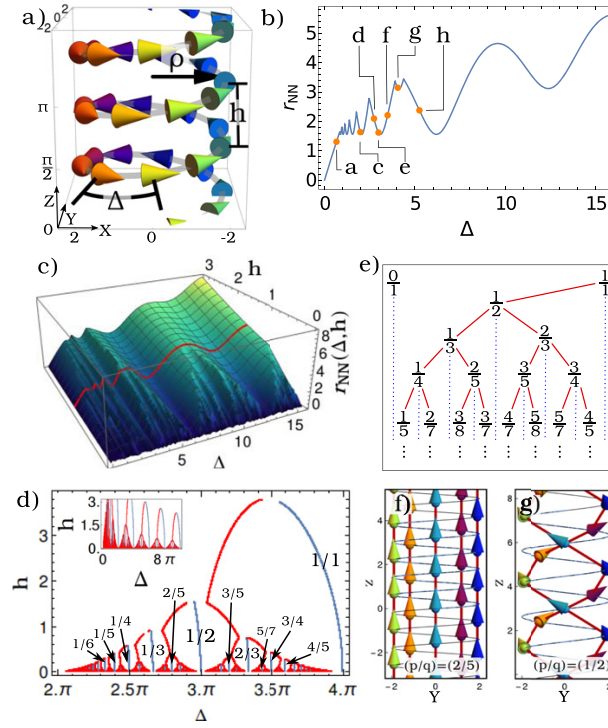


**Figure 1.** (a) Visualization of the helical dipole chain and parameters for a helix radius  $\rho = 2$ , a helix pitch  $h = \pi/2$  and angular dipole-distance  $\Delta = 0.21\pi$ . Coloring indicates the position within a winding. (b) Euclidean distance  $r_{NN}$  to the NN for  $h = \pi/2$  and  $\rho = 2$  as a function of the dipole-distance  $\Delta$ . Configurations corresponding to the orange points are visualized in sub-figure 1(a) and in sub-figures 2(d)–(i). (c) Euclidean distance of NNs  $r_{NN}$  as a function of the dipole-distance  $\Delta$  and helix pitch  $h$ . The red line corresponds to configurations of figure 1(b). (d) Bifurcation tree that shows the minima (blue) and maxima (red) of cross-sections of  $r_{NN}(h, \Delta)$  for various  $h$ , corresponding to the valleys (blue) and ridges (red) of  $r_{NN}(h, \Delta)$  in (c). The fractions  $(p/q)$  classify the configurations between ridges. Note that the gaps in the drawing close to the bifurcation points reflect the subtle transition in the number of maxima (ridges) which is accompanied by intermediates of non-smooth derivatives. The inset depicts these extrema for a larger parameter regime. (e) Visualization of the Stern–Brocot tree. (f) and (g) Transition between a  $(2/5)$  and a  $(1/2)$  state by increasing the helix pitch  $h$  from 0.8 to 1.5. Connections between NNs are indicated by red lines.

where  $\Delta$  is the angular distance between two dipoles along the helix. We consider an all-to-all dipole interaction. The interaction potential experienced by the  $n$ th dipole is then given by

$$V_n = \sum_{i=-\infty, i \neq n}^{\infty} \frac{1}{4\pi} \left[ \frac{\mathbf{d}_i \cdot \mathbf{d}_n}{r_{in}^3} - \frac{3(\mathbf{d}_i \cdot \mathbf{r}_{in})(\mathbf{d}_n \cdot \mathbf{r}_{in})}{r_{in}^5} \right], \quad (2)$$

where  $\mathbf{d}_i$  is the dipole moment of the  $i$ th dipole in the chain and  $\mathbf{r}_{in} = \mathbf{r}_i - \mathbf{r}_n$  is the separation vector between the dipoles  $i$  and  $n$  and  $r_{in}$  is the corresponding magnitude. It should be noted,

that due to the embedding of the dipoles in three-dimensional space, the nearest neighbor (NN) in Euclidean space does not necessarily agree with the corresponding next neighbor along the helical chain. As a result the alignment of the dipoles depends inherently on the geometrical parameters ( $\rho$ ,  $h$ ) of the helix and the chosen dipole angular spacing  $\Delta$ .

Our setup is scale invariant in the sense that for a given ratio of  $\rho/h$ , changes in the dipole strength  $|\mathbf{d}_i|$  or helix radius  $\rho$  only scale the potential energy given by equation (2) but do not lead to new equilibria. This allows us to normalize the helix radius  $\rho$ , as well as the dipole moments  $\mathbf{d}_i$ . Without loss of generality, we therefore set  $\rho = 2$  and  $|\mathbf{d}_i| = 1$ . The relevant parameters describing our system are then  $h$  and  $\Delta$ . If not explicitly stated otherwise, we focus on GS configurations. These presented GS configurations of our many-body dipolar system are obtained as follows: first the GS is approximated by optimizing the energy with a simulated annealing method while constraining the dipole alignment to the surface of the cylinder spanned by the helix. Using the resulting configuration as an initial condition, the GS is found through optimization with a principal axis method.

### 1.2. Phyllotaxis in cylindrical geometries

The considered system of equidistant particles on a 1D helix can also be interpreted as a cylindrical lattice where all lattice points can be accessed by a single generating helix. This set of cylindrical lattices has been studied in the past, and has been especially relevant in the field of Phyllotaxis [49]—the study of the arrangement of lateral organs in plants. In the context of Phyllotaxis, geometrical aspects of these lattices are used to explain the emergence of mathematical sequences, such as the Fibonacci sequence or the Lucas sequence in nature, e.g., in the arrangement of the scales of pine cones or pineapples. Patterns similar to those that emerge in phyllotactic systems can also be used to classify the GS configurations in our helical dipole chain. We will now give a brief overview of the phyllotactic patterns emerging directly from the geometry of the setup.

To understand these phyllotactic patterns, it is necessary to understand the so-called parastichy helices [50]. The parastichy helices are the secondary helices connecting all lattice points that can be reached by translation along the two shortest lattice vectors; either the NN vector  $\mathbf{r}_{NN}$  or the next-nearest neighbor (NNN) vector  $\mathbf{r}_{NNN}$ . In nature, such as e.g. for the scales of pine cones, parastichy helices are usually much easier to visually identify than the underlying generating helix. Due to the lattice site indexing defined in equation (1), the index  $n$  of the lattice sites changes by a constant integer  $s$  when translating along  $\mathbf{r}_{NNN}$  and by a constant integer  $q$  when translating along  $\mathbf{r}_{NN}$ . In Phyllotaxis (and the physical systems where similar geometrical considerations become important [51–54]), it is these parastichy numbers  $s$  and  $q$  that are usually used to demonstrate mathematical sequences that govern the behavior of cylindrical lattices as a function of the parameters  $h$  and  $\Delta$ . However, as we will show, in our setup the NNN interaction becomes negligible for large parameter regions (compare figures 2(a)–(c)). Consequently, it can happen that  $s$  changes, while our GS remains qualitatively unchanged when  $h$  and  $\Delta$  are varied. To uniquely classify the GS configurations of our helical dipole chains, we therefore need to deviate from the standard Phyllotaxis notation and classify the lattice configuration with the parameter  $q$ .

To understand how the NN index  $q$  can describe arbitrary GS configurations of helical dipole chains, it is instructive to first focus on the case of  $h = \pi/2$  and inspect the Euclidean distance  $r_{NN}$  of NNs for varying  $\Delta$  shown in figure 1(b). When increasing  $\Delta$  by starting at  $\Delta = 0$ ,  $r_{NN}$  first increases almost linearly, and changes to an oscillatory behavior showing cusps at the maxima once  $r_{NN}$  exceeds the helix pitch  $h$ . The cusp-like maxima of  $r_{NN}(\Delta)$  correspond to sudden changes of the NN—and therefore to sudden changes of  $q$ . The overall behavior of  $r_{NN}$

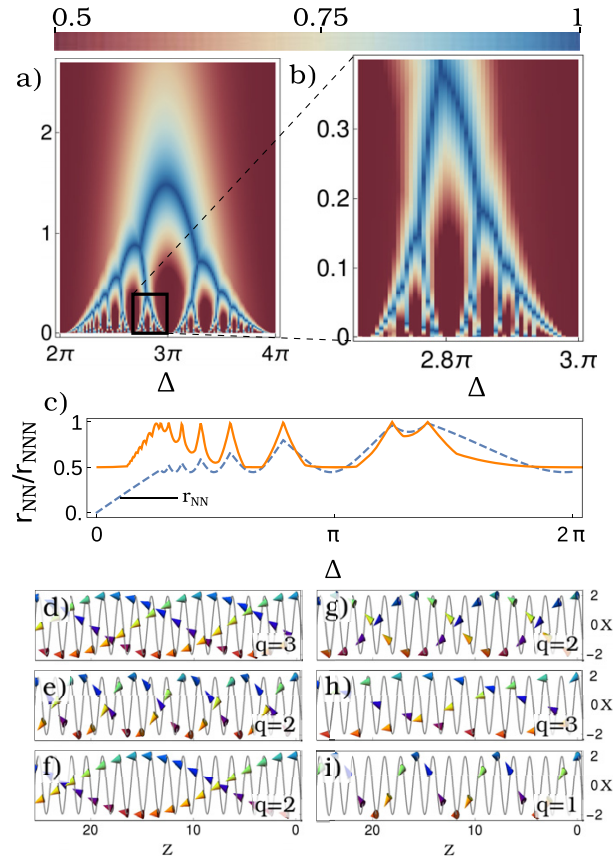


**Figure 2.** (a) Ratio ( $r_{NN}/r_{NNN}$ ) of the NN to the NNN distance as a function of  $h$  and  $\Delta$ . Interaction between different chains is (mostly) negligible in the red regions. (b) Zoom-in on (a). (c) Cross-section of  $r_{NN}/r_{NNN}$  for  $h = \pi/2$  along  $\Delta$ . The maxima of  $r_{NN}/r_{NNN}$  coincide with the maxima of  $r_{NN}$  (dashed blue line). The width of the peaks of  $r_{NN}/r_{NNN}$  are proportional to  $h \Delta$ . (d)–(i) Side views of example configurations for  $\Delta = 0.63\pi, 0.87\pi, 0.95\pi, 1.11\pi, 1.29\pi, 1.67\pi$  respectively. The angular position of the dipoles within a helix winding, and thereby the chirality of the chains is encoded in the color. The parameter  $q$  corresponds to the number of chains.

for arbitrary  $h$  is similar to the above description for  $h = \pi/2$ . The NN distance as a function of  $h$  and  $\Delta$  i.e.  $r_{NN}(\Delta, h)$  is shown in figure 1(c). For reference, the intersection corresponding to figure 1(b) is highlighted by a red line. For any cross-section with constant  $h$  we observe, that once  $r_{NN}$  exceeds  $h$ , the behavior changes from an almost linear increase to an oscillation with cusp-like maxima. In general, the number of extrema in each cross-section increases with decreasing  $h$ . Again, configurations with different parastichy number  $q$  are separated by the maxima of the cross section. Consequently, configurations for different values of  $q$  are separated by the ridges of  $r_{NN}(\Delta, h)$ . The positions of the ridges and valleys of  $r_{NN}$  (i.e. positions of the minima and maxima of cross-sections of  $r_{NN}(h, \Delta)$  for different  $h$ ) are shown in the inset of figure 1(d) for a broad range of values of  $h$  and  $\Delta$ . We immediately recognize that their

behavior follows a series of self-similar bifurcation trees. Each of the ‘trees’ is confined to a region of  $2\pi m \leq \Delta \leq 2\pi(m+1)$  (for  $m \in \mathbb{N}$ ) and the overall behavior is the same for all the trees. They characterize the same set of lattices—just with a different parameterization of the generating helix. In the  $m$ th tree, there are  $m-1$  empty windings without dipoles between next neighbor lattice sites along the helix (i.e. sites  $n$  and  $n+1$ ). On close examination, the trees differ in shape mainly by a scaling factor  $1/\Delta$ . This allows us to focus our analysis on a single tree. The structure of one such tree is shown figure 1(d). Several features can be noticed here: for decreasing  $h$ , each ridge splits via a pitchfork bifurcation into a new valley and two ridges. When a new valley appears below a certain threshold value of  $h$ , it persists further for arbitrarily small values of  $h$ . In contrast, each ridge will only persist for some finite range of  $h$  before separating into a valley and two new ridges.

The classification of the parameter regions between the extrema of  $r_{NN}(h, \Delta)$  with integers  $q$  follows a pattern. Firstly, when considering the  $m$ th tree, for each (reduced) fraction  $(p/q) \in [m, m+1]$  we can find a parameter region classified by a parastichy number  $q$  that for  $h \rightarrow 0$  contracts towards  $\Delta = 2\pi(p/q)$  (shown in figure 1(d)). Secondly, during a bifurcation of a ridge that separates a  $(p_1/q_1)$  state from a  $(p_2/q_2)$  state, the newly created state after the bifurcation can be described by the reduced fraction  $(p_1 + p_2)/(q_1 + q_2)$ . This is the same rule that generates new elements in the so-called Farey sequence [55]. And indeed, the possible configurations  $(p/q)$  map exactly to the elements of the Farey sequence: with decreasing  $h\Delta$  the Farey sequence is replicated to a higher order. For a better overview, the generic structure of the bifurcation tree is shown in figure 1(e). The resulting tree is also known as the Stern–Brocot tree—a tree representation of the Farey sequence.

An intuitive understanding for the corresponding lattice configurations can be gained by considering the  $m$ th tree and the limit case of the circle ( $h = 0$ ). Placing dipoles on a circle with progressing angular winding of  $\Delta = 2\pi(m-1 + p/q)$  will provide  $q$  points on the simple circle  $[0, 2\pi]$  with a distance of  $2\pi/q$ . Therefore, for every rational number  $(p/q)$  there exists a pitch  $h_0$  so that for  $h \leq h_0$  a helical GS configuration classified by the fraction  $(p/q)$  can be found. The number of possible configurations  $(p/q)$  decreases with increasing  $h$ . The reason, why certain  $(p/q)$  states only persist for finite values of  $h$  is illustrated in figures 1(f) and (g). In both figures the angular positions of the dipoles are the same while  $h$  is varied. The NN’s are indicated by red connecting lines. Figure 1(f) depicts a  $(2/5)$  state for  $h = 0.8$ . Above a certain value of  $h$ , the NN suddenly changes leading to the  $(1/2)$  state shown in figure 1(g) for  $h = 1.5$ .

The Farey sequence, as well as geometric considerations similar to the ones above, have previously been employed in the description of physical systems, including layered superconductors [52], repulsively interacting cylindrical lattices [51], and the domain wall dynamics in a magnetic cactus [53, 54]. However, there are notable differences between the helical dipole chains and other Phyllotaxis related works, such as the above mentioned examples. In Phyllotaxis and related works, usually only those configurations with the closest packing density are of interest—corresponding to the ridges of  $r_{NN}(h, \Delta)$ . The configurations in between those ridges may (depending on the employed model) be accessible, but do not correspond to any equilibrium configuration. Consequently, in these works, it is the classification of these closest packing configurations which follows the Stern–Brocot tree and maps to the fractions of the Farey sequence.

Before continuing with the physics of interacting dipoles in helical geometries, a comment on the choice of coordinate system is in order. Using the geometrical parameters  $h$  and  $\Delta$  allows to uniquely describe all possible cylindrical lattices of interest. In contrast, such a unique description of classifications is not achieved with all coordinate systems. Using e.g. the ratio of primitive lattice vector magnitudes and the angle between those vectors is not sufficient,

since in that case additional information relating the magnitude of one lattice vector to the circumference of the cylinder is required.

### 1.3. Phyllotactic patterns in ground-state configurations of helical dipole chains

In this section, we will use the geometrical considerations and classification scheme provided above to describe the GS configurations of the helical dipole chains for arbitrary  $h$  and  $\Delta$ . These GS configurations are for a large range of parameters dominated by NN interactions. This is demonstrated in figure 2(a), which shows the ratio  $r_{NN}/r_{NNN}$  of NN to NNN distances as a function of  $h$  and  $\Delta$ . Comparing this to the bifurcation tree in figure 1(d), we realize that the NNN interaction only becomes significant close to the maxima of  $r_{NN}$ . The cross section for  $h = \pi/2$  in figure 2(c) shows that the ratio  $r_{NN}/r_{NNN}$  possesses pronounced peaks; in between those peaks flat regions emerge. In the flat regions, an asymptotic saturation tendency towards the value of 0.5 can be observed (the relation  $r_{NN}/r_{NNN} \geq 0.5$  is guaranteed by the symmetric arrangement of dipoles within a single chain). As indicated by figure 2(b), this behavior continues for arbitrary low  $h$ . This dominance of NN interactions allows us to directly translate the classification of lattice configurations with fractions of the Farey sequence to our helical dipole chain GS configurations whenever  $r_{NN} \ll r_{NNN}$ .

Examples for various GS configurations in regimes of dominating NN interactions are shown in figures 2(d)–(i). In these GS configurations, the dipoles generally align themselves with their NN's along several intertwined helical chains. Due to the symmetrical arrangement of dipole positions within a chain, dipoles will align in the plane spanned by the helix axis ( $z$ -axis) and the tangent vector  $d\mathbf{r}_n/d\Delta$ . These intertwined helical dipole chains map exactly to the first parastichy helix. Therefore, the number of intertwined helical chains corresponds directly to the integer  $q$  of the underlying lattice classification  $p/q$ . In addition to controlling the number of chains  $q$ , changing  $h$  and  $\Delta$  also allows to control the dipole density along the chain, as well as the length scale  $\lambda$  (wavelength) on which the chains wind around each other. This change of  $\lambda$  with varying  $\Delta$  can be clearly seen in figures 2(e)–(g). In figure 2(f), close to the minimum of  $r_{NN}$ , NN dipoles show very gradual changes across the chain, thereby exposing the character of each separate chain. For smaller (larger) values of  $r_{NN}$ , the chains wind clockwise (counterclockwise) around each other (see figures 2(e) and (g)). When  $\Delta$  is increased further, such that  $r_{NN}$  crosses a maximum, the GS configuration changes from counterclockwise chirality to a new set of chains with clockwise chirality.

The classification ( $p/q$ ) allows us to determine an analytical expression for the dipole alignments in a NN approximation. For a given state ( $p/q$ ) and a given helix geometry  $h$  and  $\Delta$ , the angle  $\phi$  between the dipoles and the helix axis ( $z$ -axis) is (approximately) given by the following equation:

$$\phi(\Delta, h) = -\tan^{-1} \left[ \frac{hq\Delta}{2\pi\rho \sin(q\Delta)} \right] \pm \frac{\pi}{2}, \quad (3)$$

where the term  $\pm\pi/2$  selects an alignment parallel (+) or anti-parallel (−) to the helix axis. The accuracy of this approximation is demonstrated in figure 3. As a representative example for the comparison shown in figure 3, we consider a cross section through our parameter space with constant helix pitch  $h$  and varying  $\Delta$ . The analytically approximated angles together with the corresponding angles obtained from numerical calculations are shown in figure 3(b) for  $h = 0.3$  and  $\Delta \in [2\pi, 3\pi]$ . Discontinuities (jumps) in the angle occur at the maxima of  $r_{NN}$  (compare figure 3(a)) when the configuration changes to a state with a different classification ( $p/q$ ). Within each of the regions where the angle changes smoothly the classification ( $p/q$ ) does not change. The difference between the two data-sets is for the most part very small.

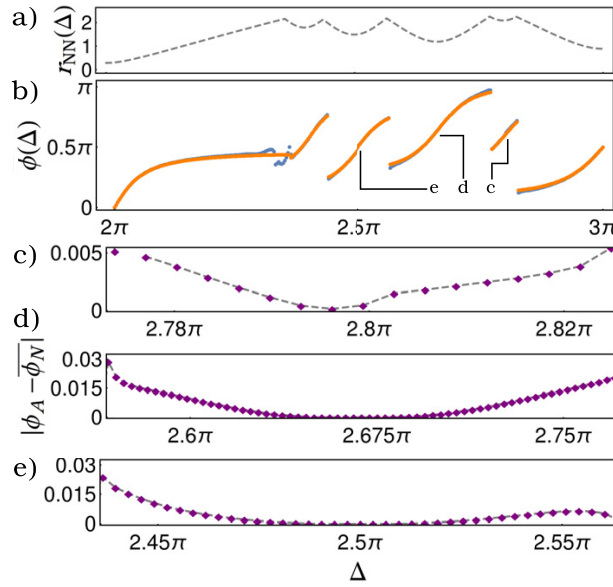


**Figure 3.** (a) Distance to the NN  $r_{NN}(\Delta)$  for  $\Delta \in [2\pi, 3\pi]$  and  $h = 0.3$ . (b) The analytically predicted angle  $\phi$  (orange) compared to the numerically determined value (blue). Note that, to minimize edge defects, the numerical value corresponds to the average angle of dipoles from the bulk. Smooth regions are classified by the same fraction  $(p/q)$ , whereas large jumps in  $\phi(\Delta)$  indicate a change to a configuration classified by a different fraction  $(p/q)$ . (c)–(e) The absolute difference  $|\phi_A - \phi_N|$  between the numerically and analytically determined angle for three of the regions with smoothly changing angle, i.e. three parameter ranges corresponding to parameter regions with different classification  $(p/q)$ .

However, visible deviations consistently occur close to the maxima of  $r_{NN}$ . For a more detailed comparison of the deviations between the analytically and numerically determined angles, we show in figures 3(c)–(e) their absolute difference for three of the ‘smooth’ regions of figure 3(b), i.e. three regions with different classifications  $(p/q)$ . In each of the three figures, the absolute difference between the analytically predicted and numerically calculated angles are shown. Close to the minima of  $r_{NN}$  the analytical predictions are very accurate. With increasing distance from this minimum the error increases and reaches a maximum close to the maximum of  $r_{NN}$ . This is expected, since equation (3) is based on the fraction  $(p/q)$  which is not well-defined for configurations in the immediate vicinity of the maxima of  $r_{NN}$ . This behavior can be summarized as follows: when the length scale on which the dipole chains wind around each other increases, the accuracy of the analytically predicted angles also increases.

#### 1.4. Significance of interactions between chains

The interaction with NNN’s can have significant effects on the dipole alignments in the GS—even in those parameter regimes where  $r_{NNN} \ll r_{NN}$ . For parameter combinations where the NN interaction dominates, the NNN interaction still influences the relative alignment of the helical dipole chains to each other. They determine whether dipoles in neighboring chains are

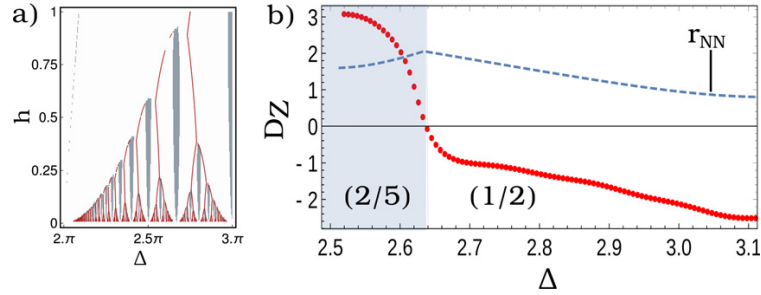


**Figure 4.** (a) Classification of dipole alignments in the GS: in the white regions, a FE alignment is preferred, whereas anti-ferroelectric (AFE) configurations are preferred in the gray regions, corresponding to configurations with very large wavelengths. For comparison, the bifurcation tree is shown in red. (e) Projected dipole density  $D_Z$  along the helix axis (red) during a transition between a  $(2/5)$  (blue area) and a  $(1/2)$  (white area) state. For better identification of the transition state (i.e. maximum of  $r_{NN}$ ),  $r_{NN}$  is shown as a blue dotted line.

aligned parallel (FE) or antiparallel (AFE) to each other. To study this, we compare the energies of FE and AFE states. As shown in figure 4(a) for a specific parameter region, the AFE alignment is energetically favorable in the vicinity of  $\Delta \approx 2\pi(p/q)$  and sufficiently small  $h$ . For smaller wavelengths, the FE alignment becomes favorable. Note that the FE and AFE configurations, based on which the energies in figure 4(a) were calculated, are obtained with the analytical formula given in equation (3) and not through numerical optimization.

Additionally, figure 2(a) suggests that close to the ridges of  $r_{NN}$  the NNN interaction becomes significant enough for the dipole configurations to deviate from the pure  $(p/q)$  classification. To analyze this, we consider the transition between states for different values of  $(p/q)$ . As a representative example, we choose the transition from a  $(2/5)$  to a  $(1/2)$  state. It is achieved by varying  $\Delta$  between  $\Delta = 2\pi(2/5)$  and  $\Delta = 2\pi(1/2)$ . In our simulations, this was done by changing  $\Delta$  in steps of 0.001 and then relaxing the configuration with a Newton method. As a matter of fact, this transition leads to a drastic change from clockwise to counterclockwise chirality and vice versa. The transition could therefore result in a noticeable change of the dipole orientations. To analyze this, we introduce the projected dipole density  $D_Z = \sum_i^N 2\pi(\mathbf{d}_i \cdot \hat{\mathbf{e}}_Z)/hN\Delta$ . For our example case,  $D_Z$  as a function of  $\Delta$  is shown in figure 4(b). Note, that since close to the transition state the FE alignment of neighboring chains is preferred we only consider FE configurations to study this transition.

In the course of the transition,  $D_Z$  inverts its sign. Exactly at the maximum of  $r_{NN}$ ,  $D_Z$  is zero. The dipoles behave as follows: at  $\Delta = 2\pi(2/5) \approx 2.513$  all dipoles are parallel to the helix axis. With increasing  $\Delta$ , the position of the NN changes and the angle between the dipole and the helix axis increases. Once  $r_{NN}/r_{NNN}$  significantly deviates from 0.5 and the NNN interaction becomes significant, the dipoles increasingly turn towards their NNN in the sense of a head-to-tail configuration. When  $r_{NN}$  reaches a maximum, the dipoles are all aligned perpendicular to the helix axis. When  $\Delta$  is increased further, the same behavior can be seen in reverse order until  $\Delta = \pi$  is reached.

## 2. Discussion and outlook

We have demonstrated that equilibrium configurations of helical dipole chains consist of a variable number of tunable dipole chains winding around each other with either positive or negative chirality. We showed how these equilibrium configurations are directly characterized by fractions of the Farey sequence, and how a variation of the helical parameters yields a metamorphosis of these equilibrium states into each other. The observed chain formations, as well as the presence of FE and AFE GS configurations is consistent with previous studies [56–58] of GSs of classical dipoles in 2D lattices.

The formation of chains is explained with the dominance of NN interactions over NNN interactions. Therefore, an educated guess would be that the mechanical and electrical response properties, as well as the information and energy transfer upon excitation is governed by the sum of the properties of these individual chains. More complex behavior is only expected in those regimes where the NNN interactions become comparable to the NN interactions (and the classification scheme with fractions of the Farey sequence breaks down).

In experimental realizations of the setup, the dipole alignments will most likely additionally depend on effects other than the geometrical constraints considered in our model system. A realization with the above mentioned MOFs will for example feature additional constraints [36] on the dipole rotations: for one, certain rotation angles may be preferred due to the so-called torsion potential (an effective potential that can possess multiple minima as a function of the rotation angle). For another, the significant rotation of linkers in MOFs is typically only possible around one rotation axis while rotations around different axes are strongly constrained. Furthermore, with the present state of the art regarding arrays of dipolar rotors, significant cooling is required for the dipole–dipole interactions to dominate over temperature effects. Finally, finite size effects could also play a significant role for any experimental realization: however, in our numerical calculations a significant deviation of dipole alignments from the bulk could only be observed for the first few dipoles of each chain.

### Data availability statement

No new data were created or analysed in this study.

### ORCID iDs

Ansgar Siemens  <https://orcid.org/0000-0003-0454-2512>

Peter Schmelcher  <https://orcid.org/0000-0002-2637-0937>

### References

- [1] Rodriguez N M, Chambers A and Baker R T K 1995 Catalytic engineering of carbon nanostructures *Langmuir* **11** 3862–6
- [2] Lau K T, Lu M and Hui D 2006 Coiled carbon nanotubes: synthesis and their potential applications in advanced composite structures *Composites B* **37** 437–48
- [3] Lan Y, Wang Y and Ren Z F 2011 Physics and applications of aligned carbon nanotubes *Adv. Phys.* **60** 553–678
- [4] Samuelson L *et al* 2004 Semiconductor nanowires for 0D and 1D physics and applications *Physica E* **25** 313–8

- [5] Iijima S and Ichihashi T 1993 Single-shell carbon nanotubes of 1 nm diameter *Nature* **363** 603–5
- [6] Ivanov V *et al* 1994 The study of carbon nanotubes produced by catalytic method *Chem. Phys. Lett.* **223** 329–35
- [7] Shaikjee A and Coville N J 2012 The synthesis, properties and uses of carbon materials with helical morphology *J. Adv. Res.* **3** 195–223
- [8] Vedmedenko E Y and Altwein D 2014 Topologically protected magnetic helix for all-spin-based applications *Phys. Rev. Lett.* **112** 017206
- [9] DeLeeuw S W, Solvaeson D, Ratner M A and Michl J 1998 Molecular dipole chains: excitations and dissipation *J. Phys. Chem. B* **102** 3876–85
- [10] Sim E, Ratner M A and de Leeuw S W 1999 Molecular dipole chains II *J. Phys. Chem. B* **103** 8663–70
- [11] de Jonge J J, Ratner M A, de Leeuw S W and Simonis R O 2004 Molecular dipole chains III: energy transfer *J. Phys. Chem. B* **108** 2666–75
- [12] de Jonge J J, Ratner M A and de Leeuw S W 2007 Local field controlled switching in a one-dimensional dipolar array *J. Phys. Chem. C* **111** 3770–7
- [13] Zampetaki A, Salas J P and Schmelcher P 2018 Energy transfer mechanisms in a dipole chain: from energy equipartition to the formation of breathers *Phys. Rev. E* **98** 022202
- [14] Fateev E G 2002 Supersensitivity in a chain of closely spaced electric dipoles with variable moments *Phys. Rev. E* **65** 021403
- [15] de Jonge J J, Ratner M A, de Leeuw S W and Simonis R O 2006 Controlling the energy transfer in dipole chains *J. Phys. Chem. B* **110** 442–6
- [16] Kornovan D F, Baryshnikova K V and Petrov M I 2020 Suppression of high-order multipole moments in a resonant periodic dipole chain *J. Phys.: Conf. Ser.* **1461** 012070
- [17] Maier S A, Kik P G and Atwater H A 2003 Optical pulse propagation in metal nanoparticle chain waveguides *Phys. Rev. B* **67** 205402
- [18] Brongersma M L, Hartman J W and Atwater H A 2000 Electromagnetic energy transfer and switching in nanoparticle chain arrays below the diffraction limit *Phys. Rev. B* **62** R16356–9
- [19] Huang Y L, Wang R, Niu T C, Kera S, Ueno N, Pflaum J, Wee A T S and Chen W 2010 One dimensional molecular dipole chain arrays on graphite via nanoscale phase separation *Chem. Commun.* **46** 9040
- [20] Jérôme R, Creuzet F and Bourbonnais C 1989 A survey of the physics of organic conductors and superconductors *Phys. Scr.* **1989** 130–5
- [21] Weckesser J, De Vita A, Barth J V, Cai C and Kern K 2001 Mesoscopic correlation of supramolecular chirality in one-dimensional hydrogen-bonded assemblies *Phys. Rev. Lett.* **87** 096101
- [22] Schnadt J *et al* 2008 Extended one-dimensional supramolecular assembly on a stepped surface *Phys. Rev. Lett.* **100** 046103
- [23] Hersam M C, Lee J, Guisinger N P and Lyding J W 2000 Implications of atomic-level manipulation on the Si(100) surface: from enhanced CMOS reliability to molecular nanoelectronics *Superlattices Microstruct.* **27** 583–91
- [24] Kornyshev A A, Lee D J, Leikin S and Wynveen A 2007 Structure and interactions of biological helices *Rev. Mod. Phys.* **79** 943–96
- [25] Marko J F and Siggia E D 1994 Bending and twisting elasticity of DNA *Macromolecules* **27** 981–8
- [26] Bracco S, Beretta M, Cattaneo A, Comotti A, Falqui A, Zhao K, Rogers C and Sozzani P 2015 Dipolar rotors orderly aligned in mesoporous fluorinated organosilica architectures *Angew. Chem., Int. Ed.* **54** 4773–7
- [27] Zhao K, Dron P I, Kaleta J, Rogers C T and Michl J 2014 Arrays of dipolar molecular rotors in tris(o-phenylenedioxy)cyclotriphosphazene *Molecular Machines and Motors: Recent Advances and Perspectives (Topics in Current Chemistry vol 354)* ed A Credi, S Silvi and M Venturi (Berlin: Springer) pp 163–211
- [28] Su Y-S *et al* 2021 Dipolar order in an amphidynamic crystalline metal-organic framework through reorienting linkers *Nat. Chem.* **13** 278–83
- [29] Winston E B, Lowell P J, Vacek J, Chocholeušová J, Michl J and Price J C 2008 Dipolar molecular rotors in the metal-organic framework crystal IRMOF-2 *Phys. Chem. Chem. Phys.* **10** 5188
- [30] Horansky R D *et al* 2006 Dipolar rotor–rotor interactions in a difluorobenzene molecular rotor crystal *Phys. Rev. B* **74** 054306
- [31] Horansky R D, Clarke L I, Price J C, Khuong T A V, Jarowski P D and Garcia-Garibay M A 2005 Dielectric response of a dipolar molecular rotor crystal *Phys. Rev. B* **72** 014302

- [32] Vacek J and Michl J 2001 Molecular dynamics of a grid-mounted molecular dipolar rotor in a rotating electric field *Proc. Natl. Acad. Sci. USA* **98** 5481–6
- [33] Horinek D and Michl J 2003 Molecular dynamics simulation of an electric field driven dipolar molecular rotor attached to a quartz glass surface *J. Am. Chem. Soc.* **125** 11900–10
- [34] Kottas G S, Clarke L I, Horinek D and Michl J 2005 Artificial molecular rotors *Chem. Rev.* **105** 1281–376
- [35] Michl J and Sykes E C H 2009 Molecular rotors and motors: recent advances and future challenges *ACS Nano* **3** 1042–8
- [36] Gonzalez-Nelson A, Coudert F-X and van der Veen M 2019 Rotational dynamics of linkers in metal-organic frameworks *Nanomaterials* **9** 330
- [37] Winston E B, Lowell P J, Vacek J, Chocholoušová J, Michl J and Price J C 2008 Dipolar molecular rotors in the metal-organic framework crystal IRMOF-2 *Phys. Chem. Chem. Phys.* **10** 5188
- [38] Bracco S, Castiglioni F, Comotti A, Galli S, Negroni M, Maspero A and Sozzani P 2017 Ultrafast molecular rotors and their CO<sub>2</sub> tuning in MOFs with rod-like ligands *Chem. Eur. J.* **23** 11210–5
- [39] Schmelcher P 2011 Effective long-range interactions in confined curved dimensions *Europhys. Lett.* **95** 50005
- [40] Zampetaki A V, Stockhofe J, Krönke S and Schmelcher P 2013 Classical scattering of charged particles confined on an inhomogeneous helix *Phys. Rev. E* **88** 043202
- [41] Zampetaki A V, Stockhofe J and Schmelcher P 2015 Degeneracy and inversion of band structure for Wigner crystals on a closed helix *Phys. Rev. A* **91** 023409
- [42] Zampetaki A V, Stockhofe J and Schmelcher P 2015 Dynamics of nonlinear excitations of helically confined charges *Phys. Rev. E* **92** 042905
- [43] Zampetaki A V, Stockhofe J and Schmelcher P 2017 Pinned-to-sliding transition and structural crossovers for helically confined charges *Phys. Rev. E* **95** 022205
- [44] Zampetaki A V, Stockhofe J and Schmelcher P 2018 Electrostatic bending response of a charged helix *Phys. Rev. E* **97** 042503
- [45] Siemens A and Schmelcher P 2020 Tunable order of helically confined charges *Phys. Rev. E* **102** 012147
- [46] Siemens A and Schmelcher P 2021 External-field-induced dynamics of a charged particle on a closed helix *Phys. Rev. E* **103** 052217
- [47] Wang Q, Otterbach J and Yelin S F 2017 Interacting in-plane molecular dipoles in a zigzag chain *Phys. Rev. A* **96** 043615
- [48] Pedersen J K, Fedorov D V, Jensen A S and Zinner N T 2014 Formation of classical crystals of dipolar particles in a helical geometry *J. Phys. B: At. Mol. Opt. Phys.* **47** 165103
- [49] Adler I, Barabe D and Jean V 1997 A history of the study of phyllotaxis *Ann. Bot.* **80** 231–44
- [50] Lee H W and Levitov L S 1998 Universality in phyllotaxis: a mechanical theory *Symmetry in Plants (Series in Mathematical Biology and Medicine vol 4)* (Singapore: World Scientific) pp 619–53
- [51] Levitov L S 1991 Energetic approach to phyllotaxis *Europhys. Lett.* **14** 533–9
- [52] Levitov L S 1991 Phyllotaxis of flux lattices in layered superconductors *Phys. Rev. Lett.* **66** 224–7
- [53] Nisoli C, Gabor N M, Lammert P E, Maynard J D and Crespi V H 2009 Static and dynamical phyllotaxis in a magnetic cactus *Phys. Rev. Lett.* **102** 186103
- [54] Nisoli C 2009 Spiraling solitons: a continuum model for dynamical phyllotaxis of physical systems *Phys. Rev. E* **80** 026110
- [55] Boeyens J C A and Levendis D C 2008 *Number Theory and the Periodicity of Matter* (Berlin: Springer)
- [56] Rozenbaum V M 1991 Orientation states of dipoles on 2D Bravais lattices *Sov. Phys. JETP* **72** 1028 <http://jetp.ras.ru/cgi-bin/e/index/e/72/6/p1028?a=list>
- [57] Feldmann J D, Kalman G J, Hartmann P and Rosenberg M 2008 Ground state of magnetic dipoles on a two-dimensional lattice: structural phases in complex plasmas *Phys. Rev. Lett.* **100** 085001
- [58] Brankov J G and Danchev D M 1987 Ground state of an infinite two-dimensional system of dipoles on a lattice with arbitrary rhombicity angle *Physica A* **144** 128–39

# Geometry induced domain-walls of dipole lattices on curved structures

Ansgar Siemens<sup>1,\*</sup>  and Peter Schmelcher<sup>1,2</sup> 

<sup>1</sup> Zentrum für Optische Quantentechnologien, Fachbereich Physik, Universität Hamburg, Luruper Chaussee 149, 22761 Hamburg, Germany

<sup>2</sup> Hamburg Center for Ultrafast Imaging, Universität Hamburg, Luruper Chaussee 149, 22761 Hamburg, Germany

E-mail: [asiemens@physnet.uni-hamburg.de](mailto:asiemens@physnet.uni-hamburg.de)

Received 23 May 2023; revised 20 October 2023

Accepted for publication 10 November 2023

Published 20 November 2023



CrossMark

## Abstract

We investigate the ground state (GS) properties of rectangular dipole lattices on curved surfaces. The curved geometry can ‘distort’ the lattice and lead to dipole equilibrium configurations that strongly depend on the local geometry of the surface. We find that the system’s GS can exhibit domain-walls separating domains with different dipole configurations. Furthermore, we show how, regardless of the surface geometry, the domain-walls (DWs) locate along the lattice sites for which the (Euclidean) distances to nearest and next-nearest neighbors are equal. We analyze the response of the DWs to an external electric field and observe displacements and splittings thereof below and above a critical electric field, respectively. We further show that the DW acts as a boundary that traps low-energy excitations within a domain.

Keywords: domain-walls, low-dimensional systems, dipolar interactions

(Some figures may appear in colour only in the online journal)

## 1. Introduction

Topology based concepts are widely used for the description of physical systems. A prominent example is that of domains and domain-walls (DWs) arising from spontaneous symmetry breaking, with applications ranging from optics, where DWs separate differently polarized regions [1, 2], to magnetic Bose–Einstein condensates [3], or even string theory [4]. Moreover, in materials or model systems described by lattices of interacting electric dipoles,

\* Author to whom any correspondence should be addressed.

the ground-state (GS) degeneracy of the dipoles, i.e. the invariance of the energy under inversion of all dipoles, can lead to the formation of local domains with different dipole orientations [5] separated by DWs. For lattices of electric dipoles (related to ferroelectrics (FEs)), experiments have shown a great controllability of these domains and DWs, allowing for their artificial creation, annihilation, or controlled shifts [6, 7]. This, together with the fact that long-range order of electric dipoles has been found at room temperature in a multitude of materials [8], has made FE materials interesting candidates for applications, such as smart sensors, capacitors, transducers, actuators, energy harvesting devices, and non-volatile memories [6, 7, 9, 10].

It has been shown that the application of strain to a FE material can be used to control the overall FE response, as well as the DW energy and mobility [11]. In some FE materials, the GS dipole configuration can even significantly change when the stress on the material exceeds a (material dependent) critical value—an effect known as ferroelasticity [5, 12–14]. The sudden change of the GS in ferroelastic materials usually emerges due to (compression-induced) changes of the underlying crystal structure. Consequently, the properties of strain-induced DWs in ferroelastic materials can drastically differ from the properties of DWs in FE materials [13].

Similar phenomenology can also be found in magnetic materials [15]. A difference between FEs and magnets is that the formation of domains in FEs is usually due to the dipole–dipole interaction, whereas in magnets other interactions, such as exchange processes [16], dominate the equilibrium dipole alignment. In this context, one notable interaction arising in some magnetic systems is the Dzyaloshinskii–Moriya (DM) interaction [17–19]: it allows for the formation of non-collinear spin structures, such as magnetic skyrmions [20–22], which have been proposed for applications [23–25] e.g. in high density storage devices [26, 27]. Studies of the influence of spatial curvature on magnetic materials (e.g. two-dimensional magnetic films on a spherical surface) have shown that curvature can effectively induce a DM type interaction and thereby significantly change the GS dipole configuration [28–30]. Naturally, the question arises: what is the influence of spatial curvature in FE materials where the material properties are dominated by dipole–dipole interactions.

The first steps in this direction were already done in studies of dipoles confined to cylindrical or helical geometries. These studies range from experimental investigations (e.g. of the dipole equilibrium configurations in stacks of BTA (trialkylbenzene-1,3,5-tricarboxamide) molecules [31, 32]) to model systems, such as Hubbard models with long-range hopping terms [33–37]. Already in such (comparatively) simple curved geometries, the GS properties show a strong dependence on the geometrical parameters: for example, for dipoles with fixed positions along a helical path, it was demonstrated that the GS configurations are described by a complex self-similar bifurcation diagram [38]. Even in systems without anisotropic interactions, such as Coulomb-interacting ions on a helix, the confinement to a curved path or surface embedded in Euclidean space induces a plethora of phenomena [39–47] that are absent in structures without curvature.

Motivated by the above facts, we focus on possible novel features introduced into model systems consisting of dipole lattices due to their curved structure. We start by explaining how the structural arrangement of dipoles influences the GS and can lead to DWs that are ‘pinned’ through geometrical parameters of the system. We investigate the static DW properties and their dependencies on system parameters for a two-dimensional prototype system, and highlight the differences to those DWs that are commonly observed in FE materials by showing the reaction of our DW to applied external fields. Then, using the example of a toroidal dipole lattice, we demonstrate and discuss the appearance of the previously introduced properties. It is further shown, how these DWs act as barriers that prevent low energy excitations from traveling freely through the system.

This work is structured as follows: Our setup and methodology for the dipoles on curved or deformed surfaces is described in section 2. Section 3 then explains the physics of domains and DWs on curved dipole lattices using a simple two-dimensional example system. In section 4, we explore and analyze the toroidal dipole lattice. Section 5 investigates the eigenmodes based on the GS of the toroidal dipole lattice and we show that DWs can act as ‘barriers’ preventing excitations from traveling through the system. Finally, our results are summarized in section 6.

## 2. General setup and methodology

We investigate the physics of dipoles placed on rectangular Bravais lattices spanned on the surface of curved structures (compare figure 1). In general, a curved surface, i.e. each point on it, can be completely described by a parametric function  $f(\theta, \phi)$  depending on two parametric coordinates  $\theta$  and  $\phi$  (being internal coordinates of the surface, not necessarily angles). For convenience we introduce  $\hat{\mathbf{e}}_\theta$  and  $\hat{\mathbf{e}}_\phi$  as unit vectors that span a basis in the parametric coordinates. These basis vectors are used to indicate directions along the surface. Without loss of generality, we define our lattice points to be equidistant in the parametric coordinates, with the parametric distances  $\Delta\theta$  and  $\Delta\phi$ . This way, the Euclidean distances, namely  $a = |\mathbf{a}|$  and  $b = |\mathbf{b}|$  (see figure 1), between neighboring lattice points along  $\hat{\mathbf{e}}_\theta$  and  $\hat{\mathbf{e}}_\phi$  become dependent on the local geometry of the surface,

$$\begin{aligned} a(\theta, \phi) &:= \|f(\theta + \Delta\theta, \phi) - f(\theta, \phi)\| \\ b(\theta, \phi) &:= \|f(\theta, \phi + \Delta\phi) - f(\theta, \phi)\|. \end{aligned} \quad (1)$$

This dependence of  $a$  and  $b$  on the local surface geometry will have immediate consequences on the arrangement (such as the orientation) of the dipoles placed in such a lattice. For instance at one point on the surface the (Euclidean) nearest neighbor (NN) of a dipole is reached through translation along  $\hat{\mathbf{e}}_\theta$ , while at another point the NN may be found along  $\hat{\mathbf{e}}_\phi$ . An example for this is shown in figure 1, where the ratio  $\gamma = a/b$  is one for the lattice point in the uppermost part of the figure (indicated by the blue dot marked  $\gamma = 1$ ), but visibly reaches values  $\gamma < 1$  for the lattice points in the right and lower part of the figure (indicated by the blue dots marked  $\gamma < 1$ ). As we will show in section 3, the properties of the many-body GS of dipoles in such a curved lattice depends mainly on this spatially varying ratio  $\gamma$ .

The dipoles on the lattice points interact with dipole–dipole interactions, and are in a second step exposed to an external electric field  $E$ . With this, the potential energy of the  $n$ th dipole in a lattice containing  $K$  dipoles is given by

$$V_n = \sum_{i=1, i \neq n}^K \frac{1}{4\pi} \left[ \frac{\mathbf{d}_i \mathbf{d}_n}{r_{in}^3} - \frac{3(\mathbf{d}_i \cdot \mathbf{r}_{in})(\mathbf{d}_n \cdot \mathbf{r}_{in})}{r_{in}^5} \right] + \mathbf{d}_n \cdot \mathbf{E} \quad (2)$$

where  $\mathbf{d}_i$  and  $\mathbf{d}_n$  are the dipole moments of the dipoles at lattice sites  $i$  and  $n$  respectively, and  $\mathbf{r}_{in}$  denotes the (Euclidean) vector between them.

For our computational approach to determine the GS configurations, we use local polar coordinates to describe the orientation of each dipole. Furthermore, since a change in the magnitude  $d = |\mathbf{d}|$  of the dipoles only leads to a scaling of the interaction term in equation (2), we will without loss of generality use  $d = 1$ . The dipole equilibrium configurations are determined using a principle axis method [48]—a derivative-free optimization method that performs line-search optimizations along a set of (continuously updated) conjugate search directions.

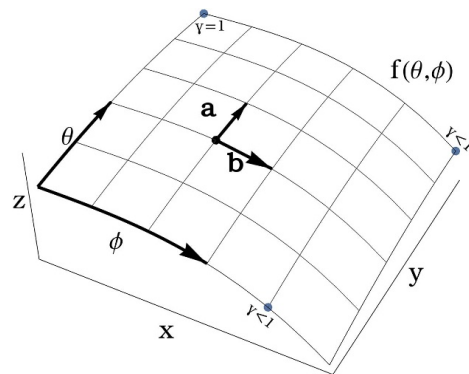


**Figure 1.** Example of a lattice spanned on a curved surface  $f(\theta, \phi)$ . As a result of the curvature, the Euclidean distances  $\mathbf{a}(\theta, \phi)$  and  $\mathbf{b}(\theta, \phi)$  between lattice points depend on the local geometry of the surface.

Specifically, we use Brent's algorithm which ensures linear independence of the search directions after they are updated. Unless explicitly stated otherwise, the results shown in the following correspond to GS configurations. Additionally, we use a NN approximation, i.e. considering only interactions with the 4 nearest dipoles. This approximation is valid as long as the lattice is dense enough to locally be considered flat. No qualitative differences were observed when comparing the NN approximations to all-to-all simulations. The validity of these approximations and the impact of interactions with more distant neighbors are discussed at appropriate places in the following.

### 3. DWs in deformed lattices

In the limit of a vanishing curvature (i.e. a flat surface) the GS dipole configuration is well known [49, 50]: The dipoles will align along head-to-tail chains with their NNs. In a rectangular (non-square) lattice, dipoles in neighboring chains (chains being defined along the shorter NN distance) will orient anti-parallel to one another in an overall anti-ferroelectric (AFE) configuration. Thus, the GS of a flat rectangular lattice cannot be a FE configuration [49, 51] when only dipole–dipole interactions are considered. In the special case of a square lattice ( $\gamma = 1$ ) the GS becomes highly degenerate [52]. Flat regions in the potential landscape allow for continuous transformations between these different GS configurations. The behavior is, however, entirely different for dipole arrays spanned on the surface of a curved or deformed structure. This section is dedicated to showing and discussing the behavior emerging when the lattice geometry becomes deformed. An application to a specific case, namely the toroidal dipole lattice is provided in section 4.

A simple flat geometry showcasing the impact of deformation is given by the following parametric surface

$$f_{2D}(\theta, \phi) := \begin{pmatrix} \theta \\ \theta \cdot \tan[\phi] \\ 0 \end{pmatrix} \quad (3)$$

where  $-\pi/2 < \phi < \pi/2$ . Adopting the nomenclature introduced in section 2, we place dipoles on the surface while maintaining constant distances  $\Delta\theta$  and  $\Delta\phi$  in the parametric coordinates. Note that  $\Delta\phi$  is considered to be small, i.e.  $\Delta\phi \ll \pi/2$ , in order to provide a sufficiently large number of lattice points along  $\hat{\mathbf{e}}_\phi$ . The system now describes a ‘lattice’ which narrows with decreasing  $\theta$ . The positions of the lattice points for dipoles on a  $(N \times (2M + 1))$  grid are given by

$$f_{2D}^{ik} := \begin{pmatrix} i\Delta\theta \\ i\Delta\theta \cdot \tan[k\Delta\phi] \\ 0 \end{pmatrix} \text{ for } \begin{cases} i \in [1, N] \\ k \in [-M, M] \end{cases} . \quad (4)$$

We also restrict the dipoles to rotate in the plane spanned by equation (3). A schematic visualization of the lattice based on equation (4) is shown in figure 2(a). Note that the surface defined in equation (3) possesses a singularity and will map all lattice points for  $\theta = 0$  (independent of  $\phi$ ) to the same position in Euclidean space. We will therefore only consider lattice points in the regime  $\theta > 0$ .

As mentioned in section 2, the GS dipole orientation mainly depends on  $\gamma = a/b$ . An interesting observation is that, for the lattice spanned by equation (4),  $\gamma$  becomes independent of  $\Delta\theta$ . This is because both  $\mathbf{a}$  and  $\mathbf{b}$  scale linearly with  $\Delta\theta$ . It can be directly shown that  $\gamma \rightarrow 0$  when  $\theta \rightarrow \infty$ . Furthermore, it can be shown that for any given point  $f_{2D}^{ik}$  in the lattice one can get  $\gamma > 1$  when  $\Delta\phi$  is chosen sufficiently small. We know that in regions where  $\gamma > 1$  the most favorable alignment of the dipoles will be head-to-tail chains along  $\hat{\mathbf{e}}_\phi$ . On the contrary, if  $\gamma < 1$  the chains will preferably align along  $\hat{\mathbf{e}}_\theta$ . This implies—provided  $\Delta\phi$  is sufficiently small—the presence of two domains with different dipole alignments in the GS. This results in the existence of a DW acting as a boundary between the two domains. Such a GS configuration exhibiting the two domains, as well as the separating DW, is shown in figure 2(b). As expected, the two domains for small and large values of  $\theta$  feature AFE dipole configurations aligned along  $\hat{\mathbf{e}}_\phi$  and  $\hat{\mathbf{e}}_\theta$  respectively. To characterize the DW, we focus on those dipoles located along a one-dimensional (1D) cut through the lattice. The cut is taken at constant  $\phi = 0$ , perpendicular to the DW. In figure 2(b) this cut is indicated by the red arrow. As an order parameter, we choose the (absolute) angle  $\chi$  between the dipoles and the direction of the 1D cut.

$$\chi = |\arccos(\mathbf{d} \cdot \hat{\mathbf{e}}_\theta|_{\phi=0})|, \quad (5)$$

where  $\hat{\mathbf{e}}_\theta|_{\phi=0}$  is the unit vector along  $\hat{\mathbf{e}}_\theta$  for  $\phi = 0$ . In the domain for large  $\theta$  (right of the DW in figure 2(b)) we approach  $\chi = 0$ , whereas in the domain for small  $\theta$  values we approach  $\chi = \pi/2$ . The angle  $\chi$  as a function of the local value of  $\gamma$  for all dipoles along the 1D cut is shown in figure 2(c) (orange-colored points). The blue and purple colored points correspond to calculations with lattices where the change of  $\gamma$  along the 1D cut (denoted by  $\Delta\gamma$ ) is smaller than in the orange curve. The solid lines correspond to a fitting sigmoid function given by

$$\Phi(\gamma) = \frac{\pi}{2 + 2e^{-\xi(\gamma(\theta) - \gamma_0)}}, \quad (6)$$

where  $\xi$  is the sigmoid steepness and  $\gamma_0$  is the value of  $\gamma$  at the midpoint of the sigmoid function. From now on, we will refer to this midpoint as the position of the DW center. In the DW profiles shown in figure 2(c), the DW center is located (almost exactly) at  $\gamma = 1$ . The deviation from  $\gamma = 1$  is of the order of  $\sim 0.01\Delta\theta$ —only a fraction of the lattice constant  $\Delta\theta$ . We determined DW profiles for a wide range of  $\Delta\phi$  and did not observe any significant deviation of the DW center from  $\gamma = 1$ . Note, that the exact location of the DW at  $\gamma = 1$  was only observed for NN interactions. When all-to-all interactions are considered, a shift of the DW center towards  $\gamma < 1$  was observed. The largest observed shift of the DW center from  $\gamma = 1$  was on the order of  $\sim \Delta\theta$ . From figure 2(c) one can see that the DW steepness (corresponding to the fit-parameter

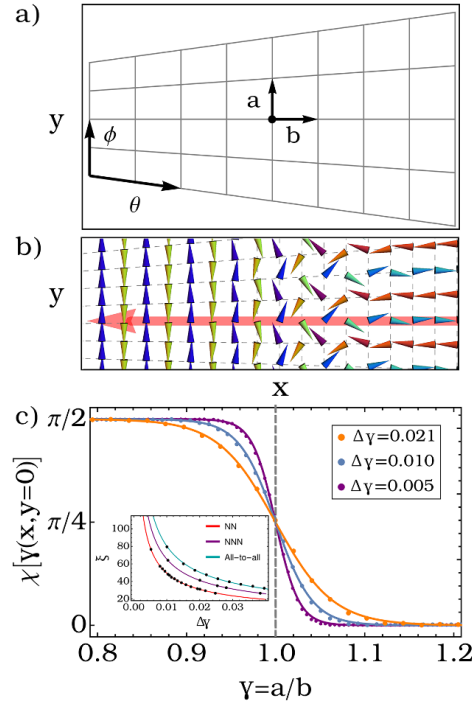


**Figure 2.** (a) Schematic visualization of a lattice spanned on the surface defined by equation (3) together with the lattice defined by equation (4). (b) GS configuration of dipoles on the lattice defined by equation (4) showing two domains separated by a DW. The red arrow indicates a one-dimensional cut through the lattice running perpendicular to the DW. (c) DW profiles obtained from the dipoles located along the one-dimensional cut (red arrow in (b)).  $\chi$  describes the angle between the dipoles and the direction of the one-dimensional cut.  $\gamma = a/b$  is the corresponding (local) ratio of the Euclidean distances to the NNs. The orange, blue, and purple curves are obtained for lattices with  $\Delta\gamma = 0.021$ , 0.01, and 0.005 respectively—with  $\Delta\gamma$  being defined as the change of  $\gamma$  between two successive dipoles along the one-dimensional cut. The inset depicts the dependency of the sigmoid steepness  $\xi$  on  $\Delta\gamma$  for calculations with nearest (red), next-nearest neighbors (purple), and all-to-all interactions (green). For a detailed discussion, see main text.

$\xi$  in equation (6) is larger for those lattices where  $\Delta\gamma$  is smaller: A comparison of the fit parameter  $\xi$  for different values of  $\Delta\gamma$  is shown in the inset of figure 2(c) for NN, next-NN (NNN), and all-to-all simulations. The only significant difference between the NN, NNN, and all-to-all data is that the DWs are consistently narrower when more interactions are considered. Consequently, DWs obtained for a given  $\Delta\gamma$  from NN and NNN calculations are wider than corresponding DWs calculated for the same  $\Delta\gamma$  with all-to-all interactions. Besides this, no qualitative differences could be observed for the DWs. For NN, NNN and all-to-all interactions the DW steepness  $\xi$  scales (approximately) with  $\xi \sim (\Delta\gamma)^{-0.67}$  (purple, red, and green fit-functions in the inset of figure 2(c)).

The above discussed geometry induced DW differs significantly from other known types of FE DWs: Firstly, it is a feature of the systems GS (i.e. not an excitation) with a (fixed)

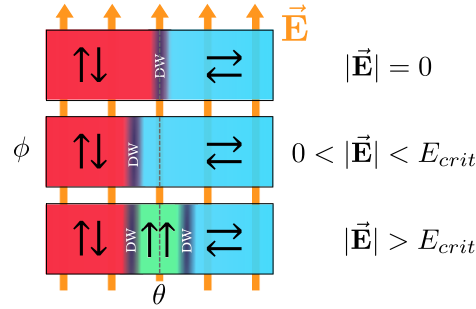


**Figure 3.** Schematic explaining how the equilibrium dipole orientations change around  $\gamma = 1$  when an electric field is applied along the  $y$ -direction (parallel to  $\hat{e}_\phi$ ). For  $|\vec{E}| = 0$ , there are two domains with dipoles aligned along  $\hat{e}_\theta$  and  $\hat{e}_\phi$  (respectively corresponding to the blue and red regions) separated by a DW (purple area between the domains). When  $|\vec{E}|$  is increased, the domain with dipoles aligned along  $\hat{e}_\theta$  expands, while the domain with dipoles aligned along  $\hat{e}_\phi$  shrinks. As a result, the DW is shifted. When the field is increased further—above a critical value  $E_{crit}$ —a new ferroelectric domain with dipoles aligned parallel to the field (green area in the lowest panel) emerges.

position that is predetermined by the geometry of the underlying lattice and surface. A second difference concerns the overall response to applied external electric fields. To illuminate the latter, we briefly address the impact of a field applied along the  $y$ -direction (parallel to  $\hat{e}_\phi$ ) using an adiabatic method: the field strength is increased stepwise, and at each step the configuration is relaxed with a Newton method that takes into account NNN interactions.

A schematic demonstrating the effects of the external field on the dipole orientations in the vicinity of the DW (i.e. in the vicinity of  $\gamma = 1$ ) is shown in figure 3. The behavior can be summarized as follows: For weak fields, the DW separating the two domains shifts to a new equilibrium position. For strong fields, a (new) third domain emerges (green area in figure 3). The dipoles in this third domain are aligned parallel to the field. This third domain will expand with increasing field strength towards both lower and larger values of  $\theta$ . We can explain this behavior in the context of dipoles in square (non-deformed) Bravais lattices (with a global  $\gamma = 1$ ): In such square lattices, the external field breaks the GS degeneracy and orients the dipoles along the field lines—in an AFE (FE) configuration for weak (strong) fields [53]. In other words: in a lattice with  $\gamma = 1$  the dipoles do not have a preferred alignment direction (w.r.t. the primitive lattice vectors) and therefore require on average (compared to lattices with  $\gamma \neq 1$ ) weaker fields to align all dipoles in a FE configuration along an arbitrary direction. This is consistent with the behavior observed in figure 3. Namely, for strong fields the dipoles around  $\gamma = 1$  form a FE domain parallel to the field—even though the field is not strong enough to significantly affect the dipole orientations in the neighboring domains.

#### 4. Toroidal dipole lattice

In the previous section, we have shown how the GS configuration of a deformed dipole lattice can be predicted based on the ratio  $\gamma = a/b$ . To demonstrate that this behavior is of a more general character and can also be observed in compact curved or deformed dipole lattices, we now demonstrate the formation of domains and DWs for a square dipole lattice spanned on the surface of a torus. A schematic of the setup is provided in figure 4(a) together with a

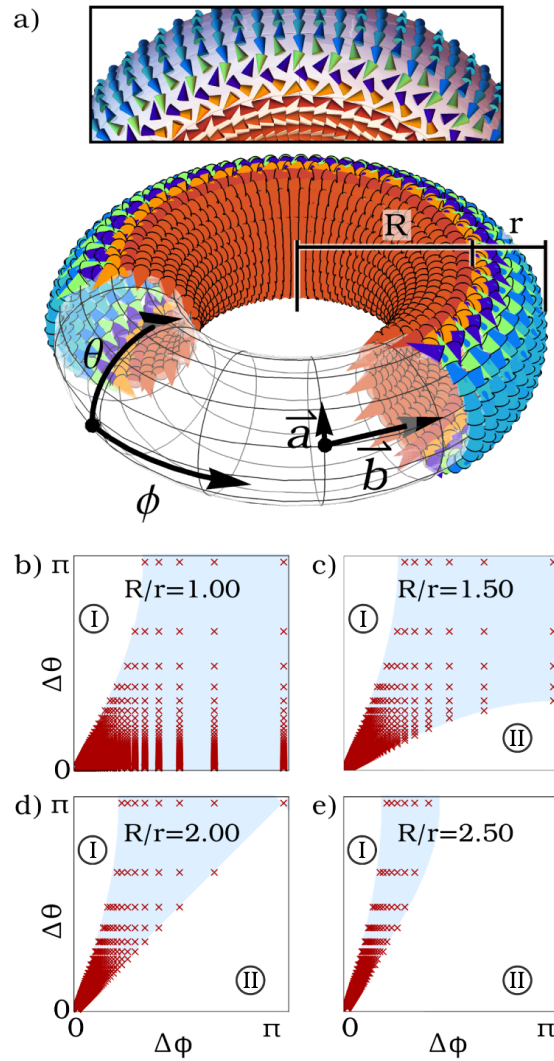


**Figure 4.** (a) Schematic representation of the toroidal lattice geometry and parameters, together with the GS for a dipole lattice with  $R/r = 2.5$ ,  $\Delta\theta = 2\pi/30$ , and  $\Delta\phi = 2\pi/80$ . Dipole orientations are shown with colored cones. Coloring varies from red (dipoles aligned along  $\phi$ ) to blue (dipoles aligned along  $\theta$ ). The upper panel depicts a top-view to better showcase the dipole orientations. For reasons of illustration the lattice constants chosen for the schematic do not exactly correspond to the shown GS. (b)–(d) Cross sections through the parameter space for various values of  $R/r$ . Inside the blue colored regions the inequality defined in equation (10) is fulfilled. Red crosses mark valid parameter combinations (i.e. parameters that fulfill the toroidal boundary conditions) for which we expect a DW in the GS.

corresponding GS dipole configuration. The torus surface can be described by the following parametric function

$$f_i(\theta, \phi) := \begin{pmatrix} (R + r \cos(\theta)) \cos(\phi) \\ (R + r \cos(\theta)) \sin(\phi) \\ r \sin(\theta) \end{pmatrix}, \theta, \phi \in [0, 2\pi] \quad (7)$$

where  $R$  and  $r$  respectively describe the major and minor radius of the torus. Due to the periodic boundary conditions enforced by the toroidal geometry, the lattice constants  $\Delta\theta$  and  $\Delta\phi$  for a lattice with dimension  $(N \times M)$  are given by

$$\begin{aligned} \Delta\theta &= 2\pi / (N + 1) \\ \Delta\phi &= 2\pi / (M + 1). \end{aligned} \quad (8)$$

Similar to the previous example system, the Euclidean distance of lattice points is constant along  $\hat{e}_\theta$ , whereas the lattice point distance along  $\hat{e}_\phi$  depends on  $\theta$ . Specifically, the Euclidean distance  $b$  between lattice points along the major torus radius direction increases with increasing distance from the torus center. The distances  $a$  and  $b$  can be analytically expressed as follows

$$\begin{aligned} a^2 &= 2r^2 [1 - \cos(\Delta\theta)] \\ b^2(\theta) &= 2(R + r \cos(\theta))^2 [1 - \cos(\Delta\phi)]. \end{aligned} \quad (9)$$

The positions of the lattice points of a lattice with dimension  $(N \times M)$  are then given by  $f_i(i\Delta\theta, k\Delta\phi)$  for  $i \in [1, N]$  and  $k \in [1, M]$ .

We start by discussing the parameter values for which DWs and domains appear on the torus. In the limit of  $a < b$  (i.e.  $\gamma < 1$ ), the dipoles will align in an AFE configuration parallel to  $\hat{e}_\theta$ . In the limit of  $a > b$  (i.e.  $\gamma > 1$ ), the dipoles will align in an AFE configuration parallel to  $\hat{e}_\phi$ . The presence of both domains is expected when  $\text{Min}[b(\theta)] < a < \text{Max}[b(\theta)]$ . Since the maximum and minimum of  $b$  are reached for  $\theta = 0$  and  $\theta = \pi$  respectively, the condition for the presence of two domains can be expressed as

$$\left(\frac{R}{r} - 1\right)^2 < \frac{[1 - \cos(\Delta\theta)]}{[1 - \cos(\Delta\phi)]} < \left(\frac{R}{r} + 1\right)^2. \quad (10)$$

It should be noted that fulfilling the above inequality is a necessary, but not a sufficient condition for the presence of two domains in the GS. In case the area on the torus where  $\gamma > 1$  (or  $\gamma < 1$ ) tends to zero (this will happen for  $a \searrow \text{Min}[b(\theta)]$  or  $a \nearrow \text{Max}[b(\theta)]$ ) the GS will feature only a single domain—even though the inequality equation (10) is fulfilled.

The inequality equation (10) depends on  $\Delta\theta$ ,  $\Delta\phi$ , and the ratio of the torus radii  $R/r$ . Figures 4(b)–(e) show for  $R/r \in [1, 1.5, 2, 2.5]$  the combinations of  $\Delta\theta$  and  $\Delta\phi$  for which equation (10) is fulfilled (blue areas). Values in the regime  $R/r < 1$  are not considered, since they correspond to configurations where the torus surface intersects itself. The subset of parameters that satisfy the toroidal boundary conditions are marked by red crosses in figures 4(b)–(e). An example for a GS configuration for  $R/r = 2.5$ ,  $\Delta\theta = 2\pi/30$ , and  $\Delta\phi = 2\pi/80$  (well within the region specified by equation (10)) can be seen in figure 4(a). Configurations outside of the blue regions in figures 4(b)–(e) consist of a single domain of dipoles covering the complete torus and being aligned either along  $\hat{e}_\theta$  or  $\hat{e}_\phi$  [regions marked I or II in figures 4(b)–(e) respectively]. For configurations within the blue region, the position of the DW can be controlled through the choice of  $\Delta\theta$  and  $\Delta\phi$ . For parameters within the blue region but close to the border with region I, a narrow domain of dipoles aligned along  $\hat{e}_\theta$  will appear on the outer side of the torus. In the blue region and close to the border with region II the domain of dipoles

aligned along  $\hat{e}_\theta$  will encompass almost the entire torus, whereas the domain of dipoles aligned along  $\hat{e}_\phi$  will only consist of a narrow band around the torus center.

The DW separating the two domains in the toroidal dipole lattice is reminiscent of the DW described in section 3: the DW separates regions with  $\gamma = a/b > 1$  from regions with  $\gamma < 1$ . As one may expect, the orientation of the dipoles in the DW is also similar to the 2D case of section 3: the dipoles in the DW align in a ‘zig-zag’ pattern similar to what we have observed in figure 2(b). Indeed, the order parameter  $\chi$  (along a 1D cut along  $\hat{e}_\theta$ ) can be well-described by a sigmoid function. However, in our toroidal dipole lattice, we notice a deviation from the behavior of the DW in the 2D lattice: The DW center is not exactly at the position where  $\gamma = 1$ , but rather shifted w.r.t. it; for the example system shown in figure 4(a), it is located at  $\gamma \approx 0.96$ —a difference of about  $\Delta\theta/2$  on the surface.

In addition to the GS properties, the corresponding response to an external electric field can also be observed in our toroidal dipole lattice. We would like to stress that the purpose of investigating the influence of electric fields is to highlight the difference to other (e.g. degeneracy induced) DWs in FEs and not an attempt at an in-depth study of the field response in itself. We consider therefore the configuration shown in figure 4(a) and apply a field along the torus plane ( $x$ -direction). Simulation results for the case of such a field are shown in figure 5. Just like for the flat lattice of section 3, a weak field causes a shift of the DW center towards the region where dipoles are aligned (anti-) parallel to the field. This is shown in figure 5(a), where the position of the DW center is indicated by the solid line on the torus surface. To highlight the deformation, the position of the DW center without external field is indicated by the gray dotted line. In the regime of strong fields, the emergence of new FE domains around  $\gamma = 1$  can also be observed. These new domains emerge in those regions where the DW center has shifted the most from its original (field-free) position and expand from there when the field strength is increased. The formation of one of these FE domains is visualized in figure 5(b). In the figure, the field strength does not quite suffice to force perfect FE order: rather than perfect head-to-tail chains, the dipoles in the highlighted region align in a zig-zag pattern along parallel chains (see black arrows in figure 5(b)). Even larger field strengths are required for these zig-zag chains to straighten into a head-to-tail alignment. However, for the considered parameters any further increase of the field strength will result in the entire outer domain aligning parallel to the field.

## 5. Domain-localized excitations

We investigate in the following the dynamics of low energy excitations of the dipole orientations for the toroidal dipole lattice. We will demonstrate a tendency of these excitations to remain confined within the boundaries of a domain, i.e. these excitations will not spread or finally cover the entire torus. Low energy excitations are treated on basis of a harmonic approximation to the total potential energy using NN interactions. Specifically, the potential energy landscape around the GS is approximated with a second order Taylor series. The first order terms of the series vanish by definition, since the GS corresponds to a minimum of the potential. Consequently, only the second order terms will contribute to the equations of motion. The orientation of each dipole in Euclidean space is described by local polar coordinates, i.e. a polar and azimuthal angle denoted  $\mu$  and  $\nu$ , respectively. We will use the shorthand notation  $\mathbf{X} = (\mu_1, \dots, \mu_K, \nu_1, \dots, \nu_K)$  to describe the dipole configuration. Using this notation, the GS

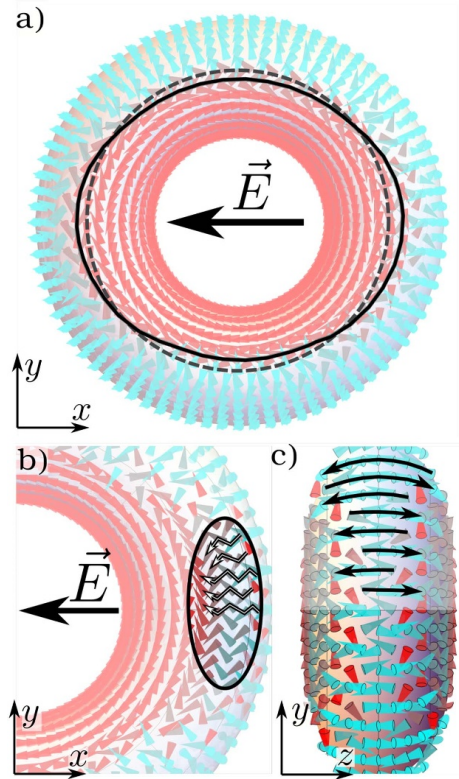


**Figure 5.** Equilibrium configurations for the toroidal dipole lattice in the regime of (a) weak and (b) and (c) strong external electric fields. Coloring indicates orientation along  $\hat{e}_\theta$  (blue) and  $\hat{e}_\phi$  (red). (a) Weak electric fields cause an elliptic deformation of the DW-region. The solid (dashed) line indicate the position of the DW center for weak fields (no field). (b) and (c) Top and side view for a strong field. Dipoles in the highlighted region in (b) align along parallel zig-zag chains. These zig-zag chains will straighten into FE head-to-tail chains when the field strength is further increased. The side-view in (c) shows the FE domain on the outside of the torus.

will be referred to as  $\mathbf{X}_0 = (\mu_1^0, \dots, \mu_K^0, \nu_1^0, \dots, \nu_K^0)$ . In this case the linearized equations of motion for the polar and azimuthal angle of the  $n$ th dipole are approximated as follows

$$\begin{aligned} d^2 \mu_n / dt^2 &= \sum_i^K \left[ \frac{\partial^2 V_n(\mathbf{X})}{\partial \nu_i \partial \mu_n} \Big|_{\mathbf{X}_0} \nu_i + \frac{\partial^2 V_n(\mathbf{X})}{\partial \mu_i \partial \mu_n} \Big|_{\mathbf{X}_0} \mu_i \right] \\ d^2 \nu_n / dt^2 &= \sum_i^K \left[ \frac{\partial^2 V_n(\mathbf{X})}{\partial \nu_n \partial \mu_i} \Big|_{\mathbf{X}_0} \mu_i + \frac{\partial^2 V_n(\mathbf{X})}{\partial \nu_i \partial \nu_n} \Big|_{\mathbf{X}_0} \nu_i \right] \end{aligned} \quad (11)$$

where  $n$  is the index of the dipole, and  $V_n$  is the corresponding potential energy as defined in equation (2). For small amplitude motion (with angles  $\alpha \leq 5^\circ$ ) around the GS the electromagnetic fields induced by the dipole motion can be neglected—as long as the NN distances are much smaller than  $c\pi/2\alpha\omega$ , where  $c$  is the speed of light and  $\omega$  is the frequency of the dipole.

This condition is derived from the ratio between the radiated and the ‘static’ components of the electric field of an oscillating dipole [54]. To put that into context: if we assume a NN distance on the nanometer scale, the emitted electromagnetic wave can be neglected as long as the dipole oscillation are frequencies much smaller than  $\omega \ll 10^{19} \text{ s}^{-1}$ . Assuming only low energy excitations, the solutions to equation (11) take the form of spatiotemporal harmonic oscillations, allowing the problem to be written as an eigenvalue equation of the form

$$\frac{d^2}{dt^2} \begin{pmatrix} \vec{\mu} \\ \vec{\nu} \end{pmatrix} = \omega^2 \begin{pmatrix} \vec{\mu} \\ \vec{\nu} \end{pmatrix} = \mathcal{H} \begin{pmatrix} \vec{\mu} \\ \vec{\nu} \end{pmatrix}, \quad (12)$$

where  $\mathcal{H}$  is the Hessian matrix of second derivatives of  $V_n(\mathbf{X})$  evaluated at  $\mathbf{X}_0$ , and  $\vec{\mu} = \{\delta\mu_1, \dots, \delta\mu_{N \times M}\}^T$ ,  $\vec{\nu} = \{\delta\nu_1, \dots, \delta\nu_{N \times M}\}^T$  are vectors containing the deviations of polar and azimuthal angles from the GS equilibrium configuration for all dipoles in the lattice. Eigenmodes of the system then correspond to the eigenvectors of the Hessian: for each eigenmode, the components of the eigenvector describe the oscillation amplitude for each lattice point on the torus. The corresponding eigenfrequencies are given by the square root of the corresponding eigenvalues of the Hessian.

An example of an eigenmode that is confined entirely to the inner domain is shown in figure 6(a). In order to characterize the eigenmodes we define the alignment variation at each lattice point as the (absolute) angular rotation of the dipole from its GS orientation  $|\cos^{-1}[\mathbf{d}(i\Delta\theta, k\Delta\phi) \cdot \mathbf{d}_0(i\Delta\theta, k\Delta\phi)]|$ . We can obtain a distribution  $\Lambda(i\Delta\theta)$  of the eigenmode through summation of the alignment variation along the  $\phi$ -direction

$$\Lambda(i\Delta\theta) = \sum_k |\cos^{-1}[\mathbf{d}(i\Delta\theta, k\Delta\phi) \cdot \mathbf{d}_0(i\Delta\theta, k\Delta\phi)]|. \quad (13)$$

An example for such a distribution  $\Lambda(i\Delta\theta)$  is shown on the right side of figure 6(a). The mean (designated  $\Lambda_o$ ) and variance of the distribution  $\Lambda(i\Delta\theta)$  provide a quantitative measure of the region to which an eigenmode is confined. Note that we define  $\Lambda_o$  by the distance to the outermost part of the torus, such that  $\Lambda_o = 0$  ( $\Lambda_o = \pi$ ) if the mean is located at the outermost (innermost) point of the torus. We analyzed the distributions  $\Lambda(i\Delta\theta)$  for all eigenmodes and find that each eigenmode is confined to a specific region on the torus surface. This allows a classification of the eigenmodes into three types of excitations: excitations confined to the inner domain, the outer domain, or excitations of the DW. The  $\Lambda_o$  of all eigenmodes are shown in figure 6(b), together with the corresponding eigenfrequencies. A discernible pattern is that  $\Lambda_o$  increases with the eigenfrequency, i.e. low frequency modes have a  $\Lambda_o$  located at the outer domain, whereas large frequency modes have a  $\Lambda_o$  located at the inner domain. Eigenmodes with a  $\Lambda_o$  located on the DWs can be found mainly for intermediate frequencies. The relation between  $\omega$  and  $\Lambda_o$  can be explained as follows: Compared to the outer domain, dipoles in the inner domain interact stronger with their neighbors (due to smaller NN distances). Consequently, dipoles in the outer domain require more energy to significantly change their orientation than dipoles in the inner domain. The result are low frequency oscillations in the outer, and large frequency oscillations in the inner domain. It is worth mentioning that excitations of the DW manifest mainly as sinusoidal deformations, resulting in star-shaped excitations on the torus, similar to those observed in e.g. Bose Einstein condensates [55] or magnetic skyrmions [56]. Examples for these DW excitations are shown in figures 6(d)–(f).

The confinement of eigenmodes to certain regions of the torus surface effectively prevents arbitrary small energy excitations from exploring the torus beyond the boundary of the DW; i.e. excitations started in the inner (outer) domain will never lead to a significant motion in the

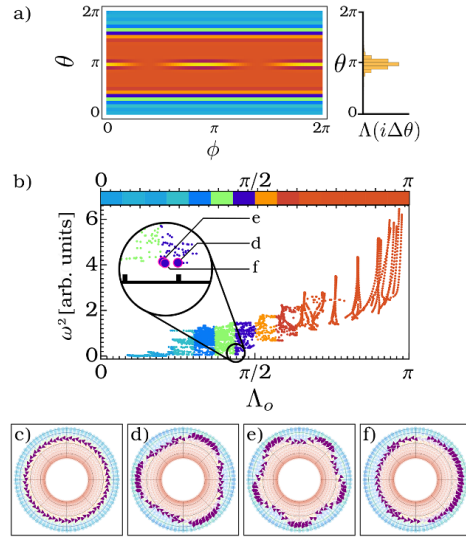


**Figure 6.** (a) Example visualization of the dipole orientations when an eigenmode is excited. Each position  $(\theta, \phi)$  is colored according to the orientation of the closest dipole. The color-function is the same as in figure 4, with blue and red colors respectively corresponding to dipoles oriented along  $\hat{\mathbf{e}}_\theta$  and  $\hat{\mathbf{e}}_\phi$ . The dipoles that are significantly excited by the eigenmode, located in the inner domain at  $\theta \approx \pi$ , appear as yellow islands. The corresponding distribution  $\Lambda(i\Delta\theta)$  on the right has been determined according to equation (13). (b) Squared eigenfrequencies  $\omega^2$  as a function of  $\Lambda_o$  (defined as the mean position of  $\Lambda(i\Delta\theta)$ ). Coloring corresponds to the position of  $\Lambda_o$  on the torus: Red (blue) colored points indicate that  $\Lambda_o$  is located in the inner (outer) domain. (c) Top-view of the GS of a toroidal dipole lattice with  $r = 0.4$ ,  $\Delta\theta = 2\pi/30$  and  $\Delta\phi = 2\pi/80$ . (d)–(f) Top-views of eigenmodes corresponding to excitations of the DW of the state shown in (c). The frequencies and localization of the eigenmodes shown in (d)–(f) are also highlighted in the zoom-in in (b).

outer (inner) domain. This can be demonstrated by simulating the time evolution of perturbations of the GS. In practice, this is done by expressing an initial excitation as a linear combination of eigenmodes, and letting the eigenmodes oscillate with their respective eigenfrequencies. Specifically, using the notation  $\mathbf{E}_i, i \in \{i | i \in \mathbb{Z}, 1 \leq i \leq 2K\}$  to refer to the  $2K$  eigenvectors, the time evolution of any initial small amplitude excitation  $\delta\mathbf{X}(t) = \mathbf{X}_{\text{ex}}(t) - \mathbf{X}_0$  can be expressed analytically as

$$\delta\mathbf{X}(t) = \sum_i^{2K} \cos(\omega_i t) [\delta\mathbf{X}(0) \cdot \mathbf{E}_i] \cdot \mathbf{E}_i / E_i^2, \quad (14)$$

where  $\omega_i$  is the eigenfrequency corresponding to the eigenvector  $\mathbf{E}_i$ . In the following, we will consider two examples where the initial excitation  $\delta\mathbf{X}(0)$  is a unit vector with a single non-zero entry. This corresponds to an excitation of a single dipole by rotating its polar angle by one radian. We visualize the time evolution of excitations showing the distribution  $\Lambda(i\Delta\theta, t)$  for discrete times  $t$ . Such a time evolution can be seen in figure 7 for an initial excitation of a single dipole in the outer domain at  $\theta = 0$  (figure 7(a)) and an excitation of a single dipole in the inner domain at  $\theta = 39\pi/40$  (figure 7(b)). As one might expect, with increasing time

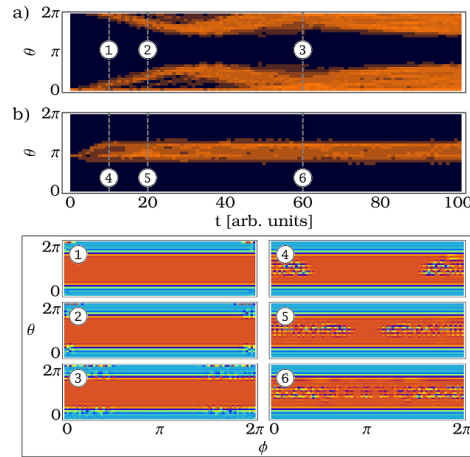


**Figure 7.** Time evolution an initial excitation at one lattice site in the outer domain (a) and in the inner domain (b). The coloring indicates the strength of the excitation. Dark colors indicate that the corresponding lattice sites are not perturbed and remain in their GS orientation (or very close to it). Bright colors indicate large amplitude deviations of the dipoles from the GS. The images marked 1–6 visualize the dipole orientations on the torus for different times  $t \in [10, 20, 60]$ . Images (1–3) and (4–6) respectively correspond to the excitations shown in (a) and (b). Just like in figure 6(a), each position  $(\theta, \phi)$  is colored according to the orientation of the closest dipole. The color-function is the same as in figure 4, with blue and red colors respectively corresponding to dipoles oriented along  $\hat{e}_\theta$  and  $\hat{e}_\phi$ .

the perturbation spreads through the system and an increasing number of dipoles begins to oscillate. However, contrary to what one might initially expect, the excitation does not cross over the DW into the other domain, but is reflected at the DW and thereby confined to the domain it originated from. The images (1–6) in the lower panel of figure 7 visualize snapshots of the dipole configuration at different times  $t \in [10, 20, 60]$ . Images (1–3) correspond to the excitation shown in figure 7(a), whereas images (4–6) correspond to the excitation shown in figure 7(b). A comparison of images (1–3) and (4–6) shows that the excitation of the outer domain in (1–3) spreads slower than the excitation of the inner domain in (4–6). This can be understood by inspecting figure 6, which shows that eigenmodes that excite mainly the outer domain oscillate at lower frequencies than eigenmodes that excite predominantly the inner domain.

## 6. Summary and outlook

We have demonstrated that dipole lattices spanned on curved structures can exhibit behavior that drastically differs from that of dipole lattices in flat geometries. In particular, the (Euclidean) distances between neighboring lattice points become dependent on the local geometry of the surface within which the lattice resides. This can lead to the presence of AFE domains in the GS of the system. While the DWs separating these domains appear similar to other DWs found in FEs, their behavior can significantly differ. Most importantly, these geometry-induced DWs are ‘pinned’ to positions where the ratio of the (Euclidean) distances

to the NNs is equal ( $\gamma = 1$ ). As a result of this ‘pinning’ of the DW center to  $\gamma = 1$ , these DWs will not simply shift when e.g. external electric fields are applied, but rather show a more complex behavior: For low field amplitudes, the DW position will be slightly displaced until a new static equilibrium is reached. For larger field amplitudes, a new FE domain will emerge between the two original domains. With increasing field amplitude, this FE domain will increasingly expand into the neighboring domains. Interestingly, this new FE domain appears before dipoles in the neighboring domains begin to significantly align with the field.

For our prototype system of a toroidal dipole lattice, we further investigated the dynamics of low energy excitations of the GS. There, we demonstrated the tendency of DWs to inhibit the thermalization of the system by (effectively) preventing small energy excitations from exploring beyond the boundary of the DW. We expect this effect to be caused by the continuous change of the lattice constants: The dipoles towards the center of the torus are much closer to one another and therefore more ‘costly’ to excite. Consequently, any excitation starting in the outer domain may be prevented by energetic considerations from exploring too far into any region where the dipoles are much closer and the interactions therefore much stronger. A similar effect of excitations being confined to certain regions has been described in certain soft matter systems and other inhomogeneous lattices [57].

#### Data availability statement

The data cannot be made publicly available upon publication because they are not available in a format that is sufficiently accessible or reusable by other researchers. The data that support the findings of this study are available upon reasonable request from the authors.

#### Acknowledgment

A S thanks A Romero-Ros and M Pyzh for helpful discussions.

#### ORCID iDs

Ansgar Siemens  <https://orcid.org/0000-0003-0454-2512>

Peter Schmelcher  <https://orcid.org/0000-0002-2637-0937>

#### References

- [1] Pitois S, Millot G and Wabnitz S 1998 Polarization domain wall solitons with counterpropagating laser beams *Phys. Rev. Lett.* **81** 1409–12
- [2] Zhang H, Tang D Y, Zhao L M and Wu X 2009 Observation of polarization domain wall solitons in weakly birefringent cavity fiber lasers *Phys. Rev. B* **80** 052302
- [3] Yu X and Blakie P B 2021 Dark-soliton-like magnetic domain walls in a two-dimensional ferromagnetic superfluid *Phys. Rev. Res.* **3** 023043
- [4] Choi K and Kim J E 1985 Domain walls in superstring models *Phys. Rev. Lett.* **55** 2637–40
- [5] Nataf G F, Guennou M, Gregg J M, Meier D, Hlinka J, Salje E K H and Kreisel J 2020 Domain-wall engineering and topological defects in ferroelectric and ferroelastic materials *Nat. Rev. Phys.* **2** 634–48
- [6] Meier D and Selbach S M 2022 Ferroelectric domain walls for nanotechnology *Nat. Rev. Mater.* **7** 157–73
- [7] Sharma P, Zhang Q, Sando D, Lei C H, Liu Y, Li J, Nagarajan V and Seidel J 2017 Nonvolatile ferroelectric domain wall memory *Sci. Adv.* **3** e1700512

- [8] Yuan S, Luo X, Chan H L, Xiao C, Dai Y, Xie M and Hao J 2019 Room-temperature ferroelectricity in MoTe<sub>2</sub> down to the atomic monolayer limit *Nat. Commun.* **10** 1775
- [9] Wang J *et al* 2022 Ferroelectric domain-wall logic units *Nat. Commun.* **13** 3255
- [10] Muralt P 2000 Ferroelectric thin films for micro-sensors and actuators: a review *J. Micromech. Microeng.* **10** 136–46
- [11] Beckman S P, Wang X, Rabe K M and Vanderbilt D 2009 Ideal barriers to polarization reversal and domain-wall motion in strained ferroelectric thin films *Phys. Rev. B* **79** 144124
- [12] Salje E K H 2012 Ferroelastic materials *Annu. Rev. Mater. Res.* **42** 265–83
- [13] Belletti G D, Dalosto S D and Tinte S 2014 Strain-gradient-induced switching of nanoscale domains in free-standing ultrathin films *Phys. Rev. B* **89** 174104
- [14] Li J, Zhu Y, Huang P Z, Fu D W, Jia Q Q and Lu H F 2022 Ferroelasticity in organic–inorganic hybrid perovskites *Chem. Eur. J.* **28** e202201005
- [15] Parkin S S P, Hayashi M and Thomas L 2008 Magnetic domain-wall racetrack memory *Science* **320** 190–94
- [16] White R M 2007 *Quantum Theory of Magnetism: Magnetic Properties of Materials (Springer Series in Solid-State Sciences)* 3rd edn (Springer)
- [17] Dzyaloshinsky I 1958 A thermodynamic theory of ‘weak’ ferromagnetism of antiferromagnetics *J. Phys. Chem. Solids* **4** 241–55
- [18] Moriya T 1960 Anisotropic superexchange interaction and weak ferromagnetism *Phys. Rev.* **120** 91–98
- [19] Camley R E and Livesey K L 2023 Consequences of the Dzyaloshinskii-Moriya interaction *Surf. Sci. Rep.* **78** 100605
- [20] Röbber U K, Bogdanov A N and Pfeiderer C 2006 Spontaneous skyrmion ground states in magnetic metals *Nature* **442** 797–801
- [21] Tokura Y and Kanazawa N 2021 Magnetic skyrmion materials *Chem. Rev.* **121** 2857–97
- [22] Bogdanov A N and Panagopoulos C 2020 Physical foundations and basic properties of magnetic skyrmions *Nat. Rev. Phys.* **2** 492–8
- [23] Lai P, Zhao G P, Tang H, Ran N, Wu S Q, Xia J, Zhang X and Zhou Y 2017 An improved racetrack structure for transporting a skyrmion *Sci. Rep.* **7** 45330
- [24] Luo S, Song M, Li X, Zhang Y, Hong J, Yang X, Zou X, Xu N and You L 2018 Reconfigurable skyrmion logic gates *Nano Lett.* **18** 1180–4
- [25] Chauwin M, Hu X, Garcia-Sanchez F, Neilesh B, Paler A, Moutafis C and Friedman J S 2019 Skyrmion logic system for large-scale reversible computation *Phys. Rev. Appl.* **12** 064053
- [26] Kiselev N S, Bogdanov A N, Schäfer R and Röbber U K 2011 Chiral skyrmions in thin magnetic films: new objects for magnetic storage technologies? *J. Phys. D: Appl. Phys.* **44** 392001
- [27] Fert A, Cros V and Sampaio J 2013 Skyrmions on the track *Nat. Nanotechnol.* **8** 152–6
- [28] Gaididei Y, Kravchuk V P and Sheka D D 2014 Curvature effects in thin magnetic shells *Phys. Rev. Lett.* **112** 257203
- [29] Streubel R, Fischer P, Kronast F, Kravchuk V P, Sheka D D, Gaididei Y, Schmidt O G and Makarov D 2016 Magnetism in curved geometries *J. Phys. D: Appl. Phys.* **49** 363001
- [30] Volkov O M, Röbber U K, Fassbender J and Makarov D 2019 Concept of artificial magnetoelectric materials via geometrically controlling curvilinear helimagnets *J. Phys. D: Appl. Phys.* **52** 345001
- [31] Cornelissen T D, Biler M, Urbanaviciute I, Norman P, Linares M and Kemerink M 2019 Kinetic Monte Carlo simulations of organic ferroelectrics *Phys. Chem. Chem. Phys.* **21** 1375–83
- [32] Urbanaviciute I, Bhattacharjee S, Biler M, Lugger J A M, Cornelissen T D, Norman P, Linares M, Sijbesma R P and Kemerink M 2019 Suppressing depolarization by tail substitution in an organic supramolecular ferroelectric *Phys. Chem. Chem. Phys.* **21** 2069–79
- [33] Xiong S J 1992 Bethe Ansatz study of 1+1 dimensional Hubbard model *Z. Phys. B* **89** 29–34
- [34] Wang W and Xiong S 1991 Possible first order phase transition in the one-dimensional helical Hubbard model *Phys. Lett. A* **156** 415–18
- [35] Stockhofe J and Schmelcher P 2015 Bloch dynamics in lattices with long-range hopping *Phys. Rev. A* **91** 023606
- [36] Stockhofe J and Schmelcher P 2016 Modulational instability and localized breather modes in the discrete nonlinear Schrödinger equation with helicoidal hopping *Physica D* **328–329** 9–20
- [37] Guo A M, Hu P J, Gao X H, Fang T F and Sun Q F 2020 Topological phase transitions of thouless charge pumping realized in helical organic molecules with long-range hopping *Phys. Rev. B* **102** 155402

- [38] Siemens A and Schmelcher P 2022 Formation and crossover of multiple helical dipole chains *J. Phys. A: Math. Theor.* **55** 375205
- [39] Schmelcher P 2011 Effective long-range interactions in confined curved dimensions *Europhys. Lett.* **95** 50005
- [40] Zampetaki A V, Stockhofe J, Krönke S and Schmelcher P 2013 Classical scattering of charged particles confined on an inhomogeneous helix *Phys. Rev. E* **88** 043202
- [41] Pedersen J K, Fedorov D V, Jensen A S and Zinner N T 2014 Formation of classical crystals of dipolar particles in a helical geometry *J. Phys. B: At. Mol. Opt. Phys.* **47** 165103
- [42] Zampetaki A V, Stockhofe J and Schmelcher P 2015 Degeneracy and inversion of band structure for wigner crystals on a closed helix *Phys. Rev. A* **91** 023409
- [43] Zampetaki A V, Stockhofe J and Schmelcher P 2015 Dynamics of nonlinear excitations of helically confined charges *Phys. Rev. E* **92** 042905
- [44] Zampetaki A V, Stockhofe J and Schmelcher P 2017 Pinned-to-sliding transition and structural crossovers for helically confined charges *Phys. Rev. E* **95** 022205
- [45] Zampetaki A V, Stockhofe J and Schmelcher P 2018 Electrostatic bending response of a charged helix *Phys. Rev. E* **97** 042503
- [46] Siemens A and Schmelcher P 2020 Tunable order of helically confined charges *Phys. Rev. E* **102** 012147
- [47] Siemens A and Schmelcher P 2021 External-field-induced dynamics of a charged particle on a closed helix *Phys. Rev. E* **103** 052217
- [48] Brent R P 2002 *Algorithms for Minimization Without Derivatives (Dover Books on Mathematics)* (Dover Publications)
- [49] Brankov J G and Danchev D M 1987 Ground state of an infinite two-dimensional system of dipoles on a lattice with arbitrary rhombicity angle *Physica A* **144** 128–39
- [50] Feldmann J D, Kalman G J, Hartmann P and Rosenberg M 2008 Ground state of magnetic dipoles on a two-dimensional lattice: structural phases in complex plasmas *Phys. Rev. Lett.* **100** 085001
- [51] Rozenbaum V M 1991 Orientation states of dipoles on 2D Bravais lattices *Sov. Phys. JETP* **72** 1028 (available at: <http://jetp.ras.ru/cgi-bin/e/index/e/72/6/p1028?a=list>)
- [52] De'Bell K, MacIsaac A B, Booth I N and Whitehead J P 1997 Dipolar-induced planar anisotropy in ultrathin magnetic films *Phys. Rev. B* **55** 15108–18
- [53] Klymenko V E, Kukhtin V V, Ogenko V M and Rosenbaum V M 1990 Steady configurations of a square dipole lattice in an external field *Phys. Lett. A* **150** 213–5
- [54] Purcell E M 2013 *Electricity and Magnetism* 3rd edn (Cambridge University Press)
- [55] Kwon K, Mukherjee K, Huh S, Kim K, Mistakidis S, Maity D, Kevrekidis P, Majumder S, Schmelcher P and Choi J-Y 2021 Spontaneous formation of star-shaped surface patterns in a driven Bose-Einstein condensate *Phys. Rev. Lett.* **127** 113001
- [56] Rózsa L, Hagemeister J, Vedmedenko E Y and Wiesendanger R 2018 Localized spin waves in isolated  $k\pi$  skyrmions *Phys. Rev. B* **98** 224426
- [57] Zhang G H and Nelson D R 2021 Phonon eigenfunctions of inhomogeneous lattices: can you hear the shape of a cone? *Phys. Rev. E* **104** 065005



**Compression-induced crossovers for the ground state of classical dipole lattices on a Möbius strip**A. Siemens<sup>1,\*</sup>, F. A. O. Silveira<sup>2</sup> and P. Schmelcher<sup>1,3,†</sup><sup>1</sup>Zentrum für Optische Quantentechnologien, Fachbereich Physik, Universität Hamburg, Luruper Chaussee 149, 22761 Hamburg, Germany<sup>2</sup>Departamento de Física, UNESP—Universidade Estadual Paulista, Av. 24A, 1515, Bela Vista, CEP: 13506-900, Rio Claro, São Paulo, Brazil<sup>3</sup>Hamburg Center for Ultrafast Imaging, Universität Hamburg, Luruper Chaussee 149, 22761 Hamburg, Germany

(Received 5 January 2024; revised 5 April 2024; accepted 24 May 2024; published 11 June 2024)

We explore the ground-state properties of a lattice of classical dipoles spanned on the surface of a Möbius strip. The dipole equilibrium configurations depend significantly on the geometrical parameters of the Möbius strip, as well as on the lattice dimensions. As a result of the variable dipole spacing on the curved surface of the Möbius strip, the ground state can consist of multiple domains with different dipole orientations which are separated by domain-wall-like boundaries. We analyze in particular the dependence of the ground-state dipole configuration on the width of the Möbius strip and highlight two crossovers in the ground state that can be correspondingly tuned. A first crossover changes the dipole lattice from a phase which resists compression to a phase that favors it. The second crossover leads to an exchange of the topological properties of the two involved domains. We conclude with a brief summary and an outlook on more complex topologically intricate surfaces.

DOI: [10.1103/PhysRevE.109.064125](https://doi.org/10.1103/PhysRevE.109.064125)**I. INTRODUCTION**

Long-range dipole interactions are ubiquitous in physics and appear in a wide range of systems, ranging from atomic setups, such as Rydberg arrays [1] or dipolar quantum gases [2,3], to solid state systems, such as magnets [4] or ferroelectrics [5,6]. Especially in crystalline lattices, such as in ferroelectric (FE) materials, the anisotropic character of the interaction can lead to the formation of complex ordered phases [7]. For example, the degeneracy of the ground-state (GS) configuration, i.e., the invariance of the energy under inversion of all dipoles, can lead to the formation of local domains separated by a domain wall (DW) [8]. For FE materials, experiments have shown a great control of these DWs, allowing for controlled shifts and even the controlled creation or annihilation of domains [8,9]. Due to this direct control of the dipole configurations, FE materials have been used for applications, such as smart sensors, capacitors, transducers, actuators, energy harvesting devices, and nonvolatile memories [8–11].

The ordered phases emerging in lattice systems of interacting dipoles can significantly depend on the underlying lattice geometry: In certain lattice geometries, the ground state becomes continuously degenerate [12,13] and allows for continuous transformations between different ground-state configurations [14,15]. Other examples include spin-glass phases emerging in disordered systems [16], and the suppression of long-range order in lattices exhibiting geometric frustration [17–19]. Besides these well-known examples, interesting geometry-dependent effects can also be found in lattice systems exhibiting mixed dimensionality: Already in a

simple one-dimensional (1D) setup consisting of dipoles that are spaced equidistant along a helical path, the ground state can be classified by a complex self-similar bifurcation diagram that depends on the helix geometry [20]. For dipoles that are arranged on two-dimensional (2D) surfaces, the curved geometries can enforce the presence of topological defects, as can be seen for self-assembling dipoles on a sphere [21]. Furthermore, it has been demonstrated that dipole lattices on a 2D curved surface can exhibit domains and domain-wall-like boundaries in their ground state [22]. Here, we build upon these results and further investigate the properties of classical dipole lattices in curved geometries. Specifically, we are interested in the effects arising when a dipole lattice is spanned on a curved surface that is topologically nontrivial.

It has been demonstrated that spatial curvature or mixed dimensionality by itself can lead to a variety of intriguing (and often counter-intuitive) effects. Already for (isotropic) Coulomb-interacting particles confined to a curved 1D path a plethora of highly nontrivial static [23–26] and dynamic [27–31] effects can emerge. Furthermore, in geometries that are topologically nontrivial, such as the Möbius strip, the surface topology can induce effects that are absent in corresponding topologically trivial systems [32,33]. Specifically magnetic dipoles dominated by exchange interactions have been studied in curved geometries [34–36], including the Möbius strip [37,38]. This motivates us to investigate the ground-state properties of a lattice of classical dipoles spanned on the surface of a Möbius strip. We find that a compression of the strip can lead to two distinct crossovers in the ground state of the embedded dipole lattice that are detected as peaks in the compression module. One of the crossovers is connected to the curvature-dependent changes of the dipole configurations and corresponds to a change of the system from resisting to favoring compression. The second crossover has its origin in the nontrivial Möbius strip topology, and

\*Contact author: [asiemens@physnet.uni-hamburg.de](mailto:asiemens@physnet.uni-hamburg.de)†Contact author: [pschmelc@physnet.uni-hamburg.de](mailto:pschmelc@physnet.uni-hamburg.de)

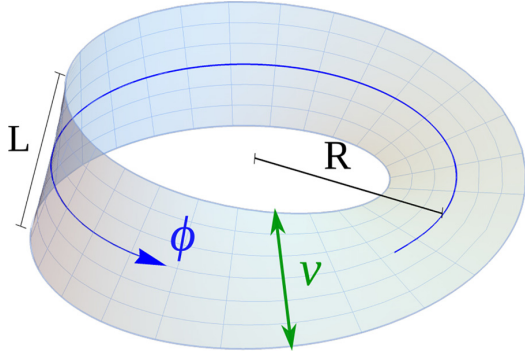


FIG. 1. Visualization of the Möbius strip surface and the parameters of Eq. (1). The mesh grid corresponds to a lattice with  $6 \times 26$  lattice points.

corresponds to a change of the topological properties of the ground-state domains.

Our work is structured as follows: The description of our setup is provided in Sec. II. An overview of the stable GS equilibrium configurations, as well as their dependence on the system parameters, is given in Sec. III. In Sec. IV, the two crossovers are discussed. Finally, we present in Sec. V our brief summary and conclusions as well as an outlook.

## II. LATTICE OF DIPOLES ON A MÖBIUS STRIP

We consider a lattice of classical dipoles spanned on the surface a Möbius strip. Each point on the Möbius strip's surface can be expressed by a parametric function  $f(u, v)$  given by

$$f(\phi, v) := \begin{pmatrix} [R + v \cos(\phi/2)] \cos(\phi) \\ [R + v \cos(\phi/2)] \sin(\phi) \\ v \sin(\phi/2) \end{pmatrix}, \quad (1)$$

where  $u$  and  $v$  are the parametric (i.e., the internal) coordinates of the surface, and  $R$  is the “radius” of the center circle of the Möbius strip. For  $\phi \in [0, 2\pi)$  and  $v \in [-\frac{L}{2}, \frac{L}{2}]$ , Eq. (1) produces a Möbius strip with a width  $L$ . Before describing the dipole lattice on the Möbius strip surface, it is helpful to introduce the unit vectors

$$\begin{aligned} \mathbf{e}_\phi &= \frac{\partial f(\phi, v)}{\partial \phi} / \left\| \frac{\partial f(\phi, v)}{\partial \phi} \right\| \\ \mathbf{e}_v &= \frac{\partial f(\phi, v)}{\partial v} / \left\| \frac{\partial f(\phi, v)}{\partial v} \right\|. \end{aligned} \quad (2)$$

At every point  $f(\phi, v)$  the two unit vectors  $\mathbf{e}_\phi$  and  $\mathbf{e}_v$  are orthogonal to each other and tangential to the Möbius strip surface. We will from now on respectively refer to  $\mathbf{e}_\phi$  and  $\mathbf{e}_v$  as the angular and the radial direction on the Möbius strip. The parametric surface  $f(\phi, v)$  is shown in Fig. 1, together with visualizations of the above-described parameters.

We now place a grid of  $(N \times M)$  dipoles on the Möbius strip. The grid points are equidistant in the parametric coordinates, with (parametric) lattice constants of  $\Delta\phi = 2\pi/N$  and

$\Delta v = L/M$ . Consequently the positions of the lattice points in Euclidean space are given by  $\mathbf{r}_{nm} = f(n\Delta\phi, m\Delta v - L/2)$ , where  $n \in [1, N]$  and  $m \in [1, M]$ . An example of such a grid with  $N = 26$  and  $M = 6$  is visualized on the Möbius surface in Fig. 1 (thin gray lines). At each position  $\mathbf{r}_{nm}$ , we place a dipole with dipole moment  $\mathbf{d}_{nm}$ . The dipoles can freely rotate and interact via dipole-dipole interactions. The potential energy  $V_{nm}^{ij}$  resulting from the interaction between two dipoles positioned at  $\mathbf{r}_{nm}$  and  $\mathbf{r}_{ij}$  is then given by

$$V_{nm}^{ij} = \frac{\mathbf{d}_{nm} \cdot \mathbf{d}_{ij}}{4\pi\epsilon_0 (r_{nm}^{ij})^3} - \frac{3(\mathbf{d}_{nm} \cdot \mathbf{r}_{nm}^{ij})(\mathbf{d}_{ij} \cdot \mathbf{r}_{nm}^{ij})}{4\pi\epsilon_0 (r_{nm}^{ij})^5}, \quad (3)$$

where  $\mathbf{r}_{nm}^{ij} = \mathbf{r}_{nm} - \mathbf{r}_{ij}$  is the (Euclidean) distance vector between the two dipoles, and  $r_{nm}^{ij} = |\mathbf{r}_{nm}^{ij}|$  the corresponding magnitude. The total energy of the system can then be determined by summing up all pairwise interactions  $V_{tot} = \sum_{n,m \neq i,j} V_{nm}^{ij}$ . We are interested in finding the ground-state dipole configuration of the lattice, i.e., the configuration that minimizes  $V_{tot}$ . Since the magnitude of the dipole moments  $\mathbf{d}$  only scales the total energy and does not affect the ground-state dipole configuration, we can - without loss of generality - set  $d = |\mathbf{d}| = 1$ . This optimization problem then depends on  $2MN + 4$  parameters: The four system parameters  $R$ ,  $L$ ,  $\Delta\phi$ , and  $\Delta v$  (which are held constant for each individual optimization), as well as the dipole moments  $\mathbf{d}$  (characterized by a total of  $2MN$  angles). For the calculation of the GS configurations we consider all-to-all interactions. Nevertheless, some of the presented results were obtained using a nearest-neighbor (NN) approximation. This NN approximation provides a very good approximation of the actual equilibrium configurations for systems where the NN distance is small compared to the curvature radius of the surface [22]. Results based on NN calculations are specifically referred to as such in the text. Furthermore, to find the GS configurations we use a principal-axis method. The principal-axis method is a numerical optimization method that does not rely on gradients. Instead, the optimizer performs line searches along a set of continuously updated search directions.

## III. GS EQUILIBRIUM CONFIGURATIONS

The ground-state dipole configuration of the above-described dipole lattice on a Möbius strip differs from the well-known ground states of dipole lattices in “flat” geometries. This is because the distances between neighboring dipoles on the Möbius strip depends on the local geometry of  $f(\phi, v)$ . This can be easily seen by calculating the Euclidean distances  $a$  and  $b$  between neighboring dipoles along the  $\mathbf{e}_\phi$  and  $\mathbf{e}_v$  directions

$$\begin{aligned} a(\phi, v) &= \|\mathbf{f}(\phi, v + \Delta v) - \mathbf{f}(\phi, v)\|, \\ b(\phi, v) &= \|\mathbf{f}(\phi + \Delta\phi, v) - \mathbf{f}(\phi, v)\|. \end{aligned} \quad (4)$$

Inserting the Möbius parametrization of  $f(\phi, v)$  from Eq. (1) into the above equations yields

$$a = \Delta v = L/M \quad (5)$$

for the Euclidean distance between next neighbors along the radial direction  $\mathbf{e}_v$ , and

$$\begin{aligned}
 b^2(\phi, v) = & 8R^2 \cos\left(\frac{\Delta\phi}{4}\right)^2 + v^2 \left[ 3 + \cos(\phi) \right. \\
 & \left. + 2 \cos\left(\phi + \frac{\Delta\phi}{2}\right) + 2 \cos(\Delta\phi/2) \right] \\
 & + v^2 [\cos(\Delta\phi) + \cos(\phi + \Delta\phi)] \\
 & + 16Rv \cos\left(\frac{\Delta\phi}{4}\right)^3 \cos\left(\frac{2\phi + \Delta\phi}{4}\right) \quad (6)
 \end{aligned}$$

for the Euclidean distance between next neighbors along the angular direction  $\mathbf{e}_\phi$ . The impact of such a varying nearest-neighbor distance on the dipole equilibrium configurations has been previously studied [22]. Following the nomenclature set in Ref. [22], we introduce the parameter  $\gamma = a/b$ . From Ref. [22], we know that the dipoles will favor aligning along  $\mathbf{e}_v$  wherever  $\gamma < 1$  (i.e.,  $a < b$ ), and along  $\mathbf{e}_\phi$  wherever  $\gamma > 1$  (i.e.,  $a > b$ ). If the parameters are chosen such that in some part of the Möbius strip  $\gamma < 1$  and in another part we have  $\gamma > 1$ , the ground state will feature two domains with different dipole orientations separated by a domain-wall-like boundary. A detailed description on the properties and the mechanism behind the formation of the domain-wall-like boundary can be found in Ref. [22]. Specifically, the properties and features discussed in Ref. [22] include the (finite) thickness of the domain-wall-like boundary, the response of this boundary to external fields, as well as a demonstration of the fact that these geometry-induced boundary regions act as barriers that prevent dynamic excitations from passing from one domain to another.

An example ground-state dipole configuration on the Möbius strip with  $N = 51$ ,  $M = 9$ ,  $R = 1$ , and  $L = 1.02$  is shown in Figs. 2(a)–2(c). Note, that an odd value of  $M$  was chosen to avoid the presence of (topological) lattice defects. In contrast,  $N$  being even or odd has no discernible impact on the ground-state configurations. In the figure, the dipoles are colored depending on their orientation: Dipoles with  $\mathbf{d} \parallel \mathbf{e}_\phi$  are colored green, whereas all dipoles with  $\mathbf{d} \parallel \mathbf{e}_v$  are colored blue. Dipoles with significant alignment normal to the surface, i.e., dipoles for which  $\mathbf{d} \parallel (\mathbf{e}_\phi \times \mathbf{e}_v)$ , could not be observed in any of our simulations. From now on, we will use the terms angular domain and radial domain to, respectively, refer to the domains where dipoles are dominantly aligned along  $\mathbf{e}_\phi$  and  $\mathbf{e}_v$ . For better visualization of this ground state, the orientation of the dipoles with respect to the parametric coordinates  $\phi$  and  $v$  is shown in Fig. 2(d). A corresponding diagram of how the parameter  $\gamma(\phi, v)$  changes with the parametric coordinates is shown in Fig. 2(e).

From the comparison in Fig. 2, as well as from Ref. [22], we know that the ground-state dipole configuration can be accurately predicted from the parameter  $\gamma$ , especially when the dipole spacing is small compared to the curvature radius of the surface. Therefore, we can get an intuition of the impact of parameter variations on the ground state by analyzing the impact of these changes on  $\gamma$ . For a given dipole lattice of dimension  $(N \times M)$ , the local value of  $\gamma$  can be impacted by the Möbius parameters  $L$  and  $R$ . To get a first impression of the overall behavior of  $\gamma$ , we expand  $b(\phi, v)$  to the first order

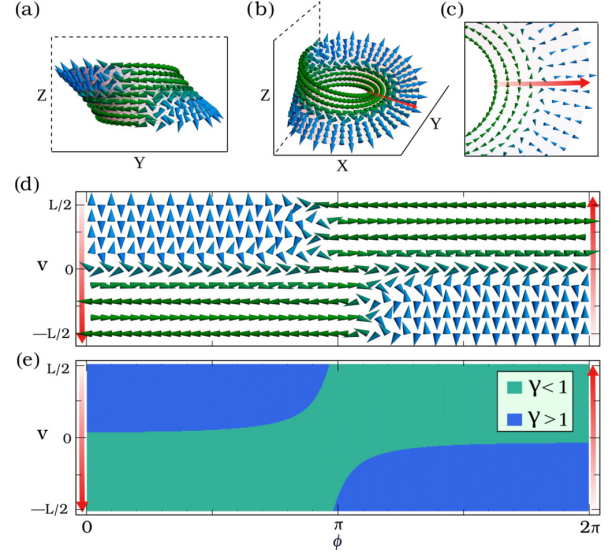


FIG. 2. Example ground-state dipole configuration for  $N = 51$ ,  $M = 9$ ,  $R = 1$ , and  $L = 1.02$ . (a)–(c) Visualizations of the ground state from different viewpoints. (d) Visualization of the ground-state dipole alignments within the surface. Dipole positions and alignments are given with respect to the parametric coordinates  $\phi$  and  $v$ . (e) A visualization of the parameter  $\gamma = a/b$  as a function of the parametric coordinates. See text for details.

in  $\Delta\phi$  around  $\Delta\phi = 0$ . Since  $\Delta\phi = 2\pi/N$ , this is a good approximation in the limit of large  $N$ . With this, the parameter  $\gamma$  can be approximated as

$$\gamma \simeq \frac{L}{\pi} \frac{(N/M)}{\sqrt{4R^2 + 3v^2 + 8Rv \cos\left(\frac{\phi}{2}\right) + 2v^2 \cos(\phi)}}. \quad (7)$$

Consequently, in grids with many lattice points, the parameter  $\gamma$  will scale globally when the ratio  $N/M$  changes. Note that any change of  $L$  will also affect the range of the parameter  $v \in [-L/2, L/2]$ . Therefore, it is possible to rewrite Eq. (7) such that it depends entirely on the ratio  $L/R$  by introducing  $v' = 2v/L \in [-1, 1]$ . Changing the ratio  $L/R$  will not lead to a simple global scaling factor for  $\gamma$ . Instead, an increase in  $L/R$  can either increase  $\gamma$  everywhere, or (below a certain value of  $L/R$ ) it can lead to an increase of  $\gamma$  in some parts of the lattice and to a decrease of  $\gamma$  in other parts.

In the following, we will study the ground GS for fixed values of  $N/M$  and  $R$ . This reduces the problem of finding all possible GS configurations on the Möbius strip to finding the GS as a function of  $L$ . The GS configurations, and especially the distribution of the two domains, are visualized in the lower four panels of Fig. 3 for various values of  $L$ . From these four panels, it can be seen that by varying  $L$ , we are able to tune the size of the two domains, with the angular domain covering the entire surface for large  $L$  and the radial domain covering it for small  $L$ . In the following, we will analyze the size change of the domains when  $L$  is increased. While we are focusing on a specific example system, the shown behavior, i.e., the evolution of the domains when  $L$  is varied, is general and occurs almost exactly the same way regardless of the specific

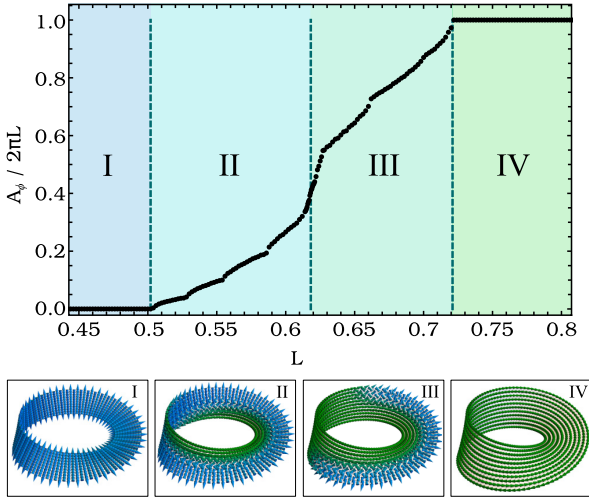


FIG. 3. Size  $A_\phi$  of the angular domain as a function of the Möbius strip width  $L$  for  $N = 101$ ,  $M = 11$ , and  $R = 1$ . All data points were obtained using a nearest-neighbor approximation. The lower panel shows example configurations from the four regimes for  $L \in [0.47, 0.6, 0.65, 0.83]$  obtained from all-to-all calculations.

values of  $R$  and  $N/M$ . However, before we analyze the domain size, a final comment on the impact of the ratio  $N/M$  is in order: The overall impact of varying  $N/M$  can be described as follows: For certain values of  $N/M$  (especially towards the extremes  $N \gg M$  or  $N \ll M$ ) it may be that (depending on the case) not all of the shown configurations are accessible, unless we make  $L$  so large that the surface intersects itself. Furthermore, in those regimes where the surface intersects itself, significantly different GS configurations can be found. However, the regime where the surface intersects itself is outside of the scope of this work.

To get an idea of how the domain sizes change with  $L$ , we classify the ground states by the area  $A_\phi \in [0, 2\pi L]$  occupied by the angular domain. Note that  $A_\phi$  refers to the area in parametric coordinates. For  $A_\phi = 0$ , the entire strip is occupied by the radial domain, whereas for  $A_\phi = 2\pi L$  the entire strip is covered by the angular domain. The value of  $A_\phi$  can be obtained for any GS configuration by simply counting all dipoles that significantly align along  $\mathbf{e}_\phi$ . Simulation results of the area  $A_\phi$  occupied by the radial domain as a function of  $L$  are presented in Fig. 3 for numerically determined ground states on a Möbius strip with  $N = 101$ ,  $M = 11$ , and  $R = 1$ . Note that the data shown in Fig. 3 are obtained using a NN approximation. In the figure, four clearly distinct regions can be seen: In region I, only the radial domain exists. In region II, both the radial and the angular domain coexist, with the angular domain increasing in size with increasing  $L$ . Note, that the small jumps (or steps) of  $A_\phi(L)$  arise due to the discreteness of the underlying dipole lattice and will vanish for  $M \rightarrow \infty$ . When the angular domain first appears (the border between regions I and II in Fig. 3), it emerges from the point  $(\phi, v) = (-\pi/N, -L/2)$ . From there, the angular domain will mainly grow along  $\mathbf{e}_\phi$  as  $L$  is increased. As the angular domain grows, it will eventually have circled around

the Möbius strip and for  $L = 2MR \sin(\pi/N)$  connect with itself at the point  $(\phi, v) = (\pi - \pi/N, 0)$ . This corresponds to the border between regions II and III in Fig. 3. At this point both the angular and the radial domain occupy equal areas of the strip. Note that due to the finite size of the domain wall this border between regions II and III occurs for  $A_\phi < 0.5$ . Around the border between regions II and III, the domain sizes change very rapidly - indicating a great sensitivity of this point to parameter variations. Note, that in the continuum limit (i.e.,  $N, M \rightarrow \infty$ ) the slope of  $A_\phi(L)$  diverges exactly at the boundary between regions II and III. In region III, the angular domain increases further in size when  $L$  is increased, until finally in region IV it encompasses the entire strip. For systems with different  $N/M$ , no discernible differences from the above-described behavior could be observed.

#### IV. COMPRESSION-INDUCED TOPOLOGICAL CROSSOVER

We will now demonstrate that the GS dipole configuration passes through two distinct crossovers if the length  $L$  is varied. The variation of  $L$  discussed above can also be interpreted as an adiabatic compression or stretching of the Möbius strip. The behavior of the lattice during such a compression can be analyzed with the 2D compression modulus or, simply, 2D modulus [39] of the strip. The 2D modulus is defined as

$$K = A_0 \frac{d^2 U}{dA^2} = \frac{L_0}{2\pi R} \frac{d^2 U}{dL^2}, \quad (8)$$

where  $A$  is the area of the strip,  $A_0$  and  $L_0$  denote the area and strip width before compression, and  $U$  is the total energy of the system. The 2D modulus describes how a change in the width changes the force that is required to compress (or stretch) the strip. Consequently, small values of  $K$  indicate that the required force changes very little when  $L$  is varied, whereas large values of  $K$  imply large changes in the required forces when  $L$  is varied.

The 2D modulus of Eq. (8) depends mainly on the behavior of the total ground-state energy  $U(L)$  of the system. This total energy  $U(L)$  as a function of the strip width  $L$  is shown in Fig. 4(a). Interestingly, the curve  $U(L)$  exhibits a global maximum. We will from now on use  $L_{\text{crit}}$  to refer to the width of the Möbius strip at this maximum. For values  $L < L_{\text{crit}}$  the energy increases with increasing strip width, implying that the strip prefers a compressed state and resists stretching. On the other hand, for  $L > L_{\text{crit}}$ , the energy decreases with increasing  $L$ , implying that in this regime the compression of the strip requires energy. This crossover from favoring compression to favoring stretching can be understood from the dipole alignments in the radial and angular domains. It is a result of the competition between the angular domain favoring stretching and the radial domain favoring compression. Within the radial domain, the dipoles are aligned along  $\mathbf{e}_v$  and will naturally prefer the distance  $a$  to their nearest neighbors along the  $\mathbf{e}_v$  direction to be as small as possible. Minimizing  $a$  can be achieved globally by decreasing  $L$ . Consequently, decreasing  $L$  will decrease the total energy proportional to the number of dipoles in the radial domain. On the other hand, in the angular domain, dipoles are aligned along  $\mathbf{e}_\phi$ . Consequently, these dipoles will prefer a decrease in the nearest neighbor

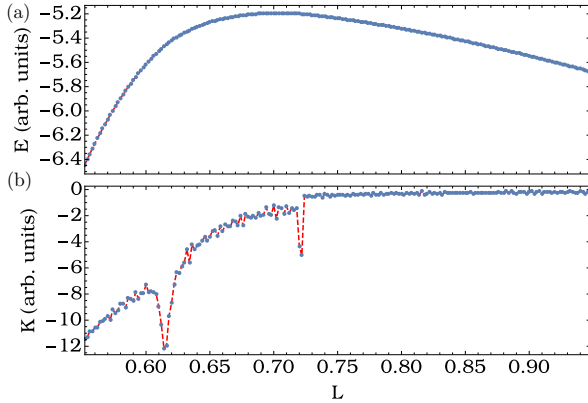


FIG. 4. (a) Total energy  $U$  as a function of the strip width  $L$ . (b) The 2D modulus  $K \sim d^2U/dL^2$  as a function of the strip width  $L$ . Both the energy and the 2D modulus data were obtained for a Möbius strip with  $N = 101$ ,  $M = 11$ , and  $R = 1$ .

distance  $b(\phi + \Delta\phi, v)$  along the  $\mathbf{e}_\phi$  direction. However, the distance  $b$  can change, depending on the position on the strip. Furthermore, when  $L$  is varied, the distance  $b$  can increase in some parts of the strip and decrease in others. However, due to the strong decay of the dipole-dipole interactions, the impact of a change in  $L$  on the energy is larger for those dipoles where  $b$  is smaller. The distance  $b(\phi + \Delta\phi, v)$  is minimized at  $(\phi, v) = (-\pi/N, -L/2)$ , i.e., at the origin of the radial domain. And around this point,  $b$  will decrease further when  $L$  is increased.

Close to the crossover point  $L_{\text{crit}}$ , the 2D modulus varies rapidly and has a local minimum [see Fig. 4(b)]. This dip in the 2D modulus, however, corresponds to the border between regions III and IV in Fig. 3. For different  $N$ ,  $M$ , and  $R$ , this dip does not necessarily coincide with the maximum of  $U(L)$ . This dip arises due to the finite thickness of the domain-wall-like boundary. This has been verified by calculations where a sharp domain boundary has been (manually) enforced. In this constructed case of a vanishing domain-boundary thickness, the 2D modulus showed only a sudden (discrete) jump instead of a dip. Interestingly, a second dip can be seen in the 2D modulus, indicating a second crossover. This second dip also originates from the finite thickness of the domain-wall-like boundary. This second dip appears at a width of  $L = 2MR \sin(\pi/N)$ —corresponding to the transition between regimes II and III. Although this second dip has no discernible effect on the total energy of the system, it does mark a significant change in the structure of the domains. For values of  $L < 2MR \sin(\pi/N)$  slightly below the dip, the radial domain not only covers the majority of the Möbius strip, but also winds around it once, giving the domain a nontrivial topology. At the same time, the angular domain has a trivial topology for  $L < 2MR \sin(\pi/N)$ . In contrast, for  $L > 2MR \sin(\pi/N)$  above the dip, it is the angular domain that has a nontrivial topology and the radial domain being topologically trivial. In summary, the domain which (azimuthally) extends over the complete Möbius strip inherits its nontrivial topology, whereas domains covering only a finite azimuthal part of the Möbius strip are topologically trivial.

As described above, during the crossover, as  $L$  is increased, the angular domain grows and connects with itself at the point  $(\phi, v) = (\pi - \pi/N, 0)$ . To better understand this crossover, it is helpful to analyze  $\gamma$  in the vicinity of this point. First, we find

$$\left. \frac{d\gamma(\phi, v)}{d\phi} \right|_{\phi \rightarrow \pi - \pi/N, v \rightarrow 0} = \left. \frac{d\gamma(\phi, v)}{dv} \right|_{\phi \rightarrow \pi - \pi/N, v \rightarrow 0} = 0, \quad (9)$$

indicating that  $\gamma$  always has a critical point at  $(\phi, v) = (\pi - \pi/N, 0)$ . Furthermore, at  $(\phi, v) = (\pi - \pi/N, 0)$  the Hessian matrix of second derivatives is indefinite, indicating that the critical point is a saddle point. Exactly for  $L = 2MR \sin(\pi/N)$  the value of  $\gamma$  at the saddle point becomes  $\gamma(\pi - \pi/N, 0) = 1$ . Any small change of  $L$  will lift (or lower)  $\gamma$  in the vicinity of the saddle point. This is why for  $L < 2MR \sin(\pi/N)$  it is the radial domain that winds around the Möbius strip and for  $L > 2MR \sin(\pi/N)$  it is the angular domain. For  $L = 2MR \sin(\pi/N)$ , the system reaches a transition point where neither of the two domains winds around the Möbius strip. For  $L = 2MR \sin(\pi/N)$ , both domains are topologically trivial; whereas for  $L \neq 2MR \sin(\pi/N)$ , one of them is not.

## V. SUMMARY AND CONCLUSIONS

We investigated a lattice of interacting dipoles that is spanned on the surface of a Möbius strip. The curved geometry of the lattice can, already for the ground state, lead to the presence of domains with different dipole orientations, as well as domain-wall-like boundaries separating these domains. Specifically, the GS of the Möbius strip contains up to two domains, referred to as the angular and the radial domain, respectively. We discussed the dependence of the ground state on the system parameters and subsequently analyzed the dependence of the GS on the width  $L$  of the Möbius strip. We demonstrated that by varying  $L$ , we are able to tune between different GS configurations. For large and small  $L$ , the entire Möbius strip is exclusively covered by either the radial or the angular domain. For intermediate  $L$ , both domains can be present simultaneously. In this intermediate regime, the relative size of the domains can be tuned by varying  $L$ . For a lattice with dimensions  $N \times M$  and a given Möbius strip radius  $R$ , one notable GS configuration is reached for  $L = 2MR \sin(\pi/N)$ . Any increase or decrease of the width from this value will lead to a drastic change in the domain topology. Specifically, for wider strips [ $L > 2MR \sin(\pi/N)$ ], the angular domain will wind around the entire strip, thereby being topologically nontrivial. And for narrower strips [ $L < 2MR \sin(\pi/N)$ ], it is the radial domain that winds around the entire strip. We explained this behavior with the presence of a saddle-point structure in the  $\gamma$  parameter which classifies the domain structure of the entire Möbius strip. Furthermore, we showed that this crossover in the domain topology can be detected as a dip in the 2D compression modulus. Additionally, the rapid change in the domain sizes that accompanies this crossover highlights the sensitivity of the crossover point to possible variations of the Möbius geometry.

In addition to this topological crossover, we also detected a second crossover that can be tuned by varying the width  $L$  of the Möbius strip. The crossover point coincides with the

maximum of the total (width-dependent) ground-state energy  $U(L)$ . During the crossover, the system changes from a state that resists compression to a state that favors compression. Consequently, this crossover point will be quite sensitive to variations of the Möbius strip width  $L$ —and by extension to variations of the system parameters  $R$ ,  $N$ , and  $M$ .

While our analysis of the dipolar lattice on a Möbius strip shows already an intricate structure formation for the ground state there is several open future directions of research. An immediate case of investigation would be the low-lying excited states and their properties. How and where do topological and nontopological defects and possibly kinks emerge in the dipolar lattice and how do they “interact” with the domain walls? Quenches of the geometrical parameters across the phase boundaries would be promising candidates for dynamical and transient structure formation in the higher-energy regime. As a longer term and promising perspective we envisage the investigation of dipolar lattices on geometrically and topologically more complex curved surfaces. While there is a plethora of such surfaces in particular in the framework of (multiply-periodic) minimal surfaces [40] the impact of the dipolar interaction on self-intersecting surfaces is an open and intriguing problem to be explored in the future.

A final remark concerning the experimental preparation of such surfaces is in order. A near-future possible experimental realization of interacting dipoles on a curved lattice can be based on dipolar ultracold molecules or Rydberg atoms which are the workhorses of modern quantum simulation [41,42]. The latter can be captured in arrays of optical

tweezers which can be arranged in almost arbitrary geometries and in particular in the here-considered curved manifold. Single atom deterministic loading and controlled excitation to Rydberg states is nowadays achieved routinely in corresponding experiments [41,42]. Their interaction can be of dipolar character due to the resonant exchange process between, e.g.,  $s$  and  $p$  Rydberg states. A competing time scale is then the de-excitation due to, e.g., radiative decay which happens typically on the time scale of dozens to hundreds of microseconds for principal quantum numbers  $n \gtrsim 60$ , leaving ample time for preparation, processing, and detection. Beyond that, curvilinear flat architectures can be prepared in the framework of nanostructures using conventional techniques based on thin-film deposition and lithographic methods [43]. Ion-beam writing techniques represent another alternative. Fabrication of complex 3D nanoarchitectures is challenging and requires even more advanced and specialized preparation tools in particular if it comes to the combination with magnetic sublattices [43]. As a conclusion, we remark that while the experimental implementation of the dipolar lattices on curved surfaces is certainly highly demanding, the richness of their phenomenology and perspectives render them highly promising candidates for future investigation.

#### ACKNOWLEDGMENT

F.A.O.S acknowledges CAPES (Grant No. 88887.670331/2022-00) for financial support.

- [1] R. Samajdar, W. W. Ho, H. Pichler, M. D. Lukin, and S. Sachdev, Complex density wave orders and quantum phase transitions in a model of square-lattice Rydberg atom arrays, *Phys. Rev. Lett.* **124**, 103601 (2020).
- [2] L. Chomaz, I. Ferrier-Barbut, F. Ferlaino, B. Laburthe-Tolra, B. L. Lev, and T. Pfau, Dipolar physics: A review of experiments with magnetic quantum gases, *Rep. Prog. Phys.* **86**, 026401 (2023).
- [3] J. Ruhman, E. G. Dalla Torre, S. D. Huber, and E. Altman, Nonlocal order in elongated dipolar gases, *Phys. Rev. B* **85**, 125121 (2012).
- [4] D. C. Johnston, Magnetic dipole interactions in crystals, *Phys. Rev. B* **93**, 014421 (2016).
- [5] H. Qiao, C. Wang, W. S. Choi, M. H. Park, and Y. Kim, Ultrathin ferroelectrics, *Mater. Sci. Eng. R-Rep.* **145**, 100622 (2021).
- [6] W. Känzig, Ferroelectrics and antiferroelectrics, in *Solid State Physics* (Academic Press, 1957), Vol. 4, pp. 1–197.
- [7] L. W. Martin and A. M. Rappe, Thin-film ferroelectric materials and their applications, *Nat. Rev. Mater.* **2**, 16087 (2017).
- [8] D. Meier and S. M. Selbach, Ferroelectric domain walls for nanotechnology, *Nat. Rev. Mater.* **7**, 157 (2022).
- [9] P. Sharma, Q. Zhang, D. Sando, C. H. Lei, Y. Liu, J. Li, V. Nagarajan, and J. Seidel, Nonvolatile ferroelectric domain wall memory, *Sci. Adv.* **3**, e1700512 (2017).
- [10] J. Wang, J. Ma, H. Huang, J. Ma, H. M. Jafri, Y. Fan, H. Yang, Y. Wang, M. Chen, D. Liu, J. Zhang, Y.-H. Lin, L.-Q. Chen, D. Yi, and C.-W. Nan, Ferroelectric domain-wall logic units, *Nat. Commun.* **13**, 3255 (2022).
- [11] P. Muralt, Ferroelectric thin films for micro-sensors and actuators: A review, *J. Micromech. Microeng.* **10**, 136 (2000).
- [12] D. Schildknecht, M. Schütt, L. J. Heyderman, and P. M. Derlet, Continuous ground-state degeneracy of classical dipoles on regular lattices, *Phys. Rev. B* **100**, 014426 (2019).
- [13] J. Brankov and D. Danchev, Ground state of an infinite two-dimensional system of dipoles on a lattice with arbitrary rhombicity angle, *Physica A* **144**, 128 (1987).
- [14] K. De’Bell, A. B. MacIsaac, I. N. Booth, and J. P. Whitehead, Dipolar-induced planar anisotropy in ultrathin magnetic films, *Phys. Rev. B* **55**, 15108 (1997).
- [15] J. D. Feldmann, G. J. Kalman, P. Hartmann, and M. Rosenberg, Ground state of magnetic dipoles on a two-dimensional lattice: Structural phases in complex plasmas, *Phys. Rev. Lett.* **100**, 085001 (2008).
- [16] J. Mydosh, Disordered magnetism and spin glasses, *J. Magn. Magn. Mater.* **157-158**, 606 (1996).
- [17] A. Ramirez, Chapter 4 Geometrical frustration, in *Handbook of Magnetic Materials* (Elsevier, 2001), Vol. 13, pp. 423–520.
- [18] P.-É. Melchy and M. E. Zhitomirsky, Interplay of anisotropy and frustration: Triple transitions in a triangular-lattice antiferromagnet, *Phys. Rev. B* **80**, 064411 (2009).
- [19] B. D. Gaulin, Geometrically-frustrated magnetism on triangular and tetrahedral lattices, *Hyperfine Interact.* **85**, 159 (1994).
- [20] A. Siemens and P. Schmelcher, Formation and crossover of multiple helical dipole chains, *J. Phys. A: Math. Theor.* **55**, 375205 (2022).

- [21] U. T. Lieu and N. Yoshinaga, Topological defects of dipole patchy particles on a spherical surface, *Soft Matter* **16**, 7667 (2020).
- [22] A. Siemens and P. Schmelcher, Geometry induced domain-walls of dipole lattices on curved structures, *J. Phys. A: Math. Theor.* **56**, 495702 (2023).
- [23] P. Schmelcher, Effective long-range interactions in confined curved dimensions, *Europhys. Lett.* **95**, 50005 (2011).
- [24] J. Plettenberg, J. Stockhofe, A. V. Zampetaki, and P. Schmelcher, Local equilibria and state transfer of charged classical particles on a helix in an electric field, *Phys. Rev. E* **95**, 012213 (2017).
- [25] A. V. Zampetaki, J. Stockhofe, and P. Schmelcher, Electrostatic bending response of a charged helix, *Phys. Rev. E* **97**, 042503 (2018).
- [26] A. Siemens and P. Schmelcher, Tunable order of helically confined charges, *Phys. Rev. E* **102**, 012147 (2020).
- [27] A. V. Zampetaki, J. Stockhofe, S. Krönke, and P. Schmelcher, Classical scattering of charged particles confined on an inhomogeneous helix, *Phys. Rev. E* **88**, 043202 (2013).
- [28] A. V. Zampetaki, J. Stockhofe, and P. Schmelcher, Degeneracy and inversion of band structure for Wigner crystals on a closed helix, *Phys. Rev. A* **91**, 023409 (2015).
- [29] A. V. Zampetaki, J. Stockhofe, and P. Schmelcher, Dynamics of nonlinear excitations of helically confined charges, *Phys. Rev. E* **92**, 042905 (2015).
- [30] A. V. Zampetaki, J. Stockhofe, and P. Schmelcher, Pinned-to-sliding transition and structural crossovers for helically confined charges, *Phys. Rev. E* **95**, 022205 (2017).
- [31] A. Siemens and P. Schmelcher, External-field-induced dynamics of a charged particle on a closed helix, *Phys. Rev. E* **103**, 052217 (2021).
- [32] W. Beugeling, A. Quelle, and C. Morais Smith, Nontrivial topological states on a Möbius band, *Phys. Rev. B* **89**, 235112 (2014).
- [33] K. Flouris, M. M. Jimenez, and H. J. Herrmann, Curvature-induced quantum spin-Hall effect on a Möbius strip, *Phys. Rev. B* **105**, 235122 (2022).
- [34] D. Makarov, O. M. Volkov, A. Kákay, O. V. Pylypovskyi, B. Budinská, and O. V. Dobrovolskiy, New dimension in magnetism and superconductivity: 3D and curvilinear nanoarchitectures, *Adv. Mater.* **34**, 2101758 (2022).
- [35] R. Streubel, E. Y. Tsybal, and P. Fischer, Magnetism in curved geometries, *J. Appl. Phys.* **129**, 210902 (2021).
- [36] R. Streubel, P. Fischer, F. Kronast, V. P. Kravchuk, D. D. Sheka, Y. Gaididei, O. G. Schmidt, and D. Makarov, Magnetism in curved geometries, *J. Phys. D: Appl. Phys.* **49**, 363001 (2016).
- [37] M. Yoneya, K. Kuboki, and M. Hayashi, Domain-wall structure of a classical Heisenberg ferromagnet on a Möbius strip, *Phys. Rev. B* **78**, 064419 (2008).
- [38] O. V. Pylypovskyi, V. P. Kravchuk, D. D. Sheka, D. Makarov, O. G. Schmidt, and Y. Gaididei, Coupling of chiralities in spin and physical spaces: The Möbius ring as a case study, *Phys. Rev. Lett.* **114**, 197204 (2015).
- [39] K. Liu and J. Wu, Mechanical properties of two-dimensional materials and heterostructures, *J. Mater. Res.* **31**, 832 (2016).
- [40] U. Dierkes, S. Hildebrandt, and F. Sauvigny, *Minimal Surfaces*, A Series of Comprehensive Studies in Mathematics Vol. 339 (Springer Berlin Heidelberg, Berlin, Heidelberg, 2010).
- [41] A. M. Kaufman and K.-K. Ni, Quantum science with optical tweezer arrays of ultracold atoms and molecules, *Nat. Phys.* **17**, 1324 (2021).
- [42] A. Browaeys and T. Lahaye, Many-body physics with individually controlled Rydberg atoms, *Nat. Phys.* **16**, 132 (2020).
- [43] D. D. Sheka, A perspective on curvilinear magnetism, *Appl. Phys. Lett.* **118**, 230502 (2021).



## Chapter 6

# Summary and outlook

This chapter contains two parts: A summary of the scientific contributions of this thesis is given in Sec. 6.1. Concluding remarks are subsequently provided in Sec. 6.2.

### 6.1 Summary of the scientific contributions [A1–A6]

This cumulative thesis explored model systems of classical long-range interacting particles confined to a curved space. The scientific contributions [A1–A3] considered Coulomb-interacting ions confined to a toroidal helix. A key feature of this model is the oscillating effective interaction potential between the ions that arises from a combination of the Coulomb interactions and the confining forces. We explored the system properties in the presence of external electric fields. In particular, this includes a study of the static (field-dependent) many-body equilibrium configurations [A1], and studies of the driven dynamics of the ions [A2, A3].

The many-body case of ions confined to a toroidal helix has been addressed to a limited extent in previous studies (see Refs. [9–12]). However, these investigations consider only selected symmetric equilibrium configurations. The scientific contribution [A1] analyzed the *general* many-body equilibrium configurations and their evolution when an external electric field is applied. We found a tendency for staggered (disordered) equilibrium configurations in the field-free case. By tuning the strength of the external electric field, it is possible to continuously switch between these staggered configurations for low field strengths and ordered configurations (akin to a 1D lattice) for large field strength. We statistically analyzed the crossover from staggered to ordered configurations and showed the robustness of the crossover to parameter variations.

The impact of time-dependent external electric fields was investigated for the single-particle case [A2]. We considered both oscillating and rotating external electric fields and performed a phase-space analysis. For low driving amplitudes the phase space showed two separate chaotic regions. These regions correspond to trajectories where the particles direction of motion cannot be inverted. This effectively allows for a directed transport of the particle. For large driving amplitudes and a rotating electric field, we found another mechanism by which the chaotic phase-space region can separate into two parts; allowing to trap the particle in a valley of the driving potential. We link these separations to those terms in the driving potential that stem from a finite helix radius.

Building directly on the scientific contribution [A2], we continued the investigation of a driven particle on a toroidal helix in [A3]. In this work, we added a static sinusoidal potential to the toroidal helix. We showed that in the limit of a vanishing helix radius, the equations of motions of the driven particle coincide with the

equations of motion of the well-known Kapitza pendulum - a driven pendulum that possesses two stable fixed points. We analyzed the impact of finite helix radii on the system in two steps: First, we performed a linear stability analysis for the two stable fixed points and analytically determined their stability with regards to variations of the helix radius, the driving amplitude, and the static potential. The analytical solutions showed good agreement with numerical calculations. Second, we investigated the impact of finite helix radii on the phase space and highlighted the most prominent types of induced phase space structures.

Moreover, we also investigated the behavior of particles with anisotropic interactions on curved manifolds. The scientific contribution [A4] considered freely rotating dipoles placed equidistant along a helical path. The ground state configuration of this system consists of interwoven helical head-to-tail dipole chains. The number and orientation of these head-to-tail chains depend significantly on the underlying geometric parameters. We were able to classify all possible dipole equilibrium configurations with a self-similar bifurcation tree. Specifically, we linked the mapping between geometric parameters and ground state dipole configurations to the Stern-Brocot tree and the number-theoretical Farey sequence.

For 2D dipole lattices on curved manifolds, we derived a number of general properties [A5]. Lattice distortions as well as spatial curvature were shown to lead to a ground state that features domains with different dipole orientations. These domains are separated by a geometry-induced domain wall. We formalized a condition, the gamma parameter, that allows the analytical prediction of the domain wall position on the surface. The width of the domain wall was also investigated and showed a strong dependence on the density of dipoles. The differences between geometry-induced domain-walls and typical (degeneracy-induced) domain walls in dipole lattices are highlighted with two effects: the domain wall response to external electric fields, and the linear excitation dynamics in systems exhibiting curvature-induced domain walls. In the case of linear excitation dynamics, we demonstrated that the domain wall acts as a hard barrier that confines arbitrary linear excitations to the domain of its origin.

Finally, we decided to investigate dipole lattices on a topologically non-trivial and non-orientable surface in [A6]. We considered a rectangular dipole lattice that is spanned on the surface of a Möbius strip. Our analysis of the ground state dipole configurations revealed several types of crossovers that take place as the Möbius strip width is varied. One type of crossover occurs during the creation and annihilation of domains and can be detected as a dip in the 2D compression modulus. Another type of crossover, which also manifests as a dip in the 2D modulus, occurs during domain-mergers at a saddle point in the surface geometry. A third type of crossover is linked to a change of the system from resisting to favoring compression.

## 6.2 Outlook

### 6.2.1 Outlook regarding the helical ion model

Perhaps the most intriguing aspect of the helical ion model is the inherent complexity and wealth of features arising despite the relative simplicity of the setup. Building on the results of the scientific contributions [A1–A3], there are a number of possible avenues for future investigations.

### Bound states

One direction is to further explore the many-body equilibrium configurations. The scientific contribution [A1] is the first work addressing general many-body equilibrium configurations of helically confined ions. However, it mainly provides statistical insight into these equilibrium configurations, while leaving a number of questions for future research. For example: is the number of particles that can form a bound state limited? If so, how does this size limit depend on the helix geometry?

Predicting size limits for the many-body equilibrium configurations is difficult due to the long-range character of the interaction. Regardless of the helix geometry, the effective interaction potential becomes repulsive (albeit very weakly) at large distances. It is not clear, whether this repulsive interaction at long ranges prevents the formation of many-body equilibrium configurations consisting of arbitrarily many particles.

Changing the helix geometry allows to tune the number and depth of wells in the effective interaction potential. The two-body bound state becomes stable only when the ratio of helix radius and helix pitch is above a critical value. It is not clear how this critical value evolves for many-body bound states. Closely related is the question of whether many-body equilibrium configurations follow a general pattern, such that the ion positions can be approximated or even predicted analytically.

### Excitations and scattering dynamics of bound states

Besides the fundamental equilibrium properties of the many-body bound states, the dynamics of bound ion configurations may also be of interest. Many-body bound states behave like a chain of non-linear oscillators. Especially in the presence of an external field (as discussed in Ref. [A1]), the Lagrangian is very similar to - but not the same as - the Lagrangian of the FK model [115]. Due to the similarities to the FK model, one can expect complex dynamics, such as the formation of solitons, from the many-body bound states in the helical ion model. In that regard, another interesting route would be to explore the collision of two or more of these bound states. As explained in Ref. [8], the center of mass motion of these bound states is decoupled from the relative motion of the ions - providing ideal prerequisites for a scattering process. First steps toward the investigation of these many-body scattering dynamics have already been taken [A9]. These first explorations have revealed a wealth of phenomena, including inelastic scattering events during which bound states frequently break up and (re)combine in a cascade of final state interactions.

### Experimental realizations

Experimental realizations of the helical ion model have so far not been a concern; neither in the scientific contributions nor elsewhere in this thesis. Nevertheless, for completeness, a final comment on such realizations is in order. Realizing the helical ion model in an experiment will be rather difficult. The most promising setups are perhaps optical traps. Recent experiments have demonstrated the possibility of confining neutral atoms to a helical path [84]. This could be used to implement the setup of the scientific contributions [A2, A3] - although realizing the time-dependent driving forces from [A2, A3] might be a challenge. Another interesting - and admittedly somewhat audacious - setup for a possible experimental realization could be counter-ions adsorbed onto macro-ions. As discussed in Sec. 2.1, these macro-ions can possess helical shapes [56], and it is possible for adsorbed counter-ions to form Wigner crystals [58, 59]. However, finding a helical macro-ion with strong counter-ion interactions and large times between adsorption and desorption will be challenging.

## 6.2.2 Outlook regarding curved dipole lattices

Dipole lattices have been studied extensively for a wide range of lattice-geometries and boundary conditions (see Sec. 4.1 for further details). Often, this research was not driven by specific experimental setups, but rather by a fundamental interest in the properties arising from the dipole-dipole interaction. In that regard, it is curious to note that the impact of spatial curvature on these systems has not been systematically explored. The scientific contributions presented in this thesis have shown that curved dipole lattices can possess intriguing (and general!) curvature-induced properties: domains and domain-walls in the ground state, unique responses of these domain-walls when exposed to external fields, curvature-induced domain-walls acting as a natural boundary that prevents dynamics from crossing from one domain into another, and structural crossovers that can be linked to the emergence or annihilation of domains as the system parameters are varied. There are several avenues for further exploration.

### Phonons and domain walls

One especially interesting feature of curved dipole lattices is that (low amplitude) dynamics are reflected at domain walls and cannot freely disperse through the system. The scientific contribution [A5] explains this behavior by stating that the excitations are prevented by ‘energetic considerations’. This statement can be further elaborated: The dispersion relation in a linear dipole chain depends significantly on the dipole orientations. When the dipoles are aligned head-to-tail along the linear chain, the dispersion relation is that of an optical phonon [145]. However, if the dipoles are aligned perpendicular to the direction of the chain, the dispersion relation is that of an acoustic phonon [146]. For the curved dipole lattices, it can therefore be assumed that any excitation that crosses the domain wall would need to transform from an acoustic to an optical phonon or vice versa. In other words, this effect likely originates purely from the dipole orientations within the domains and not from the specific change of the lattice constant across the domain boundary. In that regard, it would be interesting to know what happens in other non-rectangular lattices, such as the rhombic lattice: It may be that the rhombic angle allows for a partial transmission of the excitation. If so, can the permeability of the domain wall be tuned (to some extent) through the rhombic angle of the lattice? And if the domain wall becomes permeable, one can imagine that the transmission of an excitation will be accompanied by a rotation of the wavevector - similar to diffraction in optics. This, in turn, raises the question of whether it is possible to describe these domain walls in terms of diffraction indices and transmission/reflection coefficients. The implications and applications of such a permeable domain wall would certainly be an interesting direction for further research.

### Exploring surface geometries

The ground state properties in the vicinity of common geometrical structures are also of interest. One example of such a structure is a conical intersection - specifically in the case where a single dipole is placed directly at the intersection point. It would be interesting to see to what extent this center-dipole impacts (or controls) the surrounding ground state dipole orientations. Another structure that will likely be encountered frequently in experimental setups are lattice defects. For lattice structures on curved surfaces, the formation of point defects can be expected. Especially when these defects are positioned with some periodicity, their impact on the dipole orientations and phonon dynamics may also be of interest. Related setups could

also include the ground state properties of dipoles in fractal lattices, such as the Sierpiński triangle.

### **Experimental realizations**

The key motivation for this thesis was to gain a fundamental understanding of properties arising due to the interplay of long-range interactions and curved geometries. Practical applications and experimental realizations of these systems were not at all considered during the conception of the individual projects. Nevertheless, several setups related to curved dipole lattices have already been mentioned in Chapters 3 and 4. In that regard, the perhaps most promising platforms for an experimental realization are Rydberg atoms (see also the last paragraph of Sec. 4.2) or curvilinear arrays of magnetic dipoles (see also the last paragraph of Sec. 4.3). Especially Rydberg atoms are promising candidates, due to the possibilities provided by tweezer-arrays in arranging these atoms, as well as their potential for exhibiting enormous permanent dipole moments (see Ref. [257]). In the case of magnetic dipole arrays on curved surfaces, the fact that exchange interactions typically dominate the dipole-dipole interaction is certainly a problem. And while there are ways to overcome this problem, such as fabricating dipoles from single-domain magnetic islands (similar to e.g. Ref. [287]), any experimental realization of curved dipole lattices from magnetic materials will certainly be a challenge. Nevertheless, the present developments regarding the fabrication and control of nano-scale systems are certainly promising.



# Bibliography

- [1] O. Ciftja, “Novel Research in Low-Dimensional Systems”, *Nanomaterials* **13**, 364 (2023).
- [2] F. J. Owens, “The Physics of Low Dimensional Materials”, *MRS Bull.* **43**, 892 (2018).
- [3] S. Dodelson, *Gravitational lensing* (Cambridge university press, Cambridge, 2017).
- [4] M. Bartelmann, “Gravitational lensing”, *Class. Quantum Grav.* **27**, 233001 (2010).
- [5] J. Von Bergmann and H. Von Bergmann, “Foucault pendulum through basic geometry”, *Am. J. Phys.* **75**, 888 (2007).
- [6] J. Oprea, “Geometry and the Foucault Pendulum”, *Am. Math. Mon.* **102**, 515 (1995).
- [7] P. Schmelcher, “Effective long-range interactions in confined curved dimensions”, *Europhys. Lett.* **95**, 50005 (2011).
- [8] A. V. Zampetaki, J. Stockhofe, S. Krönke, and P. Schmelcher, “Classical scattering of charged particles confined on an inhomogeneous helix”, *Phys. Rev. E* **88**, 043202 (2013).
- [9] A. V. Zampetaki, J. Stockhofe, and P. Schmelcher, “Degeneracy and inversion of band structure for Wigner crystals on a closed helix”, *Phys. Rev. A* **91**, 023409 (2015).
- [10] A. V. Zampetaki, J. Stockhofe, and P. Schmelcher, “Dynamics of nonlinear excitations of helically confined charges”, *Phys. Rev. E* **92**, 042905 (2015).
- [11] A. V. Zampetaki, J. Stockhofe, and P. Schmelcher, “Pinned-to-sliding transition and structural crossovers for helically confined charges”, *Phys. Rev. E* **95**, 022205 (2017).
- [12] A. V. Zampetaki, J. Stockhofe, and P. Schmelcher, “Electrostatic bending response of a charged helix”, *Phys. Rev. E* **97**, 042503 (2018).
- [13] E. Wigner, “On the Interaction of Electrons in Metals”, *Phys. Rev.* **46**, 1002 (1934).
- [14] H. Li, S. Li, E. C. Regan, D. Wang, W. Zhao, S. Kahn, K. Yumigeta, M. Blei, T. Taniguchi, K. Watanabe, S. Tongay, A. Zettl, M. F. Crommie, and F. Wang, “Imaging two-dimensional generalized Wigner crystals”, *Nature* **597**, 650 (2021).
- [15] V. J. Goldman, M. Santos, M. Shayegan, and J. E. Cunningham, “Evidence for two-dimensional quantum Wigner crystal”, *Phys. Rev. Lett.* **65**, 2189 (1990).
- [16] J. Jang, B. M. Hunt, L. N. Pfeiffer, K. W. West, and R. C. Ashoori, “Sharp tunnelling resonance from the vibrations of an electronic Wigner crystal”, *Nature Phys.* **13**, 340 (2017).

- [17] E. C. Regan, D. Wang, C. Jin, M. I. Bakti Utama, B. Gao, X. Wei, S. Zhao, W. Zhao, Z. Zhang, K. Yumigeta, M. Blei, J. D. Carlström, K. Watanabe, T. Taniguchi, S. Tongay, M. Crommie, A. Zettl, and F. Wang, “Mott and generalized Wigner crystal states in WSe<sub>2</sub>/WS<sub>2</sub> moiré superlattices”, *Nature* **579**, 359 (2020).
- [18] C. C. Grimes and G. Adams, “Evidence for a Liquid-to-Crystal Phase Transition in a Classical, Two-Dimensional Sheet of Electrons”, *Phys. Rev. Lett.* **42**, 795 (1979).
- [19] Y. Xu, S. Liu, D. A. Rhodes, K. Watanabe, T. Taniguchi, J. Hone, V. Elser, K. F. Mak, and J. Shan, “Correlated insulating states at fractional fillings of moiré superlattices”, *Nature* **587**, 214 (2020).
- [20] M. Drewsen, I. Jensen, J. Lindballe, N. Nissen, R. Martinussen, A. Mortensen, P. Staantum, and D. Voigt, “Ion Coulomb crystals: a tool for studying ion processes”, *Int. J. Mass Spectrom.* **229**, 83 (2003).
- [21] M. Drewsen, “Ion Coulomb crystals”, *Physica B* **460**, 105 (2015).
- [22] L. Schmöger, O. O. Versolato, M. Schwarz, M. Kohnen, A. Windberger, B. Piest, S. Feuchtenbeiner, J. Pedregosa-Gutierrez, T. Leopold, P. Micke, A. K. Hansen, T. M. Baumann, M. Drewsen, J. Ullrich, P. O. Schmidt, and J. R. C. López-Urrutia, “Coulomb crystallization of highly charged ions”, *Science* **347**, 1233 (2015).
- [23] J. M. Taylor and T. Calarco, “Wigner crystals of ions as quantum hard drives”, *Phys. Rev. A* **78**, 062331 (2008).
- [24] H. M. Van Horn, “Dense Astrophysical Plasmas”, *Science* **252**, 384 (1991).
- [25] M. Baus, “Statistical mechanics of simple coulomb systems”, *Phys. Rep.* **59**, 1 (1980).
- [26] T. Saigo and S. Hamaguchi, “Shear viscosity of strongly coupled Yukawa systems”, *Phys. Plasmas* **9**, 1210 (2002).
- [27] P. Vieillefosse and J. P. Hansen, “Statistical mechanics of dense ionized matter. V. Hydrodynamic limit and transport coefficients of the classical one-component plasma”, *Phys. Rev. A* **12**, 1106 (1975).
- [28] J. P. Hansen, “Statistical Mechanics of Dense Ionized Matter. I. Equilibrium Properties of the Classical One-Component Plasma”, *Phys. Rev. A* **8**, 3096 (1973).
- [29] E. L. Pollock and J. P. Hansen, “Statistical Mechanics of Dense Ionized Matter. II. Equilibrium Properties and Melting Transition of the Crystallized One-Component Plasma”, *Phys. Rev. A* **8**, 3110 (1973).
- [30] S. Ichimaru, “Strongly coupled plasmas: high-density classical plasmas and degenerate electron liquids”, *Rev. Mod. Phys.* **54**, 1017 (1982).
- [31] J. P. Schiffer, “Order in confined ions”, *J. Phys. B: At. Mol. Opt. Phys.* **36**, 511 (2003).
- [32] F. J. Rogers and H. E. Dewitt, eds., *Strongly Coupled Plasma Physics* (Springer US, Boston, MA, 1987).
- [33] J. Daligault, K. Ø. Rasmussen, and S. D. Baalrud, “Determination of the shear viscosity of the one-component plasma”, *Phys. Rev. E* **90**, 033105 (2014).

- [34] J. P. Hansen, I. R. McDonald, and E. L. Pollock, "Statistical mechanics of dense ionized matter. III. Dynamical properties of the classical one-component plasma", *Phys. Rev. A* **11**, 1025 (1975).
- [35] B. Bernu and P. Vieillefosse, "Transport coefficients of the classical one-component plasma", *Phys. Rev. A* **18**, 2345 (1978).
- [36] Z. Donkó, B. Nyíri, L. Szalai, and S. Holló, "Thermal Conductivity of the Classical Electron One-Component Plasma", *Phys. Rev. Lett.* **81**, 1622 (1998).
- [37] Z. Donkó and P. Hartmann, "Thermal conductivity of strongly coupled Yukawa liquids", *Phys. Rev. E* **69**, 016405 (2004).
- [38] T. Kamimura and O. Ishihara, "Coulomb double helical structure", *Phys. Rev. E* **85**, 016406 (2012).
- [39] T. W. Hyde, J. Kong, and L. S. Matthews, "Helical structures in vertically aligned dust particle chains in a complex plasma", *Phys. Rev. E* **87**, 053106 (2013).
- [40] N. G. Gusein-zade and V. N. Tsytovich, "Spectral properties of an N-pole helical structure consisting of like-charged equal-size dust grains", *Plasma Phys. Rep.* **32**, 668 (2006).
- [41] H. Landa, B. Reznik, J. Brox, M. Mielenz, and T. Schaetz, "Structure, dynamics and bifurcations of discrete solitons in trapped ion crystals", *New J. Phys.* **15**, 093003 (2013).
- [42] L. G. D'yachkov, M. I. Myasnikov, O. F. Petrov, T. W. Hyde, J. Kong, and L. Matthews, "Two-dimensional and three-dimensional Coulomb clusters in parabolic traps", *Phys. Plasmas* **21**, 093702 (2014).
- [43] G. Piacente, I. V. Schweigert, J. J. Betouras, and F. M. Peeters, "Generic properties of a quasi-one-dimensional classical Wigner crystal", *Phys. Rev. B* **69**, 045324 (2004).
- [44] N. G. Gusein-zade, "Helical Structures in Complex Plasma I: Noncollective Interaction", *Plasma Phys. Rep.* **31**, 392 (2005).
- [45] V. N. Tsytovich, "Helical Structures in Complex Plasma II: Collective Interaction", *Plasma Phys. Rep.* **31**, 824 (2005).
- [46] G. Birkel, S. Kassner, and H. Walther, "Multiple-shell structures of laser-cooled  $24\text{Mg}^+$  ions in a quadrupole storage ring", *Nature* **357**, 310 (1992).
- [47] J. J. Bollinger, D. J. Wineland, and D. H. E. Dubin, "Non-neutral ion plasmas and crystals, laser cooling, and atomic clocks", *Phys. Plasmas* **1**, 1403 (1994).
- [48] R. Hasse and J. Schiffer, "The structure of the cylindrically confined Coulomb lattice", *Ann. Phys.* **203**, 419 (1990).
- [49] V. E. Fortov, A. G. Khrapak, S. A. Khrapak, V. I. Molotkov, and O. F. Petrov, "Dusty plasmas", *Phys.-Usp.* **47**, 447 (2004).
- [50] V. Fortov, A. Ivlev, S. Khrapak, A. Khrapak, and G. Morfill, "Complex (dusty) plasmas: Current status, open issues, perspectives", *Phys. Rep.* **421**, 1 (2005).
- [51] A. M. Ignatov, "Basics of dusty plasma", *Plasma Phys. Rep.* **31**, 46 (2005).
- [52] G. S. Manning and J. Ray, "Counterion Condensation Revisited", *J. Biomol. Struct. Dyn.* **16**, 461 (1998).
- [53] G. S. Manning, "Counterion Condensation on Charged Spheres, Cylinders, and Planes", *J. Phys. Chem. B* **111**, 8554 (2007).

- [54] H.-K. Tsao, "Counterion Distribution Enclosed in a Cylinder and a Sphere", *J. Phys. Chem. B* **102**, 10243 (1998).
- [55] D. A. J. Gillespie, J. E. Hallett, O. Elujoba, A. F. Che Hamzah, R. M. Richardson, and P. Bartlett, "Counterion condensation on spheres in the salt-free limit", *Soft Matter* **10**, 566 (2014).
- [56] M. D. Frank-Kamenetskii, V. V. Anshelevich, and A. V. Lukashin, "Polyelectrolyte model of DNA", *Sov.Phys.Usp* **30**, 317 (1987).
- [57] S. P. Singh and M. Muthukumar, "Electrophoretic mobilities of counterions and a polymer in cylindrical pores", *J. Chem. Phys.* **141**, 114901 (2014).
- [58] B. I. Shklovskii, "Screening of a macroion by multivalent ions: Correlation-induced inversion of charge", *Phys. Rev. E* **60**, 5802 (1999).
- [59] B. I. Shklovskii, "Wigner Crystal Model of Counterion Induced Bundle Formation of Rodlike Polyelectrolytes", *Phys. Rev. Lett.* **82**, 3268 (1999).
- [60] O. Kibis, "Electron-electron interaction in a spiral quantum wire", *Phys. Lett. A* **166**, 393 (1992).
- [61] P. Drude, *Lehrbuch der Optik*, 2nd ed. (Hirzel, Leipzig, 1906).
- [62] J. F. Marko and E. D. Siggia, "Bending and twisting elasticity of DNA", *Macromolecules* **27**, 981 (1994).
- [63] A. A. Kornyshev, D. J. Lee, S. Leikin, and A. Wynveen, "Structure and interactions of biological helices", *Rev. Mod. Phys.* **79**, 943 (2007).
- [64] M. Ilamaran, A. Janeena, S. Valappil, K. N. Ramudu, G. Shanmugam, and A. Niraikulam, "A self-assembly and higher order structure forming triple helical protein as a novel biomaterial for cell proliferation", *Biomater. Sci.* **7**, 2191 (2019).
- [65] U. Meierhenrich, *Amino acids and the asymmetry of life: caught in the act of formation*, Advances in Astrobiology and Biogeophysics (Springer, Berlin Heidelberg, 2008).
- [66] Z. Ren and P.-X. Gao, "A review of helical nanostructures: growth theories, synthesis strategies and properties", *Nanoscale* **6**, 9366 (2014).
- [67] A. Shaikjee and N. J. Coville, "The synthesis, properties and uses of carbon materials with helical morphology", *J. Adv. Res.* **3**, 195 (2012).
- [68] V. Percec, M. Glodde, T. K. Bera, Y. Miura, I. Shiyonovskaya, K. D. Singer, V. S. K. Balagurusamy, P. A. Heiney, I. Schnell, A. Rapp, H.-W. Spiess, S. D. Hudson, and H. Duan, "Self-organization of supramolecular helical dendrimers into complex electronic materials", *Nature* **419**, 384 (2002).
- [69] E. Yashima, K. Maeda, H. Iida, Y. Furusho, and K. Nagai, "Helical Polymers: Synthesis, Structures, and Functions", *Chem. Rev.* **109**, 6102 (2009).
- [70] D. Pijper and B. L. Feringa, "Control of dynamic helicity at the macro- and supramolecular level", *Soft Matter* **4**, 1349 (2008).
- [71] R. C. Merkle and K. E. Drexler, "Helical logic", *Nanotechnology* **7**, 325 (1996).
- [72] D. Das Gupta and S. K. Maiti, "Implementation of logical operations using antiferromagnetic helical molecule", *J. Phys. D: Appl. Phys.* **56**, 465304 (2023).
- [73] A. V. Malyshev, "DNA Double Helices for Single Molecule Electronics", *Phys. Rev. Lett.* **98**, 096801 (2007).

- [74] J. Li, S. Sattayasamitsathit, R. Dong, W. Gao, R. Tam, X. Feng, S. Ai, and J. Wang, "Template electrosynthesis of tailored-made helical nanoswimmers", *Nanoscale* **6**, 9415 (2014).
- [75] J. G. Gibbs, A. G. Mark, T.-C. Lee, S. Eslami, D. Schamel, and P. Fischer, "Nanohelices by shadow growth", *Nanoscale* **6**, 9457 (2014).
- [76] H. Liu, X. Shen, Z.-G. Wang, A. Kuzyk, and B. Ding, "Helical nanostructures based on DNA self-assembly", *Nanoscale* **6**, 9331 (2014).
- [77] S. N. Fejer, D. Chakrabarti, H. Kusumaatmaja, and D. J. Wales, "Design principles for Bernal spirals and helices with tunable pitch", *Nanoscale* **6**, 9448 (2014).
- [78] L. Liu, L. Zhang, S. M. Kim, and S. Park, "Helical metallic micro- and nanostructures: fabrication and application", *Nanoscale* **6**, 9355 (2014).
- [79] K. T. Lau, M. Lu, and D. Hui, "Coiled carbon nanotubes: Synthesis and their potential applications in advanced composite structures", *Compos. B. Eng.* **37**, 437 (2006).
- [80] V. Ivanov, J. Nagy, P. Lambin, A. Lucas, X. B. Zhang, X. F. Zhang, D. Bernaerts, G. Van Tendeloo, S. Amelinckx, and J. Van Landuyt, "The study of carbon nanotubules produced by catalytic method", *Chem. Phys. Lett.* **223**, 329 (1994).
- [81] Y. Wang, J. Xu, Y. Wang, and H. Chen, "Emerging chirality in nanoscience", *Chem. Soc. Rev.* **42**, 2930 (2013).
- [82] M. Yang and N. A. Kotov, "Nanoscale helices from inorganic materials", *J. Mater. Chem.* **21**, 6775 (2011).
- [83] D. B. Amabilino, "Chiral nanoscale systems: preparation, structure, properties and function", *Chem. Soc. Rev.* **38**, 669 (2009).
- [84] D. Reitz and A. Rauschenbeutel, "Nanofiber-Based Double-Helix Dipole Trap for Cold Neutral Atoms", *Opt. Comm.* **285**, 4705 (2012).
- [85] E. Vetsch, D. Reitz, G. Sagué, R. Schmidt, S. T. Dawkins, and A. Rauschenbeutel, "Optical Interface Created by Laser-Cooled Atoms Trapped in the Evanescent Field Surrounding an Optical Nanofiber", *Phys. Rev. Lett.* **104**, 203603 (2010).
- [86] E. Vetsch, S. T. Dawkins, R. Mitsch, D. Reitz, P. Schneeweiss, and A. Rauschenbeutel, "Nanofiber-Based Optical Trapping of Cold Neutral Atoms", *IEEE* **18**, 1763 (2012).
- [87] T. Tokihiro and E. Hanamura, "Geometrical effects on one-dimensional excitons", *Phys. Rev. Lett.* **71**, 1423 (1993).
- [88] R. Sarma and Y. Gartstein, "Wannier–Mott excitons on a helically-shaped one-dimensional semiconductor", *Phys. Lett. A* **374**, 3076 (2010).
- [89] J. K. Pedersen, D. V. Fedorov, A. S. Jensen, and N. T. Zinner, "Formation of classical crystals of dipolar particles in a helical geometry", *J. Phys. B: At. Mol. Opt. Phys.* **47**, 165103 (2014).
- [90] J. K. Pedersen, D. V. Fedorov, A. S. Jensen, and N. T. Zinner, "Quantum few-body bound states of dipolar particles in a helical geometry", *J. Phys. B: At. Mol. Opt. Phys.* **49**, 024002 (2016).
- [91] J. K. Pedersen, D. V. Fedorov, A. S. Jensen, and N. T. Zinner, "Quantum single-particle properties in a one-dimensional curved space", *J. Mod. Opt.* **63**, 1814 (2016).

- [92] K. T. Law and D. E. Feldman, “Quantum Phase Transition Between a Luttinger Liquid and a Gas of Cold Molecules”, *Phys. Rev. Lett.* **101**, 096401 (2008).
- [93] Y. N. Gartstein, T. D. Bustamante, and S. O. Castillo, “Polarons and excitons on a cylinder: a simplified model for nanotubes in polar environments”, *J. Phys.: Condens. Matter* **19**, 156210 (2007).
- [94] G. Napoli, O. V. Pylypovskiy, D. D. Sheka, and L. Vergori, “Nematic shells: new insights in topology- and curvature-induced effects”, *Soft Matter* **17**, 10322 (2021).
- [95] J. Thomson, “XXIV. *On the structure of the atom: an investigation of the stability and periods of oscillation of a number of corpuscles arranged at equal intervals around the circumference of a circle; with application of the results to the theory of atomic structure*”, *The London, Edinburgh, and Dublin Philosophical Magazine and Journal of Science* **7**, 237 (1904).
- [96] J. Plettenberg, J. Stockhofe, A. V. Zampetaki, and P. Schmelcher, “Local equilibria and state transfer of charged classical particles on a helix in an electric field”, *Phys. Rev. E* **95**, 012213 (2017).
- [97] R. C. T. da Costa, “Quantum mechanics of a constrained particle”, *Phys. Rev. A* **23**, 1982 (1981).
- [98] R. C. T. da Costa, “Constraints in quantum mechanics”, *Phys. Rev. A* **25**, 2893 (1982).
- [99] M. Encinosa and L. Mott, “Curvature-induced toroidal bound states”, *Phys. Rev. A* **68**, 014102 (2003).
- [100] Y. Ohta, S. Nishimoto, T. Shirakawa, and Y. Yamaguchi, “Ring-exchange mechanism for triplet superconductivity in a two-chain Hubbard model: Possible relevance to Bechgaard salts”, *Phys. Rev. B* **72**, 012503 (2005).
- [101] K. Hamacher, C. Gros, and W. Wenzel, “Interaction-Induced Collapse of a Section of the Fermi Sea in the Zigzag Hubbard Ladder”, *Phys. Rev. Lett.* **88**, 217203 (2002).
- [102] C. Gros, K. Hamacher, and W. Wenzel, “Breakdown of the Luttinger sum rule at the Mott-Hubbard transition in the one-dimensional  $t_1 - t_2$  Hubbard model”, *Europhys. Lett.* **69**, 616 (2005).
- [103] S. Kim and H. Lee, “Properties of the  $t_1 - t_2$  one-dimensional Hubbard model at finite temperature”, *J. Korean Phys. Soc.* **71**, 191 (2017).
- [104] L. F. Tocchio, F. Becca, and C. Gros, “Interaction-induced Fermi-surface renormalization in the  $t_1 - t_2$  Hubbard model close to the Mott-Hubbard transition”, *Phys. Rev. B* **81**, 205109 (2010).
- [105] J. Stockhofe and P. Schmelcher, “Bloch dynamics in lattices with long-range hopping”, *Phys. Rev. A* **91**, 023606 (2015).
- [106] J. Stockhofe and P. Schmelcher, “Sub- and supercritical defect scattering in Schrödinger chains with higher-order hopping”, *Phys. Rev. A* **92**, 023605 (2015).
- [107] J. Stockhofe and P. Schmelcher, “Modulational instability and localized breather modes in the discrete nonlinear Schrödinger equation with helicoidal hopping”, *Physica D* **328–329**, 9 (2016).
- [108] W. Qi, Z.-H. Li, J.-T. Cai, G.-Q. Li, and H.-F. Li, “Modulational instability and localized breather in discrete Schrödinger equation with helicoidal hopping and a power-law nonlinearity”, *Phys. Lett. A* **382**, 1778 (2018).

- [109] J. Ding, T. Wu, X. Chang, and B. Tang, “Modulational instability and discrete breathers in a nonlinear helicoidal lattice model”, *Commun. Nonlinear Sci. Numer. Simul.* **59**, 349 (2018).
- [110] A.-M. Guo, P.-J. Hu, X.-H. Gao, T.-F. Fang, and Q.-F. Sun, “Topological phase transitions of Thouless charge pumping realized in helical organic molecules with long-range hopping”, *Phys. Rev. B* **102**, 155402 (2020).
- [111] B. Tang, X. Chang, and K. Deng, “Anharmonic Bloch oscillations in a helicoidal lattice”, *Phys. Lett. A* **381**, 3701 (2017).
- [112] S.-J. Xiong, “Bethe ansatz study of 1+1 dimensional Hubbard model”, *Z. Phys. B - Condensed Matter* **89**, 29 (1992).
- [113] W. Wang and S. Xiong, “Possible first order phase transition in the one-dimensional helical Hubbard model”, *Phys. Lett. A* **156**, 415 (1991).
- [114] P.-J. Hu, T.-F. Fang, A.-M. Guo, and Q.-F. Sun, “Aharonov–Bohm-like effects and Fano resonances in circular DNA molecular junctions”, *Appl. Phys. Lett.* **121**, 154102 (2022).
- [115] O. M. Braun and Y. S. Kivshar, *The Frenkel-Kontorova model: concepts, methods, and applications*, Theoretical and Mathematical Physics (Springer, Berlin Heidelberg, 2004).
- [116] T. Kontorova and J. Frenkel, “On the theory of plastic deformation and twinning I”, *Zh. Eksp. Teor. Fiz* **8**, 89 (1938).
- [117] T. Kontorova and J. Frenkel, “On the theory of plastic deformation and twinning II”, *Zh. Eksp. Teor. Fiz* **8**, 1340 (1938).
- [118] A. Kochendörfer and A. Seeger, “Theorie der Versetzungen in eindimensionalen Atomreihen I”, *Zeitschrift für Physik* **127**, 533 (1950).
- [119] A. Seeger and A. Kochendörfer, “Theorie der Versetzungen in eindimensionalen Atomreihen II”, *Zeitschrift für Physik* **130**, 321 (1951).
- [120] A. Seeger and A. Kochendörfer, “Theorie der Versetzungen in eindimensionalen Atomreihen III”, *Zeitschrift für Physik* **134**, 173 (1953).
- [121] R. Döttling, J. Eßlinger, W. Lay, and A. Seeger, “Radiative damping of driven sine-Gordon breathers”, in *Nonlinear coherent structures*, edited by M. Barthes and J. Léon (1990), pp. 193–201.
- [122] S. Flach, O. Yevtushenko, and Y. Zolotaryuk, “Directed Current due to Broken Time-Space Symmetry”, *Phys. Rev. Lett.* **84**, 2358 (2000).
- [123] P. Reimann, “Brownian motors: noisy transport far from equilibrium”, *Phys. Rep.* **361**, 57 (2002).
- [124] H. Schanz, M.-F. Otto, R. Ketzmerick, and T. Dittrich, “Classical and Quantum Hamiltonian Ratchets”, *Phys. Rev. Lett.* **87**, 070601 (2001).
- [125] N. R. Quintero, J. A. Cuesta, and R. Alvarez-Nodarse, “Symmetries shape the current in ratchets induced by a biharmonic driving force”, *Phys. Rev. E* **81**, 030102(R) (2010).
- [126] S. Denisov, S. Flach, and P. Hänggi, “Tunable transport with broken space-time symmetries”, *Phys. Rep.* **538**, 77 (2014).
- [127] F. Renzoni, in *Advances In Atomic, Molecular, and Optical Physics*, Vol. 57 (Elsevier, 2009), pp. 1–32.

- [128] D. Cubero and F. Renzoni, “Hidden Symmetries, Instabilities, and Current Suppression in Brownian Ratchets”, *Phys. Rev. Lett.* **116**, 010602 (2016).
- [129] S. Matthias and F. Müller, “Asymmetric pores in a silicon membrane acting as massively parallel brownian ratchets”, *Nature* **424**, 53 (2003).
- [130] C. Petri, F. Lenz, B. Liebchen, F. Diakonov, and P. Schmelcher, “Formation of density waves via interface conversion of ballistic and diffusive motion”, *Europhys. Lett.* **95**, 30005 (2011).
- [131] T. Wulf, C. Petri, B. Liebchen, and P. Schmelcher, “Analysis of interface conversion processes of ballistic and diffusive motion in driven superlattices”, *Phys. Rev. E* **86**, 016201 (2012).
- [132] J. F. Wambaugh, C. Reichhardt, and C. J. Olson, “Ratchet-induced segregation and transport of nonspherical grains”, *Phys. Rev. E* **65**, 031308 (2002).
- [133] A. K. Mukhopadhyay, B. Liebchen, and P. Schmelcher, “Simultaneous Control of Multispecies Particle Transport and Segregation in Driven Lattices”, *Phys. Rev. Lett.* **120**, 218002 (2018).
- [134] P. Hänggi and F. Marchesoni, “Artificial Brownian motors: Controlling transport on the nanoscale”, *Rev. Mod. Phys.* **81**, 387 (2009).
- [135] R. D. Astumian, “Thermodynamics and Kinetics of a Brownian Motor”, *Science* **276**, 917 (1997).
- [136] P. L. Kapitza, “A pendulum with oscillating suspension”, *Usp. Fiz. Nauk* **44**, 7 (1951).
- [137] J. Quintanilla, M. Perez, R. Balderas, A. Gonzalez, A. Cardenas, M. Maya, and D. Piovesan, “Inertial Stabilization of Upright Posture while walking”, in *2021 10th International IEEE/EMBS Conference on Neural Engineering (NER)* (May 2021), pp. 849–852.
- [138] I. Adler, D. Barabe, and V. Jean, “A History of the Study of Phyllotaxis”, *Ann. Bot.* **80**, 231 (1997).
- [139] Y. L. Huang, R. Wang, T. C. Niu, S. Kera, N. Ueno, J. Pflaum, A. T. S. Wee, and W. Chen, “One dimensional molecular dipole chain arrays on graphite via nanoscale phase separation”, *Chem. Commun.* **46**, 9040 (2010).
- [140] D. Jérôme, F. Creuzet, and C. Bourbonnais, “A Survey of the Physics of Organic Conductors and Superconductors”, *Phys. Scr.* **T27**, 130 (1988).
- [141] J. Weckesser, A. De Vita, J. V. Barth, C. Cai, and K. Kern, “Mesoscopic Correlation of Supramolecular Chirality in One-Dimensional Hydrogen-Bonded Assemblies”, *Phys. Rev. Lett.* **87**, 096101 (2001).
- [142] M. Hersam, J. Lee, N. Guisinger, and J. Lyding, “Implications of atomic-level manipulation on the Si(100) surface: From enhanced CMOS reliability to molecular nanoelectronics”, *Superlattices Microstruct.* **27**, 583 (2000).
- [143] J. Schnadt, E. Rauls, W. Xu, R. T. Vang, J. Knudsen, E. Lægsgaard, Z. Li, B. Hammer, and F. Besenbacher, “Extended One-Dimensional Supramolecular Assembly on a Stepped Surface”, *Phys. Rev. Lett.* **100**, 046103 (2008).
- [144] J. Vacek and J. Michl, “Molecular dynamics of a grid-mounted molecular dipolar rotor in a rotating electric field”, *Proc. Natl. Acad. Sci. U.S.A.* **98**, 5481 (2001).
- [145] S. W. DeLeeuw, D. Solvaeson, M. A. Ratner, and J. Michl, “Molecular Dipole Chains: Excitations and Dissipation”, *J. Phys. Chem. B* **102**, 3876 (1998).

- [146] E. Sim, M. A. Ratner, and S. W. de Leeuw, "Molecular Dipole Chains II", *J. Phys. Chem. B* **103**, 8663 (1999).
- [147] J. J. de Jonge, M. A. Ratner, S. W. de Leeuw, and R. O. Simonis, "Molecular Dipole Chains III: Energy Transfer", *J. Phys. Chem. B* **108**, 2666 (2004).
- [148] G. S. Kottas, L. I. Clarke, D. Horinek, and J. Michl, "Artificial Molecular Rotors", *Chem. Rev.* **105**, 1281 (2005).
- [149] J. M. Speight and Y. Zolotaryuk, "Kinks in dipole chains", *Nonlinearity* **19**, 1365 (2006).
- [150] E. Y. Vedmedenko and D. Altwein, "Topologically Protected Magnetic Helix for All-Spin-Based Applications", *Phys. Rev. Lett.* **112**, 017206 (2014).
- [151] R. González-Férez, M. Iñarrea, J. P. Salas, and P. Schmelcher, "Analysis of the classical phase space and energy transfer for two rotating dipoles with and without external electric field", *Phys. Rev. E* **95**, 012209 (2017).
- [152] H. Zorski and E. Infeld, "New soliton equation for dipole chains", *Phys. Rev. Lett.* **68**, 1180 (1992).
- [153] L. Chotorlishvili and J. Berakdar, "Dynamics of dipolar molecular chains: from low excitations to soliton formation and classical chaotic dynamics", *J. Phys. B: At. Mol. Opt. Phys.* **40**, 3757 (2007).
- [154] M. Remoissenet, "Non-linear excitations in a compressible chain of dipoles", *J. Phys. C: Solid State Phys.* **14**, L335 (1981).
- [155] J. J. de Jonge, M. A. Ratner, and S. W. de Leeuw, "Local Field Controlled Switching in a One-Dimensional Dipolar Array", *J. Phys. Chem. C* **111**, 3770 (2007).
- [156] A. Zampetaki, J. P. Salas, and P. Schmelcher, "Energy transfer mechanisms in a dipole chain: From energy equipartition to the formation of breathers", *Phys. Rev. E* **98**, 022202 (2018).
- [157] E. G. Fateev, "Supersensitivity in a chain of closely spaced electric dipoles with variable moments", *Phys. Rev. E* **65**, 021403 (2002).
- [158] D. F. Kornovan, K. V. Baryshnikova, and M. I. Petrov, "Suppression of high-order multipole moments in a resonant periodic dipole chain", *J. Phys.: Conf. Ser.* **1461**, 012070 (2020).
- [159] S. A. Maier, P. G. Kik, and H. A. Atwater, "Optical pulse propagation in metal nanoparticle chain waveguides", *Phys. Rev. B* **67**, 205402 (2003).
- [160] M. L. Brongersma, J. W. Hartman, and H. A. Atwater, "Electromagnetic energy transfer and switching in nanoparticle chain arrays below the diffraction limit", *Phys. Rev. B* **62**, R16356 (2000).
- [161] A. V. Dolgikh and D. S. Kosov, "Out-of-equilibrium one-dimensional disordered dipole chain", *Phys. Rev. E* **88**, 012118 (2013).
- [162] R. P. Feynman, *The Feynman lectures on physics. Volume 2: Mainly electromagnetism and matter*, The new millennium edition, paperback first published (Basic Books, New York, 2011).
- [163] D. D. Stancil and A. Prabhakar, *Spin Waves: Theory and Applications* (Springer US Springer e-books, Boston, MA, 2009).
- [164] J. Van Kranendonk and J. H. Van Vleck, "Spin Waves", *Rev. Mod. Phys.* **30**, 1 (1958).

- [165] J. Cisternas, M. Navarro, S. Duarte, and A. Concha, "Equilibrium and symmetries of altitudinal magnetic rotors on a circle", *Chaos* **32**, 123120 (2022).
- [166] J. J. de Jonge, M. A. Ratner, S. W. de Leeuw, and R. O. Simonis, "Controlling the Energy Transfer in Dipole Chains", *J. Phys. Chem. B* **110**, 442 (2006).
- [167] T. D. Cornelissen, M. Biler, I. Urbanaviciute, P. Norman, M. Linares, and M. Kemerink, "Kinetic Monte Carlo simulations of organic ferroelectrics", *Phys. Chem. Chem. Phys.* **21**, 1375 (2019).
- [168] I. Urbanaviciute, S. Bhattacharjee, M. Biler, J. A. M. Lugger, T. D. Cornelissen, P. Norman, M. Linares, R. P. Sijbesma, and M. Kemerink, "Suppressing depolarization by tail substitution in an organic supramolecular ferroelectric", *Phys. Chem. Chem. Phys.* **21**, 2069 (2019).
- [169] A. Wada, "The alpha-helix as an electric macro-dipole", *Adv Biophys*, 1 (1976).
- [170] A. D. Suprun and L. V. Shmeleva, "Alpha-helical regions of the protein molecule as organic nanotubes", *Nanoscale Res. Lett.* **9**, 200 (2014).
- [171] A. Liwo, R. J. Wawak, H. A. Scheraga, M. R. Pincus, and S. Rackovsky, "Calculation of protein backbone geometry from A-carbon coordinates based on peptide-group dipole alignment", *Protein Sci.* **2**, 1697 (1993).
- [172] L. Piela and H. A. Scheraga, "On the multiple-minima problem in the conformational analysis of polypeptides. I. Backbone degrees of freedom for a perturbed  $\alpha$ -helix", *Biopolymers* **26**, S33 (1987).
- [173] A. Korniienko, V. Kravchuk, O. Pylypovskiy, D. Sheka, J. Van Den Brink, and Y. Gaididei, "Curvature induced magnonic crystal in nanowires", *SciPost Phys.* **7**, 035 (2019).
- [174] D. D. Sheka, V. P. Kravchuk, K. V. Yershov, and Y. Gaididei, "Torsion-induced effects in magnetic nanowires", *Phys. Rev. B* **92**, 054417 (2015).
- [175] Q. Wang, J. Otterbach, and S. F. Yelin, "Interacting in-plane molecular dipoles in a zigzag chain", *Phys. Rev. A* **96**, 043615 (2017).
- [176] N. R. Ghimire and S. F. Yelin, "Frustrated plane-polarized dipoles in one dimension", *Phys. Rev. B* **100**, 115110 (2019).
- [177] S. Gammelmark and N. T. Zinner, "Dipoles on a two-leg ladder", *Phys. Rev. B* **88**, 245135 (2013).
- [178] H. Mosadeq and R. Asgari, "Two-leg ladder systems with dipole-dipole Fermion interactions", *J. Phys.: Condens. Matter* **30**, 205601 (2018).
- [179] D. Reinhardt, E.-R. Pesce, P. Stieger, T. Mandel, K. Baltensperger, M. Bennett, J. Traas, J. Friml, and C. Kuhlemeier, "Regulation of phyllotaxis by polar auxin transport", *Nature* **426**, 255 (2003).
- [180] R. S. Smith, S. Guyomarc'h, T. Mandel, D. Reinhardt, C. Kuhlemeier, and P. Prusinkiewicz, "A plausible model of phyllotaxis", *Proc. Natl. Acad. Sci. U.S.A.* **103**, 1301 (2006).
- [181] Y. Deb, D. Marti, M. Frenz, C. Kuhlemeier, and D. Reinhardt, "Phyllotaxis involves auxin drainage through leaf primordia", *Development* **142**, 1992 (2015).
- [182] N. Bhatia, B. Bozorg, A. Larsson, C. Ohno, H. Jönsson, and M. G. Heisler, "Auxin Acts through MONOPTEROS to Regulate Plant Cell Polarity and Pattern Phyllotaxis", *Curr. Bio.* **26**, 3202 (2016).

- [183] C. Kuhlemeier, "Phyllotaxis", *Curr. Bio.* **27**, R882 (2017).
- [184] L. F. Bravais and A. Bravais, "Essai sur la disposition des feuilles curvisériées", *Ann. Sci. Nat. Bot. Biol. Veg.* **7**, 42, 193, and 291 (1837).
- [185] F. M. Van Der Linden, "Creating phyllotaxis: the dislodgement model", *Math. Biosci.* **100**, 161 (1990).
- [186] G. van Iterson, *Mathematische und mikroskopisch-anatomische Studien über Blattstellungen nebst Betrachtungen über den Schalenbau der Miliolinen* (Gustav Fischer, Jena, 1907).
- [187] J. Ridley, "Packing efficiency in sunflower heads", *Math. Biosci.* **58**, 129 (1982).
- [188] H. Coxeter, "The Role of intermediate convergents in Tait's explanation for phyllotaxis", *J. Algebra* **20**, 167 (1972).
- [189] I. Adler, "A model of contact pressure in phyllotaxis", *J. Theor. Biol.* **45**, 1 (1974).
- [190] I. Adler, "The consequences of contact pressure in phyllotaxis", *J. Theor. Biol.* **65**, 29 (1977).
- [191] J. C. A. Boeyens and D. C. Levendis, *Number theory and the periodicity of matter* (Springer, Dordrecht, 2008).
- [192] L. S. Levitov, "Phyllotaxis of flux lattices in layered superconductors", *Phys. Rev. Lett.* **66**, 224 (1991).
- [193] A. Frey-Wyssling, "Divergence in Helical Polypeptide Chains and in Phyllotaxis", *Nature* **173**, 596 (1954).
- [194] R. O. Erickson, "Tubular Packing of Spheres in Biological Fine Structure: Protein monomers of viruses, flagella, and microtubules form patterns like those of leaves of plants.", *Science* **181**, 705 (1973).
- [195] H.-W. Lee and L. S. Levitov, in *Symmetry in Plants*, Vol. 4, Series in Mathematical Biology and Medicine (World Scientific, 1998), pp. 619–653.
- [196] L. S. Levitov, "Energetic Approach to Phyllotaxis", *Europhys. Lett.* **14**, 533 (1991).
- [197] L. Levitov, "Fibonacci numbers in botany and physics : phyllotaxis", *JETP Lett.* **54**, 546 (1991).
- [198] S. Douady and Y. Couder, "Phyllotaxis as a physical self-organized growth process", *Phys. Rev. Lett.* **68**, 2098 (1992).
- [199] C. Nisoli, N. M. Gabor, P. E. Lammert, J. D. Maynard, and V. H. Crespi, "Static and Dynamical Phyllotaxis in a Magnetic Cactus", *Phys. Rev. Lett.* **102**, 186103 (2009).
- [200] C. Nisoli, "Spiraling solitons: A continuum model for dynamical phyllotaxis of physical systems", *Phys. Rev. E* **80**, 026110 (2009).
- [201] C. Nisoli, N. M. Gabor, P. E. Lammert, J. D. Maynard, and V. H. Crespi, "Annealing a magnetic cactus into phyllotaxis", *Phys. Rev. E* **81**, 046107 (2010).
- [202] J. Brankov and D. Danchev, "Ground state of an infinite two-dimensional system of dipoles on a lattice with arbitrary rhombicity angle", *Physica A* **144**, 128 (1987).
- [203] V. M. Rozenbaum, "Orientation states of dipoles on 2D Bravais lattices", *Zh. Eksp. Teor. Fiz* **99**, 1836 (1991).

- [204] J. D. Feldmann, G. J. Kalman, P. Hartmann, and M. Rosenberg, “Ground State of Magnetic Dipoles on a Two-Dimensional Lattice: Structural Phases in Complex Plasmas”, *Phys. Rev. Lett.* **100**, 085001 (2008).
- [205] M. Maksymenko, V. R. Chandra, and R. Moessner, “Classical dipoles on the kagome lattice”, *Phys. Rev. B* **91**, 184407 (2015).
- [206] M. S. Holden, M. L. Plumer, I. Saika-Voivod, and B. W. Southern, “Monte Carlo simulations of a kagome lattice with magnetic dipolar interactions”, *Phys. Rev. B* **91**, 224425 (2015).
- [207] J. M. Luttinger and L. Tisza, “Theory of Dipole Interaction in Crystals”, *Phys. Rev.* **70**, 954 (1946).
- [208] P. I. Belobrov and R. S. Gekht, “Ground state in systems with dipole interaction”, *Sov. Phys. JETP* **57**, 636 (1983).
- [209] D. Schildknecht, M. Schütt, L. J. Heyderman, and P. M. Derlet, “Continuous ground-state degeneracy of classical dipoles on regular lattices”, *Phys. Rev. B* **100**, 014426 (2019).
- [210] S. Prakash and C. L. Henley, “Ordering due to disorder in dipolar magnets on two-dimensional lattices”, *Phys. Rev. B* **42**, 6574 (1990).
- [211] E. Rastelli, S. Regina, and A. Tassi, “Planar triangular model with long-range interactions”, *Phys. Rev. B* **66**, 054431 (2002).
- [212] A. R. Way, K. P. W. Hall, I. Saika-Voivod, M. L. Plumer, and B. W. Southern, “Continuous degeneracy of the fcc kagome lattice with magnetic dipolar interactions”, *Phys. Rev. B* **98**, 214417 (2018).
- [213] J. Schönke, T. M. Schneider, and I. Rehberg, “Infinite geometric frustration in a cubic dipole cluster”, *Phys. Rev. B* **91**, 020410 (2015).
- [214] C. L. Henley, “Ordering due to disorder in a frustrated vector antiferromagnet”, *Phys. Rev. Lett.* **62**, 2056 (1989).
- [215] P. Politi, M. G. Pini, and R. L. Stamps, “Dipolar ground state of planar spins on triangular lattices”, *Phys. Rev. B* **73**, 020405 (2006).
- [216] E. Vedmedenko, A. Ghazali, and J.-C. Lévy, “Magnetic vortices in ultrathin films”, *Phys. Rev. B* **59**, 3329 (1999).
- [217] S. S. P. Parkin, M. Hayashi, and L. Thomas, “Magnetic Domain-Wall Race-track Memory”, *Science* **320**, 190 (2008).
- [218] L. Desplat, *Thermal Stability of Metastable Magnetic Skyrmions*, Springer Theses (Springer International Publishing, Cham, 2021).
- [219] M. Eto, Y. Hamada, and M. Nitta, “Composite topological solitons consisting of domain walls, strings, and monopoles in O(N) models”, *J. High Energ. Phys.* **2023**, 150 (2023).
- [220] M. Daraktchiev, G. Catalan, and J. F. Scott, “Landau theory of domain wall magnetoelectricity”, *Phys. Rev. B* **81**, 224118 (2010).
- [221] J. C. Tolédano and P. Tolédano, *The Landau Theory of Phase Transitions: Application to Structural, Incommensurate, Magnetic and Liquid Crystal Systems*, World Scientific Lecture Notes in Physics Volume 3 (World Scientific, Aug. 1987).
- [222] S. Pitois, G. Millot, and S. Wabnitz, “Polarization Domain Wall Solitons with Counterpropagating Laser Beams”, *Phys. Rev. Lett.* **81**, 1409 (1998).

- [223] H. Zhang, D. Y. Tang, L. M. Zhao, and X. Wu, "Observation of polarization domain wall solitons in weakly birefringent cavity fiber lasers", *Phys. Rev. B* **80**, 052302 (2009).
- [224] X. Yu and P. B. Blakie, "Dark-soliton-like magnetic domain walls in a two-dimensional ferromagnetic superfluid", *Phys. Rev. Research* **3**, 023043 (2021).
- [225] K. Choi and J. E. Kim, "Domain Walls in Superstring Models", *Phys. Rev. Lett.* **55**, 2637 (1985).
- [226] G. M. De Luca and A. Rubano, "Two-Dimensional Ferroelectrics: A Review on Applications and Devices", *Solids* **5**, 45 (2024).
- [227] Q. Pan, Z.-X. Gu, R.-J. Zhou, Z.-J. Feng, Y.-A. Xiong, T.-T. Sha, Y.-M. You, and R.-G. Xiong, "The past 10 years of molecular ferroelectrics: structures, design, and properties", *Chem. Soc. Rev.* **53**, 5781 (2024).
- [228] W. X. Zhou and A. Ariando, "Review on ferroelectric/polar metals", *Jpn. J. Appl. Phys.* **59**, SI0802 (2020).
- [229] R. C. G. Naber, C. Tanase, P. W. M. Blom, G. H. Gelinck, A. W. Marsman, F. J. Touwslager, S. Setayesh, and D. M. De Leeuw, "High-performance solution-processed polymer ferroelectric field-effect transistors", *Nature Mater* **4**, 243 (2005).
- [230] P. Muralt, "Ferroelectric thin films for micro-sensors and actuators: a review", *J. Micromech. Microeng.* **10**, 136 (2000).
- [231] S. Abe, T. Joichi, K. Uekusa, H. Hara, and S. Masuda, "Photonic integration based on a ferroelectric thin-film platform", *Sci Rep* **9**, 16548 (2019).
- [232] J. F. Scott, *Ferroelectric memories*, Advanced Microelectronics 3 (Springer, New York, Berlin Heidelberg, 2000).
- [233] P. Lenarczyk and M. Luisier, "Physical modeling of ferroelectric field-effect transistors in the negative capacitance regime", in *2016 International Conference on Simulation of Semiconductor Processes and Devices (SISPAD)* (Sept. 2016), pp. 311–314.
- [234] X. Chai, J. Jiang, Q. Zhang, X. Hou, F. Meng, J. Wang, L. Gu, D. W. Zhang, and A. Q. Jiang, "Nonvolatile ferroelectric field-effect transistors", *Nat. Commun.* **11**, 2811 (2020).
- [235] T. Mikolajick, M. H. Park, L. Begon-Lours, and S. Slesazeck, "From Ferroelectric Material Optimization to Neuromorphic Devices", *Adv. Mater.* **35**, 2206042 (2023).
- [236] I.-J. Kim and J.-S. Lee, "Ferroelectric Transistors for Memory and Neuromorphic Device Applications", *Adv. Mater.* **35**, 2206864 (2023).
- [237] L. Chen, M. E. Pam, S. Li, and K.-W. Ang, "Ferroelectric memory based on two-dimensional materials for neuromorphic computing", *Neuromorph. Comput. Eng.* **2**, 022001 (2022).
- [238] X. Niu, B. Tian, Q. Zhu, B. Dkhil, and C. Duan, "Ferroelectric polymers for neuromorphic computing", *Appl. Phys. Rev.* **9**, 021309 (2022).
- [239] S. Oh, H. Hwang, and I. K. Yoo, "Ferroelectric materials for neuromorphic computing", *APL Mater.* **7**, 091109 (2019).
- [240] J. Hwang, S. Lim, G. Kim, S.-O. Jung, and S. Jeon, "Non-Volatile Majority Function Logic Using Ferroelectric Memory for Logic in Memory Technology", *IEEE Electron Device Lett.* **43**, 1049 (2022).

- [241] X. Yin, X. Chen, M. Niemier, and X. S. Hu, "Ferroelectric FETs-Based Non-volatile Logic-in-Memory Circuits", *IEEE Trans. VLSI Syst.* **27**, 159 (2019).
- [242] X. Yin, A. Aziz, J. Nahas, S. Datta, S. Gupta, M. Niemier, and X. S. Hu, "Exploiting ferroelectric FETs for low-power non-volatile logic-in-memory circuits", in *Proceedings of the 35th International Conference on Computer-Aided Design* (Nov. 2016), pp. 1–8.
- [243] C.-L. Jia, K. W. Urban, M. Alexe, D. Hesse, and I. Vrejoiu, "Direct Observation of Continuous Electric Dipole Rotation in Flux-Closure Domains in Ferroelectric Pb(Zr,Ti)O<sub>3</sub>", *Science* **331**, 1420 (2011).
- [244] J. Michl and E. C. H. Sykes, "Molecular Rotors and Motors: Recent Advances and Future Challenges", *ACS Nano* **3**, 1042 (2009).
- [245] H.-C. Zhou and S. Kitagawa, "Metal–Organic Frameworks (MOFs)", *Chem. Soc. Rev.* **43**, 5415 (2014).
- [246] M. Safaei, M. M. Foroughi, N. Ebrahimpoor, S. Jahani, A. Omid, and M. Khatami, "A review on metal-organic frameworks: Synthesis and applications", *Trends Anal. Chem.* **118**, 401 (2019).
- [247] A. Gonzalez-Nelson, F.-X. Coudert, and M. A. Van Der Veen, "Rotational Dynamics of Linkers in Metal–Organic Frameworks", *Nanomaterials* **9**, 330 (2019).
- [248] E. B. Winston, P. J. Lowell, J. Vacek, J. Chocholoušová, J. Michl, and J. C. Price, "Dipolar molecular rotors in the metal–organic framework crystal IRMOF-2", *Phys. Chem. Chem. Phys.* **10**, 5188 (2008).
- [249] S. Bracco, F. Castiglioni, A. Comotti, S. Galli, M. Negroni, A. Maspero, and P. Sozzani, "Ultrafast Molecular Rotors and Their CO<sub>2</sub> Tuning in MOFs with Rod-Like Ligands", *Chem. Eur. J.* **23**, 11210 (2017).
- [250] Y. Zheng, F.-Z. Sun, X. Han, J. Xu, and X.-H. Bu, "Recent Progress in 2D Metal–Organic Frameworks for Optical Applications", *Adv. Opt. Mater.* **8**, 2000110 (2020).
- [251] U. Khan, A. Nairan, J. Gao, and Q. Zhang, "Current Progress in 2D Metal–Organic Frameworks for Electrocatalysis", *Small Struct.* **4**, 2200109 (2023).
- [252] S. Zang, Y. Su, Y. Li, Z. Ni, H. Zhu, and Q. Meng, "Interweaving of Triple-Helical and Extended Metal-O-Metal Single-Helical Chains with the Same Helix Axis in a 3D Metal–Organic Framework", *Inorg. Chem.* **45**, 3855 (2006).
- [253] L.-L. Wen, D.-B. Dang, C.-Y. Duan, Y.-Z. Li, Z.-F. Tian, and Q.-J. Meng, "1D Helix, 2D Brick-Wall and Herringbone, and 3D Interpenetration d<sup>10</sup> Metal–Organic Framework Structures Assembled from Pyridine-2,6-dicarboxylic Acid N -Oxide", *Inorg. Chem.* **44**, 7161 (2005).
- [254] X.-J. Liu, Y.-H. Zhang, Z. Chang, A.-L. Li, D. Tian, Z.-Q. Yao, Y.-Y. Jia, and X.-H. Bu, "A Water-Stable Metal–Organic Framework with a Double-Helical Structure for Fluorescent Sensing", *Inorg. Chem.* **55**, 7326 (2016).
- [255] W. Zhang and R.-G. Xiong, "Ferroelectric Metal–Organic Frameworks", *Chem. Rev.* **112**, 1163 (2012).
- [256] P. Jain, A. Stroppa, D. Nabok, A. Marino, A. Rubano, D. Paparo, M. Matsubara, H. Nakotte, M. Fiebig, S. Picozzi, E. S. Choi, A. K. Cheetham, C. Draxl, N. S. Dalal, and V. S. Zapf, "Switchable electric polarization and ferroelectric domains in a metal-organic-framework", *npj Quant Mater* **1**, 16012 (2016).

- [257] D. Booth, S. T. Rittenhouse, J. Yang, H. R. Sadeghpour, and J. P. Shaffer, "Production of trilobite Rydberg molecule dimers with kilo-Debye permanent electric dipole moments", *Science* **348**, 99 (2015).
- [258] M. Schlosser, D. Ohl De Mello, D. Schöffner, T. Preuschoff, L. Kohfahl, and G. Birkl, "Assembled arrays of Rydberg-interacting atoms", *J. Phys. B: At. Mol. Opt. Phys.* **53**, 144001 (2020).
- [259] A. Browaeys and T. Lahaye, "Many-body physics with individually controlled Rydberg atoms", *Nat. Phys.* **16**, 132 (2020).
- [260] M. Saffman, T. G. Walker, and K. Mølmer, "Quantum information with Rydberg atoms", *Rev. Mod. Phys.* **82**, 2313 (2010).
- [261] O. Firstenberg, C. S. Adams, and S. Hofferberth, "Nonlinear quantum optics mediated by Rydberg interactions", *J. Phys. B: At. Mol. Opt. Phys.* **49**, 152003 (2016).
- [262] S. J. Barnett, "Magnetization by Rotation", *Phys. Rev.* **6**, 239 (1915).
- [263] O. W. Richardson, "A Mechanical Effect Accompanying Magnetization", *Phys. Rev. (Series I)* **26**, 248 (1908).
- [264] A. Einstein and W. J. de Haas, "Experimental proof of the existence of Ampère's molecular currents", *Deut. Phys. Gesellsch. Verhandlungen* **17**, 152 (1915).
- [265] R. J. D. Tilley, *Understanding solids: the science of materials*, 2nd edition (Wiley, Chichester, West Sussex, United Kingdom, 2013).
- [266] R. P. Feynman, *The Feynman lectures on physics. Volume 3: Quantum mechanics*, New millennium edition, paperback [edition] (Basic Books, New York, 2011).
- [267] L. Landau and E. Lifshits, "On the theory of the dispersion of magnetic permeability in ferromagnetic bodies", *Phys. Z. Sowj.* **8**, 153 (1935).
- [268] T. Gilbert, "Classics in Magnetism A Phenomenological Theory of Damping in Ferromagnetic Materials", *IEEE Trans. Magn.* **40**, 3443 (2004).
- [269] R. M. White, *Quantum theory of magnetism: magnetic properties of materials*, 3rd, completely rev. ed, Springer Series in Solid-State Sciences (Springer, Berlin ; New York, 2007).
- [270] I. Dzyaloshinsky, "A thermodynamic theory of "weak" ferromagnetism of antiferromagnetics", *J. Phys. Chem. Solids* **4**, 241 (1958).
- [271] T. Moriya, "Anisotropic Superexchange Interaction and Weak Ferromagnetism", *Phys. Rev.* **120**, 91 (1960).
- [272] R. E. Camley and K. L. Livesey, "Consequences of the Dzyaloshinskii-Moriya interaction", *Surf. Sci. Rep.* **78**, 100605 (2023).
- [273] M. Bode, M. Heide, K. Von Bergmann, P. Ferriani, S. Heinze, G. Bihlmayer, A. Kubetzka, O. Pietzsch, S. Blügel, and R. Wiesendanger, "Chiral magnetic order at surfaces driven by inversion asymmetry", *Nature* **447**, 190 (2007).
- [274] P. Ferriani, K. Von Bergmann, E. Y. Vedmedenko, S. Heinze, M. Bode, M. Heide, G. Bihlmayer, S. Blügel, and R. Wiesendanger, "Atomic-Scale Spin Spiral with a Unique Rotational Sense: Mn Monolayer on W(001)", *Phys. Rev. Lett.* **101**, 027201 (2008).
- [275] U. K. Rößler, A. N. Bogdanov, and C. Pfleiderer, "Spontaneous skyrmion ground states in magnetic metals", *Nature* **442**, 797 (2006).

- [276] Y. Tokura and N. Kanazawa, "Magnetic Skyrmion Materials", *Chem. Rev.* **121**, 2857 (2021).
- [277] A. N. Bogdanov and C. Panagopoulos, "Physical foundations and basic properties of magnetic skyrmions", *Nat. Rev. Phys.* **2**, 492 (2020).
- [278] P. Lai, G. P. Zhao, H. Tang, N. Ran, S. Q. Wu, J. Xia, X. Zhang, and Y. Zhou, "An Improved Racetrack Structure for Transporting a Skyrmion", *Sci. Rep.* **7**, 45330 (2017).
- [279] N. S. Kiselev, A. N. Bogdanov, R. Schäfer, and U. K. Rößler, "Chiral skyrmions in thin magnetic films: new objects for magnetic storage technologies?", *J. Phys. D* **44**, 392001 (2011).
- [280] A. Fert, V. Cros, and J. Sampaio, "Skyrmions on the track", *Nat. Nanotech.* **8**, 152 (2013).
- [281] S. Luo, M. Song, X. Li, Y. Zhang, J. Hong, X. Yang, X. Zou, N. Xu, and L. You, "Reconfigurable Skyrmion Logic Gates", *Nano Lett.* **18**, 1180 (2018).
- [282] M. Chauwin, X. Hu, F. Garcia-Sanchez, N. Betrabet, A. Paler, C. Moutafis, and J. S. Friedman, "Skyrmion Logic System for Large-Scale Reversible Computation", *Phys. Rev. Applied* **12**, 064053 (2019).
- [283] J. S. Gardner, M. J. P. Gingras, and J. E. Greedan, "Magnetic pyrochlore oxides", *Rev. Mod. Phys.* **82**, 53 (2010).
- [284] J. P. C. Ruff, R. G. Melko, and M. J. P. Gingras, "Finite-Temperature Transitions in Dipolar Spin Ice in a Large Magnetic Field", *Phys. Rev. Lett.* **95**, 097202 (2005).
- [285] K. De'Bell, A. B. MacIsaac, and J. P. Whitehead, "Dipolar effects in magnetic thin films and quasi-two-dimensional systems", *Rev. Mod. Phys.* **72**, 225 (2000).
- [286] P. W. Anderson, "Antiferromagnetism. Theory of Superexchange Interaction", *Phys. Rev.* **79**, 350 (1950).
- [287] C. Nisoli, R. Moessner, and P. Schiffer, "Colloquium : Artificial spin ice: Designing and imaging magnetic frustration", *Rev. Mod. Phys.* **85**, 1473 (2013).
- [288] D. D. Sheka, O. V. Pylypovskyi, O. M. Volkov, K. V. Yershov, V. P. Kravchuk, and D. Makarov, "Fundamentals of Curvilinear Ferromagnetism: Statics and Dynamics of Geometrically Curved Wires and Narrow Ribbons", *Small* **18**, 2105219 (2022).
- [289] Y. Gaididei, V. P. Kravchuk, and D. D. Sheka, "Curvature Effects in Thin Magnetic Shells", *Phys. Rev. Lett.* **112**, 257203 (2014).
- [290] D. D. Sheka, O. V. Pylypovskyi, P. Landeros, Y. Gaididei, A. Kákay, and D. Makarov, "Nonlocal chiral symmetry breaking in curvilinear magnetic shells", *Commun. Phys* **3**, 128 (2020).
- [291] V. P. Kravchuk, D. D. Sheka, A. Kákay, O. M. Volkov, U. K. Rößler, J. Van Den Brink, D. Makarov, and Y. Gaididei, "Multiplet of Skyrmion States on a Curvilinear Defect: Reconfigurable Skyrmion Lattices", *Phys. Rev. Lett.* **120**, 067201 (2018).
- [292] N. L. Schryer and L. R. Walker, "The motion of 180° domain walls in uniform dc magnetic fields", *J. Appl. Phys.* **45**, 5406 (1974).
- [293] Y. Nakatani, A. Thiaville, and J. Miltat, "Faster magnetic walls in rough wires", *Nat. Mater.* **2**, 521 (2003).

- [294] M. Yan, C. Andreas, A. Kákay, F. García-Sánchez, and R. Hertel, “Fast domain wall dynamics in magnetic nanotubes: Suppression of Walker breakdown and Cherenkov-like spin wave emission”, *Appl. Phys. Lett.* **99**, 122505 (2011).
- [295] K. V. Yershov, V. P. Kravchuk, D. D. Sheka, and Y. Gaididei, “Curvature-induced domain wall pinning”, *Phys. Rev. B* **92**, 104412 (2015).
- [296] K. V. Yershov, V. P. Kravchuk, D. D. Sheka, O. V. Pylypovskyi, D. Makarov, and Y. Gaididei, “Geometry-induced motion of magnetic domain walls in curved nanostripes”, *Phys. Rev. B* **98**, 060409 (2018).
- [297] V. Brajuskovic and C. Phatak, “Understanding curvature effects on the magnetization reversal of patterned permalloy Archimedean spirals”, *Appl. Phys. Lett.* **118**, 152409 (2021).
- [298] Y. Gaididei, V. P. Kravchuk, F. G. Mertens, O. V. Pylypovskyi, A. Saxena, D. D. Sheka, and O. M. Volkov, “Localization of magnon modes in a curved magnetic nanowire”, *Low Temp. Phys.* **44**, 634 (2018).
- [299] R. Hertel, W. Wulfhekel, and J. Kirschner, “Domain-Wall Induced Phase Shifts in Spin Waves”, *Phys. Rev. Lett.* **93**, 257202 (2004).
- [300] V. K. Dugaev, P. Bruno, B. Canals, and C. Lacroix, “Berry phase of magnons in textured ferromagnets”, *Phys. Rev. B* **72**, 024456 (2005).
- [301] R. Streubel, E. Y. Tsymlal, and P. Fischer, “Magnetism in curved geometries”, *J. Appl. Phys.* **129**, 210902 (2021).
- [302] D. D. Sheka, “A perspective on curvilinear magnetism”, *Appl. Phys. Lett.* **118**, 230502 (2021).
- [303] D. Makarov, O. M. Volkov, A. Kákay, O. V. Pylypovskyi, B. Budinská, and O. V. Dobrovolskiy, “New Dimension in Magnetism and Superconductivity: 3D and Curvilinear Nanoarchitectures”, *Adv. Mater.* **34**, 2101758 (2022).
- [304] R. Streubel, P. Fischer, F. Kronast, V. P. Kravchuk, D. D. Sheka, Y. Gaididei, O. G. Schmidt, and D. Makarov, “Magnetism in curved geometries”, *J. Phys. D* **49**, 363001 (2016).
- [305] K. Liu and J. Wu, “Mechanical properties of two-dimensional materials and heterostructures”, *J. Mater. Res.* **31**, 832 (2016).



## *Acknowledgements*

This thesis would not have been possible without the guidance and support of my supervisor Prof. Dr. Peter Schmelcher.

I am also grateful for the help and support from the following people: Anja Cordes, Flemming Gloy, Daniel Jordan Bosworth, Friethjof Theel, Alejandro Romero-Ros, Maxim Pyzh, Malte Röntgen, Christian Morfonios, Alexandra Zampetaki, Aritra K. Mukhopadhyay, Ilias Englezos, Felipe A. O. Silveira, and Jie Chen.

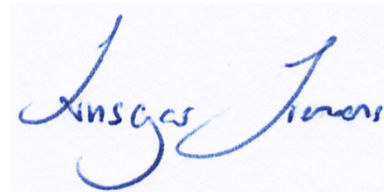


# Eidesstattliche Versicherung / Declaration of oath

Hiermit versichere ich an Eides statt, die vorliegende Dissertationsschrift selbst verfasst und keine anderen als die angegebenen Hilfsmittel und Quellen benutzt zu haben.

Sofern im Zuge der Erstellung der vorliegenden Dissertationsschrift generative Künstliche Intelligenz (gKI) basierte elektronische Hilfsmittel verwendet wurden, versichere ich, dass meine eigene Leistung im Vordergrund stand und dass eine vollständige Dokumentation aller verwendeten Hilfsmittel gemäß der Guten wissenschaftlichen Praxis vorliegt. Ich trage die Verantwortung für eventuell durch die gKI generierte fehlerhafte oder verzerrte Inhalte, fehlerhafte Referenzen, Verstöße gegen das Datenschutz- und Urheberrecht oder Plagiate

*Hamburg, den*  
19.09.2024



---

Ansgar Frederik SIEMENS